Statement of Originality

This thesis contains no material which has been accepted for the award of a degree or diploma in this or any other university. To the best of the candidate's knowledge and belief, this thesis contains no previously published or written material by another person except where due reference is made in the text of this thesis.

.....

Candidate : Y.S.K. Liow

Sound Radiation From Vortex Flows

by

Yoon Soon Keith Liow

Thesis submitted to Monash University
for the degree of
Doctor Of Philosophy

September 2003

Department of Mechanical Engineering,
Monash University

Abstract

This is a study on the aeroacoustic phenomena of unsteady flow fields. The main aim of this research is to understand the relationship between the vorticity dynamics and the far-field acoustic response. The scope of the problems presented in this project is restricted to flow fields that are periodic or semi-periodic and two-dimensional while the Mach number of the sound field is small. By virtue of the low Mach number assumption, the flow and acoustic fields are decoupled, i.e., the sound field (a linear response) is driven by the flow field (a non-linear source). In this study, the acoustic prediction models of Lighthill's acoustic analogy (1952), and Powell's vortex sound theory (1964) are used to predict the acoustic effects. The numerical implementation of the acoustic analogies is often known as the two-step method because it involves separate computations of the flow and acoustic fields.

In the first step of the aeroacoustic prediction method, the flow is predicted by solving the incompressible Navier-Stokes equations numerically using a commercial CFD code (FLUENT). The spatial and temporal discretisation schemes of the flow solver are both of second-order accuracy. The hydrodynamic fields are then exported from the grid used in the flow calculations to a different grid that is used to advance the acoustic solution. In the second step, the acoustic pressure is predicted by numerically solving the forced acoustic wave equation. The acoustic wave equation is essentially an inhomogeneous wave equation where the forcing is calculated using either Lighthill's acoustic analogy or Powell's vortex sound theory.

Many numerical issues involved in the calculation of an acoustic solution are not encountered in typical aerodynamic computations. This is because the nature and characteristics of acoustic wave propagation are different to those of incompressible fluid dynamics. A combination of a sixth-order spatial discretisation scheme and a fourth-order Runge-Kutta temporal scheme is employed to solve the acoustic wave equation. Such high-order methods are necessary to minimise the dispersion and dissipation errors in the time-evolving acoustic field. Two preventive measures are taken to ensure that the predicted acoustic solution is not contaminated by spurious noise. A start-up ramp is used to gradually introduce the acoustic source into the wave equation computation. In addition, the rate of spatial stretching of the acoustic grid is restricted to typically just a few percent. Both steps are necessary to limit the impact of the artificial initial transients. In addition to the two steps, prior to evaluating the acoustic source, the hydrodynamic velocity field is artificially decayed to zero away from the region of high velocity gradients. This is to ensure that the acoustic source terms converge smoothly to zero far from the true acoustic source region. As a result of all these steps, neither artificial dissipation nor explicit filtering are required to successfully predict the acoustic response for all three flow situations considered in this research program.

Three different problems of varying degrees of complexity in the flow dynamics were considered as part of this research. Besides providing a greater insight into the aeroacoustic phenomena, the three

cases also contribute to validating the computational approach used in this project. In the first two cases, the flow field is *compact*, i.e., the characteristic lengthscale of the flow is much smaller than the acoustic wavelength. The vortex dynamics is relatively simple and well-defined. In the first case, the acoustic waves generated by the co-rotation motion of an isolated vortex pair is investigated. This test case is widely recognised as a benchmark problem in aeroacoustics. The Reynolds number based on the circulation of the vortex core is $Re = 7500$ while the Mach number based on the induced co-rotation velocity is $\mathrm{Ma} = 0.06$. Comparison of the numerical results are made with the solution calculated using the method of matched asymptotic expansions, and numerical solutions computed using direct simulations. Prior to the vortex merger, the amplitudes and waveforms of the acoustic signals are in excellent agreement with the analytical predictions.

The second case considers the acoustic field generated by the motion of a pair of co-axial vortex rings moving in the same direction along a common axis of symmetry. The Reynolds number of the flow based on the circulation of each ring is $Re = 7500$, while the Mach number based on the translational velocity of the vortex ring in isolation covers the range $\mathrm{Ma} = 0.0025$, 0.005 and 0.01. The effect of the ratio of the initial axial distance between the vortex rings z_o, to the toroidal ring radius y_o, on the sound radiation is investigated. At low Mach numbers, the far-field directivity of the acoustic signals is similar to a lateral axisymmetric quadrupole. In contrast to the first case where the amplitude and time variations of the acoustic signals are in excellent agreement with the solution obtained using the method of matched asymptotic expansions, here there are some obvious discrepancies between the numerical results and the analytical predictions. This was attributed to the quasi-periodic distortion of the vortex cores during the leapfrogging motion.

In both cases, the acoustic source is associated with the unsteady motion of the vortices. Because the flow dynamics is simple, the acoustic analysis could be carried out without the added complication of an extensive vorticity field. While the flow is viscous, the modification to the acoustic source owing to the presence of physical viscosity is initially relatively negligible at the Reynolds numbers considered. The vorticity in the fluid is assumed to be generated by a force which vanishes thereafter. Furthermore, because there are no external forces acting, there is no further generation of vorticity in the fluid.

In the final case the acoustic radiation from laminar flow past a two-dimensional cylinder of rectangular cross section is considered. Here, the motion of vorticity as well as the changes in the strength of the vortices has to be included in the acoustic analysis. The flow instability controlled by a feedback loop between the leading- and trailing-edge vortex shedding results in a dipolar sound field. The instability mechanism synchronising the leading- and trailing-edge shedding is known as the *Impinging Leading Edge Vortex* (ILEV) instability. The Reynolds number of the flow is based on the freestream velocity, U_∞ and the plate thickness, d. The Mach number is based on the freestream velocity, $\mathrm{Ma} = U_\infty/c_o$. The effect of Reynolds number on the sound radiation is considered by predicting the acoustic fields for $Re = 300$ and 400. It was envisaged that the presence of the leading- and trailing-edge region would result in

distinct and separate source regions. For each Reynolds number, acoustic simulations are performed for Ma = 0.05, 0.1 and 0.2. At $Re = 300$, the amplitudes and far-field directivity patterns of the acoustic signals are in excellent agreement with the solution (numerical and experimental) obtained for laminar flow past a circular cylinder at a similar Reynolds number. In contrast, at $Re = 400$ the time variation of the acoustic signal becomes less sinusoidal. This is attributed to the phase difference between the sources associated with vortices shedding from the trailing edge and that from leading-edge vortices passing the trailing edge. In addition the vortex structures that shed into the wake are more compact which may also contribute to the non-sinusoidal far-field signal. As the Mach number is increased, the propagation angle starts to shift towards the upstream direction due to the Doppler effect. By isolating certain parts of the plate, we found that the dominant sound source is associated with the region around the trailing edge.

Several conclusions can be drawn from the simulations performed in this study. Firstly, our results have shown that in compact vortical flows in free space, the sound field has a mainly quadrupole character. However, when the flow is driven by natural shedding caused by the presence of a rigid body in a fluid stream, the flow instability, described as a regular shedding of vortices into the wake, causes a dipolar radiation field. There is a strong link between the vorticity field, aerodynamic forces and the directivity of the sound field. This particular sound field is also known as an Aeolian tone.

Secondly, at low Mach numbers, Lighthill's acoustic analogy, and Powell's vortex sound theory effectively produce identical far-field acoustic signals. This implies that the additional term $\nabla^2(\mathbf{u}^2/2)$ present only in Lighthill's acoustic analogy is negligible compared to the other term $\nabla \cdot (\omega \times \mathbf{u})$ which is found in both acoustic theories. As such, Powell's vortex sound theory is highly recommended for future work on aeroacoustic phenomena since the additional term in Lighthill's formulation decays only slowly which leads to many practical difficulties in numerical implementations.

Finally, the effect of the Mach number, which is synonymous with the effect of source compactness, is considered through a harmonic expansion of the predicted acoustic solution. Such a decomposition of the pressure field into a sum of harmonic modes is possible owing to the linearity of the acoustic wave equation. This analysis shows that the far-field directivity is affected by Mach number. It must be noted that in the analytical solution (which is valid only at the asymptotic limit), the far-field directivity remains independent of Mach number.

Acknowledgements

The author wishes to take this opportunity to thank the following persons (in no particular order) for providing invaluable support and guidance throughout the course of this study.

1. My two supervisors, Associate Professor Mark C. Thompson, and Professor Kerry Hourigan, for their unwavering faith in my ability and also providing me with excellent support and supervision.

2. My good friend and colleague, Dr. Tan Boon Thong, for his technical assistance in various aspects of the aeroacoustic algorithm, and providing me with moral as well as financial support.

3. My fellow research students, Kris Ryan, Lewis Mununga, and Mervyn Tan, for the many honest and yet heartfelt discussions.

The author also wishes to acknowledge the financial support from the Monash Graduate Scholarship (MGS), and the International Overseas Postgraduate Research Scholarships (IPRS).

Nomenclature

A	zeroth order wave mode,
B_m	m^{th} order cos wave mode,
C_m	m^{th} order sin wave mode,
c	plate chord length,
c_d	drag coefficient based on plate thickness and free-stream velocity,
c_l	lift coefficient based on plate chord and free-stream velocity,
c_p	pressure coefficient based on plate thickness and free-stream velocity,
c_o	wave propagation speed in the acoustic medium,
CAA	computational aeroacoustics,
CFD	computational fluid dynamics,
d	plate thickness length,
e_o	radius of the vortex core,
f_t	start-up function for the initial condition for CAA,
f_x, f_y	spatial filter functions for the Cartesian coordinate system,
f_z, f_y	spatial filter functions for the polar coordinate system,
H_l	the acoustic source terms in Lighthill's acoustic analogy,
H_p	the acoustic source terms in Powell's vortex sound theory,
$H^2_{(2)}$	second kind Hankel function of order 2,
l_{fx}, l_{fy}	lengths of the filter functions in the Cartesian coordinate system,
l_{fz}, l_{fy}	lengths of the filter functions in the polar coordinate system,
k	wave number,
K	total kinetic energy in the flow,
m	harmonic mode of the multipole expansion,
Ma	Mach number based on the flow characteristic velocity and wave propagation speed,
n	shedding mode of flow around rectangular plate,
p	normalised acoustic pressure,
p	kinematic pressure,
$Q(t)$	second-order moments of vorticity,
$Q^{'''}(t)$	quadrupole sound source,
r_c	radial distance from the core centroid,
Re	Reynolds number based on circulation around the vortex,
St	Strouhal number based on freestream velocity and plate thickness,

T_{ij}	Lighthill's stress tensor,
t	non-dimensionalised simulation time,
t_r	period of the start-up function,
t^*	retarded non-dimensionalised simulation time,
Δt	size of the time step,
u_o	translational velocity of the vortex ring in isolation,
U_o	induced rotational velocity of the spinning vortex pair,
U_∞	freestream velocity,
$\mathbf{u}$	velocity vector of the flow field,
Δx	size of the grid spacing,
y_o	toroidal radius of the vortex ring,
z_o	initial axial distance separating the vortex rings,
Z_o	initial distance separating the spinning vortex pair,
u, v	velocity in the Cartesian/polar coordinate system,
$u^{'}, v^{'}$	velocity in the Cartesian/polar coordinate system after application of spatial filter,
(x, y)	2D Cartesian coordinate system,
(z, y)	polar coordinate system,
Γ_o	initial circulation of the fluid,
λ	wavelength of the acoustic waves,
ω	vorticity in the azimuthal direction,
μ_o	mean kinematic viscosity of fluid,
ρ	kinematic density,
ρ_o	mean fluid density,

Contents

Chapter 1

Introduction

The subject of sound generated aerodynamically is an aspect of fluid mechanics that is of fundamental importance as it underpins a wide range of engineering issues such as acoustic-induced structural vibrations, automobile aerodynamics, mixing of fluids and jet noise. In this thesis, the term aerodynamic sound refers to acoustic fluctuations generated purely by an unsteady flow in an otherwise ambient medium at rest. In other words, the vibrational effects of solid bodies if present are not considered to contribute to aerodynamic sound.

Most textbooks on classical acoustics (e.g., Rayleigh's Theory of Sound (1896)) have concentrated on 'pleasant' sound generated from vibrating musical instruments. Yet, in the current era of industrialisation, engineers and scientists are more likely to be interested in noise generated by large volumes of air being displaced by rotating machinery. This area is sometimes known as modern acoustics. The primary objective of studying modern acoustics is to understand aeroacoustic phenomena and subsequently to devise effective methods of noise and vibration control. This is relevant to many modern engineering applications such as turbo-machinery, high speed trains and jet-engines. For example, in the civil aviation industry more stringent noise regulations may mean that the new generation of high carrying capacity aircraft may not be allowed to land at particular airports, or at least will need to obey stringent curfews during the night. In the automobile industry, new cars are carefully designed to reduce transmission of noise to the interior which would interfere with passenger comfort and the functionality of high-fidelity sound systems.

This chapter aims to provide the reader with a basic knowledge of aerodynamic sound generation and propagation. Firstly, a review of the classical acoustic analogies of Lighthill (1952), Powell (1964), and Möhring (1978) is presented. This is followed by a brief description of the various solution approaches, both theoretical and numerical, which were developed specifically for the field of aeroacoustics over the past forty years or so. It has been pointed out by various aeroacoustic workers that the field of

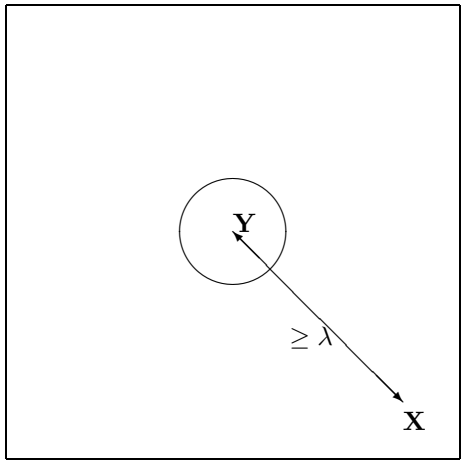

Figure 1.1: Sketch of the definitions of the localised flow region **Y** and a certain far field position vector **X** in an ambient fluid (not to scale).

computational aeroacoustics (CAA) is different to that of computational fluid dynamics (CFD). As such, the numerical requirements for an accurate aeroacoustic solution are unique to CAA.

Relevant results on aeroacoustic phenomena ranging from simple flow configurations (i.e., involving line and ring vortices) to the classical Aeolian tone (sound radiated from self-sustained vortex shedding in bluff body flows) are reported. Furthermore, an overview of the various numerical issues encountered in implementing the acoustic analogies, and modelling the propagation of acoustic waves is included in this chapter. This chapter concludes with a brief mention of the stated goals of this research program.

1.1 Far-field subsonic aerodynamic sound

As the term 'far-field' suggests, acoustic waves are generated by flow unsteadiness which is localised in an ambient medium. The concept of the near-field (denoted by the symbol **Y**) and the far-field (represented by the symbol **X**) regions is illustrated in Figure 1.1. The lengthscale of the near-field region is defined by the size of the eddies, l, which are enclosed within some imaginary boundary, while the far-field region is represented by the acoustic wavelength, λ. The acoustic waves generated from the near-field region propagate radially towards infinity in an ambient fluid. In the far-field region, the condition that only outwardly travelling waves exist was first formulated by Sommerfeld (also known as the Sommerfeld radiation condition). Such wave propagation is linear and is governed by the homogeneous wave equation. The ambient acoustic medium is defined with a uniform density ρ_o, pressure p_o, and speed of wave propagation c_o, while the acoustic fluctuations in pressure p and density ρ are at least several orders of magnitude smaller than the former. Typical far-field observation positions are in the range of multiple wavelengths λ in the radial direction away from a fixed origin. With the propagation distance from the

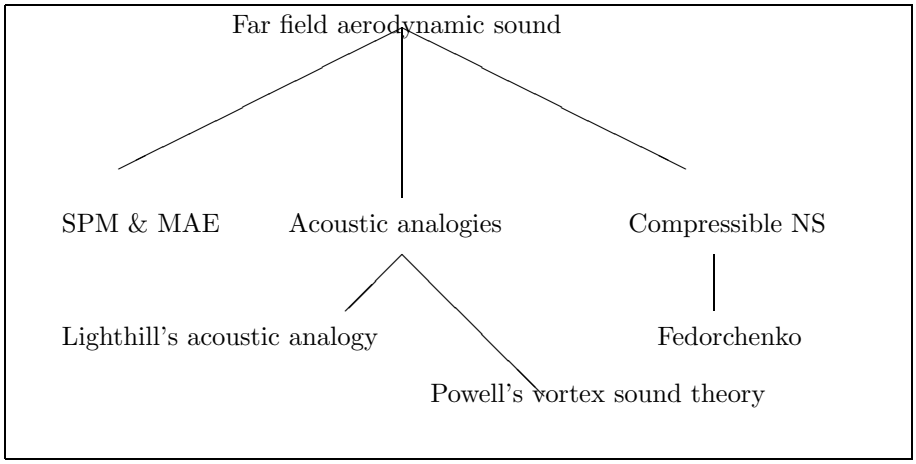

Figure 1.2: Diagram highlighting the different solution approaches used to predict aerodynamic sound emission. For convenience of notation, the term 'SPM' refers to the singular perturbation method while 'MAE' denotes matched asymptotic expansions.

fixed origin to the observation position, the time taken for the waves to travel from the origin to the position is known as the retarded-time, $t^* = t - \lambda/c_o$ where $\lambda = |\mathbf{x} - \mathbf{y}|$.

Analysis of the definition of the sound source by Dowling & Ffowcs Williams (1983) assumes that there is an external known forcing function $\mathbf{Q}$. The function $\mathbf{Q}$ is somewhat arbitrarily placed on the right-hand side of the homogeneous wave equation and is limited to the near-field region $\mathbf{Y}$. The inhomogeneous wave equation is then formally solved to yield the solution as a function of the volume integral of $\mathbf{Q}$. The three main elementary sound sources are the monopole, dipole and quadrupole. Mathematically, the sources are considered to emit sound waves from a fixed point.

Properties of a monopole source are that the sound field is omni-directional and has a $(1/r)$ decay rate, where r is the radial distance from the fixed origin. When the total source strength is zero, the resulting sound field can only be made up of dipoles, quadrupoles and higher-order multipoles. Assuming that $\mathbf{Q}$ is expressed as the divergence of a function $\mathbf{f}$, i.e., $\mathbf{Q} = \nabla \cdot \mathbf{f}$, the condition for a dipole sound field to exist is that the volume integral of $\nabla \cdot \mathbf{f}$ is zero. Similar to $\mathbf{Q}$, the function $\mathbf{f}$ is also limited to the near-region and as such vanishes in the far-field acoustic region. Conceptually, an acoustic dipole is formed when two monopoles of opposite strengths are placed a close distance apart (relative to the far field). Due to the effects of time retardation, phase cancellations will occur. As a consequence, near the two monopoles, the acoustic pressure decays as $1/r$. However, far from the monopoles, the sum of these two sources leads to a pressure that decays as $1/r^2$. In addition, there is a $\cos\theta$ directivity in the sound field. The strength of the dipole source is related to the magnitude of the force. The quadrupole can be imagined mathematically as the divergence of the dipole or double divergence of the monopole. The efficiency of sound generation decreases in the ascending order of the multipoles.

Figure 1.2 shows a tree-diagram featuring the various solution approaches to predicting the sound generated by a slightly compressible flow. Though there are other methods, these listed approaches represent the common ones adopted by most researchers in the aeroacoustic community. The combined approach of SPM and MAE is an analytical technique and has been widely used in inviscid flows. Lighthill's (1952) acoustic analogy was developed independently of the analytical methods of SPM and MAE. Powell's (1964) theory of vortex sound is considered by Howe (1975) to be similar to Lighthill's (1952) acoustic analogy in the limit of low Mach number. The acoustic analogies can be applied numerically to predict the far-field sound and are used exclusively in the present study. The third method is that the flow field and the sound field can be solved simultaneously on the same computational domain through integrating the Navier-Stokes equations directly in time. This approach adopts the direct numerical simulation (DNS) and large eddy simulation (LES) techniques. It makes no distinction between the flow region and the acoustic region. Both the DNS and LES methods were developed initially to study turbulent flows and shear layer flows. As such, the acoustic waves, which are many orders of magnitude smaller than the hydrodynamic fluctuations, were often left unresolved. To accurately resolve the generation of the acoustic waves, high-order spatial and temporal schemes are used. If both the near-field and far-field regions of the aeroacoustic phenomena are of interest to the researcher, then either the direct method or Fedorchenko's (2000) approach should be the answer.

Briefly, the acoustic analogy attempts to relate the generation of sound waves to a local function varying in time and space. One of the foremost assumptions of the acoustic analogy is that the flow characteristic velocity is assumed to be much smaller than the propagation speed of the sound wave. The acoustic variable is a scalar quantity and the source function $\mathbf{Q}$ is a function of the vector velocity field. To complete the whole picture, the source function has to be known in advance of the sound field. In the next section, a review of the acoustic analogies developed separately by Lighthill (1952) and Powell (1964) are presented.

1.1.1 Lighthill's acoustic analogy

Lighthill's acoustic analogy published in 1952 is one of, if not, the most important contribution towards the general understanding of aerodynamic sound generation. The focus of that paper was on the small-scale sound energy generated as a result of fluctuating flow. Lighthill's (1952) hypothesis of aerodynamic sound generation states that the sound is generated as a result of the transfer of momentum from the fluctuating flow to the acoustic field. Because the energy of the acoustic field is estimated to be at least several orders of magnitude smaller than that of the flow, feedback from the sound field to the flow field is not considered; thus resonate situations cannot be modelled. The sound field, being the response function, is driven by the flow which acts as an external forcing in an otherwise ambient acoustic medium.

In deriving the acoustic analogy, Lighthill first considered the continuity and Navier-Stokes momen-

tum equations under zero external body force. Furthermore, solid boundaries (if present) were assumed to be rigid, thereby excluding any possibility of changes in the mass flux and rate of change of mass flux into the fluid. The fluid is assumed to be Newtonian (i.e., the viscous stresses are proportional to the rate of deformation) and isotropic. Furthermore, thermal sound sources (i.e., kinetic heating or cooling) are explicitly excluded from the analysis.

The continuity equation is as follows

$$\frac{\partial \rho}{\partial t} + \rho \nabla \cdot \mathbf{u} = 0, \tag{1.1}$$

and the Reynolds form of the momentum equation is

$$\frac{\partial \rho u}{\partial t} + \nabla u_i u_j + \nabla p = 0, \tag{1.2}$$

while the approximate momentum equation for momentum density ρu in vector notation form is

$$\frac{\partial \rho u_i}{\partial t} + c_o^2 \nabla \rho = 0. \tag{1.3}$$

Through manipulation of these three equations, the following inhomogeneous wave equation results

$$\frac{\partial^2 \rho}{\partial t^2} - c_o^2 \nabla^2 \rho = \frac{\partial^2 T_{ij}}{\partial x_i \partial x_j}, \tag{1.4}$$

where the term T_{ij} on the right-hand side of the equation is known as the Lighthill's stress tensor and is as follows

$$T_{ij} = \rho u_i u_j + p_{ij} + c_o^2 \rho \delta_{ij}. \tag{1.5}$$

Here, p_{ij} is the compressive stress tensor and u_i is the velocity component in the x_ith direction. The symbol δ_{ij} refers to the Kronecker delta function.

The momentum density ρu_i in the acoustic medium is governed by the approximate momentum equation in Equation 1.3. Solving the continuity and momentum equations 1.1 and 1.2 and eliminating the terms ρu_i yields the inhomogeneous acoustic wave equation. Thus, equation 1.4 (also known as the acoustic wave equation) has been derived from an exact rearrangement of the continuity and momentum equations. Lighthill's acoustic equation is a partial differential equation that contains five unknown flow variables. At this point, there is no distinction between the near-field and far-field properties of the terms in the acoustic wave equation. Two assumptions relating to Lighthill's hypothesis are then invoked in order to satisfy the following statement, '*Thus outside the airflow the density satisfies the ordinary equations of sound ...*' (Lighthill (1952) pp. 21) are as follows

1. **The flow is assumed to be 'compact'.** The hydrodynamic field which enters through quadratic terms in T_{ij} is assumed to decay rapidly (of order $1/x^3$) outside the airflow. This implies that in the far-field region, the velocity field assumes only the characteristics of the acoustic particle velocity (which are much smaller in magnitude but larger in lengthscale compared to the flow velocity). In

addition, the acoustic waves generated from the near field are expected to propagate freely towards infinity. The effects of convection and refraction are implicitly included in the acoustic forcing.

2. **No sound sources exist outside the airflow.** Potential sound sources like viscous stresses and heat conduction effects which might be present in the airflow are assumed to be non existent in the acoustic far-field. For a low Mach number and high Reynolds number flow, the viscous terms in the airflow are also assumed to be negligible (neglecting kinetic heating or cooling as potential acoustic sources), leaving the quadrupole term $T_{ij} \approx \rho_o u_i u_j$ as the principal acoustic source.

1.1.2 Powell's theory of vortex sound

In Powell's (1964) theory of vortex sound, the region of non-vanishing vorticity vector corresponds to the acoustic source region. Powell has hypothesised that generation of sound is related to the change in vorticity, either spatially or temporally in an unsteady fluid flow. The vorticity is considered to induce both the flow field and sound field. The theory of vortex sound relates the sound sources to (i) changes in vortex strength and (ii) motion of vorticity. The change in vortex strength is thought to cause a locally dipolar-like behaviour while unsteady motion of vortices lead to a quadrupole radiation field. The procedure for the derivation of the acoustic equation is similar to Lighthill's in that an exact rearrangement of the continuity and momentum equations is required. Beginning with non-conservative form of the Euler momentum equation in the absence of body forces

$$\frac{\partial \mathbf{u}}{\partial t} + (\omega \times \mathbf{u}) + \nabla \frac{1}{2} u^2 + \frac{1}{\rho} \nabla p = 0. \tag{1.6}$$

Using the adiabatic gas assumption, $p = \rho c^2$,

$$\frac{\partial^2 \rho}{\partial t^2} = -\nabla \cdot \frac{\partial (\rho \mathbf{u})}{\partial t}, \tag{1.7}$$

$$\frac{\partial^2 p}{\partial t^2} - c_o^2 \nabla^2 p = -c_o^2 \nabla \cdot \frac{\partial (\rho \mathbf{u})}{\partial t} - c_o^2 \nabla \cdot \nabla p. \tag{1.8}$$

Using the momentum equations, the right-hand side of equation 1.8 representing the acoustic forcing is rewritten as follows

$$\nabla \cdot \left[\nabla \cdot \rho(\omega \times \mathbf{u}) + \nabla \frac{\rho u^2}{2} - \mathbf{u} \frac{\partial \rho}{\partial t} - \frac{1}{2} u^2 \nabla \rho \right]. \tag{1.9}$$

At this point, Powell's acoustic solution describes the acoustic pressure from four distinct source terms. The first term represents the Coriolis acceleration term. The contribution of each term can be deduced by comparing the relative magnitude of the each term scaled to both the Strouhal number St, and Mach number Ma. The last two terms of equation 1.9 were subsequently discarded by assuming a low speed flow (i.e., $\mathrm{Ma} \ll 1$ and $\mathrm{St} \times \mathrm{Ma} \ll 1$). Formal solution of the acoustic wave equation in terms of the first two contribution then results in four distinct integrals. The acoustic field is made up of (i) dipoles distributed in the volume with strength proportional to $\omega \times \mathbf{u}$, (ii) a volume distribution of monopoles

of strength $(\partial^2/\partial t^2)\frac{1}{2}\rho u^2$, (iii) a surface distribution of dipoles over the solid boundaries with strength proportional to the Bernoulli pressure, and (iv) a monopole source over the surface boundary due to its motion normal to itself. Powell further simplified the source term by disposing of the dipole source associated with the $\nabla^2\rho u^2/2$ term. By considering a flow which varies slowly with Strouhal number, the vorticity distribution on the surface is then assumed to be time-invariant. Furthermore, if the surface is assumed to be fixed and rigid, there would be no motion normal to itself and hence there would be no associated monopole source.

On the sound generated by flows in a free-space environment

In Powell's (1964) analysis of aerodynamic sound generation, the sound source is limited to the rotational part of the flow. Möhring's (1978) noted the difficulty in implementing Powell's vortex sound theory because in vortex sheets, the velocity is singular at the centre of the vortex. To avoid the singularity, the far-field pressure was shown to be an integral of the product of a vector Green's function $\mathbf{G}$ and Powell's source term, $\nabla \times \mathbf{L}$. Using the Helmholtz equation for vorticity in an incompressible flow, the term $\nabla \times \mathbf{L}$ was rewritten as $\partial\omega/\partial t$. Hence, the acoustic pressure is shown to be a function of the time-dependent vorticity and does not include any velocity terms. For the vector Green's function to exist, two assumptions were made: (i) the flow was assumed to be compact and (ii) $c_o \ll \partial^2 G/\partial t^2$, where G represents an appropriate Green's function for the wave equation. For the general aeroacoustic problem of sound emission by flows in free space, Möhring approximated the Green's function (to be known as Q) as follows

$$Q(t) = -\frac{1}{12\pi}\int_V y_i(\mathbf{y}\times\boldsymbol{\omega})_j d^3y. \tag{1.10}$$

The analytical expression for the far-field acoustic pressure is then rewritten as follows

$$p(\mathbf{x},t^*) = \frac{\rho_o x_i x_j}{c_o^3 x^3}\frac{\partial^3 Q^*}{\partial t^3}. \tag{1.11}$$

The above equation expresses the acoustic pressure as being a linear function of the vorticity. Müller & Obermeier (1978), Kambe & Minota (1981), and Kambe (1986) have subsequently applied singular perturbation methods and the method of matched asymptotic expansions to the general free-space aeroacoustic problem and derived a far-field expression which was identical to Möhring's equation. This 'linear theory' has been extensively applied to simple flow configurations (e.g., ring collisions, co-axial vortex rings, co-rotating vortex pairs). It should be noted that this particular theory refers to the sound generated in free-space, i.e., there are no external forces acting on the flow and, in addition, the total kinetic energy of the flow is also conserved. Under such circumstances, the quadrupole term $Q^{'''}(t)$ is the leading-order sound source from unsteady flows in free-space.

1.1.3 Common assumptions found in acoustic analogies

In deriving the acoustic theories, it is clear that several assumptions are frequently invoked. While these assumptions would pose no difficulty when applied to simple flow configurations, deviations might arise when applying the theories to complicated flows which may not obey the assumptions used to derive the theories in the first place. Presented briefly in the following sections are the two most commonly used assumptions being source compactness and flow compactness.

Source compactness

The acoustic analogies were developed to predict sound generated aerodynamically for flow situations at low Mach number, $\mathrm{Ma} \ll 1$. The implication of a slightly compressible flow is that while the time scales of the eddies and the acoustic waves remain the same, the lengthscale of the eddies is much smaller than the acoustic wavelength. In acoustic terminology, such a lengthscale disparity is known as the *compact source* assumption. Actually, mathematical acoustic sources satisfy the source compactness criteria since they are based on point singularities. The method of matched asymptotic expansions is one solution method that invokes the compact source assumption. In numerical applications of the acoustic analogies, the issue of source compactness can be investigated by performing the acoustic simulations on an identical flow problem but at different Mach numbers and analysing the various modes present in the predicted acoustic field.

Flow compactness

The assumption of *flow compactness* was used in Lighthill's (1952) acoustic analogy to imply that the fluctuating flow is finite only in the near field. This precludes the scenario of the acoustic waves encountering a vorticity field as they propagate radially away from the source region. Specifically, in Lighthill's (1952) acoustic analogy, both the refractive and convective effects present in the fluctuating flow are included implicitly in the stress tensor T_{ij}. When the flow is assumed to be compact, the lengthscale of the fluctuating flow field is considered to be of the same order of magnitude as that of the characteristic lengthscale of the flow. Note that the non-zero vorticity field may consist of one or more spatially-distributed structures as in multiple vortex pairings. However, in general, viscous flows in the presence of solid boundaries have an extensive wake (eg., shear layers and bluff body flows) and do not satisfy the compact flow assumptions.

The singular perturbation method has been used to analyse both Lighthill's (1952) and Ribner's (1962) acoustic analogies. Crow (1970) aimed to mathematically clarify the definition of the flow compactness assumption adopted in Lighthill's acoustic analogy. The acoustic domain was decomposed to an

inner slightly compressible core and an outer acoustic field. Invoking the compact flow assumption, the velocity field was further decomposed into a solenoidal component and an irrotational acoustic potential. Crow further pointed out that if the flow is assumed to be compact, then the rate of convergence of the hydrodynamic velocity to zero away from the source region is guaranteed. This is due to Kelvin's theorem of constant circulation which states that vorticity once generated locally by some force, will stay confined within a finite region as long as the time-scale of the eddies is much less than that of the associated acoustic wavelength. As a result, the integral of the vortex dipole moment converges and this implies that the decay of the solenoidal velocity is of order $1/x^3$.

Crow introduced a spatial dimension L to investigate two hypothetical cases, namely, $L \approx l$ and $L \gg l$. Crow argued that one of the requirements of successful implementation of Lighthill's theory requires some advance knowledge of the spatial extent of the source region, and hence $T_{ij} = \rho_o u_i u_j$. Crow also identified Kelvin's theorem for compressible flow as central to the aerodynamic sound problem. Furthermore, in the limits of low Mach numbers, if the flow is assumed to be compact, then the source compactness assumption is also well satisfied.

1.2 Previous studies

In the previous section, a brief review of the acoustic theories (also commonly known as the classical acoustic analogies) of Lighthill (1952), Powell (1964), and Möhring (1978) was presented. Here, we report on the results of various aeroacoustic studies; experimental, analytical and numerical. Firstly, the different solution approaches used to predict the flow field and the acoustic field are described. Secondly, past studies relevant to current aeroacoustic research are mentioned. The final part of this section examines in greater detail, the results of flow situations that will be studied by the author. The specific aeroacoustic problems are (i) the sound generated by a pair of co-rotating vortex cores, (ii) the acoustic emissions from a pair of co-axial vortex rings moving along a common axis and (iii) sound radiation from vortex shedding in bluff body flows.

The three main approaches used in solving computational aeroacoustics problems are (i) the classical acoustic analogies, (ii) acoustic/viscous splitting techniques and (iii) direct numerical simulations. Predating these computational aeroacoustic techniques is the analytical method known as the matched asymptotic expansions.

1.2.1 Matched asymptotic expansions

One of the commonly used approaches in the theoretical analysis of aeroacoustics problems is the method of singular perturbation and matched asymptotic expansions (MAE). Müller & Obermeier (1967) has used

the MAE method to derive an analytical expression for the far-field sound of a spinning point vortex pair. Crow (1970) treated the aerodynamic sound problem using the singular perturbation method. Kambe & Minota (1981) has extended Powell's (1964) vortex sound theory and Möhring's (1978) moment of vorticity theory to derive an analytical solution for the sound generated from the leap-frogging of a pair of like-signed co-axial vortex rings, and collision of a pair of co-axial opposite-signed vortex rings.

In the MAE approach, the complex potential function ϕ is used to represent the variables in the flow field and acoustic field. In the limit of small Mach number, the rotational flow is confined within the near-field while the acoustic perturbations lie in the far-field region. In the near-field, the flow variable ϕ is governed by the continuity equation, the incompressible Euler equations and the adiabatic gas equation, while in the far-field ϕ is governed by the homogeneous compressible wave equation. Next, an intermediate domain is assumed whereby terms from the flow solution are matched with those from the far-field solution with harmonic assumptions to provide a solution which is asymptotically valid as $\mathrm{Ma} \to 0$, everywhere in the domain from the near-field to the far-field. The solution in the intermediate region is also known as the composite solution. The acoustic perturbations caused by the unsteadiness in the hydrodynamic region is then obtained through the leading term in the matched asymptotic expansion solution of the complex potential function.

1.2.2 Acoustic analogies

The classical acoustic analogies have been used to study sound generated by low Mach number vortical flows which include bluff body flows. This approach is limited to situations where the size of the eddies is compact relative to the acoustic wavelength. Numerical implementation of the acoustic analogy involves separate computations of the flow field and the sound field. Hence, it has been described by some researchers as the two-step approach. Typically, the flow field is assumed to be incompressible. The source terms of the acoustic analogy are evaluated using the incompressible flow field quantities. In Lighthill's acoustic analogy and Powell's vortex sound theory, the source function $H(x, y, t)$ depends on the spatial derivatives of the incompressible velocity field. The sound pressure field has to be calculated through solving the inhomogeneous wave equation either analytically or numerically. Unfortunately, the formal solution to Lighthill's inhomogeneous acoustic wave equation suffers from a nominally divergent area integral of T_{ij} (Ffowcs Williams & Hawkings (1968), Crow (1970)) in compact flows with non-zero circulation. Hence it is not possible to obtain a solution from the Lighthill's acoustic analogy directly. Mitchell *et al.* (1995) has avoided the divergent integral by decomposing the velocity field and only using the component that decays faster than $(1/r)$ in calculating T_{ij}.

Curle's acoustic analogy has been used by amongst others, Kato *et al.* (1995), Wang *et al.* (1996), and Inoue & Hatakeyama (2002) to investigate sound generated by bluff body flows. In the study by Wang *et al.*, the sound was generated from uniform flow past a NACA 0014 aerofoil while Inoue &

Hatakeyama predicted the sound caused by vortex shedding from flow past a circular cylinder. The first step of the solution approach is to predict the flow field by numerically integrating the Navier-Stokes (NS) equations. In Inoue & Hatakeyama, the quantities in the integrals of Curle's acoustic analogy were evaluated using the compressible flow quantities. Next, the pressure field is calculated as a postprocessing step by numerical integration of the volume and surface integrals.

Möhring (1978) extended Powell's (1964) theory of vortex sound to derive a far-field expression for the acoustic pressure as a function of the moments of vorticity and position vector. Kambe & Minota (1986) adopted Möhring's moment of vorticity sound theory (1978) in their study of interactions of a pair of vortex rings, namely the leapfrogging motion and head-on collision. Dyson's (1893) equations were used to calculate the trajectories of the vortex rings. Tang & Ko (1993, 1995, 1997) used Möhring's formula to predict the sound generated from a pair of rectilinear vortex cores, and a pair of co-axial vortex rings. In both cases, the flow field was assumed to be inviscid. The method of contour dynamics was used to predict the flow field. Mitchell *et al.* (1995) attempted to implement Lighthill's acoustic analogy and Powell's theory of vortex sound to predict the far-field sound of a spinning, viscous vortex pair. DNS was used to integrate the compressible NS equations in time. Once the flow map is obtained, the velocity field is used to calculate the acoustic source terms in both formulations. Mitchell *et al.* (1999) predicted the sound radiated from an axisymmetric jet using Lighthill's acoustic analogy. Verzicco *et al.* (1997) used the MAE equation derived by Kambe & Minota (1981) to quantify the behaviour of the quadrupole and monopole source terms for vortex pair in a viscous fluid.

1.2.3 The acoustic/viscous splitting technique

The acoustic/viscous splitting technique (hereinafter AVS) for aeroacoustics was developed by Hardin & Pope (1994). This approach is also known as the 'expansion about the incompressibility assumption' method. In this approach, the compressible flow field is divided to an incompressible flow and an inviscid acoustic perturbation field. The flow variables u, v, p are then decomposed to incompressible and perturbation components. However, the treatment of the density variable is different from the rest of the flow variables. Hardin & Pope argues that in the incompressible flow, there are hydrodynamic density fluctuations that are much greater than the acoustic fluctuations. Thus, the density variable was decomposed to an incompressible term ρ_o, a perturbation term $\rho^{'}$, and finally, a term describing the differences between the compressible flow and corrected incompressible flow. The density is shown as follows

$$\rho = \rho_o + \rho^{'} + \frac{p(\mathbf{y},t) - \bar{p}(\mathbf{y})}{c_o^2}, \tag{1.12}$$

where $\bar{p}$ refers to the time-averaged pressure and is defined as

$$\bar{p} = \frac{1}{T}\int_0^T p(\mathbf{y},t)dt. \tag{1.13}$$

Here the subscript o denotes incompressible terms. In the near-field, the perturbation quantities describe the difference between the compressible and incompressible flow variables. In the far-field, the perturba-

tion properties are acoustic. The acoustic quantities are obtained from inviscid equations describing the differences from the incompressible flow. This method, similar to the acoustic analogies, involves separate computations of the flow field and the sound field. It also does not allow for resonant situations.

Amongst others, the AVS method has been used by Ekaterinaris (1999), Lee & Koo (1995), Hardin & Pope (1995), and Slimon *et al.* (1999) in studying sound generated from a spinning vortex pair. The subject of sound generated from uniform flow past a two-dimensional cavity was studied using the AVS approach by Hardin & Pope (1995). Slimon *et al.* (1999) used the AVS technique to model sound emission from uniform flow past a fixed cylinder.

1.2.4 Direct numerical simulations

Direct numerical simulation (DNS) has been used by some researchers to study the acoustic emissions of both bounded and unbounded flow situations. The compressible Navier-Stokes equations are integrated numerically in time using high-order spatial and temporal schemes. The flow field and a significant part of the sound field are modelled on a single computational domain simultaneously without decoupling. Furthermore, the DNS method does not involve any assumptions of source and flow compactness commonly used in the acoustic analogy. As well as sound generated by low speed flows, DNS is equally capable of predicting sound generated by flow situations at the other end of the spectrum i.e., screech and shocks in high Mach number flows. In addition, resonant flow conditions can be investigated using DNS directly. In the application of the DNS method to low Mach number problems, high order methods (spatial and temporal) must be used since the typical energy levels associated with the acoustic field is several orders of magnitude smaller than the fluctuating flow.

Mitchell *et al.* (1995) have used direct simulation methods to predict the sound generated by the co-rotating motion of a pair of vortex cores. Inoue & Hatakeyama (2002) used DNS to model sound generated from uniform flow past a fixed circular cylinder. In addition, Colonius *et al.* (1997) have used the DNS technique to investigate the resonant instabilities of uniform flow past a two-dimensional cavity.

1.2.5 Comparison of solution approaches

In most of the publications listed above, a variety of different methods were used to solve the selected aeroacoustic problems. This allows a quantitative assessment of the various solution approaches. For example, Ekaterinaris (1999), and Lee & Koo (1995) compared the MAE solution with the AVS approach. Mitchell *et al.* (1995) compared the DNS results with numerical results of Powell's acoustic analogy and Lighthill's acoustic analogy. Inoue & Hatakeyama (2002) compared their DNS results with Curle's acoustic analogy.

The main reasons for using different prediction methods to the same aeroacoustic problem are to allow the solution field to be assessed quantitatively, and also to reveal the limitations and advantages of the each method. Another point, though less explicit, is that no solution approach has been developed rigorously enough to dominate over the others. To a large extent, the choice of the solution approach should depend on the type of aeroacoustic phenomena studied and the associated costs of running the simulations in terms of computational time and storage.

In the first two solution approaches, namely, the acoustic analogies and the AVS technique, two computations are performed separately on two different grids. As such, the choice of grid construction and the numerical schemes can be tailored to the specific needs of that particular computation. However, with DNS, both the flow field and sound field are modelled on the same grid. Apart from having to resolve the viscous gradients, the grid stretching in the domain has to be relatively smooth to avoid generating artificial spurious noise. This means that the governing equations (being the Navier-Stokes equations) have to be solved in the entire domain with a fine mesh at a high cost. In a study of the computational costs involved with implementing the solution approaches, the DNS method was found to be the much more expensive when compared to the numerical prediction using Powell's theory of vortex sound (Mitchell *et al.* 1995). Also, although DNS is perhaps generally more well-known, it is still almost necessary to return to the acoustic analogies to explore the details of the sources and relate the flow dynamics to the acoustic behaviour.

1.2.6 On the sound generated by a pair of co-rotating vortices

Historically, the subject of the sound generated by the spinning motion of a pair of point vortices has been one of the most widely studied aeroacoustic problems. Powell (1964) has used this flow configuration to show that the sound pressure was proportional to the eighth power in the vortex velocity. Müller & Obermeier (1967) have used the singular perturbation method to derive an analytical expression for the far-field sound. Yates (1978) derived an acoustic solution in term of high-order multipoles and used the spinning vortex pair to highlight the effect of non-compactness on the sound pressure levels. With the development of the various models to predict aerodynamic sound numerically and the associated issues like initial conditions and boundary conditions, the spinning co-rotating vortex pair has come under renewed interest. This particular flow configuration has been used in the validation of the different numerical schemes applied in CAA (Lee & Koo (1995), Ekaterinaris (1999). This is because under the ideal conditions of infinitesimally thin cores and an inviscid fluid, the flow and acoustic solutions can be obtained analytically for comparison. Furthermore, this flow configuration can also been used to understand the physics of the sound generation mechanism, for instance, the effect of different vortex core models on the sound radiation (Lee & Koo (1995)), and the effect of non-compactness (Mitchell *et al.* (1995).

Classical model

In the flow configuration considered by Müller & Obermeier, two point vortices of circulation Γ_o initially separated apart by a distance $2Z_o$, spins about a fixed point in an inviscid fluid. Using the singular perturbation method, the far-field acoustic expression is as follows

$$p(r,t) = \frac{\Gamma_o^4}{64\pi^3 Z_o^4 c_o^4} H_2^2(kr). \tag{1.14}$$

Several conclusions on the acoustic properties can be drawn from the above equation. The acoustic field has a double spiral pattern. In addition, the frequency of the sound field is twice that of the co-rotation frequency owing to the symmetry of the flow. Furthermore, the time variations of the acoustic signals are sinusoidal.

Initial transients

One of the common features found in the numerical simulations by Lee & Koo (1995), Mitchell *et al.* (1995), and Ekaterinaris (1999) is the presence of a large initial peak in the time varying acoustic signal. The transient wave is a likely cause of a crude initial condition which results in large-scale grid-to-grid oscillations as it propagates through numerical interfaces such as a stretched grid. To minimise the effects of such spurious waves, Mitchell *et al.* applied a compact Padé filter scheme during the initial stages of the compressible flow calculations to explicitly remove any associated high-frequency spurious waves. This is in addition to a relatively small rate of stretching of 5%. Ekaterinaris also employed some form of short-wavelength removal scheme in his computations prior to reporting the acoustic signals.

Effect of vortex core model

In most analytical aeroacoustic analyses, a point-vortex model is used to represent the line vortices. However, in reality vortices are finite. Two different types of vortex core models were considered by Lee & Koo (1995), namely the Scully model and the Rankine model. Their results showed that the time variations of the acoustic signals from the Scully model was smoother than the Rankine model. This was attributed to the smoother spatial variation of initial vorticity and velocity distributions in the Scully model compared with the Rankine model (which has a discontinuity in the velocity gradient at the radius of the vortex core). A vortex core with a Gaussian distribution in vorticity was used in Mitchell *et al*'s. (1995) simulations. No difficulties associated with those reported by Lee & Koo were observed. The possible explanation is that in addition to the Gaussian vortex being similar to the Scully model (in terms of the distributions of vorticity and tangential velocity), the presence of dissipation from a viscous fluid acts to reduce the peak vorticity and therefore smoothens the velocity gradients.

Effect of Mach number

Yates (1978) has argued that for the simple isolated co-rotating vortex pair structure, the assumption of flow compactness is only valid if the co-rotation Mach number is smaller than 0.1. At an intermediate range between Mach number of 0.1 and 0.3, the sound power was found to diminish by about 15dB. The reduction in the sound power was attributed by Yates to the presence of higher-order poles. The higher-order poles start to dominate as the non-compactness of the flow configuration increases.

Mitchell *et al.* (1995) considered the issue of flow compactness by conducting numerical simulations at two different co-rotation Mach numbers, namely Ma = 0.06 and 0.18. At the former Mach number, there was good agreement between the DNS results and the theoretical predictions of Möhring's (1978) and Powell's (1964) numerical simulations. However, at Ma = 0.18, Möhring's analytical solution over-predicted the amplitude of the sound pressure when compared to the DNS results. Furthermore, the over-prediction at 65% is consistent with the results of Yates (1978). This is because Möhring's solution was derived on the limiting assumption of Ma $\rightarrow$ 0. In contrast, Powell's vortex sound theory which is valid for low Mach numbers resulted in good agreements with the DNS simulations at both co-rotation Mach numbers. Lee & Koo (1995) has found that the amplitudes of the pressure field were smaller (calculated using the AVS approach) when compared with MAE theoretical predictions at the higher co-rotation Mach number of 0.1273.

Effect of physical viscosity

Mitchell *et al.* (1995) have investigated the influence of physical viscosity on the acoustic fluctuations. Aeroacoustic theories developed by Kambe (1981) have shown that physical viscosity behaves like an acoustic monopole. Mitchell *et al*'s. direct numerical simulation results were used to calculate the amplitudes of the monopole and quadrupole sound sources. The monopole was calculated from the area integral of the entropy S. The amplitude of the monopole contribution, $S^{''}(t)$ was found to be at least two orders of magnitude smaller than that of the quadrupole, $Q^{'''}(t)$, indicating that the acoustic influence of monopole source from viscosity is minor.

1.2.7 On the sound emitted from the interactions of a pair of co-axial vortex rings

The behaviour of a pair of identical and like-signed co-axial vortex rings has fascinated many fluid dynamicists (e.g., Dyson (1893), Lamb (1932), Batchelor (1967), Oshima *et al.* (1975), Yamada & Matsui (1979)) because gaining understanding of the coherent flow structures exiting from axisymmetric round jets can provide further insight into the turbulence phenomena in jet flows. Amongst others, Yule (1978)

has experimentally identified coherent structures present from axisymmetric round jets at moderate Reynolds numbers. These flow structures have been described as multiple pairs of vortex rings. This has led many to contend that the pairing of the co-axial vortex rings is the dominant sound source in axisymmetric jets at moderate Reynolds number. While Bridges & Hussain (1992) have argued that the vortex pairing of the co-axial vortex rings cannot be the main sound source for turbulent jets, DNS results from Mitchell *et al.* (1999) have indicated that at a Reynolds number of $Re = 2500$ and a Mach number of 0.4, the sound radiated from an axisymmetric round jet is similar to that generated from a pair of co-axial vortex rings.

The study of the sound waves generated from the mutual interactions of a pair of vortex rings moving along a common axis of symmetry in the same direction has been considered by many previous investigators, for instance, Möhring (1978), Kambe & Minota (1981), Kambe (1984), Shariff *et al.* (1988), Tang & Ko (1995), Verzicco *et al.* (1997). The flow is assumed to be axisymmetric with no swirl component. Apart from the relevance of the problem because of the clear link to the aeroacoustics phenomena of axisymmetric round jets, this study is also widely used in the validation of low Mach number aeroacoustic problems because of two important factors. Firstly, by using the assumptions of an inviscid fluid and an infinitesimally thin core, both flow and acoustic solutions can be obtained analytically. Secondly, the characteristic lengthscale of the flow is much smaller than the acoustic wavelength, thereby resulting in a compact acoustic source region.

Möhring (1978) has shown that the vortex pairing of two thin vortex rings close to each other results in an axisymmetric lateral quadrupole pattern. Kambe & Minota (1981) have considered the effect of the ratio of the initial axial separation of the vortex rings to the ring toroidal radius. The assumptions of an inviscid fluid and an infinitesimally thin core were used so that the flow and acoustic solutions could be obtained analytically. The far-field acoustic expression was then derived by using the method of matched asymptotic expansions (MAE). The trajectories of the vortex rings were obtained using Dyson's (1893) classical model. In the classical model, the interactions of a pair of co-axial vortex rings is described as either the mutual slip-through or leapfrogging motion. To describe the flow event, the identical vortex rings are assumed to be placed along each other. The vortex ring initially behind its counterpart accelerates and contracts as it slips underneath the other ring. While this is happening, the other ring decelerates as it expands. The roles of the vortex rings reverses as soon as both rings reach the slip-through instant. The slip-through instant is the point where both vortex rings are aligned vertically, i.e., the radial distance between the two vortex rings is maximum. Because the vortex rings are assumed to remain circular at all times with no straining effect imposed, the leapfrogging cycle repeats itself indefinitely. The acoustic expression using the MAE technique in cylindrical coordinates (z, y) is as follows

$$p(z, y, t^*) = \frac{\rho_o}{4c_o^2\sqrt{(z^2+y^2)}}\frac{\partial^3 Q^*}{\partial t^3}(\cos^2\theta - \frac{1}{3}), \tag{1.15}$$

where the second-order moment of vorticity $Q(t)$, is defined as

$$Q(t) = \int_A \omega y^2 z \, dy \, dz. \tag{1.16}$$

The above expression from Kambe & Minota (1981), similar to the one derived by Möhring (1978), relates the acoustic pressure to a linear function of vorticity. The angle θ is measured from the axisymmetric axis. The term $(\cos^2\theta - 1/3)$ dictates two properties of the acoustic field. Firstly, the signals at $\theta = 0°$ and $\theta = 90°$ are out-of-phase by π. Secondly, the acoustic field has distinct silent regions located at angles of 55° and 125° (otherwise known as the polar extinction angles). Such a far-field directivity can be described mathematically as an axisymmetric lateral quadrupole. Hence the acoustic source term $Q(t)'''$ is also known as a quadrupole sound source. While $(\cos^2\theta - 1/3)$ dictated the spatial characteristics of the acoustic field, the time variations of the acoustic pressure at any point is defined by the temporal quantity of $\partial^3 Q/\partial t^3$. In contrast to the almost sinusoidal variations of the acoustic signals generated by an isolated co-rotating vortex pair, the time variations of the acoustic signals in this case consists of a series of peaks and troughs. The frequency of the acoustic signals was twice that of the leapfrogging motion owing to the symmetry of the flow. The local peak of the acoustic signals was found to correspond to the slip-through instant. Furthermore as the ratio of the initial axial separation to the toroidal radius is increased, the time variation of the mean axial position of the vortex rings as well as the acoustic signals become less sinusoidal. Another important point to note is that the vortex system in the acoustic space is effectively radiating sound from a fixed position, i.e., the sound source is spatially-invariant even though the motion of the vortex rings include a convective component. This is a particular feature of the MAE technique. However, the validity of the far-field expression away from the asymptotic limit of $\mathrm{Ma} \to 0$ is very much questionable.

While Kambe & Minota (1981) have predicted the behaviour of the quadrupole sound source from the motion of an infinitesimally thin vortex ring, in reality, vortex rings have finite cores. The effect of a pair of co-axial vortex rings of finite thickness on the sound radiation was considered by Shariff *et al.* (1988). The flow was predicted numerically by using the method of contour dynamics which allows for the deformation of the vortex cores. The initial shape of the vortex core was based on Norbury (1973). The acoustic analysis was based on Kambe & Minota's MAE acoustic expression. Shariff *et al.* have found that in addition to the fundamental acoustic component caused by the leapfrogging motion, there was a secondary component. The frequency of the secondary component was much higher than the fundamental component. This was attributed by Shariff *et al.* to the distortion of the vortex cores into an ellipses caused by the straining imposed by each other.

The effect of different types of vortex pairing was considered by Tang & Ko (1995). Similar to Shariff *et al.* (1988), the dynamics of the vortex rings are obtained numerically through the method of contour dynamics. By varying the ratio of core size to the axial separation, four different types of vortex pairing were predicted. These were the mutual slip-through, partial slip-through, partial coalescence, and full coalescence. In an inviscid fluid, the four types of ring interactions occur without mutual contact.

Kambe & Minota's analysis has considered the quadrupole sound source in terms of time variations of the impulses and spatial positions of the two vortex rings. To better understand the generation mechanism, the quadrupole source term of Kambe & Minota was expanded to relate the quadrupole source term to the time variations of the impulses of the vortex rings, and the positions, axial velocities and axial accelerations of the vortex rings. In the event of the mutual slip-through, Tang & Ko have observed wavy oscillations consistent with Shariff *et al.*, which the former had argued were related to the rate of change of the axial acceleration of the vortex rings.

Verzicco *et al.* (1997) analysed the sound generated by a pair of viscous co-axial vortex rings with consideration of the effect of Reynolds number, initial vorticity distribution, and initial core thickness respectively. With a Gaussian vortex and a core-to-ring ratio of 0.3, the magnitudes of the quadrupole and viscous sound sources were analysed for three different Reynolds numbers $Re = 1500$, 2500 and 4000. At the selected Reynolds number, the second passage of the leapfrogging motion was accompanied with large core deformations. Subsequently, viscosity causes the two vortex rings merge into a single vortex ring with a weak tail. The dynamics of the viscous interactions are quite different compared with the inviscid case as there is no mutual contact in the latter, i.e., the inviscid vortex rings pair but do not come into contact with each other. Verzicco *et al.* found that the quadrupole term was only slightly affected by the change in the Reynolds number which implies that the leapfrogging motion is a largely inviscid phenomenon. In contrast, there was a significant increase in the monopole as the Reynolds number is increased, as the monopole amplitude is proportional to the rate of dissipation of the kinetic energy. However, in general the quadrupole term dominates over the monopole sound source at all three Reynolds numbers. Another interesting finding from Verzicco *et al.* was that the frequency of the secondary acoustic component depended on the vortex core nutation, i.e., by manipulating the initial thickness of the vortex core, the time-scale of the secondary component could either be smaller or larger than the fundamental period.

Summary

The study of the mutual interactions of a pair of co-axial vortex rings moving along a common axis of symmetry in the same direction presents a slightly more advanced aeroacoustic problem compared to the isolated co-rotating vortex pair structure. This is because the acoustic analysis has to consider the effects of the acceleration and deceleration of the vortex rings on the sound radiation. This study is also widely used in the validation of aeroacoustic theories and numerical schemes developed for the field of aeroacoustics because of two important factors. Firstly, both the hydrodynamic and acoustic solution can be obtained analytically if the assumptions of an inviscid fluid and an infinitesimally thin core are made. Secondly, the characteristic lengthscale of the flow is very small compared to the acoustic wavelength thereby ensuring that the flow is compact.

In the studies reviewed here, the acoustic analyses by Kambe & Minota (1981), Shariff *et al.* (1988), Tang & Ko (1995), and Verzicco *et al.* (1997) have focused on the time variations of the quadrupole and monopole sound sources. However, the validity of the analytical solution away from the asymptotic limit of Ma $\rightarrow$ 0 is very much open to question. In addition, the effect of non-compactness of the acoustic source (which has been shown by Yates (1978) to have a significant influence on the sound pressure levels) cannot be considered at all when the analytical approach is used.

In terms of the dynamics of the motion, the sound radiation is related to the mean axial position of the vortex system. The role of the relative motions of the vortex rings, and the velocities and accelerations of the core centroids was also examined. In particular, the rate of change of the axial acceleration was found to be the main contributor to the acoustic amplitude.

1.2.8 Aeolian tone

In the previous sections, we devoted our attention to the subject of acoustic radiation from the unsteady motion of an isolated co-rotating vortex pair structure, and a pair of co-axial vortex rings moving along a common axis of symmetry. In either flow situation, the vorticity in the initially irrotational fluid was assumed to be generated by a force which vanishes thereafter. Thus, the total impulse and total kinetic energy of the flow were assumed to be conserved due to the fact that there were no external forces acting on the system. Furthermore, there were no solid boundaries present in these flows. As a result, the emphasis was placed on the sound waves generated solely as a result of the motion of vorticity in a free flow.

In this section, our focus is shifted towards the sound generated aerodynamically from self-sustaining flow instabilities. Hence the sound is generated by the motion of vorticity as well as by the changes in the vortex strength. The flow instability might be caused by the shedding of shear layers in an open cavity resulting in a vortex roll-up which is then ejected into the wake (Hardin & Pope (1995)). Another type of flow instability is that caused by the placement of a bluff body in a fluid stream which triggers the well-known von-Karman vortex shedding downstream of the body. This study is mainly concerned with the latter because it is one of the most intensely studied topics both in the fields of fluid dynamics and aeroacoustics. To be able to study the acoustic radiation associated solely with the fluctuating flow, the bluff body is assumed to be fixed and rigid, i.e., the body is not allowed to vibrate. This study is limited to flow situations where the acoustic wavelength is much larger than the characteristic lengthscale of the rigid body (i.e., Ma $<<$ 1). Under such circumstances, Powell (1964) has pointed out that the shape of the body is largely irrelevant. In addition, flow instabilities resulting in resonant conditions are excluded. This is because the classical acoustic analogies do not allow for feedback of sound energy to the flow.

The flow around a cylinder of circular cross-section is one the most widely studied problem in fluid

mechanics (the interested reader is advised to refer to a recent review by Williamson (1996)). Associated with the flow phenomena is one of aeroacoustic phenomena of flow instabilities that has also been coming under increasing attention. This particular subject is associated with the *Aeolian tone*. Physically, the Aeolian tone is used to describe the sound phenomenon of wind blowing past a telephone wire/string. Strouhal (1878) has experimentally measured the frequency of sound generated by the translating motion of a circular cylinder in a fluid stream and found that it was identical to the vortex shedding frequency. Roshko (1954) found that the shedding frequency was approximately proportional to the freestream velocity, U_∞, and inversely proportional to the characteristic lengthscale, d, in the Reynolds number range of $300 < Re < 10^4$. This results in a Strouhal number range of $St = fd/U_\infty$ of 0.2 to 0.22.

The acoustic fluctuations were initially thought to be caused by the vibration of the circular cylinder. However, this incorrect view was later addressed by Rayleigh (1896) who concluded that the sound was actually generated by the fluid rather than by the motion of the body itself. Rayleigh further found that the sound field was related to the eddy pattern in the wake also commonly known as the von-Karman vortex sheet. Subsequent experiments by amongst others, Gerrard (1955), Phillips (1956), and Etkin *et al.* (1957) have confirmed Rayleigh's findings. In addition to establishing the directional directivities of the sound field, another conclusion drawn from the experiments was that the fundamental tone is most intense at right angles to the fluid stream while the first harmonic is weaker and radiates in the direction of the fluid stream.

Curle (1955) has argued that in bluff body flows, the general solution to Lighthill's acoustic analogy consists of a volume integral over the entire fluid, and a surface integral over the solid boundaries. The surface integral is related to the force experienced by the fluid owing to the interaction between the hydrodynamic flow and the solid boundaries. He predicted that the force exerted by the body on the fluid would give rise to the presence of acoustic dipoles while the turbulent wake results in a distribution of quadrupoles. Furthermore, by using dimensional analysis, Curle showed that when the Mach number is small, the dipoles are expected to dominate over the quadrupoles since the former is a more efficient sound source. Drawing on Gerrard's (1955) experimental findings that the sound radiation is a dipole field normal to the fluid stream, Curle went on to suggest that the dipole generated by the lift force would have a frequency equal to the shedding frequency while the dipole due to the drag force would have a frequency twice that of the shedding frequency.

The association between the acoustic dipoles and the aerodynamic forces acting on the circular cylinder was first made by Yudin (1947) who postulated that the direction of the Aeolian tone coincides with that of the fluctuating aerodynamic forces acting on the circular cylinder. Even though the body is sustaining the aerodynamic forces, it could not possibly be the source of sound. This is because the body is not allowed to vibrate. To solve this dilemma, Etkin *et al.* (1957) replaced the rigid body under the influence of the aerodynamic forces with a volume of fluid under a body force so that the volume of fluid remains stationary. In other words, the body force experienced by the volume of fluid is equal in

magnitude but opposite in direction to the aerodynamic forces acting on the body. The forces distributed over the surface of the cylinder were reduced to concentrated lift and drag forces. Using the assumption of a sinusoidally varying lift and drag forces, Etkin *et al.* showed that near the plane of symmetry that the sound pressure is proportional to the amplitude of the fluctuating force and has the same oscillation frequency. Furthermore, the variation of the aerodynamic forces over the length of the cylinder can be ignored if the Reynolds number is low enough. Thus, Etkin *et al.* have related the mathematical acoustic dipoles to the aerodynamic forces concentrated at a point in the cylinder.

While the theoretical analyses (Curle (1955), and Etkin *et al.* (1957)) and experimental findings have resulted in the Aeolian tones interpreted as being related to the aerodynamic forces and therefore, are dipolar in nature, they offered very little insight into the actual physical generation mechanism of the sound waves. This is because the acoustic waves must originate from the vortical part of the flow instead of the aerodynamic forces (Powell 1964) experienced by the body. Further understanding in the characteristics of Aeolian tones was gained through numerical simulations using various solution approaches (i.e., classical acoustic analogies, acoustic/viscous splitting, and direct simulations) by amongst other, Brentner *et al.* (1996), Cox *et al.* (1998), Hardin & Pope (1984), Inoue & Hatakeyama (2002), Shen & Sorenson (1999), and Slimon *et al.* (1999).

In Cox *et al.* (1998), the Reynolds number of the flow ranged from 100 to 5×10^6 while the Mach number of the sound field was Ma = 0.2. In Shen & Sorensen (1999), the Reynolds number of the flow was $Re = 200$ while the Mach number of the acoustic field was Ma = 0.2. In order to compare with experimental data, Slimon *et al.* predicted the flow field at a Reynolds number of $Re = 5 \times 10^4$ while the Mach number of the acoustic field was Ma = 0.2. One of the most recent numerical studies of the Aeolian tone was conducted by Inoue & Hatakeyama (2002). The compressible Navier-Stokes equations were solved numerically using high-order spatial and temporal methods in order to predict both the flow field and acoustic field simultaneously on the same computational domain. The Mach number ranged from Ma = 0.05 to 0.2 while the Reynolds number of the flow was kept at $Re = 150$. The results of the numerical simulations of sound radiated from flow past a circular cylinder showed qualitative agreement with the experimental studies of Gerrard (1955), Phillips (1956), and Etkin *et al.* (1957). In addition, the numerical simulations also provided a further insight into the aeroacoustic phenomena of Aeolian tones by clarifying the relationship between the vorticity dynamics of the flow, and the generation and propagation characteristics of the sound waves. This is possible through correlating the time-dependent vorticity dynamics and acoustic quantities. These issues will now be addressed in the following subsections.

Properties of the lift and drag dipoles

Numerical results by Wang *et al.* (1996) on airfoil-induced sound, and Cox *et al.* (1998) on the present subject have already showed that at low Mach numbers, the quadrupoles are much weaker than the dipoles. Shen & Sorenson *et al.* (1999) have shown that the acoustic waves propagate away from the cylinder normal to the fluid stream. In the results of Inoue & Hatakeyama (2002), the time histories of the acoustic pressure fluctuations due to the fluctuating lift force (lift dipole) placed directly above the cylinder showed a sinusoidal waveform. From the results of Inoue & Hatakeyama, it is clear that the time development of the acoustic pressure field showed only the presence of the lift dipole (see figure 6 in Inoue & Hatakeyama). The appearance of the dipole due to the fluctuating drag force (drag dipole) was masked by that of the lift dipole. This was linked to the fact that the fluctuations in the lift forces was much more significant than the fluctuations in the drag force. Subsequent decomposition of the pressure field into a multipole expansion revealed that the amplitude of the drag dipole was approximately one order of magnitude smaller than that of the lift dipole.

On the location of the source region of the acoustic dipoles

Hardin & Pope (1984) has suggested that the location of the source region is close to the formation of the vortices near the cylinder. This is because in their simulations, the computational domain only captured up to approximately five diameters of the wake flow. Hardin & Pope's hypothesis was vindicated by Inoue & Hatakeyama (2002) who through analysing the time-development of the near-field acoustic pressure fluctuations and the shedding of the vortices argued that the pulsing of the acoustic waves occurred from where the vortices are shed from the cylinder into the wake. These findings are consistent with Howe's (1975) interpretation of the acoustic source generation mechanism. While the vortices shed into the wake, they traverse the hypothetical acoustic field lines at angle of 90°. Hence, the vortices can inject significant energy into the acoustic field.

On the relationship between the aerodynamic forces, vortex shedding and acoustic quantities

To correlate the fluctuating aerodynamic forces with the time development of the vorticity field around the circular cylinder, Inoue & Hatakeyama showed that the positive peaks in fluctuating lift forces, c_l, correspond to the shedding of a vortex from the upper side of the cylinder into the wake. Conversely, the negative peaks correspond to the shedding of a vortex from the bottom side of the cylinder. The pulsing of the acoustic waves is in phase with the shedding of the vortices from the upper and lower edges of the cylinder into the wake.

The positive peaks in the lift fluctuations correspond to negative pressure pulses while the negative peaks correspond to the positive pressure pulses. As such, the development of the acoustic signals has been defined as the pulsing generated from the upper and lower sides of the cylinder. To generate a dipole field, the pulses on each side is equal in strength but opposite in phase.

Decomposition of the sound pressure

The theoretical argument presented by Etkin *et al.* (1957) suggested that with the lift and drag forces oscillating in a sinusoidal fashion being replaced by concentrated point forces, the acoustic field would consist solely of two dipolar fields orthogonal to each other. In other words, the theoretical analysis precludes the possible presence any other modes in the acoustic field. In experiments, the positions of the microphones are limited mostly to the planes of symmetry making it very difficult to carry out a spectral analysis of the sound field. However, in numerical simulations, Inoue & Hatakeyama (2002) generalised the predicted pressure field into a multipole expansion. This is possible because the acoustic waves are linear. In sharp contrast to Etkin's argument, Inoue & Hatakeyama found the presence of a monopole and quadrupoles. The presence of a monopole in the acoustic field is due to a non-constant force coefficient. It is still unclear if the presence of the quadrupole mode is due to the wake pattern or the phase variations in the oscillating aerodynamic forces.

On the effect of finite Mach numbers on sound propagation

Based on the fact that the fluctuations in the lift and drag forces were approximately constant across the Mach number range, Inoue & Hatakeyama argued that the sound generation mechanism is effectively independent of Mach number variations. While the source field is unaffected, the propagation characteristics of the sound waves in the acoustic medium change as the medium is now no longer at rest. Inoue & Hatakeyama have observed that the acoustic pressure field directivity shifts towards the upstream direction as the Mach number is increased from $\mathrm{Ma} = 0.05$ to $\mathrm{Ma} = 0.2$. This shift in the propagation angle (from $\approx 90^\circ$ at $\mathrm{Ma} = 0.05$ to $\approx 78.5^\circ$ at $\mathrm{Ma} = 0.2$) is caused by the Doppler effect which is retarding the wave propagation speed upstream of the cylinder.

It is worth mentioning that in the acoustic analogies of Lighthill (1952) and Powell (1964), the acoustic medium is assumed to be at rest. As such, there is no Doppler shift of the predicted acoustic field. When the acoustic analogies are used to predict sound fields, the far-field directivity remains the same at different Mach numbers. However, having said that, the implementation of a Doppler shift as a postprocessing step in the numerical solution of the acoustic analogies is not a complicated task. It involves a spatial transformation of the acoustic solution to include the dependence of both the freestream velocity and wave propagation speed. This will be discussed in greater detail in Chapter 5 of this thesis.

On the assumption of a concentrated point force

In the analysis by Hardin & Pope (1984), the drag coefficient was found to contain a fourth-order harmonic in addition to the second harmonic. Furthermore, the results indicated that the fourth-order harmonic has a greater amplitude than the second-order harmonic. This is in sharp contrast to the theoretical argument of a point force representation suggested by Etkin *et al.* (1957). This was attributed to the phase variations in the force distributed over the entire surface of the cylinder.

1.2.9 Rectangular plate

One of the main goals of this research is to determine the feasibility of Lighthill's acoustic analogy and Powell's theory of vortex sound in a variety of flow situations. The isolated co-rotating vortex pair structure, and the co-axial vortex rings are compact vortical structures and as such, the acoustic source region of both cases at low Mach numbers is limited. However, bluff body flows are characterised by an extensive wake region implying that the flow is not as compact. Thus, the study of the acoustic waves generated by bluff body flows represents a more rigorous test of the two-step aeroacoustic prediction method because it tests the capability of the numerical method used in predicting the sound field from non-compact acoustic sources.

Because the geometry of a two-dimensional circular cylinder has been investigated quite thoroughly by previous investigators, a slightly more complicated geometry is selected for the present acoustic study. Hence, the acoustic effects of the laminar flow past a two-dimensional cylinder of rectangular cross-section is considered in this investigation. This study can be considered as an extension to the circular cylinder. The plate has square leading and trailing edges and is immersed in a fluid of uniform freestream velocity. This particular plate geometry will be referred to as the rectangular plate for the remainder of this thesis. The dynamics of the laminar flow past a rectangular plate is expected to be more complex than the circular cylinder because of the shedding that occurs at the leading and trailing edges of the plate.

To provide the reader with some understanding of the flow instabilities from flow past a plate of rectangular cross-section, a brief review of natural shedding from rectangular plate is presented in this section. It must be noted that the aim of this project is not to study these flow instabilities in detail. Flows past elongated bluff bodies has been widely studied by fluid dynamicists, for instance Parker & Welsh (1983), Stokes & Welsh (1986), Nakamura *et al.* (1991), Hourigan *et al.* (1993), Naudascher & Wang (1993), Mills *et al.* (1995), and Tan (2000). This is because it underpins a wide range of engineering applications such as aerodynamic loading of structures, flow-induced structural and acoustic vibrations, mixing of fluids, and automobile aerodynamics. The chord of the plate, c is placed in parallel to the fluid stream. The plate thickness is represented by d.

Stokes & Welsh (1986) have found that there were four distinct natural shedding regimes when the plate aspect ratio c/d was varied over a wide range. The properties of the four regimes are summarised below.

1. At plate aspect ratio of $c/d < 3.2$, the separation from the leading edge does not reattach. The separation interacts with the shear layers to form a regular vortex street.
2. When the slightly longer plate aspect ratio c/d is between 3.2 and 7.6, the separation from leading edge reattaches in a periodic manner. In addition, the trailing edge is enveloped by the separation bubble along the plate chord. A regular vortex street is also formed.
3. At plate aspect ratio $7.6 < c/d < 16$, the separation from the leading edge always reattaches upstream from the trailing edge. The shedding is irregular as the vortices from the leading edge are generated in random and interact with the trailing edge vortices. The vortex street is irregular.
4. When the plate aspect ratio $c/d > 16$, similar to 3. the separation from the leading edge always reattaches. However, the random vortices generated from the leading edge diffuse prior to reaching the trailing edge.

In experiments of the vortex shedding from a rectangular plate conducted at a Reynolds number of 1000, Nakayama *et al.* (1993) have shown that the Strouhal number based on the plate chord showed a stepwise increase equal to integral multiple of $0.6n$, where n is an integer defining the shedding mode. Furthermore, phase measurements along the plate chord indicate that n corresponds to the number of vortices distributed along the upper or lower plate chord. A sketch of the shedding modes is presented in figure 1.3. For the first regime, with shedding mode of $n = 1$, the shear layers from the leading edge interacts directly with the trailing edge. The feedback loop which is started from a pressure pulse emitted from the trailing edge controls the leading-edge shear layers, thereby locking the shedding of the leading and trailing edges of the plate. As the plate aspect ratio is increased, the leading edge reattaches to form discrete vortices along the plate chord. The interaction of the trailing edge now switches from the leading edge shear layers to the second (for $n = 2$) or third (for $n = 3$) or fourth (for $n = 4$) vortex shed from the leading edge. A mechanism that encompasses all four shedding modes has been described by Naudascher & Wang (1993) as the *Impinging Leading Edge Vortex* (ILEV) instability. The reader is advised to refer to Naudascher & Rockwell (1994), and Mills *et al.* (1995) for further details on the ILEV instability mechanism.

1.3 Computational aeroacoustics considerations

In this section, an overview of the numerical issues relevant to the implementation of the acoustic analogies of Lighthill (1952) and Powell (1964), and accurate modelling of acoustic waves propagation are discussed.

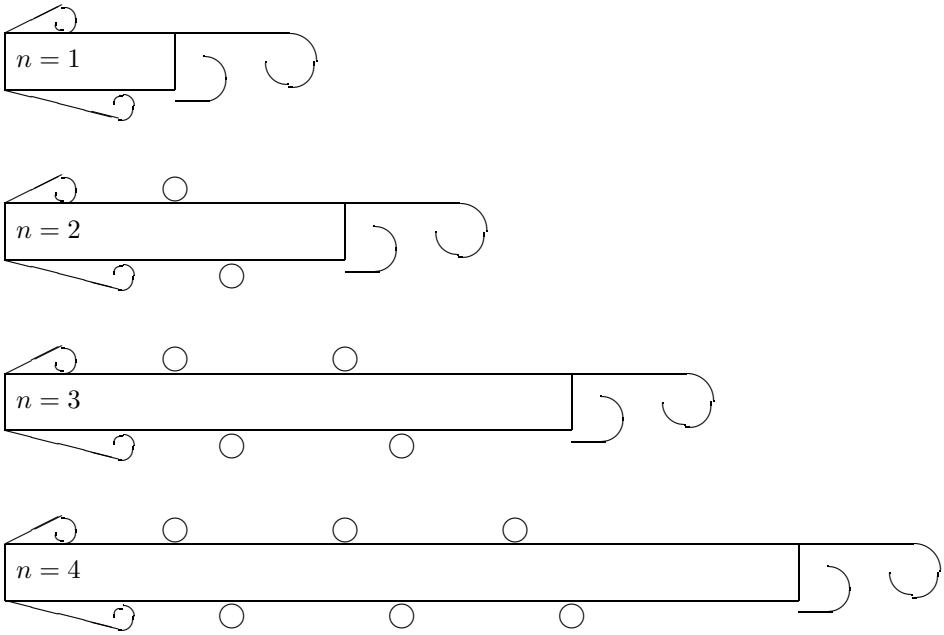

Figure 1.3: Sketch of the four different natural shedding regimes from laminar flow past a rectangular plate. Note that the illustrations are not to scale.

For a more comprehensive review of the numerical issues surrounding the development of CAA, the reader is advised to refer to Powell (1990), Crighton (1993), Tam (1995), and Wells & Renaut (1997). Of particular concern in aeroacoustic simulations are spurious waves and artificial dissipation. Spurious waves in general, have high frequencies and are primarily caused by errors in the initial conditions, boundary conditions and under-resolution of the source terms. The effects of the spurious waves are further exacerbated by grid stretching in the domain. In general, a high-quality acoustic solution should be free from any artificially-generated spurious noise. Besides, the presence of spurious noise is certain to indicate under-resolution in the simulation, spatially and/or temporally.

1.3.1 Grid considerations

The grid used in the aeroacoustic computations must be able to resolve the generation and propagation of the acoustic waves. Due to the nature of low Mach number flows, the acoustic wavelength is significantly greater than that of the eddies generating the sound field. To accurately predict the various acoustic properties such as the far-field directivity and spatial decay of the pressure signals, it is a requirement that the grid be able to capture at least several acoustic wavelengths. As a result, the physical size of the CAA domain will typically be much larger than that of the CFD domain. The CAA domain can be thought of as being made up of two regions, the near-field and the far-field. In the near-field, the local pressure is a function of both the acoustic and incompressible flow quantities. Stretching is used

to extend the grid from the near-region to the far-region as it would be too expensive and inefficient to adopt a uniform grid over the entire CAA domain. The grid spacing has to be smoothly varied from the near-field to the far-field. This is to allow the initial wave transient and subsequent acoustic waves to pass freely without generating significant reflections.

1.3.2 Numerical discretisation

In order to be able to model the propagation of linear acoustic waves accurately, the numerical scheme has to be non-dispersive and non-dissipative. Both explicit and compact finite difference methods have been used in the discretisation of the acoustic waves. To minimise the dispersion errors, high-order methods are used since Fourier analysis of the differencing shows that the approximate wave numbers match the exact wave number over a wider range as the scheme increases in order of accuracy. Most investigators have used a sixth-order spatial scheme as a compromise between performance and computational costs. The implementation of a high-order method may present some difficulties for implementation of the far-field boundary conditions and wall boundary conditions, or when more complicated flow geometries are considered. As an alternative to a truncated Taylor's series expansion, Tam (1994) has proposed a dispersion-relation preserving (DRP) scheme when determining the coefficients of the finite-difference stencil. The optimisation of the stencil is carried out so that the approximate wavenumber is closer to its exact counterpart.

In the temporal discretisation of the acoustic waves, in general, explicit methods are used because they better approximate the physics of the wave propagation. Similar to the spatial schemes, a high-order temporal scheme is used to minimise dispersion errors. In addition, numerical dissipation errors caused by the time-differencing is also reduced through a high-order method. Tam & Webb (1993) proposed a four-stage multi-step scheme using Adams-Bashforth type time-stepping. The fourth-order Runge-Kutta scheme is one of the more commonly used temporal advancement methods due to its excellent dispersion properties, high-order accuracy and relatively high CFL limit.

1.3.3 Initial conditions

A homogeneous wave equation is classified as a hyperbolic partial differential equation. To obtain a solution to the hyperbolic partial differential equation, two initial conditions have to be specified. If we define the variable in the homogeneous wave equation as p, then the requirement is satisfied by defining $p(x, y, t = 0)$ and $p^{'}(x, y, t = 0)$.

In the case of an acoustic analogy, there is effectively an extra initial condition. This is because there is a source function, $H(x, y, t = 0)$ placed on the right-hand side of the wave equation. It is important

to select an appropriate initial condition for the source function. The initial condition represents a temporal discontinuity and as a result, generates what are classified as wave transients. Even though such waves are transient and can be ignored in typical aerodynamic simulations, the same cannot be said for aeroacoustic simulations. Wave transients have been known to generate artificial noise which can contaminate the entire acoustic field (Mitchell *et al.* (1995)). The aim then is to produce a wave transient which is at the very least comparable in both the amplitude and frequency of the acoustic waves. Provided that the acoustic wavelength is well-resolved by the grid, a wave transient similar in characteristics to the acoustic waves is less likely to create artificial spurious noise compared to a sharp, short-frequency discontinuity.

1.3.4 Far-field boundary condition

The Sommerfeld radiation boundary condition is designed to resolve outgoing planar waves. The first-order radiation boundary condition constructed by Bayliss & Turkel (1980) is widely used in linearised Euler equations. These planar waves consists of the initial wave transient and the subsequent acoustic waves. The planar wave condition requires the outgoing waves to be only a function of radial distance from the source. At a grid distance of two or more acoustic wavelengths, this condition is well satisfied. The situation is more complicated if the flow field and sound field are to be solved directly. The boundary condition would have to be reformulated so as to allow the acoustic, entropy and vorticity waves to exit the domain.

1.3.5 Spatial filtering of the acoustic analogies

One of the main difficulties of applying the acoustic analogies to complex flows relates to the large spatial extent of the source terms. In simple flow configurations, both velocity and vorticity fields decays rapidly to ensure that the source terms are zero outside the generation region. However, in practical flows, the hydrodynamic region is extensive and the spatial decay in the downstream direction is slow with respect to distance from the generation region. This has been observed by Mankbadi (1990), Colonius *et al.* (1997), and Mitchell *et al.* (1999) in axisymmetric vortex pairings from jets and mixing layers. The difficulty arises because sudden termination of the source terms (away from the generation region) is bound to create large spurious noise sources. To reduce the impact of the truncation, a sponge region was used by Colonius *et al.* to slowly remove the source terms in an exit region. Mitchell *et al.* have used a mathematical model to describe the region away from the generation region.

1.3.6 Short wave components

In an ideal case, to resolve the acoustic wavelength spatially, a minimum of 20 grid points placed across the acoustic wavelength is deemed to be sufficient and thus, presents no computational difficulties. However, since aeroacoustic problems usually involve a range of frequencies, propagation of the short wave components through grid stretching poses a problem in any numerical aeroacoustic simulation. This difficulty is not found in steady-state aerodynamic simulations where viscosity, physical or numerical, stabilises the solution. However, in aeroacoustic simulations, the presence of artificial viscosity is generally frowned upon as it may damp both short and long wavelength components leading to an inaccurate solution. The application of artificial damping has to be treated with caution. In view of this, artificial selective damping was introduced by Tam *et al.* (1993) to filter out the short wave components. Mitchell *et al.* (1995) used a compact high-order Padé filter to remove the short wave components associated with the transient waves moving through the stretched grid.

1.4 Goal of this research

The main goal of this project is to investigate the capability of Lighthill's acoustic analogy and Powell's vortex sound theory to predict aerodynamic sound from unsteady flows in a variety of situations. To achieve this goal, a two-step aeroacoustic prediction method is used where the flow and acoustic solutions are computed separately. Whilst there are other theories developed by various researchers on aerodynamic sound generation, in the author's opinion, the two most important acoustic theories are the Lighthill's acoustic analogy and Powell's theory of vortex sound. Both theories have been proven to be mathematically sound and provide a simple and yet insightful argument into the source of sound. In addition, there are still many issues that need to be addressed.

For example, even though the acoustic theories of Lighthill (1952) and Powell (1964) have been widely used in one form or another in the analytical analysis of aerodynamic sound generation, numerical application of the acoustic theories has been quite limited to flow situations where the flow is compact (e.g., a simple co-rotating vortex pair, collision of vortex rings, vortices moving past forward/backward facing steps). The acoustic solutions of such idealised flow fields predicted using Powell's vortex sound theory at low Mach number have been validated by numerous investigations. However, in more complicated flows such as shear layers and bluff body flows, the application of Powell's vortex sound theory has been thus far, very limited. This maybe due to the difficulties in obtaining a convergent acoustic simulation from numerically solving the acoustic wave equation. The difficulty of numerically applying Lighthill's acoustic analogy to obtain a convergent solution even on the relatively simple case of the co-rotating vortex pair was noted by Mitchell *et al.* (1995).

The FLAIR group based in Monash University (Clayton campus) has had extensive experience with the commercial flow solver software, FLUENT. Thus, it was used to model the unsteady flow fields. The associated computational aeroacoustic code was specifically developed by the author. The code is written in the Fortran-90 programming language and is compiled on a Linux platform.

Three case studies have been selected based on the criteria of complexity and availability of previous data for comparison and benchmarking purposes. The widely-studied case of an isolated co-rotating vortex pair structure forms the first test of this investigation. A logical progression from the spinning vortex pair would be to apply the numerical techniques of the two-step method to predict the sound generated from a pair of co-axial vortex rings moving along a common axis of symmetry in the same direction. The final case of the sound generated by laminar flow past a two-dimensional plate of rectangular cross-section represents a complete and rigorous test of both the flow and acoustic solvers. The results of the co-rotating vortex pair and co-axial vortex rings are validated through comparison of the results with the published works of various researchers (both analytical and numerical). The simulations of the sound radiation from flow past a rectangular plate is compared with those for the circular cylinder. This is because to the knowledge of the author, there have not been any published scientific studies of acoustic radiation from laminar flow past a two-dimensional rectangular plate.

Chapter 2

Numerical Techniques

2.1 Summary

Extensive studies into aeroacoustic phenomena have been undertaken since the pioneering paper on aerodynamic sound generation was presented by Lighthill in 1952. Since that time most problems have been tackled analytically, often examining either simplified or idealised cases. In the research presented in this thesis, our aim is to simulate numerically some flow problems tackled previously analytically but to extend these to include the effects of viscosity on the flow dynamics, and therefore on the sound generation. In addition, we examine a more complex problem of flow past a long rectangular plate, which does not appear to have been treated in full previously except by very much simplified treatments.

In both Lighthill's (1952) acoustic analogy and Powell's (1964) theory of vortex sound, the aeroacoustics is made tractable by decoupling the fields into hydrodynamic and acoustic components. As a consequence, to predict the sound field, two separate sets of computations have to be performed in a sequential (or a coupled) manner. The incompressible flow field is first calculated which allows acoustic sources to be evaluated so that the far-field acoustic field can be predicted. Hence, numerical implementation of acoustic analogies is commonly referred to as the 'two-step' approach.

Three flow problems of varying complexity have been investigated. The first problem primarily forms a validation study of this two-step approach. It is the widely-studied problem of sound generation from an isolated co-rotating vortex pair in an otherwise stationary fluid. The second study examines the induced acoustic field associated with the leapfrogging motion of a pair of co-axial vortex rings advecting along a common axis of symmetry. These two cases have been studied in the past, both analytically and numerically. Hence, the results can be compared with published works by other aeroacoustic researchers. For the second case, the effects of viscosity on vortex merging generally has been neglected in the past,

and this can be important for some parameter ranges. The third and final case is the sound generation associated with natural shedding from flow past a rectangular plate with square leading and trailing edges.

In this chapter, we will describe in detail the implementation procedure of the two-step approach. This chapter is divided into two sections. In the first section, the numerical techniques used to generate an accurate hydrodynamic field are presented. The commercial CFD software package FLUENT is used to predict the unsteady flow fields. The flow domain is discretised using a structured mesh. Numerical issues relevant to modelling an unbounded flow on a finite domain such as grid generation and resolution, spatial and temporal discretisation schemes, imposition of the appropriate boundary conditions, and judging the flow convergence for each case are considered. In the second section, the computational aeroacoustics (CAA) techniques used to accurately predict the acoustic behaviour of the three flow fields are described. The aim is to predict the acoustic field without any ad-hoc filtering or artificial dissipation being added to the numerical scheme. As Colonius (1995) has pointed out, if a stable numerical solution requires any form of damping or filtering, this serves to indicate under-resolution. While filtering or artificial dissipation can sometimes be tolerated in hydrodynamic simulations, the same cannot be said for aeroacoustic simulations.

According to the classical acoustic analogies, the governing equation for the acoustic field is an inhomogeneous wave equation whereby the right-hand side term is the acoustic forcing. Due to the relatively simple geometry of the flows studied here, a high-order finite-difference scheme can be used to approximate the spatial derivatives without any significant difficulties or penalties. The classical four-stage Runge-Kutta scheme is used to advance the acoustic simulation temporally. In general, a high-order method is preferred in aeroacoustic computations since both dispersion errors and dissipation errors can be minimised. In addition, the implementation of high-order methods if done correctly does not increase the computational memory required substantially.

The grid used in the acoustic simulation is stretched gradually. Truncation of the hydrodynamic fields in the acoustic domain is performed by employing spatial filtering. This is to ensure that artificial acoustic forcing is not introduced. A start-up function is used to temporally ramp the acoustic forcing from zero to its actual value during the initial stage of the acoustic computation. The treatment of the asymmetric stencil near the far-field boundaries is also presented. The procedure for spatial interpolation of the velocity fields from the grid used in flow simulations to the grid used in the acoustic simulations is described. Temporally, the instantaneous source field is interpolated using a high-order spline.

2.2 Overview of the two-step approach

In using acoustic analogies to predict the far-field sound numerically, computation of the acoustic solution is divided into two steps. In the first step, the time-dependent viscous incompressible velocity field is obtained through numerically solving the incompressible flow equations. These time-dependent velocities are then used in calculating the acoustic forcing term of either Lighthill's (1952) acoustic analogy or Powell's (1964) vortex sound theory. The accuracy of the acoustic forcing term depends on the accuracy of the hydrodynamic simulation. In the second step, the acoustic solution is obtained from numerically solving the inhomogeneous wave equation. The right-hand side term of the inhomogeneous wave equation represents the acoustic forcing.

The two-step approach enables each of the solvers to be optimised for the coupled solution procedure for the flow and acoustic fields, which are governed by different length and velocity scales. As a result, the computational costs of the two-step approach can be significantly less than the direct simulation of the compressible flow fields.

2.3 Numerical modeling of the flow field

The fluid studied in this investigation is assumed to be incompressible and Newtonian. The equation of mass conservation, (also known as the incompressibility constraint), and the Navier Stokes (NS) momentum equations are shown as follows

$$\nabla \cdot \mathbf{u} = 0, \tag{2.1}$$

$$\frac{\partial \mathbf{u}}{\partial t} = -(\mathbf{u} \cdot \nabla)\mathbf{u} - \nabla p + \frac{1}{Re}\nabla^2 \mathbf{u}. \tag{2.2}$$

A commercial CFD solver, FLUENT (version 5.5), is used to numerically solve the time-dependent, incompressible NS equations. The solver uses the finite-volume technique to model the flow. The computations were performed using the double-precision version of the FLUENT solver for greater numerical accuracy.

In the finite-volume approach, the incompressibility constraint and momentum equations are integrated over all the control volumes of the flow solution domain. The integrals are converted to a system of algebraic equations involving non-linear equations between flow variables at neighbouring grid points. The discretized equations are then linearised and the resulting system of equations is solved in an iterative manner to yield the updated solution. For more information on the finite-volume approach, the reader is referred to, amongst other authors, Fletcher (1991), and Versteeg & Malalakesera (1995). In addition, FLUENT provides details of the numerical implementation in their software manuals.

FLUENT provides two different formulations for linearising the discretized equations and then solving

the system of linearised equations. These are the *segregated* and *coupled* solvers. Both formulations can be used, but by default FLUENT uses the segregated formulation for incompressible and slightly incompressible flows. A difference between the segregated solver and the coupled solver is that the former is less memory intensive (about two times less) at the expense of increased computational time and perhaps slightly less convergence stability. In this study, all flow simulations were performed using the segregated solver. No convergence problems were experienced. In the segregated solver formulation, the continuity and momentum equations for each component are uncoupled and are solved sequentially. The procedure, as described in the FLUENT help manual, is presented here for completeness.

1. Update the fluid properties u, v, p based on the current solution at time level t.
2. Obtain a *guessed* velocity field from solving the momentum equations by using the current values of pressure and mass fluxes.
3. Since the *guessed* velocity field does not satisfy continuity, a Poisson equation for the pressure correction is solved. This is used to derive corrections to the velocity field to drive the flow field towards mass conservation.
4. Iterate the previous 2 steps until convergence is obtained.
5. Update flow quantities at time level $t + \Delta t$.

For the case of co-axial vortex rings, equations (2.1) and (2.2) are solved using an axisymmetric formulation with zero swirl component. For axisymmetric geometries, there are two restrictions imposed on the coordinate system. Firstly, the axis of rotation must be the x axis. Secondly, the entire grid must lie either on or above the axis of rotation.

2.3.1 Grid generation

The important preprocessor stage to solving for the flow involves defining the geometry of the problem and constructing a mesh for it. The auxiliary software program, GAMBIT, which is part of the FLUENT package, was used to generate the mesh. Structured meshes with quadrilateral cells were used for all three case studies. Selection of quadrilateral cells ensures that most of the grid cells are aligned with the direction of the flow, especially at boundaries. This is favourable because numerical grid diffusion is minimised. For practical reasons discussed in more detail in the discussion on the treatment of the acoustics, a mesh with non-uniform grid-spacing is used. A linear stretching function as provided by Gambit, is used to implement this, and is defined as follows

$$\sum_{i=1}^{n} R^{i-1} = \frac{L}{l_1}, \tag{2.3}$$

where L is the edge length, n is the total number of intervals along the edge, R is the interval length ratio and l_1 is the length of smallest interval. In general, structured meshes are generally preferred for flow problems with simple geometries, such as we have here, because of better convergence rates and the smoothness of mesh point density variation.

2.3.2 Spatial discretisation and temporal marching

Convective variables are discretised by using the Quadratic Upstream Interpolation for Convective Kinetics (QUICK) scheme developed by Leonard (1979). It uses a three-point upstream-weighted quadratic interpolation scheme to minimise artificial diffusion errors.

In FLUENT, all flow quantities are stored at the cell centres. However, the finite-volume scheme computes the pressure gradient at the faces of the cell. Therefore, a second-order upwind scheme is used to interpolate the values of the pressure at the cell centres to the faces of the cells.

Pressure-velocity coupling is performed by using the semi-implicit method for the pressure-linked equation (SIMPLE) algorithm which was developed by Patankar & Spalding (1972). Basically, the SIMPLE method is an iterative scheme used for calculating pressure on a staggered grid arrangement. A relatively small value was used for the under-relaxation factor for pressure (≈ 0.3) during the initial phase of the computations. This guarantees solution stability and convergence at the expense of computational time. Once the flow has developed to a periodic state, the under-relaxation factor for pressure was gradually increased to 0.7. Even though the under-relaxation factor for pressure can be dependent on the type of flow studied, nevertheless, we found that the computations were stable and convergent for all the flow situations considered in this research without excessive dependence on the choice of relaxation coefficient.

To perform the integration in time, a second-order accurate, implicit time-stepping scheme was used. The temporal derivatives were evaluated using backward differencing. An implicit scheme has the added advantage of being unconditionally stable.

2.3.3 Monitoring flow convergence

In this investigation, the asymptotic or periodic state of the flow field is of interest. For the first two flow situations, the vortex system is 'imposed' on the flow domain prior to initiation of the flow solver, i.e., the simulation is started with the velocity field equal to the sum of the isolated vortex velocities. During the timestepping, to determine if the simulation is converged sufficiently, the field quantities at the centroids of the vortex cores are used for monitoring, (in addition to the standard convergence criteria described below). During the initial phases of the computations, (typically first and second flow periods), both

vorticity and pressure at the two nominated positions are monitored at every time-step. Convergence is assumed if the absolute changes in the magnitudes of all the flow measurements are within nominated tolerance levels.

For the aeroacoustic problem of periodic shedding from a long rectangular plate in uniform flow, the simulation is started with the fluid having a freestream velocity U_∞ everywhere in the domain. As with the previous case studies, we are primarily concerned with the *asymptotic* periodic state. For the cases studied, the flow eventually reaches a purely periodic state for shedding from both the leading and the trailing edge of the plate. Typically, the simulations take approximately 30–40 shedding periods to reach an asymptotic state. There are approximately 500 time-steps per shedding cycle.

With FLUENT various different criteria can be used to ensure the solution has converged from timestep to timestep. The convergence criteria used were based on the change in the magnitude of the residuals of the continuity and momentum equations at each time step. Typically, the residuals for the segregated formulation are scaled using the velocity and length scales characteristic to the problem. Each residual is obtained by summation over the entire solution flow field domain. The unscaled residuals were used for the flow problems of an isolated vortex pair, and a pair of co-axial vortex rings. In the final study of flow past a plate, normalised residuals were used. For the continuity equation, normalisation is performed through division by the maximum residual value after a fixed number of iterations. For the three flow situations considered in this thesis, the nominated tolerance criteria were set so that the spanwise vorticity and pressure were converged to four significant figures over the entire field before moving to the next timestep.

2.3.4 Computational domain and boundary conditions

The ideal situation for modelling an unsteady flow in free space is that the domain is unbounded and extends to infinity. However, this is not possible in a computational model. As such, an artificial truncation of the domain needs to be made. To minimise blockage effects, the computational domain size has to be sufficiently large not to unduly affect the flow solution in the region of interest. This is difficult to determine a priori, although various books on computational fluid dynamics provide guidelines. In any case, domain-size independence studies were carried out for each case study to determine an appropriate size of the computational domain.

Boundary conditions for the co-rotating vortex pair and co-axial vortex ring systems

For these flow situations, the vortex systems are relatively compact and isolated, i.e., the vortices do not exit the computational boundaries. As such, the approximate velocity can be specified at the outer boundaries.

For the co-axial ring, an axisymmetric boundary condition was imposed at the internal radial boundary.

Boundary conditions for flow past a rectangular plate

With the direction of the freestream velocity from left to right, a freestream condition with unit velocity in the horizontal direction is imposed on the inlet, top and bottom boundaries. The pressure condition (which enforces a zero-normal gradient for all velocity components) is imposed on the outflow boundary. On the surfaces of the plate, a no-slip condition is applied so that the velocity on the plate is zero.

2.3.5 Spatial and temporal resolution

Naturally, both flow and acoustic simulations are sensitive to temporal and spatial resolution, and hence, it is important to undertake validation studies as a mandatory component of each study. Independent resolution studies were conducted for both the CFD and CAA components of each study. The results of these tests are described in the chapters that follow.

2.3.6 Aerodynamic forces

In the study of bluff body flows, the lift and drag forces acting on the body are relevant parameters associated with the wake behaviour and sound generation. In various experiments and numerical simulations discussed in the previous chapter, there was a direct correlation between the magnitude of the fluctuating aerodynamic forces and the acoustic dipoles (commonly known as the Aeolian tones).

The total force acting on the plate has two components. These are surface forces due to viscous shear and hydrodynamic pressure. These components are combined to form a total vector force, with a horizontal component, i.e., the drag, and a vertical component, i.e., the lift. As usual, the non-dimensionalised coefficients of the respective force components are obtained by dividing the forces by the term $0.5\rho_o U_\infty^2 A$. Here, U_∞ is the freestream velocity and A is the frontal area of the plate.

2.3.7 Exporting the hydrodynamic field to the acoustic domain

Within FLUENT, the hydrodynamic field is exported through a user-defined function (UDF) for use within the aeroacoustic solver. The exporting is carried out at pre-defined time intervals. The velocity components are located at the centre of the cells.

2.4 Numerical aspects of CAA

A primary objective of computational aeroacoustics (CAA) is to accurately model the generation and propagation of sound waves generated aerodynamically from the hydrodynamic field. To achieve this, the physical behaviour of acoustic wave propagation over a long time integration in a large domain has to be preserved. In particular, the numerical scheme used to discretise the acoustic equations should introduce very little numerical dispersion or dissipation. To illustrate the issues relevant to CAA, we consider acoustic radiation from flow interactions at a low Mach number. For CAA issues pertinent to supersonic jet noise, the reader is advised to refer to Tam (1995).

In this section, we present the techniques adopted in the acoustic simulation. We also discuss parameter selection and other choices appropriate for accurate modelling. Many of these choices have been discovered, or at least optimised, through a considerable amount of testing and validation. In addition to a discussion of the high-order discretisation scheme and implementation of grid stretching, two important issues relevant to this investigation are spatial truncation of the acoustic domain and starting up acoustic simulations without introducing slowly-decaying, spurious acoustic noise into the acoustic field. The combined approach described here has been successfully implemented in all three different aeroacoustic problems with only minor adjustment between scenarios, indicating the robustness of the techniques. One of the main advantages of the current approach is that the acoustic radiation for each flow situation was obtained without any added filtering or artificial dissipation often used to prevent the build-up of artificial noise.

2.4.1 The acoustic wave equation

The governing equation for the far-field acoustics consists of the linear wave equation with a non-linear forcing term, $H(x, y, t)$, on the right-hand side

$$\frac{\partial^2 p}{\partial t^2} - c_o^2 \nabla^2 p = H, \tag{2.4}$$

where the acoustic pressure p has been non-dimensionalised by $\rho_o c_o^2$. For convenience, hereinafter, equation (2.4) will be referred as the acoustic wave equation. Two different forms of the acoustic source term are used for simulations described in this thesis. These are $H_l(x, y, t)$, corresponding to the source term developed by Lighthill (1952), and $H_p(x, y, t)$ referring to the source term developed from Lighthill's form by Powell (1964). These are given by

$$H_l(x, y, t) = \frac{\partial^2 u_i u_j}{\partial x_i \partial x_j}, \tag{2.5}$$

$$H_l(x, y, t) = \nabla \cdot (\omega \times \mathbf{u}) + \nabla^2 \frac{\mathbf{u}^2}{2}, \tag{2.6}$$

$$H_p(x, y, t) = \nabla \cdot (\omega \times \mathbf{u}). \tag{2.7}$$

The acoustic source term in equation (2.5) is as derived by Lighthill while Powell showed that Lighthill's acoustic source could be represented alternately by the form given in equation (2.6), and subsequently identified the acoustic source with the first term.

It is convenient from a numerical implementation point-of-view, to recast the acoustic wave equation as a set of first-order partial differential equations (PDEs). This facilitates the application of a multi-stage scheme for temporal advancement of the acoustic field. The first-order equations in a Cartesian coordinate system can be expressed as follows

$$\frac{\partial \mathbf{q}}{\partial t} + \frac{\partial \mathbf{E}}{\partial x} + \frac{\partial \mathbf{F}}{\partial y} = \mathbf{H}(x, y, t), \tag{2.8}$$

where the vector fields in equation (2.8) are defined as

$$\mathbf{H} = \begin{vmatrix} H \\ 0 \\ 0 \end{vmatrix},$$

$$\mathbf{q} = \begin{vmatrix} \frac{\partial p}{\partial t} \\ \frac{\partial p}{\partial x} \\ \frac{\partial p}{\partial y} \end{vmatrix},$$

$$\mathbf{E} = \begin{vmatrix} \frac{\partial p}{\partial x} \\ \frac{\partial p}{\partial t} \\ 0 \end{vmatrix},$$

$$\mathbf{F} = \begin{vmatrix} \frac{\partial p}{\partial y} \\ 0 \\ \frac{\partial p}{\partial t} \end{vmatrix}.$$

2.4.2 Spatial discretisation

Discretisation of the spatial terms in the acoustic wave equation was performed using the finite-difference method. As discussed in Chapter 1, high-order spatial and temporal schemes are required to resolve the propagation of acoustic waves over long time periods in a large spatial domain. These are required to capture the compact source region together with the much larger acoustic region. Using the finite-difference approach, the spatial derivatives can be discretised in the general form given by,

$$\frac{\partial f(x)}{\partial x} \approx \frac{1}{\Delta x} \sum_{j=-M}^{N} a_j f(x + j\Delta x). \tag{2.9}$$

Here, $M + N + 1$ is the number of grid points required for the particular stencil. The right-hand side of equation (2.8) is expanded using a Taylor series expansion. Equating terms with the common derivatives

results in $M + N$ equations for the coefficients a_j. It is obvious that for a central-difference stencil, the odd-order derivatives cancel out. A three-point stencil yields a second-order accurate scheme while a five-point stencil results in a fourth-order scheme, and a seven-point stencil yields a sixth-order scheme. In all three cases, the central coefficient a_0 is zero. For this investigation, the sixth-order central-difference scheme is used and the coefficients a_j are as follows

$$\begin{aligned} a_0 &= 0, \\ a_1 = -a_{-1} &= -\frac{1}{60}, \\ a_2 = -a_{-2} &= \frac{9}{60}, \\ a_3 = -a_{-3} &= -\frac{45}{60}. \end{aligned} \tag{2.10}$$

A further complication is the requirement of deriving the difference schemes for stretched grids. The conservative form of the Laplacian is as follows, provided the grid is only stretched independently in the two major directions,

$$\nabla^2 f = \frac{1}{x_\zeta}\frac{\partial}{\partial \zeta}\left(\frac{f_\zeta}{x_\zeta}\right) + \frac{1}{y_\eta}\frac{\partial}{\partial \eta}\left(\frac{f_\eta}{y_\eta}\right), \tag{2.11}$$

where the metrics of the grid stretching in the x and y direction are represented by x_ζ and y_η, respectively. The are defined explicitly when the acoustic mesh is constructed (see equation (2.12) below). Hence the stencil defined by equation (2.10) can be used on the computational mesh (ζ, η) where the spacing is uniform.

2.4.3 Temporal marching

An explicit method is used to discretise the acoustic wave equation in time since it provides a better approximation of acoustic wave propagation according to Wells & Renaut (1997). Temporal marching of the aeroacoustic simulation is conducted using the classical four-stage Runge-Kutta (RK4) method. With a high-order temporal scheme, the time-step used to advance the flow can be increased while maintaining stability. Since low-order time differencing can implicitly introduce both dispersion and dissipation errors, a high-order scheme is warranted. The time-step used in the acoustic simulation corresponds to the limit of stability of the RK4 scheme.

2.4.4 Grid considerations

The grid used in the acoustic calculations is structured and is divided into $(N_x)_a \times (N_y)_a$ points where $(N_x)_a$ and $(N_y)_a$ represent the number of grid points in the x and y directions. In the near-field, a small grid-spacing, Δx_n, is used to adequately resolve the acoustic source term. The far-field region, typically one or two wavelengths away from the source requires a less fine grid spacing, Δx_f, to resolve the acoustic

waves. The lower the Mach number, the greater the disparity between Δx_n and Δx_f. Between the near-field and the far-field parts of the domain lies a transition region, where the mesh is stretched. In typical aerodynamic flow simulations, the region of interest lies where the viscous gradients are large (i.e., around the surface/s of an external body). As a result, there is generally less emphasis on smoothly stretching the mesh away from where the flow gradients are large towards the domain boundary. In sharp contrast, for aeroacoustic simulations, the entire domain requires acceptable resolution since acoustic waves propagate radially away from the source position and need to be adequately resolved throughout the domain. It is well known that spurious waves are generated if acoustic waves propagate through a region of rapid stretching (Mitchell *et al.* (1995)). This problem is often especially acute during the initial stages of the computation, since the initiation of the acoustic calculation may introduce large temporal gradients into the solution field.

For the current implementation, a one-dimensional stretching function is used for each coordinate direction. Grid stretching is implemented using the following algorithm

$$\begin{aligned} x_{i+1} &= x_i + r(x_i - x_{i-1}), \\ r &= r + \Delta r. \end{aligned} \tag{2.12}$$

where x_i is the spatial coordinate at the i^{th} node. The control parameter of the grid stretching algorithm is Δr. By changing the value of Δr, the local rate of the stretching can be increased or decreased. Since the acoustic domain is in general made up of a square, the same rate of stretching is applied in both x and y directions.

2.4.5 Far-field boundary conditions

In the physical model of the hyperbolic equation governing wave propagation, the waves radiate outward to infinity and obey the Sommerfeld radiation condition at infinity. However, in numerical computations, the domain is finite and as such, it is truncated with an artificial boundary. The objective of acoustic modelling is to apply a boundary condition that approximates the Sommerfeld radiation condition at the domain boundary, i.e., it should allow acoustic waves to exit the domain freely without generating any substantial reflections. Bayliss & Turkel (1980) derived both first- and second-order local boundary conditions by using the asymptotic expansions for the hyperbolic equations. The solutions are valid at large distances away from the source region. Bayliss & Turkel showed that the domain of integration can be very constricted with the second-order boundary condition. Since the sizes of the domains used in these investigations are relatively large (typically about two or three wavelengths from the source which is assumed to be fixed in space), the implementation of the first-order boundary condition is assumed to be adequate.

The first-order boundary condition as defined by Bayliss & Turkel is as follows

$$\frac{\partial p}{\partial t} + \frac{\partial p}{\partial r} + \frac{p}{r} = 0. \tag{2.13}$$

Here, r denotes the radial distance from the source to the boundaries. The source is assumed to be spatially fixed. The accuracy of the boundary condition is of order of $O(r^{-2})$.

One of the added costs of a high-order interior spatial stencil is that the stencil has to be adjusted for many points near the boundary. This is necessary to maintain the same spatial accuracy throughout the entire domain since errors at boundaries can propagate into the rest of the domain through reflections. Application of the seven-point stencil in the interior region at grid points close to a boundary results in reference to up to three points beyond the boundary. The stencils for the last three grid points as the interior boundary is approached are one-sided and are adjusted to use interior points as well as the ghost points.

At the third node away from the interior, the following asymmetric stencil in the backward direction is used

$$\begin{aligned} a_0 &= -2.45, \\ a_1 &= 6.0, \\ a_2 &= -7.5, \\ a_3 &= (20/3), \\ a_4 &= -3.75, \\ a_5 &= 1.2, \\ a_6 &= -(5/30). \end{aligned} \tag{2.14}$$

At the second node away from the interior, the seven-point stencil also pointing in the backward direction, is defined by the following coefficients

$$\begin{aligned} a_{-1} &= -5/3, \\ a_0 &= -385/300, \\ a_1 &= 2.5, \\ a_2 &= -5/30, \\ a_3 &= 25/30, \\ a_4 &= -0.25, \\ a_5 &= (1/30). \end{aligned} \tag{2.15}$$

Finally, at the first node away from the interior, the seven-point stencil consists the coefficients

$$\begin{aligned} a_{-2} &= 1/30, \\ a_{-1} &= -0.4, \\ a_0 &= -175/300, \\ a_1 &= 4/3, \\ a_2 &= -0.5, \\ a_3 &= 4/30, \\ a_4 &= -5/300. \end{aligned} \tag{2.16}$$

2.4.6 Boundary conditions for solid surfaces for the acoustic field calculation

A no-slip boundary condition is imposed on any solid surfaces present in the flow. In the acoustic simulation, stationary solid surfaces do not radiate sound but reflect sound waves that impinge on them. This is implemented through the following equation for the pressure

$$\frac{\partial p}{\partial \mathbf{n}} = 0. \tag{2.17}$$

where $\mathbf{n}$ is the normal vector at the surface.

A further complication arises with a high-order governing equation as an extended set of wall boundary conditions has to be created (e.g., see Tam (1995)). Following Tam *et al.* (1993), since there are three boundary points for a sixth-order spatial scheme, as such, three ghost points are needed so that the central-difference stencil can be applied at the surface. The values of the acoustic variable at the ghost points is obtained by reflecting the interior nodes about the surface. The implementation of the above procedure is quite straight forward since the flow geometry is relatively simple (i.e., the walls are aligned with the coordinate axes). The issue of the singularity at the square edges of the plate is addressed in the relevant chapter.

For the case of the co-axial vortex rings, the acoustic wave equation is solved using a (y, z) polar coordinate system. It is clear from the governing equations that there is a coordinate singularity at the centreline $y = 0$. To treat the singularity, the acoustic variable along the centreline is updated by using the interior nodes. Since the coefficient of the node of the symmetric stencil is zero, it cannot be used to evaluate the acoustic variable. As a result, a one-sided seven point stencil was used maintaining the overall accuracy of the discretisation.

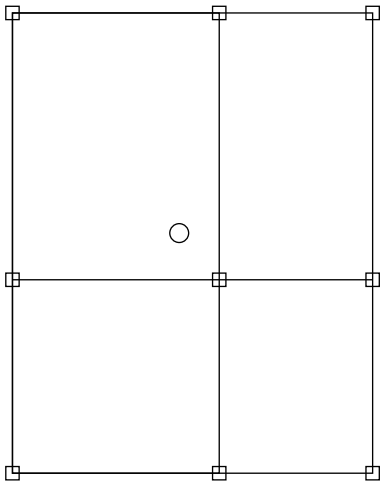

Figure 2.1: Illustration of the spatial interpolation routine. The circle denotes the acoustic node which may be randomly placed within the CFD mesh. The nine neighbouring nodes (squares) are used for interpolation.

2.4.7 Interpolating the hydrodynamic velocities from the CFD domain to the CAA domain

As has been discussed in Section 2.3.4, the number and distribution of the grid points of the CFD domain is different to the CAA domain. Hence, the hydrodynamic terms appearing in the acoustic wave equation have to be interpolated in space from the grid used in the flow simulation onto the acoustic grid. The acoustic source term $H(x, y, t)$ is then evaluated using the 'interpolated' hydrodynamic terms. This is set up as a two-step procedure. The first step is a pre-processing step in which the interpolation coefficients are evaluated. Subsequently, during the time integration of the CAA problem, these coefficients are used to interpolate the current hydrodynamic field to the acoustic grid so that the source terms can be evaluated.

To interpolate the (u, v) variables across the grids, a second-order polynomial was used instead of the standard bilinear method. This is done so that the interpolation maintains the same order of accuracy as that of the flow solver. The velocity components, (u_a, v_a) which are located on the cell corners in the acoustic domain are defined as follows

$$u_a(x_a, y_a) = \sum_{i=0,j=0}^{2} c_{ij} x_a^i y_a^j, \tag{2.18}$$

$$v_a(x_a, y_a) = \sum_{i=0,j=0}^{2} d_{ij} x_a^i y_a^j. \tag{2.19}$$

Here, (x_a, y_a) refers to the spatial coordinates of the acoustic grid. The arrays c_{ij} and d_{ij} are the

coefficients of the respective polynomials. For second-order accuracy, there is a total of 9 unknowns in each interpolating polynomial. Hence, each acoustic node is surrounded by nine flow nodes (as seen in Figure (2.1)).

The details of the interpolation procedure are as follows. Firstly, matrix inversion is carried out to determine the coefficients, c_{ij} and d_{ij}. This is done by finding the spatial locations of the 9 flow nodes and their respective velocity magnitudes. Secondly, the values of the velocity components on the acoustic grid, (u_a, v_a), are easily found through multiplication of the coefficients with the spatial location of the respective acoustic node. To facilitate this transfer process, a map file which contains the coefficients c_{ij} and d_{ij} is created once the two grids have been generated.

2.4.8 Spatial filtering of the hydrodynamic velocities in the CAA domain

In Lighthill's acoustic analogy, the acoustic source term H_l is assumed to decay to zero outside the region of the fluctuating flow. Powell's acoustic source term H_p is explicitly zero outside regions of non-zero vorticity. In the idealised acoustic model, the flow velocity components approach a constant value away from source regions resulting in the magnitude of the acoustic source converging to zero (since the source depends on velocity gradients). However, in practical flows of interest, the spatial decay of the hydrodynamic field can be gradual. This is especially true for flow situations like shear layers, multiple vortex pairings exiting a jet, and periodic shedding from uniform flow past a compact body. This can lead to problems since, unless the CFD domain is large enough so that the velocity components effectively converge to constant values, interpolating from the CFD domain to the CAA domain will result in a discontinuity where the numerical interface of the artificial boundary of the CFD domain is located.

Therein lies the problem of defining the 'size' of the hydrodynamic region in the acoustic domain. Both Mankbadi (1990) and Colonius *et al.* (1997) have recognised that any sudden termination of the hydrodynamic terms in the acoustic domain will result in spurious errors being introduced to the acoustic solution.

To be able to numerically implement the acoustic analogies, an approximation of the acoustic source term has to be made so that it smoothly converges to zero outside the region of potential acoustic sources. In this investigation, the mechanism to achieve this is through a spatial filter zone. The concept of a spatial filter zone is similar to the sponge region used in the direct simulations of compressible flows by Colonius *et al.* (1997) and Inoue & Hatakeyama (2002)).

For the first two case studies, the vortex system is confined in an otherwise irrotational fluid. The application of a spatial buffer is relatively straight forward and unambiguous. This is because vorticity does not actually come into contact with the buffer region boundaries. In the isolated co-rotating vortex pair structure, the centre of the vortex system is stationary, thus implying a stationary source. In the

second case study of a pair of co-axial vortex rings moving in the same direction, the vortex system is self-convecting and thus the source is also convecting. As a result, prior to application of the spatial filters, the translational component of the hydrodynamic term is first removed.

At a defined radial distance away from the centre of the vortex system, the hydrodynamic terms in the acoustic domain have to be artificially truncated to zero. This results in the computed acoustic source field converging smoothly to zero. The size of the spatial filter region is varied appropriately so that the magnitude of any resulting fluctuations is at least several orders of magnitude smaller than the acoustic fluctuations. The spatial truncation of the hydrodynamic velocities is performed as follows

$$\begin{aligned} u_a^{'} &= u_a f_x f_y, \\ v_a^{'} &= v_a f_x f_y. \end{aligned} \tag{2.20}$$

where f_x and f_y are the filter functions applied in the directions of the respective axes. The filter functions have a value of unity in the region of the potential source and decay gradually to zero as a function of distance from the centre of the vortex system.

In contrast to the first two case studies, the final case study of uniform flow past a rectangular plate is characterised by a very slowly decaying vortex street downstream of the plate. The wake vorticity is made up of a series of convecting vortices, resulting in a non-compact acoustic source region. This forms a severe test of the ability of the spatial filter to successfully truncate the hydrodynamic field. Through extensive testing, we found that the truncation of the wake vorticity if performed carefully had negligible impact on the predicted sound field. This is expected since according to various acoustic theories (e.g., Howe (1975)), the wake vortices do not contribute to any net energy transfer between the flow and acoustic fields when they convect away from the plate at a relatively constant speed. This point is addressed in greater detail in the chapter dealing with the final case study. For this third case, there is a slight modification to the horizontal velocity component as follows

$$u_a^{'} = u_a f_x f_y + U_\infty (1 - f_x f_y). \tag{2.21}$$

where U_∞ represent the freestream velocity.

The exact location and size of the spatial filters is dependent on the case study in question and is detailed in the corresponding chapters of this thesis.

2.4.9 Evaluating the instantaneous acoustic source term, $H(t)$

One of the benefits of the two-step aeroacoustic prediction approach is that the flow solver and the acoustic solver can be optimised individually. For instance, the flow simulation is advanced in time using the maximum permissible time step while satisfying the criteria for flow convergence. In the acoustic

simulation, the Mach number is very small. As such, the time step used to advance the acoustic solution temporally is significantly smaller than the hydrodynamic time step. As Slimon *et al.* (1999) has pointed out, the time step used to advance the acoustic simulation in an explicit formulation should be adjusted such that the CFL condition approaches unity (to minimise dissipation and dispersion errors).

At first glance, it would seem that the instantaneous acoustic source term, $H(x, y, t)$ has to be interpolated in time between successive hydrodynamic time steps. This is certainly feasible though rather costly in terms of computational time and data storage. The approach adopted here is to use a reasonably high-order smooth interpolation procedure with fewer points per cycle. Tests indicate that for the three cases considered in this thesis, approximately 16-32 frames per acoustic period is more than adequate to resolve the temporal evolution of the acoustic source term.

As a consequence, instead of using successive hydrodynamic time steps for interpolation to the acoustic problem, the flow field is saved at a number of equi-spaced time intervals. A note to the reader is that since all three flow situations examined are time-periodic or near periodic, the number of intervals/frames can be fixed throughout the evolution of the acoustic events. Presumably, if the flow period was to vary significantly, this would imply that the acoustic behaviour would also change and as such, the number and temporal spacing of the intervals may have to be adjusted accordingly.

The hydrodynamic field from the flow solver is exported at pre-defined time intervals. The source distribution for each acoustic time step can then be constructed from the saved velocity field frames. There are various ways of fitting a curve through such a data series. A high-order polynomial is not considered as it may lead to wiggles. An initial attempt was to use a Fourier series; however, because the source distribution can vary rapidly in time, this can cause problems with a global method. Two options considered which preserve smoothness properties and do not suffer from contamination properties of global methods were cubic and quintic splines. While the cubic-spline was acceptable in the co-rotating vortex-pair problem, it led to wiggles in the far-field time traces for the co-axial vortex rings irrespective of the sampling interval. This is believed due to the discontinuity in the second-order derivative. As such, a quintic spline is used to fit a curve through the frames. For uniformity, all three case studies employed quintic spline interpolation. At the end-points of the spline, we impose the condition that both slope and curvature of the spline be smooth and continuous. The quintic spline is defined as follows

$$H(t) = \alpha_0 H_0 + \beta_0 H_1 + \alpha_1 H_0^{'} + \beta_1 H_1^{'} + \alpha_2 H_0^{''} + \beta_2 H_1^{''}, \tag{2.22}$$

where t_0 and t_1 represent the end points of the interval, H_0 and H_1 represent the source evaluated at the stored hydrodynamic time steps. The primes denote differentiation in time of the acoustic source terms. Here, the coefficients $\alpha_{0..2}$ and $\beta_{0..2}$ are defined as follows

$$\begin{aligned} \alpha_0 &= \frac{t_1 - t}{t_1 - t_0}, \\ \beta_0 &= \frac{t - t_0}{t_1 - t_0}, \end{aligned}$$

$$
\begin{aligned}
\alpha_1 &= \frac{1}{6}(\alpha_0^3 - \alpha_0), \\
\beta_1 &= \frac{1}{6}(\beta_0^3 - \beta_0), \\
\alpha_2 &= \frac{1}{360}(3\alpha_0^5 - 10\alpha_0^3 + 7\alpha_0), \\
\beta_2 &= \frac{1}{360}(3\beta_0^5 - 10\beta_0^3 + 7\beta_0).
\end{aligned}
$$

2.4.10 Initial condition to CAA

A common source of spurious waves in an aeroacoustic simulation is through generation via an artificial initial condition. For example, if the acoustic forcing field is suddenly turned on at the initial time, artificial transient acoustic waves with very sharp gradients result. This can be a serious problem when these waves advect through a mesh with non-uniform spacing and can lead to large-scale, non-physical reflections. Apart from contaminating the 'real' acoustic field, such spurious waves may also cause the solution to diverge.

Through considerable testing, a more suitable initial condition for the CAA calculation was found. A simple solution is for the acoustic source term, $H(x, y, t)$, to be ramped up gradually. This prevents the large gradients that are not well resolved on the grid and prevents divergence of the acoustic computation. This is implemented by multiplying the acoustic source by a ramping function $f(t)$ over the time interval t_r. The ramping function is zero at the initialisation of the acoustic computation and increases smoothly and gradually to unity (see the description below). The time interval is adjusted depending on the stretching of the acoustic grid so that the initial transient does not generate fluctuations that exceed the amplitude of the physically generated acoustic waves. Note that this is sufficient to produce stable solutions which become accurate once the transient has passed out of the computational domain. After that time, the acoustic solution field reflects the physical situation which we are trying to model.

2.4.11 The spatial filtering functions, f_x, f_y, and the temporal ramping function, f_t

The spatial filter functions, f_x, f_y share the same requirements and characteristics as that of the ramping function f_t. Hence, they are all represented by a polynomial function as follows

$$
f_t = \sum_{i=0}^{n} b_i \left(\frac{t - t_i}{t_f - t_i} \right)^i . \tag{2.23}
$$

The end conditions for the function ensure smoothness. These are $f(t_i) = f^{'}(t_i) = f^{''}(t_i) = f^{'''}(t_i) = 0$ and $f(t_f) = 1$, $f^{'}(t_f) = f^{''}(t_f) = f^{'''}(t_f) = 0$. (In the event of the spatial filter, the variables t are replaced with the spatial variables). The end conditions guarantees that the curves are smooth and continuous up to the third derivative. It must be mentioned that prior to selection of this particular

polynomial function, a number of 'natural' functions were tested, i.e., second-order exponential, tanh, sine, and cosine functions. The results of these functions were not satisfactory as the functions and/or its derivatives were either not continuous at the ends, or the rate of change of the function was too severe for the purpose of wave propagation modelling.

By using the above-stated end boundary conditions, the coefficients of the spatial filter and temporal ramping functions were evaluated numerically and found to be as follows

$$\begin{aligned} b_1 = 0, \quad b_2 = 0, \quad b_3 &= 0, \quad b_4 = 0, \quad b_5 = 70, \\ b_6 = -315, \quad b_7 = 540, \quad b_8 &= -420, \quad b_9 = 126. \end{aligned} \tag{2.24}$$

2.5 Concluding remarks

In this chapter, we have described the procedures employed to carry out the two-step approach. The commercial flow solver, FLUENT, is used to predict the hydrodynamic flow fields. To predict the acoustic radiation associated with the low Mach number flows, a computational aeroacoustic program was developed by the author. The acoustic solver reads in the hydrodynamic velocity components, interpolates to the acoustic nodes and evaluates the source using finite-differencing to calculate the derivatives involved.

A combination of a sixth-order spatial scheme and a fourth-order temporal scheme is used to compute the time evolution of the acoustic field. This ensures that the solution preserves the dispersion properties of the acoustic waves and has minimal dissipation. We have also discussed the spatial filtering and temporal ramping of the acoustic forcing. These two steps enabled us to solve the acoustic wave equation without any filtering and/or artificial smoothing being added. Importantly, the temporal ramping managed to reduce the amplitude and increase the time-scale of the initial transient stabilising future evolution.

It is a fact that the requirements of an accurate acoustic simulation are different to that of a flow simulation. This is because the nature of acoustic problems is quite different to that of flow problems. Issues of significant relevance in acoustic simulations such as spurious noise, excessive dissipation, wave reflection do not pose any major problems in aerodynamic simulations if they occur at all. On the other hand, resolution of viscous boundary layers and shear layers demand a relatively fine grid which is not as important for the acoustic calculation. In addition, the acoustic field is of interest over the entire computational domain. Again, this is in contrast to aerodynamic situations where only regions with high velocity gradients and/or where aerodynamic forces are present (as in bluff body flows) are relevant. Because the goals and requirements of the flow and acoustic subproblems are so different, the field of computational aeroacoustics is unique and should not be described as a branch of computational fluid dynamics.

Chapter 3

On the sound generated by a co-rotating vortex pair

3.1 Summary

This chapter describes a numerical investigation into the far-field sound generated by a pair of spinning vortices in a viscous fluid. This study forms the first part of the three cases used to validate the two-step aeroacoustic prediction method. In the present study, specifications of the flow configuration are identical to those used in Mitchell *et al*'s. (1995) study. Results from the flow simulations showed that there were a total of five and a half co-rotation cycles prior to the merging of the two vortex cores into a single entity. From the second part of the computation, it was found that the acoustic signals calculated by using Lighthill's acoustic analogy, and Powell's vortex sound theory, were effectively identical at the Mach number simulated. The time variations of the acoustic signals were nearly sinusoidal and the acoustic peak was maximum at the instant of vortex merger. The numerical results were compared with the DNS results of Mitchell *et al.*, and analytical predictions obtained using the method of matched asymptotic expansions. There was good agreement in both comparisons. This study has also clearly demonstrated that the steps used to obtain an accurate acoustic solution (as described in the previous chapter) have been successfully implemented.

3.2 Introduction

One of the most widely studied aeroacoustic problems is that of acoustic waves generated by a pair of co-rotating vortices. Powell (1964) has used the spinning vortex pair to demonstrate that the sound

power from such a flow varies to the eighth power of the vortex velocity. Using the method of matched asymptotic expansions, Müller & Obermeier (1967) have derived the far-field expression of the flow problem and showed that the acoustic far-field has a double-spiral pattern.

With the development of new and existing acoustic theories, this particular flow configuration has become one of the most common benchmark problems in the field of aeroacoustics. There are two main reasons as to why this is so. Firstly, both the hydrodynamic and acoustic solutions can be obtained analytically. Secondly, the flow field is compact and is spatially—fixed as the vortices spins about a common centre of rotation. Hence, the acoustic source can be modelled without the complications of an advection component and an extensive wake region. Thus, it satisfies the assumptions of flow compactness and source compactness invoked in various acoustic theories of sound generation for low Mach number vortical flows.

The objectives of this study are two-fold. Firstly, we aim to demonstrate the implementation procedure and the selection criteria of the parameters in the steps used to predict the acoustic radiation numerically. As described in the previous chapter, these measures are significant in the efforts to numerically solve the acoustic wave equation without needing any artificial dissipation or explicit filtering schemes. The associated issue of the spatial extent of the source terms in Lighthill's acoustic analogy, and Powell's vortex sound theory is also examined. Secondly, this study provides us with further insight into the basic acoustic generation mechanism of simple, unsteady flow fields. Such understanding into the physics of sound generation is vital as the complexity of the flow fields was increased as this research progressed from simple, compact, vortical flows to the natural shedding from laminar flow past an elongated bluff body.

3.3 Analytical prediction

In the classical version of the flow configuration that is being considered in this chapter, the vortex cores are assumed to be infinitesimally thin and the fluid is inviscid. As a result, the spinning point vortices rotate about the fixed centre of rotation with an angular velocity of $\Omega_o = \Gamma_o/(4\pi Z_o^2)$, where Z_o is the radial distance from the centre of rotation to the core centroid. The periodic motion of the spinning vortices results in the generation of sound waves. Furthermore, owing to the symmetry of the flow, the acoustic frequency is twice that of the co-rotation frequency. Using the method of matched asymptotic expansions, Müller & Obermeier (1967) have derived an analytical far-field acoustic expression as follows

$$p(x,y) = \frac{\rho_o \Gamma_o}{64\pi^3 Z_o^4 c_o^4} H_2(kr). \tag{3.1}$$

A typical plot of the far-field pressure calculated using the MAE method is shown in figure 3.1. The pressure contours clearly show a quadrupole rotating in the same direction as that of the spinning vortex

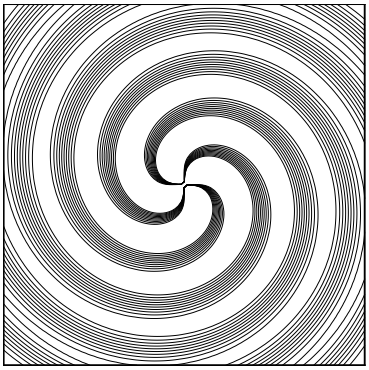

Figure 3.1: Instantaneous plot of the typical analytical acoustic pressure field generated from a pair of spinning point vortices.

pair.

3.4 Numerical issues

In the present study, the flow is assumed to be incompressible and viscous. As such, it is governed by the incompressible Navier-Stokes equation. In the first step of the aeroacoustic prediction method, the incompressible flow equations are solved numerically by using the commercial finite-volume CFD software, FLUENT. The CFD techniques used to generate an accurate flow solution have been previously described in chapter 2 and thus, are omitted here. The hydrodynamic fields over the entire flow domain are exported for the acoustic computation at a sampling rate of 16 frames per co-rotation period. These snapshots are sufficient to faithfully reconstruct the time-dependent velocity field. In the second step, the acoustic source term is evaluated from the 'interpolated' hydrodynamic terms and subsequently, the acoustic wave equation is solved numerically.

3.4.1 Initial conditions

The schematic of the flow configuration is shown in figure 3.2. The two vortex cores, which are like-signed with initial circulation Γ_o, are separated from the centre of the rotation by a distance Z_o. The Reynolds number, which is based on the circulation of the vortex core Γ_o, is defined as $Re = \rho_o \Gamma_o / \mu_o = 7500$. The Mach number is defined as $\mathrm{Ma} = \Omega_o Z_o / c_o = 0.06$, where $(\Omega_o Z_o)$ is the induced co-rotation velocity. The vorticity distribution of the core in the azimuthal direction, $\omega(r_c)$, is Gaussian and is defined as follows

$$\omega(r_c) = \frac{1.2495\Gamma_o}{\pi e_o^2} e^{-1.25(\frac{r_c}{e_o})^2} \tag{3.2}$$

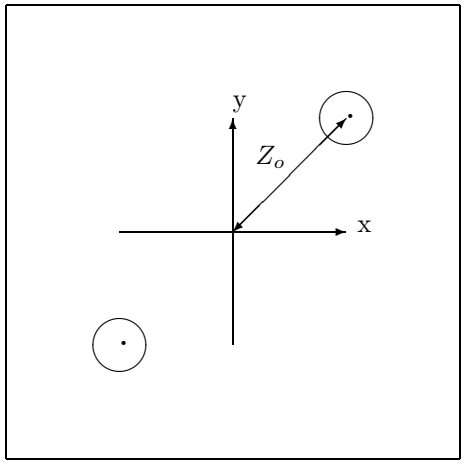

Figure 3.2: Illustration of the flow configuration. Circles denote vortex cores. Note that the sketch is not to scale.

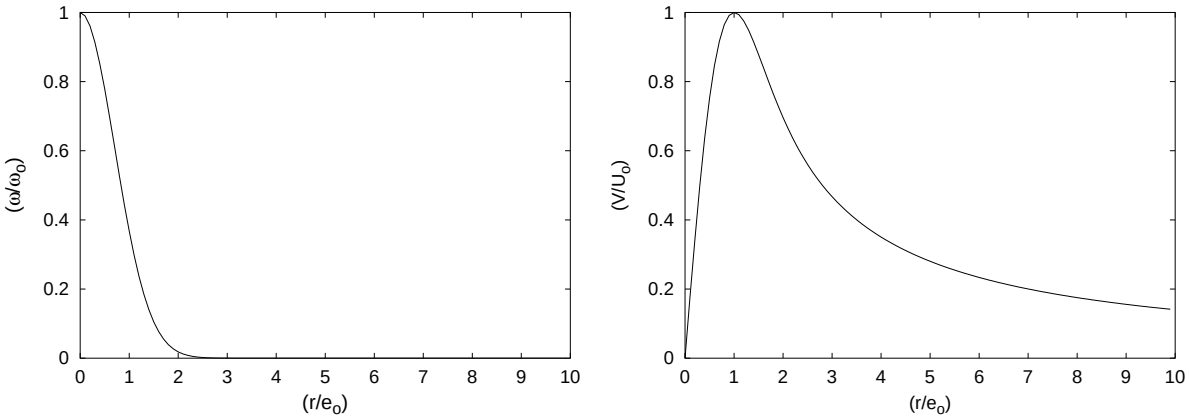

Figure 3.3: Distributions of the azimuthal vorticity and tangential velocity of the Gaussian vortex core model. Note that ω_o is the peak vorticity at the centre while $U_o = \Gamma_o/(4\pi Z_o)$.

and the tangential velocity distribution V_t, is as follows

$$V_t(r_c) = \frac{0.5\Gamma_o}{\pi r_c}(1 - e^{-1.25(\frac{r_c}{e_o})^2}), \tag{3.3}$$

where r_c is the radial distance from the centre of the core. The ratio of the core radius, e_o, to the separation distance, Z_o, is 0.15. It should be mentioned that the selection of the Reynolds number, Mach number and initial flow configuration is identical to that used by Mitchell *et al.* (1995). It should also be noted that the Gaussian vortex profile is favoured by many researchers when numerically defining vortex core structures because it is smooth and continuous in both vorticity and tangential velocity distributions (as shown in figure 3.3).

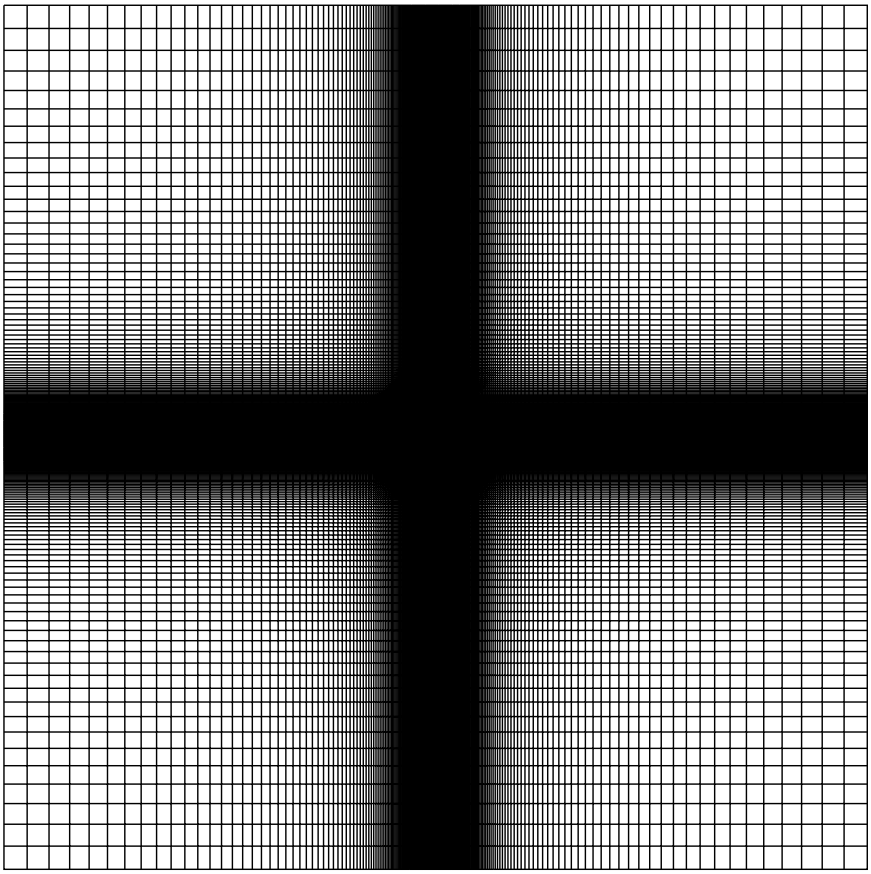

Figure 3.4: Typical mesh used in the flow simulations.

3.4.2 Computational aerodynamics issues

The flow solution is modelled on a square domain which extends to $20Z_o$ in both directions. The CFD domain is discretised into a structured mesh with $N_x \times N_y$ grid points. A typical mesh used in the flow simulations is shown in figure 3.4.

The grid is uniformly spaced in the region surrounding the vortex core (approximately $2Z_o$ radially from the centre of the vortex system). A linear stretching function with a maximum rate of 6% is then used to extend the grid to the external computational boundaries. A pressure outlet boundary condition was imposed on all four external boundaries. Prior to the execution of the flow solver, the solution field is initialised with the sum of the velocity components of the two vortex cores.

In order to ensure that the physics of the flow is well captured, preliminary simulations were performed whereby spatial- and-temporal resolutions studies were carried out. Three different minimum near-field grid spacings of $\Delta x/e_o = 0.225$, 0.45 and 0.9 were used in the spatial resolution study, while the time-step used to temporally march the incompressible flow equations was tested at $\Delta t U_o/Z_o = 8.84 \times 10^{-4}$, 1.768×10^{-3} and 3.536×10^{-3}. The total kinetic energy was used to monitor the flow convergence. Based on the results of these preliminary simulations, the minimum grid spacing $\Delta x/e_o = 0.45$, which amounted to approximately 20 points across the vortex core was found to be adequate in capturing the flow dynamics. Temporal-wise, there was little difference in results between a time-step of $\Delta t U_o/Z_o = 1.768 \times 10^{-3}$ and 8.84×10^{-4} and as such, the former time-step was adopted for further flow simulations.

3.4.3 Computational aeroacoustic issues

Similar to the CFD domain, the acoustic solution is modelled on a square domain. The CAA domain extends to two acoustic wavelengths away. As discussed by Mitchell *et al.* (1995), this is ideal for capturing the propagation and spatial decay of the acoustic waves. In the near-field, a grid spacing identical to that used to resolve the velocity gradients in the flow simulations is used. In the far-field, the grid is spaced such that there are approximately 20 points across the acoustic wavelength. As a uniform mesh is both impractical and too costly, the disparities of the near- and far-field grid spacings are reconciled through the use of a structured non-uniform mesh. The typical mesh used in the acoustic simulations is shown in figure 3.5.

A maximum local rate of stretching of 3% was used in both directions. The time-step used to advance the acoustic wave equation is chosen to be approximately at the stability limit of the RK4 scheme. At the external boundaries, the radiation condition based on Bayliss & Turkel (1980) is implemented.

Mitchell *et al.* (1995) have used a maximum local rate of grid stretching of 5% in their computational mesh to ensure that the wave propagation is not influenced by the grid. However, in spite of a moderately stretched grid, a filter function was used during the initial stages of the direct simulations because of the presence of large grid-to-grid oscillations caused by the initial transient. It will be shown in the following section that a moderate local rate of grid stretching must be coupled with a suitable initial condition to avoid such spurious noise which might otherwise occur from the sudden introduction of an acoustic source into the acoustic computation.

Another issue of major concern is the spatial extent of the source field in both aeroacoustic theories. Mitchell *et al.* (1995) have shown that if the slow decay rate of the source terms are not treated carefully, this will lead to a divergent acoustic solution. This issue along with the start-up function is discussed in further detail in the following subsections.

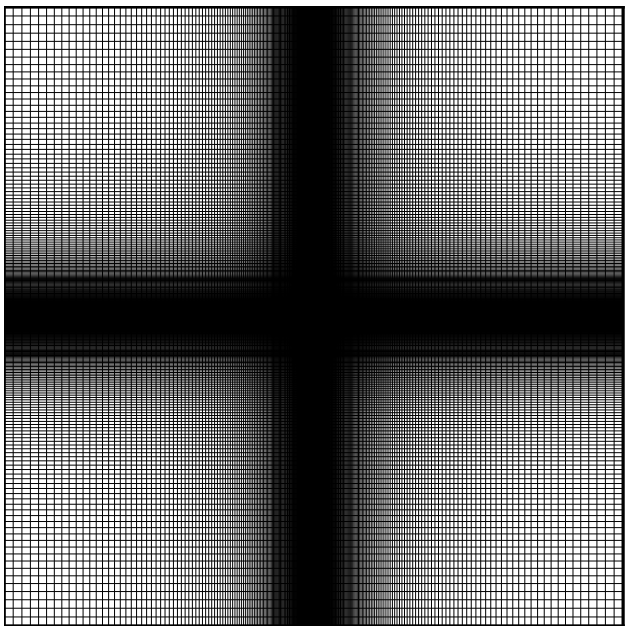

Figure 3.5: Typical mesh used in the acoustic simulations.

On the effect of the spatial filter

One of the main difficulties in recovering a convergent acoustic solution from the numerical implementation of the acoustic analogies relates to the spatial extent of the acoustic source terms. While the hydrodynamic flows in ideal cases are assumed to decay rapidly and thus ensure that the source terms converge to zero, in reality (as demonstrated in the present study), real flows do not particularly obey this ideal scenario. The problem arises because the CFD domain is much smaller than the CAA domain. As such, even if the velocity located in the entire CFD domain is interpolated in space back to the CAA domain, there remains a discontinuity because the bounds of the CFD domain still lies in the interior region of the CAA domain. In any case, it is impractical to use the velocity field of the entire CFD domain as the active acoustic region is confined to the highly rotational part of the flow field. This difficulty has been highlighted by Mitchell *et al.* (1995) who were unsuccessful in their attempt to obtain a meaningful far-field acoustic solution when the acoustic wave equation with Lighthill acoustic source as the forcing term was numerically solved. This was attributed to the slow algebraic decay of the the source terms in Lighthill's acoustic analogy.

To consider the effect of the sudden termination of the hydrodynamic field in the acoustic domain, two identical preliminary simulations but with different limits to the size of the hydrodynamic region were performed. In these tests, the flow velocity located outside the region is zero, thus resulting in

a spatial discontinuity in the source. In the first simulation, the Lighthill acoustic source is evaluated within a square of dimensions $4Z_o \times 4Z_o$. In the second simulation, the region where the source is evaluated is extended slightly to $6Z_o \times 6Z_o$. In both preliminary simulations, the sources were gradually ramped from zero to their true values over a ramping time of $t_r U_o/Z_o = 2.652$. The results of the two preliminary simulations are shown through the instantaneous contours of the pressure field in figure 3.6a-b. The pressure contours were taken at the simulation time of $t^* U_o/Z_o = 7.07$. It is clear that while the double spiral pattern is still visible in the near-field, its propagation to the far-field has, however, been severely distorted. Furthermore, the amount of distortion decreases as the size of the square was increased. Hence, the contamination of the acoustic solution is argued to be caused by the sudden termination of the hydrodynamic velocities outside the designated region. It was initially thought that by further enlarging the non-zero hydrodynamic region, the effect of the sudden termination as artificial noise sources might eventually disappear. As such, in a third simulation, the size of the region was increased to $10Z_o \times 10Z_o$. While the presence of spurious noise sources as seen in contour plots had indeed largely disappeared, the time histories of the acoustic signals located at $(r, \theta) = (0.5\lambda, 0°)$ and $(0.5\lambda, 90°)$, shown in figure 3.7, clearly indicate that the acoustic solution is diverging. Hence, the results from these three preliminary simulations have shown the difficulties of numerically solving Lighthill's acoustic wave equation. It is clear to us that the velocity field away from the region of the active sound source must be filtered to zero gradually so that the source term converges to zero smoothly.

To show that the acoustic source term in Powell's vortex sound theory is not as severely affected as for Lighthill's acoustic analogy, a fourth preliminary simulation was conducted using the hydrodynamic region of $10Z_o \times 10Z_o$ but this time, the acoustic source from Powell is used instead of that of Lighthill. Typical acoustic pressure contours for this simulation at the simulation time of $t^* U_o/Z_o = 7.07$ are shown in figure 3.8. In contrast to the three previous simulations, the double-spiral pattern did not contain any spurious noise in the near-field and the far-field. Furthermore, the acoustic solution did not show any signs of divergence. Thus, in the application of Powell's vortex sound theory to the present flow field, sudden termination of the velocity field does not affect the acoustic solution provided that the discontinuity is at least $5Z_o$ away from the centre of the vortex system.

These preliminary studies clearly show the advantage of a spatial filter region when implementing the acoustic analogies in a real flow situation. In the present acoustic simulations, the length of the spatial filter in both directions was $l_{fx}/Z_o = l_{fy}/Z_o = 1.33$. The filters f_x and f_y were applied at a radial distance of $1.67Z_o$ from the centre of the vortex system. Implementation-wise, the filter region can be smaller when Powell's vortex sound theory is used. This is because the source contribution $\nabla \cdot (\omega \times \mathbf{u})$ decays faster than the additional term $\nabla^2(\mathbf{u}^2/2)$ present in Lighthill's acoustic analogy (but not Powell's).

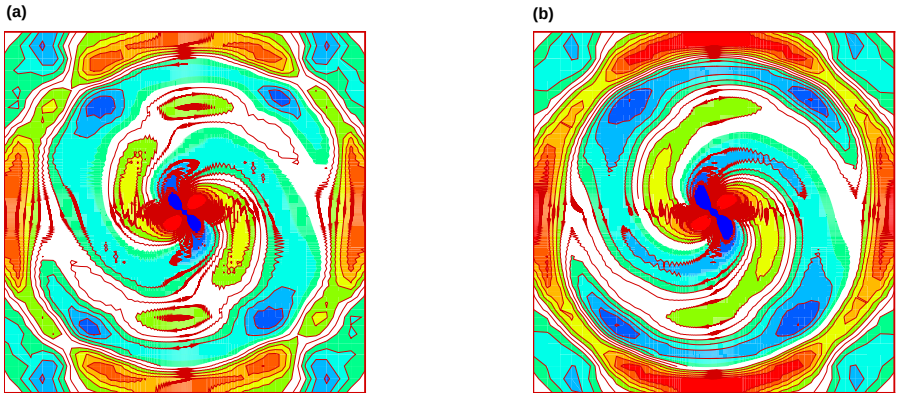

Figure 3.6: Instantaneous contours of the acoustic pressure fluctuations at $t^*U_o/Z_o = 7.07$. The region of the Lighthill acoustic source field with (0,0) as the centre limited to (a) $4Z_o \times 4Z_o$, and (b) $6Z_o \times 6Z_o$. The contour levels are $\pm 1 \times 10^{-4}$ with $\Delta p = 1 \times 10^{-5}$.

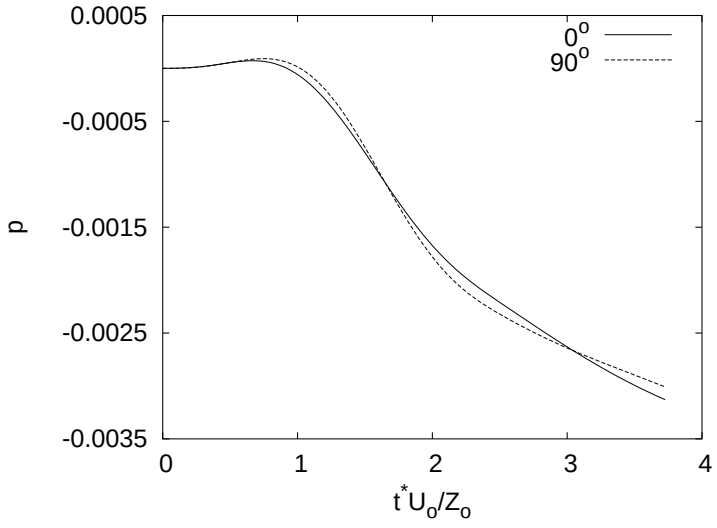

Figure 3.7: A sample trace of the time history of the acoustic pressure located at a radial distance of $r = 0.5\lambda$ (showing divergence in the far-field). The region of the Lighthill acoustic source field with (0,0) as the centre limited to $10Z_o \times 10Z_o$.

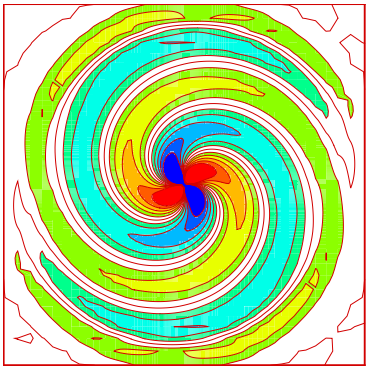

Figure 3.8: Instantaneous contours of the acoustic pressure fluctuations at $t^* U_o/Z_o = 7.07$. The region of the Powell acoustic source field with (0,0) as the centre limited to (a) $10Z_o \times 10Z_o$. The contour levels are $\pm 1 \times 10^{-4}$ with $\Delta p = 0.00001$.

On the effect of the start-up function

In the numerical simulations of the viscous spinning vortex pair by Mitchell *et al.* (1995), and Lee & Koo (1997), there was a sharp initial peak in the time variation of the acoustic signal. This is almost certain to be followed by spurious high-frequency oscillations as the transient wave propagates through the stretched grid. The presence of such sharp gradients was most probably a result of the sudden introduction of the source into the acoustic computations. This effect can be reproduced in the study here by performing the acoustic simulations on two stretched grids with a zero start-up ramp t_r in each test. Figure 3.9a shows that the time variation of the acoustic signal at the first maxima was dominated by large grid-to-grid oscillations. Thus, it is clear that an impulsively started initial condition to the acoustic computation has resulted in the generation of large amplitude, high-frequency initial transients regardless of the rate of stretching. As the transients propagate into the region of grid stretching, the spurious waves become increasingly intense. As the spurious waves propagate, the near-field as well as the far-field region are affected. While a grid with even finer or more moderate stretching would show an improvement, the computational costs associated with a finer grid increase quite dramatically. As the main purpose of the computation is to resolve the acoustic waves, which have relatively large length-scale and long time-scale, it is illogical to construct a grid primarily to resolve the initial transient. To circumvent this problem, a start-up function is used whereby the acoustic forcing is gradually ramped up from zero to its final true value over a certain period t_r.

The objective then is to create an initial transient having properties similar to the acoustic waves. As such, instead of a zero ramp period, three preliminary simulations are conducted on the previous grid with $t_r U_o/Z_o = 0.884$, 1.768 and 2.652. The time history of the same monitoring position is presented in figure 3.9b. It is clear that there is considerable improvement in the properties of the initial transient.

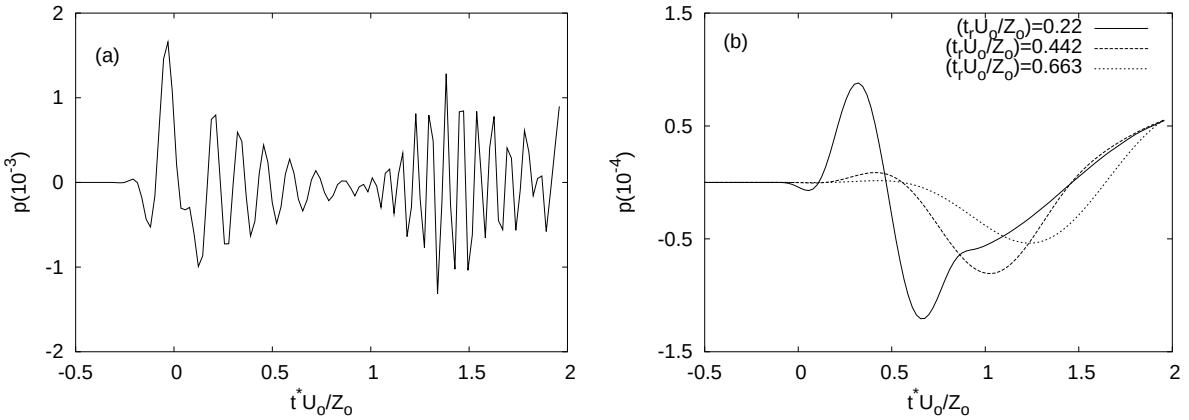

Figure 3.9: Time histories showing the initial transient at $r = 0.5\lambda$ along the positive x axis with different start-up ramp times of $t_r U_o/Z_o$ = (a) 0, (b) 0.22, 0.44 and 0.66.

For all three ramps, there were no grid-to-grid oscillations and the magnitude of the initial peak decreases as the ramp interval is increased.

The introduction of a start-up function has effectively decreased the magnitude while increasing the time-scale of the initial transient. While the period of the start-up function can be as gradual as possible, the selection depends on a compromise between minimising the impact of the initial transient, and preserving the properties of the subsequent acoustic waves. Ideally, if the number of co-rotation cycles was infinite, selection of the period t_r, would not be an issue. However, in viscous flows, there is a finite number of cycles as demonstrated in this investigation. As such, the ramping time, t_r, was set at approximately half the co-rotation period so that only the first peak is affected.

3.5 Results and Discussion

In the classical model, the co-rotation of the vortices repeats indefinitely. However, only a finite number of corotation periods are observed in the present case of finite-sized vortices in a viscous fluid. By tracking the position of the core centroids as a function of time, we found that there were approximately five and a half co-rotation cycles prior to the merging of the vortices. In contrast to the results of Mitchell *et al.*, there were two additional co-rotation cycles here. The reason may lie in the fact that compressibility affects the lead-up time to vortex merger. In the study by Mitchell *et al.*, the Mach number associated with the swirling flow in each core was 0.56 while in the present simulation, the flow field was assumed to be incompressible.

Figure 3.11 shows a composite picture of the vorticity snapshots totalling one co-rotating cycle. The first snapshot is taken at approximately the start position of the second co-rotating cycle. The vortices rotate about the centre/pivot point in a clock-wise direction. From the snapshots, it is evident that the

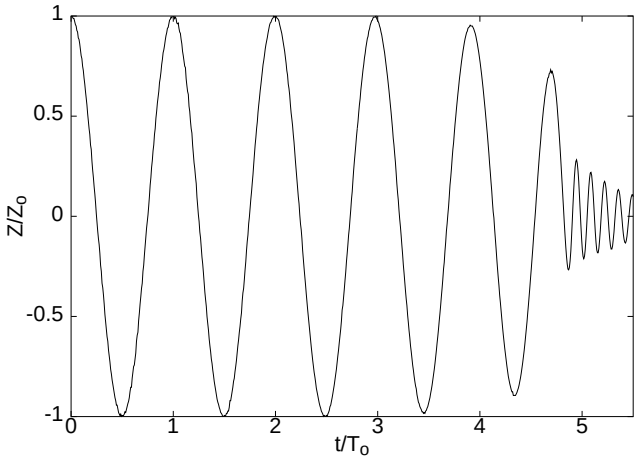

Figure 3.10: Time history of the horizontal distance between the vortex cores.

peak vorticity of the vortex cores is decreasing because of viscous spreading, resulting in the gradual 'coming together' of the vortices over successive cycles of co-rotation.

At a Mach number of Ma = 0.06, the source compactness as defined by the ratio of the acoustic wavelength λ, to the separation distance, Z_o, is 52.36. Time histories of the acoustic pressure fluctuations computed using Lighthill's acoustic analogy and located at $(r, \theta) = (0.5\lambda, 0°)$ and $(0.5\lambda, 90°)$, are shown in figure 3.12a. Figure 3.12b shows the time histories at identical observation positions, but Powell's vortex sound theory is used instead. The term r is the polar radius while the angle θ is measured from the x axis. It is clear that apart from the initial transient, there is only minor difference in the time variations of the acoustic signals. The acoustic waves show a nearly sinusoidal variation. This observation is consistent with the MAE analytical predictions and the direct simulations of Mitchell *et al.* (1995).

It is also clear that there is a gradual increase in the amplitude of the acoustic peaks over successive co-rotation cycles culminating in a maximum acoustic peak at the instant of vortex merger. The explanation for this acoustic behaviour lies in the fact that the sound power is proportional to the vortex velocity as has been pointed out by Powell (1964). While the angular velocity in the classical model remains constant, it is not so in viscous flows. As the peak vorticity is reduced by viscosity, the core becomes less compact and as such, the separation distance between the vortex cores also decreases. This results in an increase in the angular rotation velocity. As a result, the sound pressure level of the acoustic signals increases with the rate of rotation.

Instantaneous contours of the acoustic pressure field calculated using the two different source formulations while the vortices are still engaged in the co-rotation motion are shown in figure 3.13a-b. Both sets of contours are taken at the same time instant of $t^* U_o/Z_o = 12.39$. Similar to the analytical predictions, the acoustic pattern resembles that of a double-spiral pattern (see figure 3.1). It is also clear that there were no significant reflections from the external boundaries.

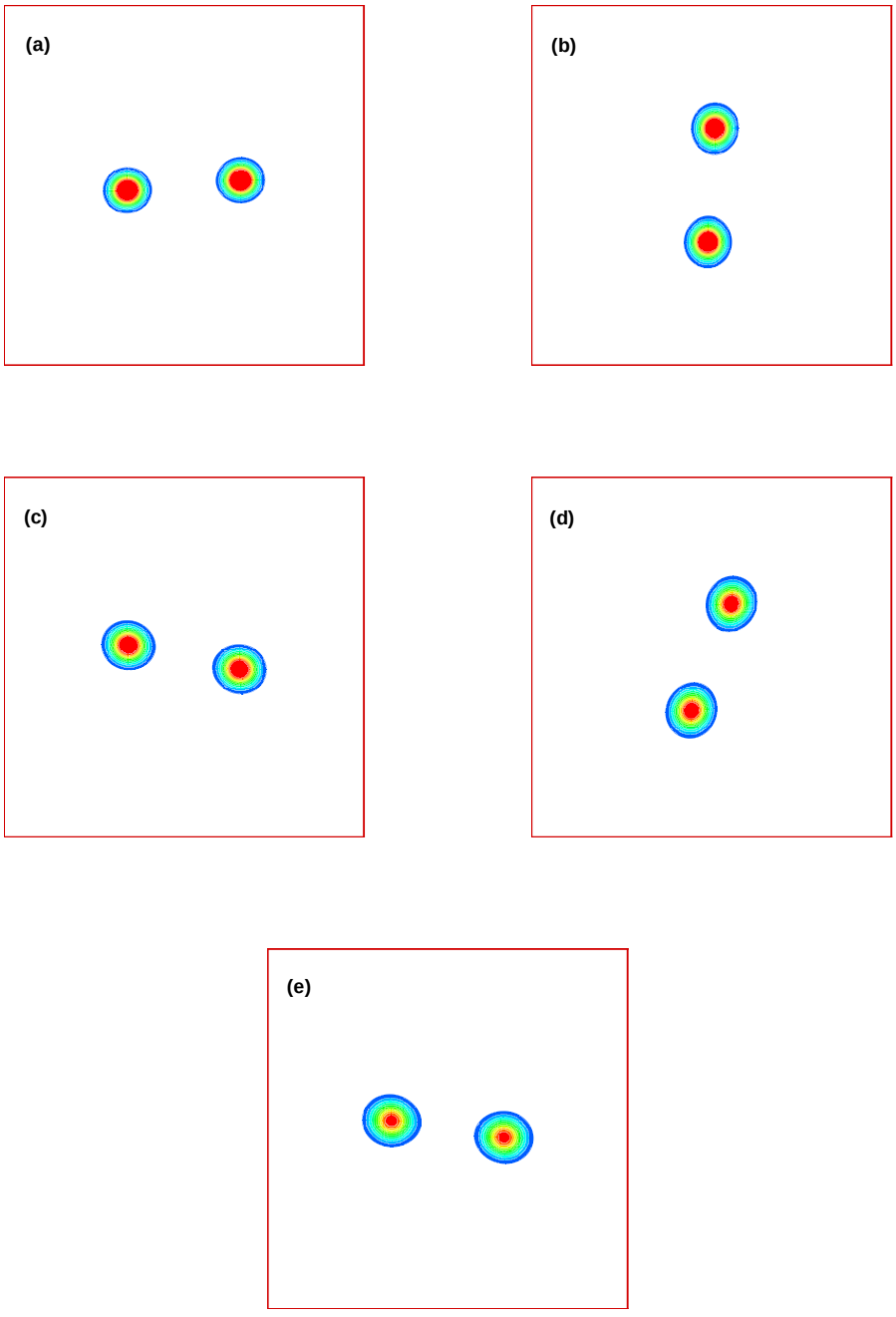

Figure 3.11: Snapshots of the instantaneous vorticity plots while the vortices are still in the co-rotating mode. t^*U_o/Z_o = (a) 6.19, (b) 7.78, (c) 9,2, (d) 10.61, (e)12.38. The min. and max. contour levels are 3.585 and 35.85, with 10 increments between them. Note, the vorticity has been non-dimensionalised with respect to the parameters, U_o and Z_o.

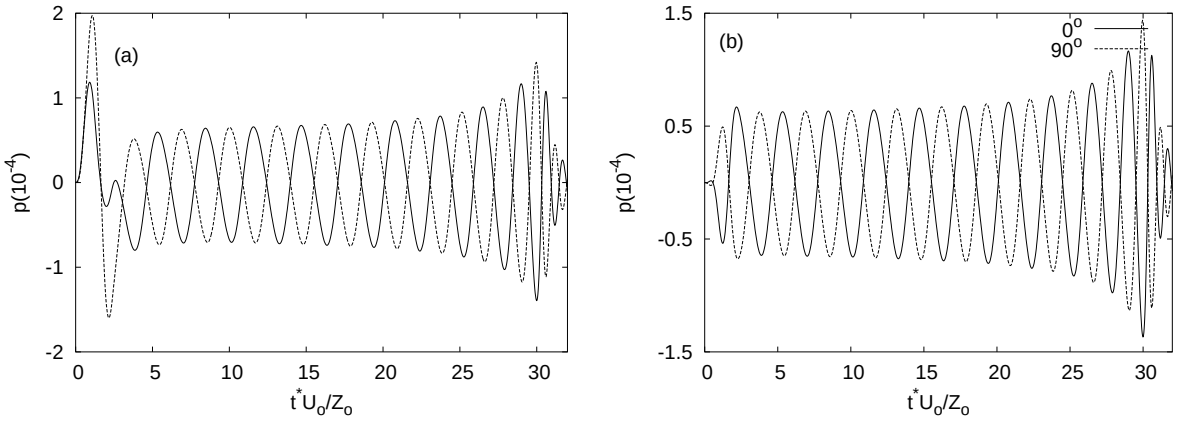

Figure 3.12: Time histories of the far-field pressure fluctuations calculated using (a) Lighthill's acoustic analogy and (b) Powell's vortex sound theory. The radial location of the observation position is $r = 0.5\lambda$.

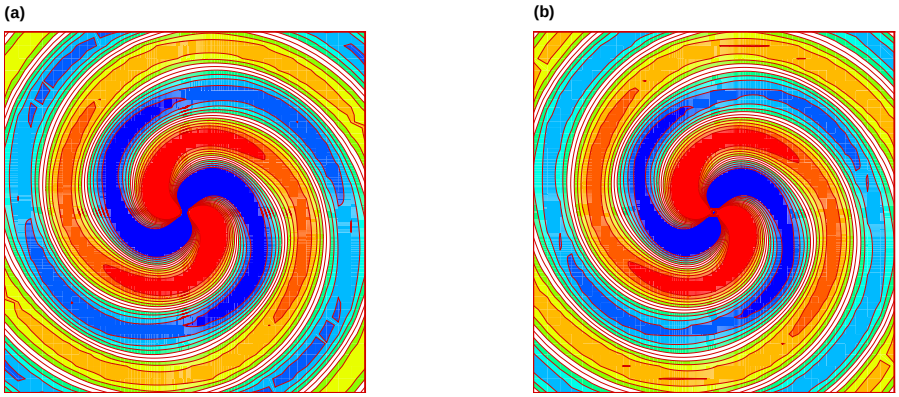

Figure 3.13: Contours of the instantaneous pressure field at a non-dimensionalised time, $tU_o/Z_o = 26.52$. (a) Lighthill's acoustic analogy, (b) Powell's vortex sound theory. Minimum and maximum contour levels are $\pm 4 \times 10^{-5}$ with increments of $\Delta p = 0.4 \times 10^{-5}$.

3.6 Concluding Remarks

In this chapter, the sound generated by the unsteady motion of an isolated co-rotating vortex pair in a viscous fluid has been studied. This study has clearly indicated that the two-step aeroacoustic prediction method is well-suited to predicting the sound radiation from low Mach number, compact, vortical flows. Two important issues related to the common goal of obtaining an accurate acoustic solution without any filtering scheme were highlighted.

The first issue concerns the large spatial extent of the source fields. In particular, the decay rate of the Lighthill acoustic source term was slower than that of Powell's vortex sound theory. Sudden termination of the source field outside the region of active sound generation is bound to result in large spurious noise which contaminates the far-field region. Hence, in order to be able to implement the acoustic analogies, spatial filtering is employed to decay the hydrodynamic terms located away from the active source region to zero so that convergence of the source term is assured. The larger spatial distribution of Lighthill's acoustic analogy implies that the spatial filter region has to be more extensive when compared to that applied for Powell's vortex sound theory.

The second issue focusses on the need for a proper initial condition to the acoustic computations. It is well known that crude initial conditions result in the generation of large transients. The problem is further worsened by the presence of grid stretching resulting in grid-to-grid saw-tooth like waveforms. While filtering or artificial dissipation routines are commonly used to remove such spurious noise, there are inherent dangers such as excessive damping of the physical acoustic field. As such, it is recommended that a start-up function be used to gradually ramp the source function to its true value over a ramping period.

The acoustic results showed that both Lighthill's acoustic analogy and Powell's vortex sound theory resulted in effectively identical acoustic signals. At the Reynolds number simulated, there were five co-rotation cycles prior to the merging of the vortices. The far-field pressure fluctuations showed nearly sinusoidal acoustic signals. In addition, the amplitude of the acoustic peaks were a maximum at the instant of vortex merger.

Chapter 4

Sound generated by a pair of co-axial vortex rings

4.1 Summary

In this chapter, the aeroacoustic phenomena associated with a pair of viscous co-axial vortex rings moving in a common direction along an axis of symmetry is investigated. In the context of this Ph.D. research project, this study in part represents the second validation test of our two-step aeroacoustic prediction method. The effect of viscosity on the flow dynamics and hence, acoustic generation mechanism is explicitly included by allowing the vortex rings to interact through cross-annihilation and diffusion. To the author's knowledge, such features have not been considered thoroughly enough in previous studies. In any case, this study poses a more rigorous examination of the two-step method owing to the increased complexity of the flow dynamics of the co-axial vortex rings relative to the isolated co-rotating vortex pair structure.

For simplicity, we confine our study to vortex rings of an initially circular core. In addition, the vortex rings are of like sign and have identical circulation. Our interest lies primarily in the acoustic effects caused by the mutual slip-through/leapfrogging interaction of the vortex rings. Such vortex pairing has been studied mathematically (Lamb (1932), Batchelor (1967)) and has also been observed in experiments (e.g., Yamada & Matsui (1979)). One of the interesting aspects of the flow behaviour is that when the rings are 'thin', the mutual slip-through process occurs without any significant core distortion, i.e., the interactions are largely periodic, at least for the initial period.

The Gaussian vortex core model which was earlier used in the isolated co-rotating vortex pair structure is once again adopted in this study. To numerically simulate thin vortex rings, the size of the vortex

cores has to be kept small relative to the initial toroidal radius of the vortex ring, and the axial distance between the two vortex rings. In this study, we consider the effect of the initial axial distance separating the two vortex rings on the sound radiation. The single parameter governing the motion of the vortex pairing is the aspect ratio z_o/y_o which is defined as the ratio of the initial axial spacing of the vortex rings z_o, to the toroidal ring radius y_o. The two aspect ratios used in this investigation, $z_o/y_o = 0.3$ and 0.5, are identical to those considered in the theoretical analysis by Kambe & Minota (1981). This is to facilitate a direct comparison between our numerical results with the predictions derived using the MAE technique.

The Reynolds number of the flow based on the circulation of the vortex ring was $Re = 7500$. Selection of this particular Reynolds number ensured that there were a number of successive leap-frogging cycles when analysing the acoustic effects of the rings' interactions. For each aspect ratio, the acoustic calculations were performed at three different Mach numbers, being Ma = 0.0025, 0.005 and 0.01. Results showed that at all three Mach numbers, both Lighthill's acoustic analogy and Powell's vortex sound theory effectively produced identical sound signatures. This implies that $\nabla \cdot (\omega \times \mathbf{u})$ is the dominant source term in vortex-pairing induced sound at low Mach numbers. Furthermore, the source terms in Powell's vortex sound theory have a faster spatial decay rate when compared to those in Lighthill's acoustic analogy. As such, the former is highly recommended for future studies on the aeroacoustic phenomena of compact vortical flows.

Prior to the merger of the vortex rings, the acoustic signature bears largely the effect of the slip-through motions. The time variations of the sound waves consisted of a series of sharp peaks and rounded troughs. Maximum sound radiation occurred at the slip-through instants. The far-field directivity was characterised by distinct polar angles of extinction in the range of 59° to 61° and 123° to 129°. These features are consistent with those predicted using the MAE technique. Slight discrepancy in the time traces of the acoustic signals between the numerical results and the MAE solution is attributed to the effects of core distortion during the leapfrogging cycles. Furthermore, the discrepancy was found to increase with aspect ratio. This is expected because the core deformation of the ring slipping underneath its counterpart during the leapfrogging cycle is more prominent as the toroidal ring radius is decreased. The distortion of the vortex core is a quasi-periodic phenomenon and as such the variations in the acoustic signals that were a result of core distortion were repeatable over the successive leapfrogging cycles. Another point about the acoustic peaks is that the amplitude of the peaks was maximum at the instant of vortex rings' merger. This particular feature has also been observed in the isolated co-rotating vortex pair structure.

Further analysis of the quadrupole and monopole sound sources of the axisymmetric vortex ring pairing revealed the former as the dominant term because the monopole source term was found to be several orders of magnitude smaller than the quadrupole. To relate the quadrupole source term in terms of the dynamics of each vortex ring, the quadrupole source term was further expanded into four terms

(Tang & Ko (1995)). A cursory analysis revealed that sound signals were strongly influenced by the radial acceleration of the vortex rings. A sample time trace of the amplitudes of the four terms revealed excellent agreement between the simulation data and the analytical model. This reinforces the argument that the discrepancies of the acoustic signals when compared to the classical model are largely due to viscous effects like diffusion and core distortion.

4.2 Introduction

The focus of this study is on the dynamics and acoustics of a pair of like-signed circular viscous vortex rings placed in an otherwise irrotational and unbounded fluid. The interactions of the co-axial vortex rings (also known as vortex pairing) has been studied by many researchers, for instance Dyson (1893), Hicks (1922), Brownard & Laufer (1975), Oshima *et al.* (1975), Yamada & Matsui (1979). One of the possible scenarios of the vortex pairing is the mutual slip-through event where the the initially leading vortex ring accelerates as it slips underneath the initially trailing vortex ring. At the same time, the initially trailing vortex rings expands and decelerates. The roles of the vortex rings are reversed at the slip-through instant. If the conditions are favorable, the mutual slip-through event may then repeat itself. Such vortex pairing have also been described as the 'mutual threading' and 'passing game'. The interest in the vortex-pairing stems mainly from the resemblance of the vorticity dynamics to the coherent flow structures seen exiting an axisymmetric round jet at moderate Reynolds number. Yule (1978) has experimentally observed coherent vortex structures at low Reynolds number. While Bridge & Hussain (1992) has disputed that the sound source is from the breakdown of the coherent structures at turbulent flows, direct simulations by Mitchell *et al.* (1999) have indicated that the sound field from low Mach number jets are similar to the axisymmetric lateral quadrupole that is typical of the sound field from a pair of co-axial vortex rings.

The acoustic radiation generated from a pair of co-axial vortex rings has been considered numerically by amongst others, Kambe & Minota (1981), Shariff *et al.* (1988), Tang & Ko (1995), and Verzicco *et al.* (1997). Several observations can be drawn from the above-mentioned studies. Firstly, Shariff *et al.* have found that the far-field acoustic signal consists of two components, a short frequency component associated with the leapfrogging cycle, and a much longer component owing to the distortion of the vortex core. The dual acoustic frequencies were also predicted in Tang & Ko's study. In direct contrast to Shariff *et al.*, Kambe & Minota predicted that the sound signal only consists of the short frequency component. Verzicco *et al.* have explained that the presence of the secondary frequency is related to the nutation of the vortex core. Secondly, at low Mach numbers, the far-field directivity of the sound signal resembles that of an axisymmetric lateral quadrupole.

Kambe & Minota (1981) considered the effect of (z_o/y_o) on the sound radiation analytically by using

the assumptions of an infinitesimally thin rings in an inviscid fluid. The assumption of an infinitesimally thin vortex ring is impractical as in reality, vortex rings are finite. In the present study, that same effect is considered but in the context of finite vortex rings in a viscous fluid. Hence, this study could be considered as a natural extension to the earlier study of Kambe & Minota. The aims of this investigation are two-fold. Firstly, this study forms the second validation test of the numerical scheme used in this research project, with the eventual aim of studying the sound radiation from natural shedding of bluff body flows. Secondly, there is a clear interest in the further understanding of vortex-pairing induced sound due to its obvious link to the field of aeroacoustics of round jets.

Results indicated that the acoustic signals at low Mach numbers have a far-field directivity which was quite similar to the stationary lateral axisymmetric quadrupole. In the implementation of the Lighthill's acoustic analogy, the spatial extent of the source term of $\nabla^2\mathbf{u}^2/2$ is larger than that of $\nabla\cdot(\omega\times\mathbf{u})$. Hence, a larger spatial filter region has to be applied when Lighthill's acoustic analogy is used.

There are several numerical issues that needed to be properly addressed in order to obtain an accurate acoustic solution. Besides having to ensure that the flow simulations were accurate in both space and time, several steps have to be taken to ensure the acoustic solution are free from any significant spurious waves. These include limiting the local rate of grid stretching in the acoustic domain and the introduction of a suitable start-up function for the acoustic computations to ensure that the initial wave transient is well resolved. In addition, spatial filtering of the source term was required to ensure that it converges smoothly to zero away from the rings. In order to be able to compare the numerical solution with the MAE prediction, the translational component of the advecting vortex system has to be removed prior to evaluating the acoustic forcing term.

A brief summary of the far-field acoustic pressure calculated using the MAE technique is presented in Section 4.3. The numerical procedure of the two-step method is summarised in Section 4.4. In Section 4.5, we first present the results of the flow simulations followed by the acoustic simulations. The acoustic quantities are compared with the theoretical predictions based on the MAE technique. The procedure of the decomposition of the sound pressure into a multipole expansion is described in Section 4.6. The far-field directivity in terms the Mach number is then discussed. Finally, concluding remarks to this study are presented in Section 4.7.

4.3 Theoretical prediction of vortex pairing induced sound

One of the earliest analysis of using Powell's vortex sound theory on the axisymmetric motion of a pair of co-axial vortex rings was conducted by Möhring (1978) who derived an analytical expression for the far-field acoustic signals solely in terms of position vectors of the rings and the axisymmetric vorticity field. Mohring's development of Powell's vortex sound theory gave rise to the 'linear theory' where the

sound field is directly proportional to the temporal variations of the vorticity field. Möhring's primary aim was to avoid the inherent problem of the singularity in the velocity field when using Powell's vortex sound theory to study the acoustics field of vortex sheets. Kambe & Minota (1981) had used the matched asymptotic expansions to derive a far-field expression which was found later to be identical to Möhring. The effect of viscosity as a sound source in free-space flows was considered by Kambe (1984). Thus, for a pair of co-axial viscous vortex rings engaging in the mutual slip-through events, the far-field acoustic pressure is defined as follow

$$p(z,y,t^*) = \frac{\rho_o}{4c_o^2\sqrt{z^2+y^2}}\left(\frac{\partial^3 Q^*}{\partial t^3}(\cos^2\theta - 1/3) + \frac{5-3\gamma}{3}\frac{\partial^2 K^*}{\partial t^2}\right). \tag{4.1}$$

where

$$Q(t) = \int_A (\omega y^2 z)dzdy, \tag{4.2}$$

$$K(t) = \int_A (\psi\omega)dzdy. \tag{4.3}$$

Owing to the directivities of the acoustic source terms, $\partial^3 Q/\partial t^3$ is known as the quadrupole while $\partial^2 K/\partial t^2$ is referred to as the monopole. While the monopole does not exist in the classical model, it is also considered to be insignificant in most viscous flow studies as the Reynolds number of the flow are typically much higher for the viscous effects to dominate over the mutual slip-through motions. Further examination of the quadrupole term reveals that its associated sound signal can be decomposed into a zeroth-order mode having a magnitude of 0.5 and a second-order cosine mode. This results in the polar angles of extinction being located at 54.7° and 125.3°. The far-field pattern can be described mathematically as a stationary lateral axisymmetric quadrupole. It is clear that the far-field directivity remains the same regardless of variations to the parameters of the vortex rings as $\partial^3 Q/\partial t^3$ is a temporal quantity. Thus, the validity of the acoustic solution away from the asymptotic limit of $\mathrm{Ma} \to 0$ is very much open to question. The effect of finite Mach numbers of the far-field directivity is one issue that is considered in this study.

In evaluating the acoustic quantities using the MAE method, the classical model of Dyson (1893) is used to provide the trajectories of the vortex cores. There are two assumptions used in the derivation of the classical model. Firstly, the vortex cores are circular. Secondly, there is no straining field imposed on each vortex core by its counterpart. The governing equations for the core trajectories were solved numerically and equation 4.1 was then used to predict the pressure fluctuations. The acoustic signals were found to peak at the slip-through instants. In addition, as the ratio of the initial axial distance of the vortex rings to the toroidal radius was increased, the time variations become increasingly less sinusoidal. Typical contour plots of the analytical pressure fluctuations are shown in figures 4.1a-b. The acoustic signals calculated using the MAE method will form the basis of the comparison study with the results obtained from the two-step aeroacoustic prediction of the viscous vortex rings.

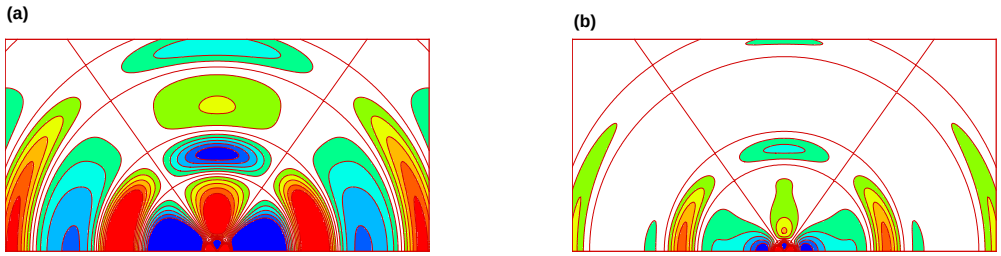

Figure 4.1: Analytical pressure contours for z_o/y_o = (a) 0.3, (b) 0.5.

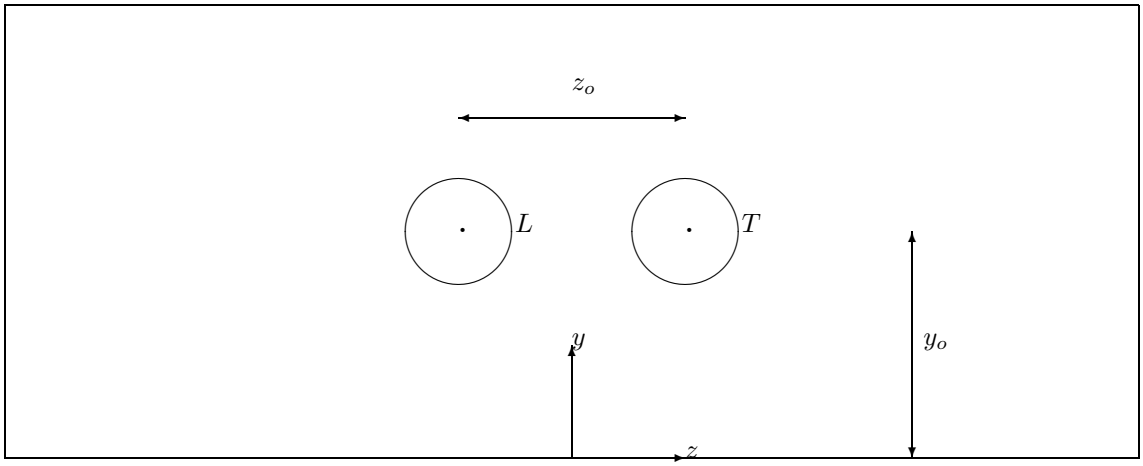

Figure 4.2: Illustration of the flow configuration. Note that the sketch is not to scale.

4.4 Numerical procedure

4.4.1 Flow configuration and parameters

In the first step of the aeroacoustic prediction method, we predict the motion of a pair of co-axial vortex rings in a viscous fluid. The flow field is assumed to be axisymmetric with zero swirl velocity component. The incompressible Navier-Stokes equations are solved on a cylindrical coordinate system. The numerical method used in solving the incompressible flow equations has already been discussed in detail in Chapter 2 and as such, is omitted in this chapter. The axial and radial axes of the coordinate system are defined using the symbols z and y, respectively. In a cylindrical coordinate system, the velocities are singular at the internal radial boundary, $y = 0$. However, since there are no explicit reference to the velocity on the axial boundary, because the grid is staggered, the spatial derivatives in the momentum equations can be discretised without any special treatment.

The schematic of the flow configuration is shown in Figure 4.2. The vortex rings are represented by two circular vortex cores of toroidal ring radius y_o, separated by an axial distance z_o. The symbol

Ring parameters	e_o/z_o	e_o/y_o	z_o/y_o
Case 1	0.075	0.0225	0.3
Case 2	0.075	0.0375	0.5

Table 4.1: Spatial parameters: vortex core radius, ring radius and ring-to-ring mean separation.

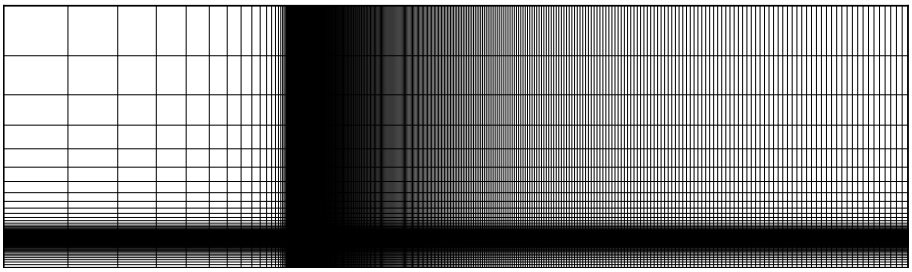

Figure 4.3: Typical grid used in the flow simulations.

L denotes the initially leading core while T represents the initially trailing vortex core. A Gaussian distribution is used to to define the vorticity, ω in each core (see Equation 4.8). For vortex passage interaction to occur, both vortex cores are like-signed. The notation for the velocity components is as follows: u is the velocity component in the axial direction and v is the radial velocity component.

The relevant vortex parameters such as core radius e_o, ring radius y_o, and vortex rings axial separation z_o are presented in Table 4.1. It is clear that the rings are 'thin' since both ratios (e_o/z_o) and (e_o/y_o) are $\ll 1$. This is a parameter study which considers the effect of varying the aspect ratio z_o/y_o. To vary the aspect ratio z_o/y_o, the initial axial distance between the vortex rings remains fixed while the toroidal ring radius y_o is changed accordingly.

In this study, the Reynolds number of the flow, based on the circulation of vortex core is fixed at $Re = \rho_o \Gamma_o/\mu_o = 7500$. The Mach number which is varied, is defined by $\mathrm{Ma} = u_o/c_o$, where $u_o = \Gamma_o/(4\pi y_o)$ is the translational velocity of the vortex ring in isolation, and c_o is the wave propagation speed in the acoustic medium.

4.4.2 Computational fluid dynamics considerations

The schematic of a typical grid used in the flow simulations is shown in Figure 4.3. The CFD domain is discretised into a structured mesh of $N_z \times N_y$ grid points. It is clear that while the grid points are mostly concentrated near the internal radial boundary and in the downstream direction, they are sparsely

distributed towards the external radial boundary and negative axial boundary.

The axisymmetrical boundary condition is assumed along the internal radial boundary while the pressure outlet condition is imposed on the external radial boundary and both axial boundaries. At the start of the flow computation, the solution field is initialised by setting the velocity field components of the entire interior cells to that of the sum of the individual vortex velocity components (including that of the image vortices).

The spatial and temporal parameters of the flow simulations were decided through firstly, a domain independence study, followed by a grid refinement study, and finally, a temporal resolution study. This is ensure that the hydrodynamic solution is both grid-and-time-step independent. These three steps were necessary since the solution field in the CFD domain is used as a pre-processing step in the CAA calculations i.e., when evaluating the acoustic source term (which contains second-order spatial derivatives of the velocity field).

Initial condition

The Gaussian vortex core model which is used in the present study defines the vorticity in the azimuthal direction as

$$\omega(r_c) = \frac{1.495\Gamma_o}{2\pi r_c}(1 - e^{-\frac{r_c}{e_o}})^2, \tag{4.4}$$

where r_c denotes the radial distance from the centre of each core (see Figure 4.1). Since the vortex core model that is used in the present study and the Reynolds number of the flow are both identical to the isolated co-rotating vortex pair structure, it was concluded that the spatial resolution that was applied in the former case could be imposed here. Hence, the grid spacing around the vortex rings is $\Delta x/e_o = 0.225$ which is equivalent to placing 20 grid points across the vortex core.

The following section presents the spatial and temporal resolution studies performed for the aspect ratio $z_o/y_o = 0.3$. There was very little difference in the computational parameters used in the flow simulations between $z_o/y_o = 0.3$ and 0.5. Hence, the results of the preliminary simulations reported below correspond exclusively to the former case.

Grid refinement and domain size independence study

In the present study, the size of the CFD domain is defined by two parameters l_1 and l_2. The symbol l_1 is used to define the distance from $y = 0$ to the external radial boundary. It is also used to represent the distance from $z = 0$ to the negative axial boundary. On the other hand, the distance from $z = 0$ to the positive axial boundary is represented by l_2.

The size of the domain has to be large enough so that the motion of the vortex rings is not significantly influenced by the blockage effect. Several simulations were conducted to determine the required domain size. The near-field resolution remained approximately the same for each simulation. The total kinetic energy in the flow, $(0.5 \int_V \mathbf{u}^2 dV)$ was used to determine if the solution is independent of the domain size and grid resolution. A tolerance level of 2% was used since it presents a reasonable compromise between accuracy and computer resource requirements, and it should be tight enough to faithfully reproduce the physics. To determine the appropriate size of the l_1, three different values of $l_1/y_o = 5$, 10 and 15 were considered while the other parameter l_2/y_o was fixed at 20. Results indicated that the variation in the monitoring property was less than the tolerance level between l_1/y_o of 10 and 15. Hence, the $l_1/y_o = 10$ was adopted for the remaining flow simulations. Through the domain tests, the length of the other parameter l_2/y_o has also been been deemed large enough so that the entire interactions (from leapfrogging to merging) was fully captured within the domain.

It is clear from figure 4.3, showing the mesh used in the CFD computations, that l_2 is greater than l_1. This is because, in contrast to the isolated co-rotating case, the vortex system in the present study is not spatially fixed. For an isolated co-rotating vortex pair structure, the mutual induction causes the vortex pair to rotate about the centre of the vortex pair. However, for the present case, the mutual induction consists of both a translational and rotational component. While the vortex rings engage in the leapfrogging cycles, the entire vortex system is also convecting in the downstream direction at an approximately constant velocity.

To resolve the velocity gradients of the vortex rings as the entire vortex system is convecting downstream, the grid stretching applied across l_2 has to more moderate compared to l_1. Otherwise, decreased resolution may lead to erroneous predictions such as a reduction in the number of leapfrogging cycles. To determine the spatial resolution required to adequately resolve the vortex system, three different rates of grid stretching were tested for l_2 at $0.5\%, 1\%$ and 2%. In contrast, the rate of stretching across l_1 which was kept at $\approx 9\%$ is not a major concern because the principal direction of the motion of the vortex system is from left to right. The difference in the total kinetic energy between the 0.5% and 1% stretching was well within the tolerance level. As such, a stretching rate of 1% across l_2 was used in the flow simulations.

Temporal resolution study

In the previous domain independence and grid refinement studies, the preliminary simulations were advanced in time using a time-step of $\Delta t u_o/y_o = 3.98 \times 10^{-5}$. To determine if there was excessive numerical dissipation caused by the selected time step, temporal resolution tests were conducted at the domain size and grid stretching specifications determined from the previous section but at two different time step of $\Delta t u_o/y_o = 1.97 \times 10{-}5$ and 7.5×10^{-5}. The volume integral of the total kinetic energy

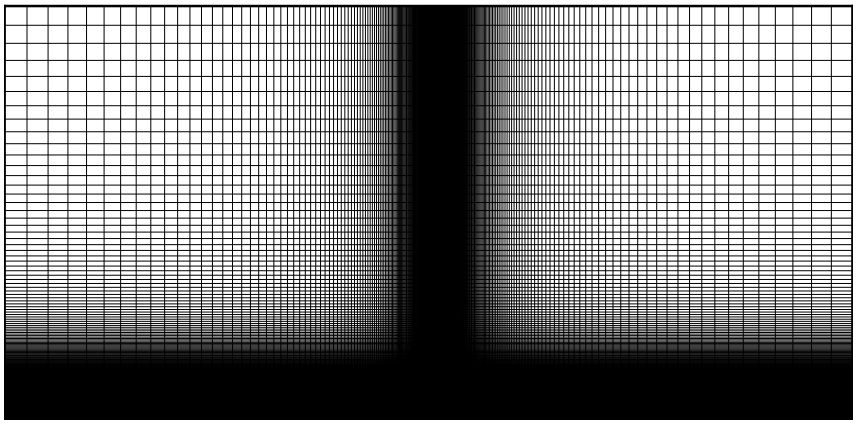

Figure 4.4: Typical mesh used in the acoustic simulations.

was monitored throughout the first leapfrogging cycle. Results indicated that there was no change to the third significant figure when $\Delta t u_o/y_o$ was reduced from 3.98×10^{-5} to 1.97×10^{-5}. This implies that the simulation is well resolved temporally with the former time-step. As such, a time-step of $\Delta t u_o/y_o = 3.98 \times 10^{-5}$ was adopted in the flow simulations..

4.4.3 Computational aeroacoustics considerations

In this section, we highlight the issues which must be carefully addressed and the steps implemented in order to obtain an acoustic solution that is free from spurious waves. The acoustic simulations are performed at three different Mach numbers (Ma = 0.0025, 0.005 and 0.01). A sixth-order central-difference scheme was used to discretise the spatial derivatives while the standard fourth-order Runge-Kutta method was used to advance the governing equations in time. As with the modelling the flow field, the azimuthal component of the sound field is ignored. The inhomogeneous acoustic wave equation written in polar form is as follows

$$\frac{\partial a}{\partial t} - c_o^2\left(\frac{c}{y} + \frac{\partial c}{\partial y} + \frac{\partial b}{\partial z}\right) = H(z, y, t). \tag{4.5}$$

where $a = \partial p/\partial t$, $b = \partial p/\partial z$ and $c = \partial p/\partial y$.

The radiation boundary condition imposed at the external radial boundary and both axial boundaries is based on that of Bayliss & Turkel (1980). As a result of the seven-point stencil for the interior equations, there are three ghost points in the boundary equations. To maintain the same spatial accuracy, high-order one-sided differencing was used to evaluate the spatial derivatives of the boundary equations.

The acoustic solution is axisymmetric about the internal radial boundary of the domain. Therefore, the reflecting boundary condition, $\partial p/\partial \mathbf{n} = 0$ where $\mathbf{n}$ is the unit normal to the boundary is applied at the internal radial boundary. In the cylindrical coordinate system, the term containing $(1/y)$ in the acoustic wave equation is singular at the internal radial boundary. To avoid the singularity, the acoustic pressure lying along the internal radial boundary is evaluated using the reflecting boundary condition with a one-sided stencil e.g., the nodes along the internal radial boundary are updated using the six interior nodes located adjacent to the boundary.

The typical grid used in the acoustic calculation is shown in figure 4.4. Notice the differences in the physical size and the grid arrangement between the CFD domain and the CAA domain. Similar to the isolated co-rotating vortex pair structure, the CAA domain which extends two acoustic wavelengths radially. It is discretised into a structured mesh of N_a^2 grid points. To resolve the acoustic source terms, the grid spacing around the vortex cores was chosen to be identical to that used to resolve the velocity gradients in the flow simulations. Far-field wise, there were 20 points across the acoustic wavelength. The disparity in the near-field and far-field grid spacings are handled through a non uniform mesh.

In contrast to the flow solution which is limited exclusively to the region around the vortex rings, the entire solution in the CAA domain is relevant because the acoustic waves propagates throughout the whole domain. This also implies that any unphysical noise sources present in the domain would also travel in all directions, thus contaminating the near-field as well as the far-field regions. One of the main sources of spurious noise comes from crude initial conditions. It has been demonstrated clearly in chapter 3 that an impulsive initial condition is bound to result in grid-to-grid oscillations which is further amplified by grid stretching. Therefore, to minimise the impact of the initial transient, a start-up function to the acoustic source term is used as an initial condition to CAA. This is further complemented with a moderate grid stretching to allow the waves (transient and acoustic) to propagate without generating any substantial reflections.

The suitable choice of the start-up period, t_r, and the maximum local rate of grid stretching is tested on the lowest Mach number acoustic simulation. This is because the acoustic signals are weakest at the lowest Mach number and thus, the susceptibility of the numerical scheme to the generation of artificial noise sources is highest. As mentioned earlier in this section, the region around the vortex cores has a uniform grid spacing. Axially, the grid starts to stretch from $z = \pm 1.5 z_o$. Radially, the grid stretching starts from $y = 1.5 y_o$. It must be noted that the same stretching function is applied in both directions. A start-up period of $t_r u_o/y_o = 0.0597$ for $z_o/y_o = 0.5$ was tested for several different rates of local stretching $(4\%, 3\%$ and $2\%)$. From these tests, we conclude that the most appropriate local rate of stretching was 3% as the signal-to-noise ratio was relatively strong and there was only negligible change in the acoustic solution from a local stretching of 3% to 2%. It was also found that in general, the stretching in the axial direction was more sensitive to spurious noise. Because the acoustic simulations at different Mach numbers have the same rate of stretching, the number of grid points in each simulations has to be varied

accordingly. In each acoustic simulation, the time-step used to advance the acoustic wave equation is sized so that it is at the limits of stability of the RK4 scheme. It is clear that because the wave propagation speed, c_o, increases as the Mach number gets smaller, the time-step also decreases. Thus, the lower the Mach number, the number of grid points increases in the domain, and the time-step used to march the solution in time decreases, and as a result, the computational costs rises.

In addition to the grid-and-time step requirements, and the initial condition to CAA, three parameters that are relevant to the acoustic forcing are (1) spatial filtering of the hydrodynamic terms, (2) the size and location of the spatial filter region, and (3) sampling interval of the hydrodynamic terms.

Spatial filtering of hydrodynamic terms

From past experience with the isolated co-rotating vortex pair structure, we found that if the acoustic source term was suddenly terminated, the acoustic solution diverges. The fact that the termination was applied far away from the vortex system implies that the divergence in the numerical solution is related to the spatial discontinuities of the source term at the truncation. This is attributed to the slow decay of the acoustic source terms. As a result, the numerical implementation of Lighthill's acoustic analogy or Powell's vortex sound theory requires a sort of a boundary condition-like treatment for the source terms. In this investigation, this is performed through a spatial filter.

The main purpose of the spatial filter is to decay the hydrodynamic velocities outside the region of acoustic waves generation to zero and hence, allow the acoustic source term (H_l or H_p) to converge. The filter is applied after the hydrodynamic terms are interpolated in space from the CFD domain to the CAA domain. The filter has a value of unity around the vortex system and decays gradually to zero away. To prevent the spatial filter itself of being an artificial sound source, the size and location of the spatial filter have to be determined carefully.

The region where the spatial filter is applied is defined in terms of the two parameters l_{fz} and l_{fy} where l_{fz} is the length of the filter applied in the axial direction and l_{fy} is the length of the filter applied in the radial direction. In the previous case of the isolated co-rotating vortex pair, the lengths l_{fx} and l_{fy} were identical since the centre of the rotation of the vortices was a fixed quantity. In the present study, had the vortex system been advecting in the acoustic domain, this would imply that l_{fz} would be dictated by the total distance traveled by the vortex system. However, by removing the translational velocity from the vortex system so that the sound source is spatially fixed (this is revealed in greater detail in the following section), the two parameters l_{fz} and l_{fy} can be made comparable.

To determine the appropriate parameters l_{fz} and l_{fy} making up the spatial filter region, three different lengths at $l_{fy}/y_o = l_{fz}/y_o = 0.42$, 0.83 and 1.67 were tested. The filter functions in the radial and axial directions is of unity at $1.25y_o$ away from $(0, y_o)$ and decays to zero over the length of the filter.

The selection criterion is that any resulting fluctuations from the spatial filter must be at least several orders of magnitude smaller than the acoustic signals. This is checked by positioning observation points just outside the spatial filter region. Results from the preliminary acoustic simulations showed that there was negligible change when the length of the filter was increased from 0.83 to 1.67. As such, the length of the filter used in the acoustic simulations was chosen to be 0.83.

Spatially-fixed sound source

The solution calculated using the MAE technique assumes that the source is localised at one point, i.e., the vortex system is a spatially-fixed sound source. In the context of this particular flow configuration, this implies that while the vortex system may be translating in the downstream direction, acoustic-wise, the sound waves are effectively radiating from a fixed and stationary position. In contrast, when implementing the two-step aeroacoustic prediction method, it is clear that the hydrodynamic quantities do not actually collapse into one point in the acoustic domain. As a result, the acoustic source calculated using Lighthill's acoustic analogy or Powell's vortex sound theory as it is, would result in an advecting acoustic source field. Thus, in order to be able to compare the numerical solution due to Lighthill's acoustic analogy and Powell's vortex sound theory with the MAE solution, the rate of change of the mean axial position of the vortex system must be removed from the axial velocity component prior to calculating the acoustic source terms. It is not possible to subtract the mean translational speed of the vortex system from the axial velocity component directly. As such, the procedure used involves a transformation of the spatial positions of the vortex system as follows

$$x_a^t = x_a + t\frac{\partial \bar{Z}}{\partial t}, \tag{4.6}$$

where x_a and x_a^t denotes the axial coordinates pre and post coordinate transformation, and $\bar{Z}$ is the mean axial position of the vortex system. At the start of the acoustic computation i.e., $t = 0$, both axial positions x_a and x_a^t are identical. However, as the simulation progresses, the acoustic coordinate x_a^t, translates along with the vortex system in the flow domain. The coordinate transformation effectively pegs the mean axial position of the vortex system back to its initial position in the acoustic domain.

There are three steps involved in this procedure. Firstly, the mean axial position of the vortex system is obtained by averaging the axial trajectories the vortex core centroids. Next, a fourth-order function is used to fit a curve through the selected data points to define the mean axial position as a function of time. Finally, once the coefficients of the fourth-order interpolating function is found, the translational velocity of the mean axial position is then obtained through evaluating the first-order derivative of fourth-order function. As such, $\partial \bar{Z}/\partial t$ is described by a cubic function.

Sampling of the acoustic source term

One of the issues related to the sampling of the acoustic source term that arose from this study was the selection of an appropriate function to interpolate the acoustic forcing term over the entire flow-map. While a local six-point Lagrange interpolating polynomial was used in the isolated co-rotating pair structure with success, in contrast, there were periodic sharp kinks in the acoustic solution when it was used in the present study. On closer examination, the kinks were found to occur at the same instant as the interchanging of the frames. Hence, it was concluded that the kinks were caused by the discontinuities in the first-order derivative of the local interpolating polynomial. After testing with several other local interpolating functions and a global cubic spline, finally, a quintic spline which was smooth and continuous to the second-order derivative of the approximating function resulted in a signal waveform without any kinks. This finding indicates that the temporal variations on the acoustic source term, if not resolved properly (i.e., smooth and continuous in the interpolating function and its higher derivatives) is a potential spurious sound source. Subsequently, the quintic spline was adopted in all three cases presented in this Ph.D. research project.

Sampling of the hydrodynamic velocities for both cases was tested at intervals of every 8, 16 and 32 frames per fundamental period. It must be noted that if the sampling interval was too large, the source function would be artificially damped. Conversely, if there were too many frames per period, local errors in the flow simulations may be amplified in the acoustic solution. As such, the appropriate choice of the sampling interval is a compromise between excessive damping of the source term and controlling the possible inclusion of errors contained in the velocity fields. For the present study, an interval of 16 frames per mutual slip-through period was found to be adequate.

4.5 Results and discussion

The results of the flow simulations are first presented and analysed followed by the acoustic simulations. It is useful to gain an understanding of the vorticity dynamics prior to analysing the acoustic field. This is because Powell (1964) has stated that in a free flow, the sound waves are related to the changes in the vorticity field. The quantitative measurements of the flow simulations have to be accurate since the acoustic forcing is calculated using high-order spatial derivatives of the hydrodynamic velocity field. In addition, the measurements are also needed in calculating both the quadrupole and monopole sound sources. In all the figures presented in this section, the spatial parameters are normalised with respect to the toroidal ring radius, y_o, while the simulation time, t, is non-dimensionalised with respect to the time-scale y_o/u_o.

4.5.1 Flow dynamics

In the classical model, the vortex rings are assumed to be infinitesimally thin and the fluid medium is inviscid. As such, the interaction of the rings can be called *elastic*. The initially leading vortex ring slips underneath the initially trailing vortex ring. As this is happening, the mean toroidal radius of the initially leading vortex ring increases and as a consequence, its velocity decreases. The moment that the radial distance between both vortices is at a maximum is known as the slip-through instant. At this instant, both vortices are lined up vertically. The role of the leading and trailing vortices alternates and this cycle, also known as the leap-frogging motion repeats itself indefinitely. There is no distortion of the shape of the vortex rings as the cores are assumed to remain circular at all times in the classical model. It will be shown in this section that the classical picture is only partially observed in the results of the viscous flow simulations.

Throughout the flow computations, the variation in the total circulation of the vortex system was at most 1% of its initial value, $2\Gamma_o$. This indicates that both the total circulation and the total impulse of the vortex system are conserved to within numerical error. This is consistent with the fact that there was no external force acting on the vortex system and the initial force assumed to generate the vortex system from rest vanishes as soon as the vortices start moving.

In the classical model, the vortex core reduces to a point singularity. As such, the definition of the core centroid is relatively straightforward. However, since a Gaussian vortex core is used in this numerical study, the core centroid is defined as the location of the peak vorticity. By monitoring the flow fields, the trajectories of the discrete vortices can be revealed through the time histories of the axial and radial positions of the vortex core centroids. The location of the core centroids are determined numerically throughout the entire flow simulation. Subsequently, the time histories of the trajectories and peak vorticity of the core centroids are shown in figures 4.4 and 4.5. The circulation of the vortex rings is positive in the clock-wise direction. As such, the vortex system moves from the left to the right. From figures 4.4(a) and (b), and 4.5(a) and (b), we can readily see that the slip-through instants occur when the radial distance between the two core centroids is at a maximum. In addition, the vortex system travels a considerable distance axially while the variation in the radial direction is noticeably less. Using the radial trajectories of the core centroids, the slip-through period could then be estimated. It is clear that the period corresponding to the first leap-frog motion is in good agreement with the theoretical counterpart prediction (see Table 4.2). However, owing to the effect of viscous dissipation, the period of the subsequent leap-frogging cycles is expected to decrease, albeit gradually.

Another effect of viscosity is that the dynamics of the leapfrogging motions are modified. From figures 4.4(c) and 4.5(c), it is also clear that there was a rapid reduction of the peak vorticity during the initial stages of the flow simulations. For $z_o/y_o = 0.3$, the drop in the magnitude of peak vorticity was about 73% over the first leapfrogging cycle. This is because at initialisation of the flow, the vorticity

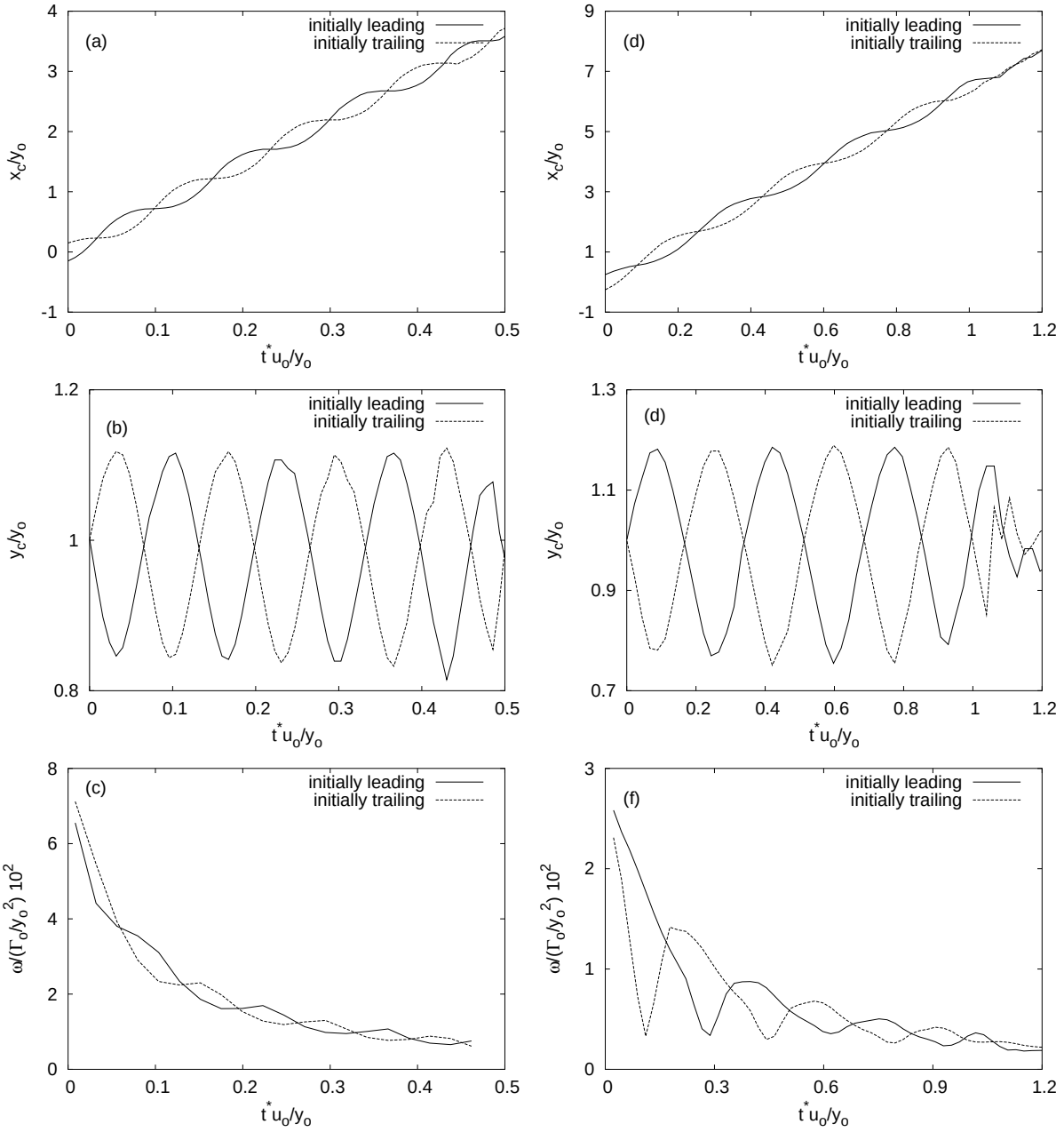

Figure 4.5: Time traces of the trajectories and peak vorticity of the initially leading- and-trailing core centroids. Here, the left column refers to $z_o/y_o = 0.3$ while the right hand column refers to $z_o/y_o = 0.5$. The trajectories of the core centroids presented are in (a)&(d) the axial direction and (b)&(e) the radial direction. The time history of the peak vorticity of the core centroids are presented in (c)&(f).

z_o/y_o	0.3	0.5
$T(u_o/y_o)$	0.13	0.328
$T(u_o/y_o)^*$	0.126	0.287

Table 4.2: Tabulation of the first slip-through period of $z_o/y_o = 0.3$ and 0.5. The values designated with an asterisk refers to Kambe & Minota's (1981) results.

distribution of the vortex core is very compact and the velocity gradients are very sharp especially near the core centroids. As a result, physical viscosity acts quickly to diffuse the sharp velocity gradients resulting in a rapid decrease of the magnitude of peak vorticity. At $tu_o/y_o > 0.13$, the temporal change in peak vorticity is more gradual as the vortex core has spread out radially and assumed a more diffuse and less intense structure. The time-scale of the peak vorticity diffusion now is much longer because viscosity takes longer to diffuse a less compact vortex core structure. For the aspect ratio $z_o/y_o = 0.5$, the drop in the magnitude of the peak vorticity between the first leapfrogging cycle was approximately 70%. The fact that the rate of vorticity diffusion was similar for both cases is expected because the initial vorticity distribution of the vortex core and the Reynolds number of the flow used in both cases are identical. As a result, this has led to a decrease in the amplitude of the sound pressure levels when compared with the analytical prediction.This will be discussed in further detail in the acoustics section. At the slip-through instant, the ring underneath (which has a smaller radius) is more compact compared to the ring above it (which has the larger radius). This is more apparent for the aspect ratio $(z_o/y_o) = 0.5$.

For the first case i.e., $(z_o/y_o) = 0.3$, there were approximately eight slip-through instants prior to vortex merger while for $(z_o/y_o) = 0.5$, there were seven slip-through instants prior to vortex merger. In Verzicco *et al*'s. (1997) study, there was only one slip-through instant prior to merger at a similar aspect ratio but at a different Reynolds number of $Re = 4000$. Hence, this highlights the effect of Reynolds number on the flow dynamics and hence the acoustics. The chosen Reynolds number of $Re = 7500$ adopted in this study has resulted in a number of successive slip-through instants occurring without significant large-scale core deformation prior to the wrap up of the vortex rings. This is important from the acoustic modelling point of view since the acoustic forcing would then be coherent and periodic over several leapfrogging cycles. Having the merger of the vortex rings occurring too soon would complicate efforts to compare the acoustic signals of the viscous vortex rings with the analytical acoustic pressure expression, even though the effect of viscosity is clearly important in its own right.

Figures 4.6(a) and 4.7(a) show the initial configuration of the two vortex cores prior to the execution of the flow solver. The vortex system moves from left to right owing to the self-induced translational velocity of the vortex rings. The time development of the vortex system is revealed through successive snapshots of vorticity totalling half a leapfrogging cycle. These are shown in figures 4.6(a) through (e) (for $z_o/y_o = 0.3$), and figures 4.7(a) through (e) (for $z_o/y_o = 0.5$). The first snapshot in both cases are taken at approximately the instant where the axial separation of the vortex rings is the largest. For case 1, the snapshots are taken between $tu_o/y_o = 0.13$ and 0.194, while for case 2, the snapshots are taken between $tu_o/y_o = 0.328$ and 0.492. The selected time intervals correspond to the second leapfrogging cycle. The second cycle was used in preference to the first cycle because the rapid change in peak vorticity during the latter made it difficult to find a common range of vorticity levels in the contour plots.

It is clear that the discrete vortices are engaging in the classical leap-frogging motion. However, contrary to the inviscid model, the cores do not remain circular throughout the leap-frogging motion, and

the vorticity distribution of the vortex core changes due to diffusion and straining effects. In particular, when the initially leading vortex ring is slipping underneath the initially trailing vortex ring, the initially leading core becomes more compact, and distorts into an elliptic shape. Comparing the vorticity snapshots of both cases, it is evident that the distortion of the initially leading vortex core is more severe at $z_o/y_o = 0.5$. The distortion of the core from a circular shape to an elliptic shape is a quasi-periodic phenomena because when both vortices are aligned horizontally with maximum axial spacing between the two vortex cores, both core shapes assumed a nearly identical circular pattern. It is a fact deduced from previous numerical studies (e.g., Shariff *et al.* (1988), Tang & Ko (1995)) that the variation of the vortex core affects the sound radiation. As a result, this implies that the predicted sound field in this study will also deviate from the MAE analytical prediction. Furthermore, we would expect that this variation would be greater for increasing aspect ratio.

In sharp contrast to the passage interaction of the vortex rings, the vortex merger process is characterised by strong core deformations. The contours of vorticity prior to merging are shown in a series of snapshots in figure 4.8 for $z_o/y_o = 0.3$ and figure 4.9 for $z_o/y_o = 0.5$. The rear ring wraps around the front ring during the final slip-through instant with a weak tail and soon after, both vortices become intertwined. The vortex merger occurs in a relatively short time-frame, about half the fundamental period. The effect of the merging of the viscous vortex rings on the sound field is expected to differ with the results of Tang & Ko (1995) because the vortex pairings that were considered by the mentioned authors had occurred without any cross-diffusion.

To summarise, in terms of the vorticity dynamics, prior to the vortex rings merging, the interaction of the rings at both aspect ratios is close to the classical leapfrogging motion with the exceptions of, firstly, the quasi-periodic phenomenon of the vortex cores distorting at the slip-through instant, and secondly, physical viscosity acting to reduce the peak vorticity and diffuse the core, and thereby smoothen the velocity gradients. In the next section, the influence of the core distortion, and the alteration to the vorticity dynamics, on the sound radiation will be explored.

4.5.2 Propagation and decay of the acoustic waves

To monitor the time variations of the acoustic signals, a series of observation positions were placed at half wavelength intervals from 0 to 2λ along the radial and axial axes. From the time histories of the acoustic signals at all the observation points, we found that the fluctuations could be classified as far-field waves when the radial location is $\geq \lambda$. Since the propagation characteristics of the far-field waves are identical across the different far-field positions, only one set of time histories of the acoustic signals are shown. Time histories of the acoustic signals for aspect ratio $z_o/y_o = 0.3$ (calculated using the Lighthill acoustic source term, H_l), are shown in figures 4.10(a)–(c). The observation positions are located at a polar distance of $r = 2\lambda$ at three different angles of $\theta = 0°, 90°$ and $180°$. The angle θ is measured from

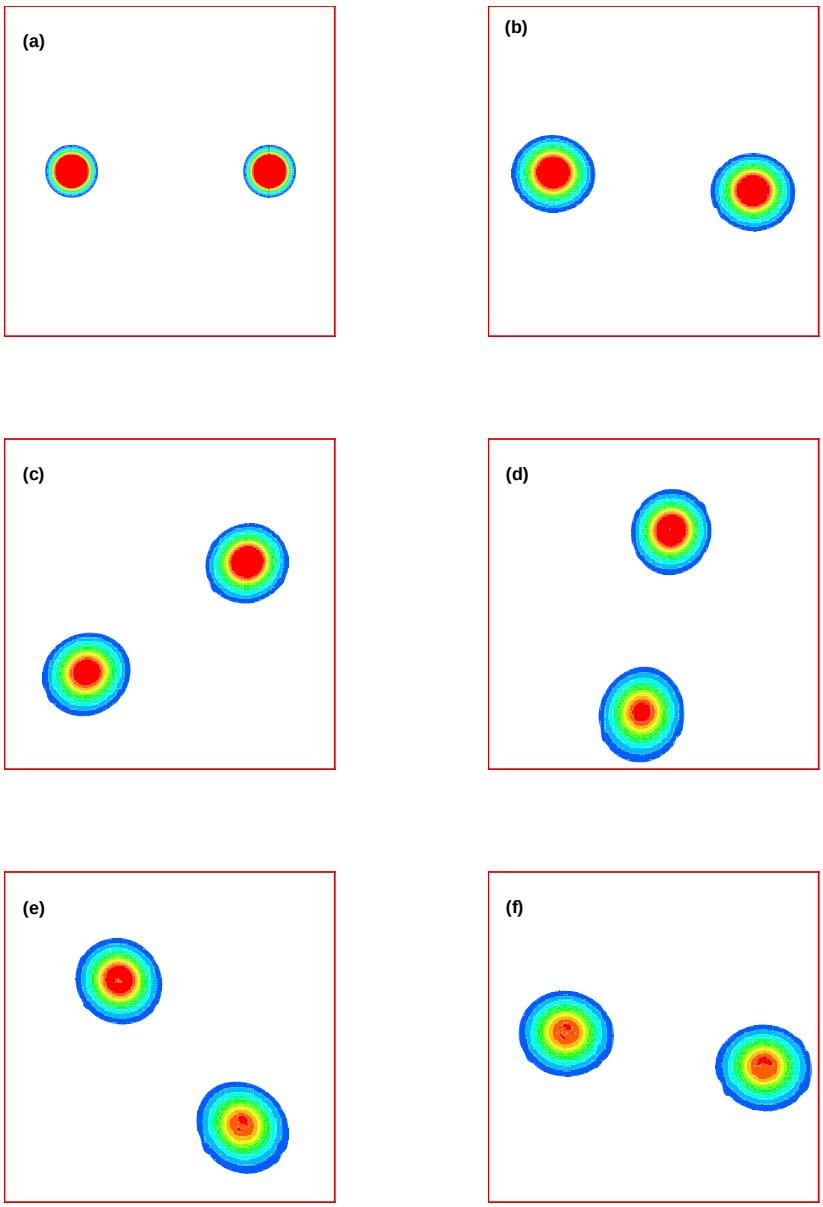

Figure 4.6: Instantaneous contours of vorticity for $z_o/y_o = 0.3$. The simulation time is $tu_o/y_o =$ (a) 0, (b) 0.13, (c) 0.146, (d) 0.162, (e) 0.178, (f) 0.194. The min. and max. contour levels are $\omega_{min}/\omega_o = 0.21$ and $\omega_{max}/\omega_o = 0.021$ with 10 increments.

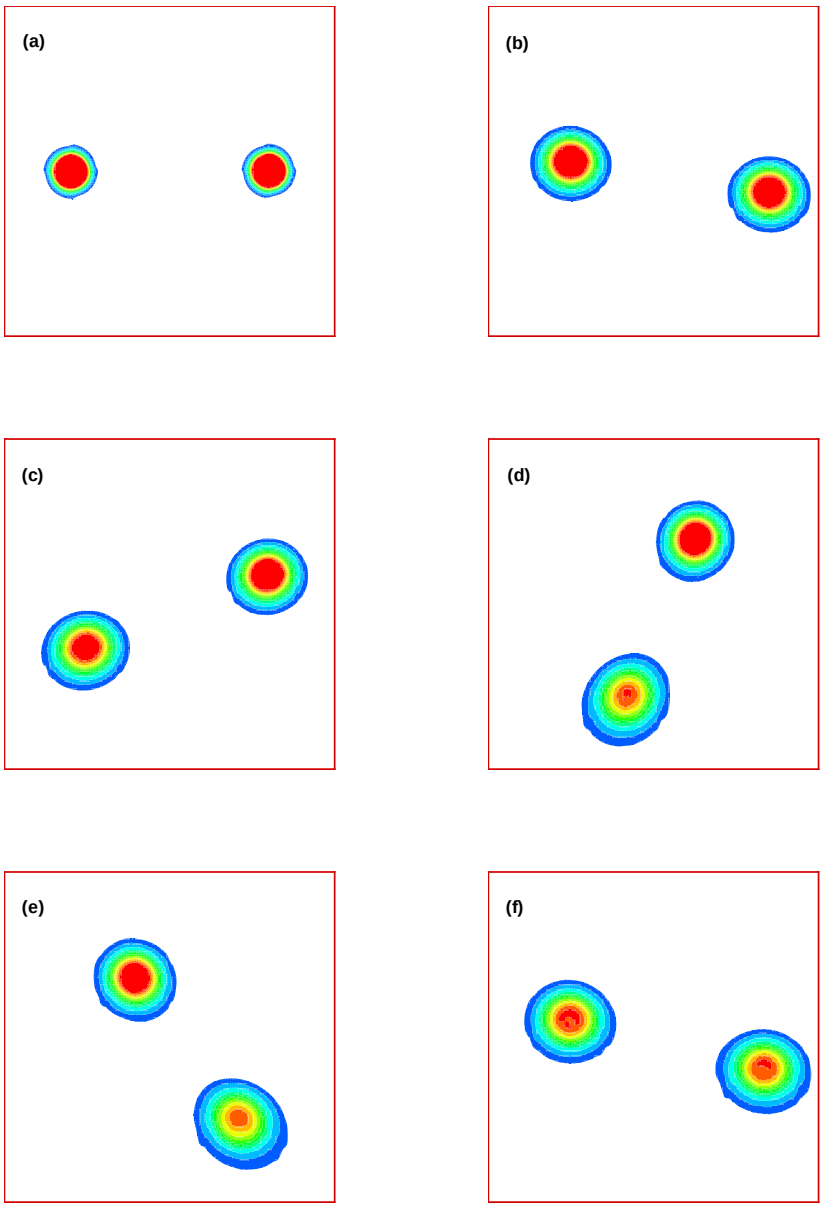

Figure 4.7: Instantaneous contours of vorticity for $z_o/y_o = 0.5$. The simulation time is $tu_o/y_o =$ (a) 0, (b) 0.328, (c) 0.368, (d) 0.409, (e) 0.451, (f) 0.492. The min. and max. contour levels are $\omega_{min}/\omega_o = 0.22$ and $\omega_{max}/\omega_o = 0.022$ with 10 increments.

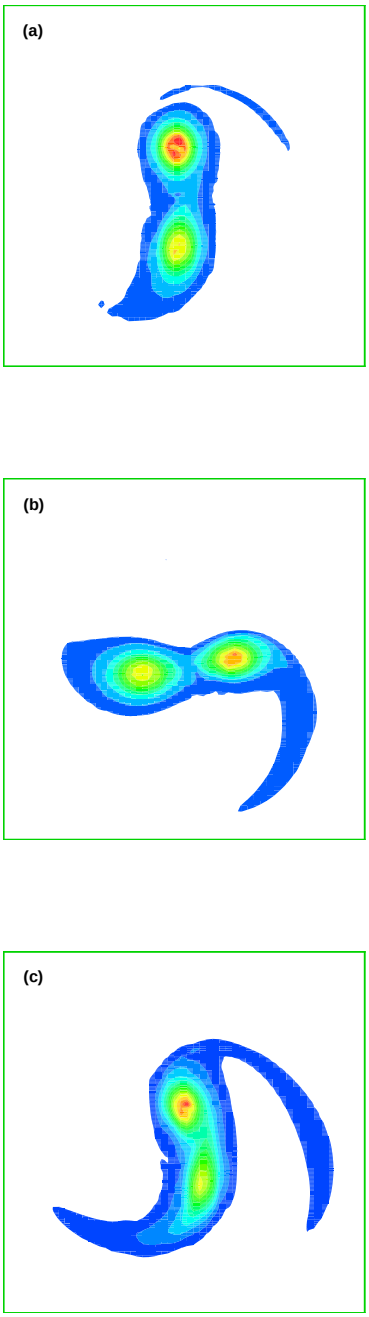

Figure 4.8: Snapshots of vorticity prior to merging instant. Here, $z_o/y_o = 0.3$ and the time instants $tu_o/y_o =$ are (a) 0.43, (b) 0.462 and (c) 0.486. The min. and max. contour levels are 10.05 and 1005. There are 10 increments between the min. and max. levels. Note that the vorticity has been non-dimensionalised with respect to u_o and y_o.

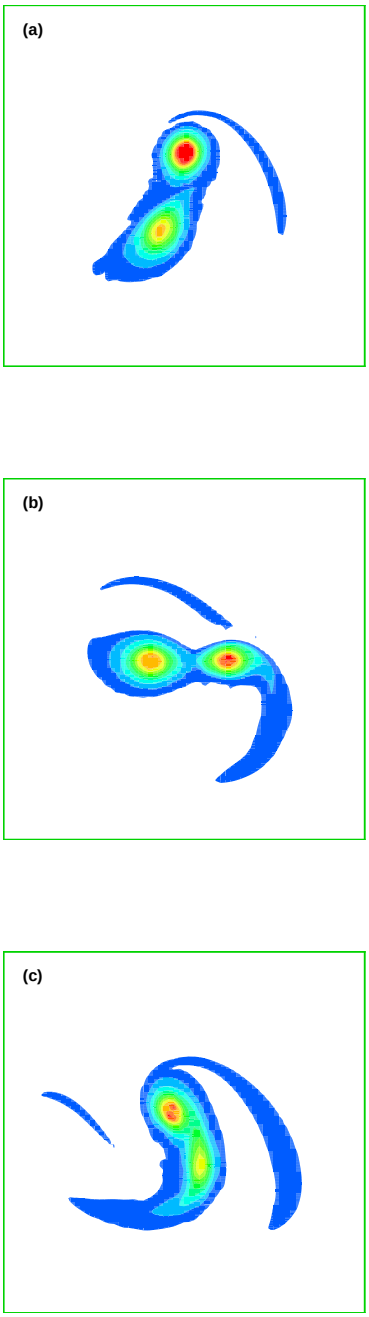

Figure 4.9: Snapshots of vorticity prior to merging instant. Here, $z_o/y_o = 0.5$ and the time instants are (a) 0.918, (b) 0.995 and (c) 1.06. The min. and max. contour levels of vorticity are 3.98 and 398. There are 10 increments between the min. and max. levels. Note that the vorticity has been non-dimensionalised with respect to u_o and y_o.

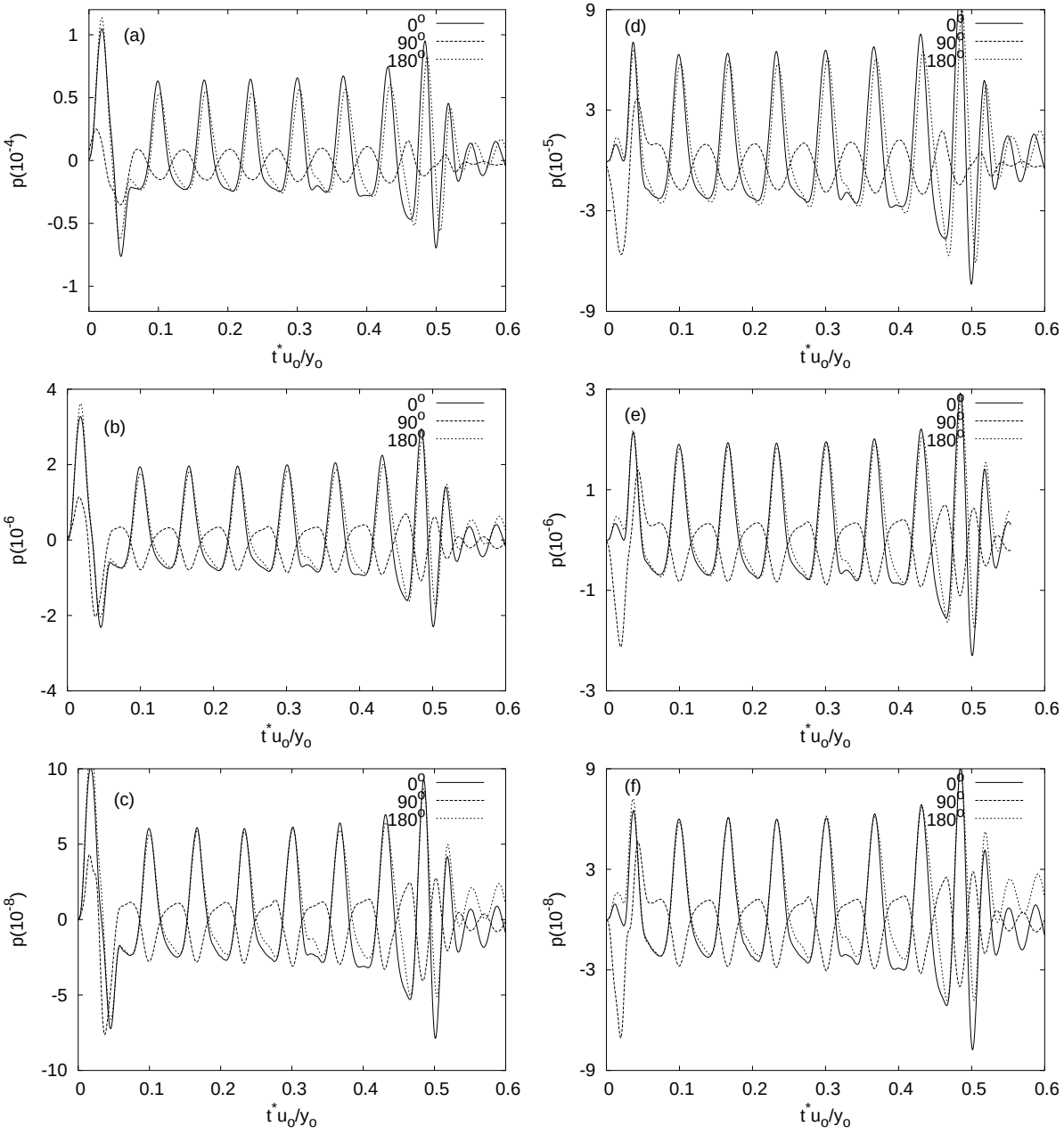

Figure 4.10: Time histories of the acoustic pressure fluctuations of aspect ratio $(z_o/y_o) = 0.3$ at the three different Mach numbers, Ma = (a)&(d) 0.01, (b)&(e) 0.005, (c)&(f) 0.0025. The left column refers to the Lighthill's source formulation while the right column refers to Powell's source formulation. The far-field observation position is located at a radial distance of $r = 2\lambda$ away at three different polar angles. The symbol t^* represent the retarded time.

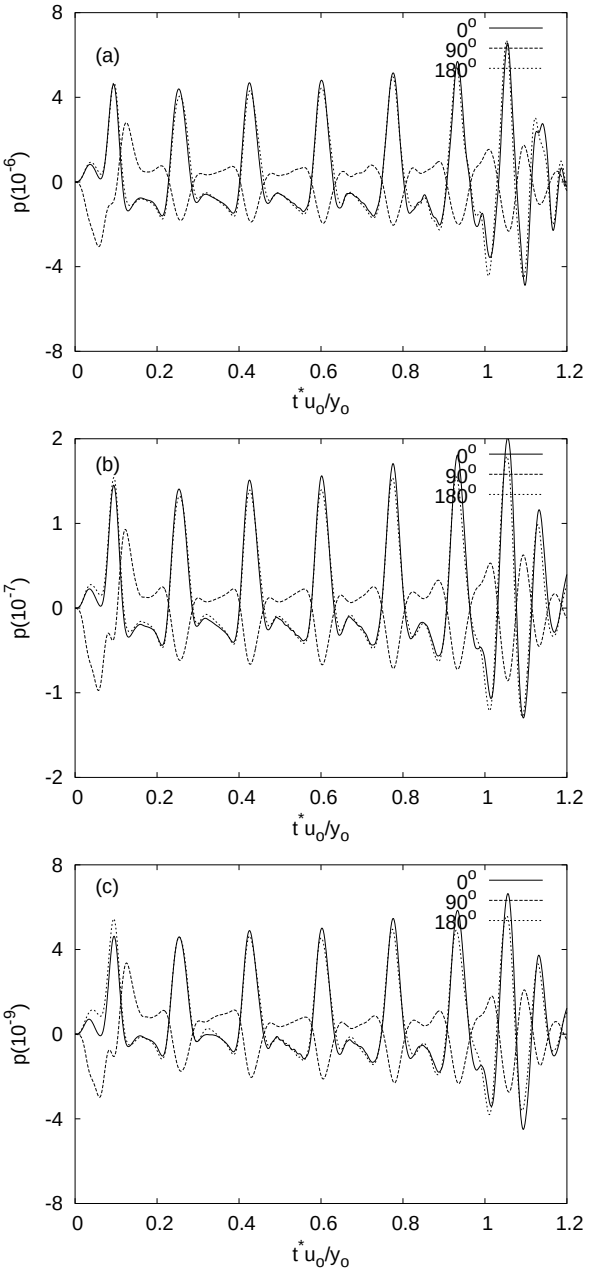

Figure 4.11: Time histories of the acoustic pressure fluctuations of aspect ratio $(z_o/y_o) = 0.5$ at the three different Mach numbers, Ma = (a) 0.01, (b) 0.005, (c) 0.0025. The far-field observation position is located at $r = 2\lambda$ at three different polar angles. The symbol t^* represent the retarded time.

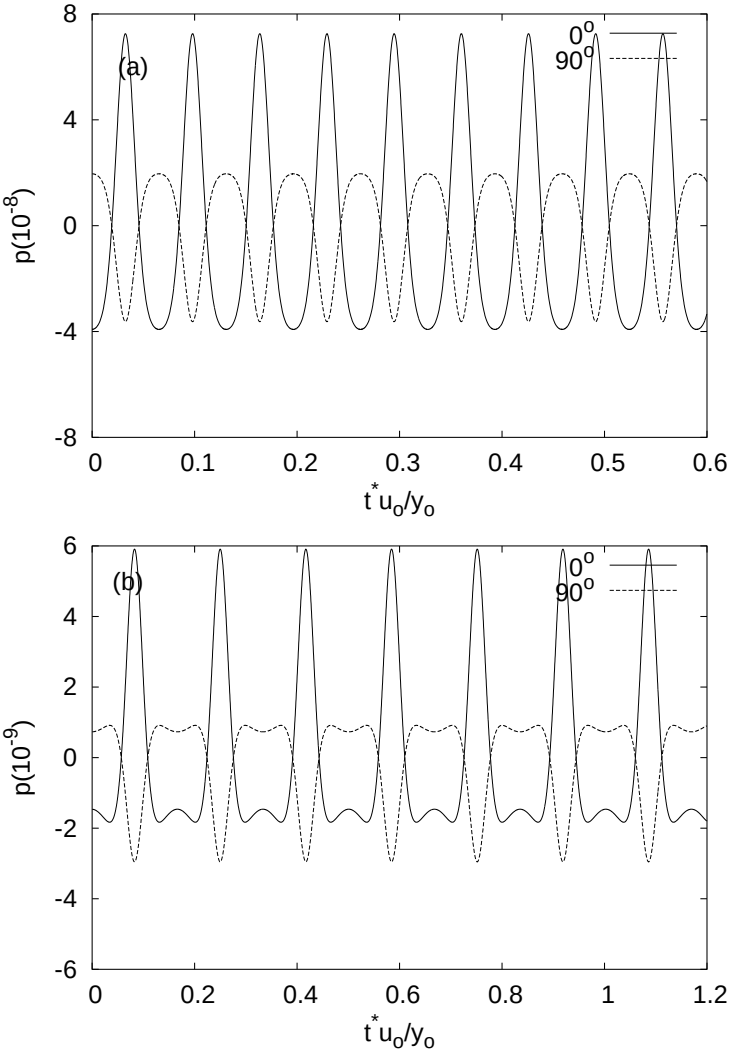

Figure 4.12: Time histories of the acoustic pressure fluctuations calculated using the MAE far-field expression at Ma = 0.0025. The far-field observation position is located at $r = 2\lambda$. The symbol t^* represent the retarded time. The left hand figure refers to $z_o/y_o = 0.3$ while the right hand figure refers to $z_o/y_o = 0.5$

the downstream axial axis. Figures 4.10 (d)–(f) show the acoustic signals at the same (r, θ) observation positions but the Powell acoustic source term, H_p, is used to evaluate the acoustic forcing instead of the Lighthill acoustic source term.

From examining the time traces of the acoustic signals for $z_o/y_o = 0.3$ (see figures 4.10), it is clear that the Lighthill acoustic source term, H_l, and the Powell acoustic source term, H_p, are effectively producing identical acoustic signals (apart from the initial wave transient). This suggests that at the Mach number range studied in this investigation, the source term contribution $\nabla^2(\mathbf{u}^2/2)$ present in Lighthill's acoustic analogy but subsequently ignored in Powell's vortex sound theory is not a significant acoustic source. Since the acoustic field predictions are only dependent on the source term, $\nabla \cdot (\omega \times \mathbf{u})$, the acoustic simulations for aspect ratio $z_o/y_o = 0.5$ are performed with only the Powell acoustic source term, H_p. The time histories of the far-field acoustic signals at the designated observation positions corresponding to aspect ratio $z_o/y_o = 0.5$ are subsequently presented in figure 4.11. Due to the fact that both acoustic source terms yielded similar far-field signals, the analysis of the acoustic quantities for the two cases can be performed without specifying if the acoustic source term was based on either Lighthill's acoustic analogy or Powell's vortex sound theory.

Owing to the symmetry of the vortex pairing, the number of acoustic waves correspond to the number of slip-through instants. As such, for the aspect ratio $z_o/y_o = 0.3$, there were eight acoustic peaks while there were seven peaks for the case of $z_o/y_o = 0.5$. In contrast to the isolated co-rotating vortex pair structure which exhibited nearly sinusoidal acoustic variations in the time-histories, the time variations of the acoustic signals consisted of a series of sharp peaks and rounded troughs. Furthermore, the amplitudes of the acoustic peaks at the axial axes $\theta = 0^\circ$ and 180° are larger than that located along $\theta = 90^\circ$.

For both aspect ratios and at all three different Mach numbers, the start-up interval was fixed at $tu_o/y_o = 0.0597$ for $z_o/y_o = 0.3$, and $tu_o/y_o = 0.166$ for $z_o/y_o = 0.5$. As a result of the start-up function coupled with a moderate grid stretching, the first acoustic peak resulting from the initial condition has similar time-scale and amplitude as that of the physical acoustic waves. No spurious waves were generated as the transient wave and subsequent acoustic waves propagate throughout the domain towards the external boundaries. This was confirmed through the time-variations of the acoustic signals at the selected observation points and plots of instantaneous contours of the acoustic pressure fluctuations (which would be shown subsequently).

Preceding the merger of the two vortex rings, there is a gradual increase in the amplitudes of the peaks. This behaviour can be explained by using the fact that the amplitude of the acoustic signals is proportional to the induction velocity. Viscosity acts to reduce the peak vorticity of the core and therefore slackens the velocity gradients. This results in the distance between the vortex rings becoming smaller over time. As the vortex rings approach each other, the induced velocity also increases (to conserve the

angular momentum of the flow). As such, leading up to the merging of the vortex rings, the amplitude of the peaks should increase over the successive leapfrogging cycles. At the instant of vortex merger, the amplitude of the acoustic peak is maximum.

In order to be able to visually observe the far-field directivity of the acoustic signals, instantaneous contours of the typical pressure field while the vortex rings are still engaged in the leapfrogging cycles are shown in figures 4.13. The contours are shown at the time $tu_o/y_o = 0.477$ for $z_o = 0.3$ and $tu_o/y_o = 1.33$ for $z_o = 1.33$. As the aspect ratio is increased, it is clear that the width of the positive peaks becomes finer. This is in agreement with the analytical pressure contours (shown in figure 4.1). However, in contrast to the MAE solution, as the Mach number is increased, it is clear that the propagation characteristics of the waves between the positive and negative sides of the axial axis changes. It seems that the waves are propagating preferentially towards the upstream direction. Furthermore, this effect is more prominent at larger Mach numbers. As such, we argue that it is related to the source compactness. Source compactness is synonymous with the low Mach number assumption. This issue will be attended to in greater detail through the decomposition of the predicted sound field via a multipole expansion.

By correlating the time histories of the trajectories of the core centroids with the far-field acoustic signals, we found that the acoustic peaks occurred at the slip-through instants while the acoustic troughs corresponded to when the axial distance between the core centroids is largest. This finding is consistent with the theoretical analysis (Kambe & Minota (1981)), and numerical results of Tang & Ko (1995), and Verzicco *et al.* (1997).

However, in contrast to the results of Shariff *et al.* (1988), and Tang & Ko (1995), there were no wavy oscillations present in the time traces of the acoustic signals. According to Shariff *et al.*, and Tang & Ko, the wavy oscillations were superimposed on the signal associated with the fundamental frequency. In addition, it had a secondary frequency which was much shorter than the fundamental one. Verzicco *et al.*, (1997) have argued that the thickness of the vortex core affects the secondary frequency. Specifically, they have found that by using different initial vorticity distributions, the secondary frequency could be either larger or smaller than the fundamental frequency. This secondary frequency is linked to the vortex core nutation. The nutation of the vortex core is defined as the time taken for a particle located at the point of maximum tangential velocity to orbit once around the core. Since the aspect ratios studied here have identical core thicknesses, the secondary frequencies are going to be equal in both cases.

With the Gaussian vortex core model, the position of maximum tangential velocity is at the core radius, $r = e_o$. The secondary period, t_s, turns out to be $t_s u_o/y_o = 0.0022$ for $z_o/y_o = 0.3$, and $t_s u_o/y_o = 0.0062$ for $z_o/y_o = 0.5$. Thus, it is clear that the secondary frequency is significantly higher than the fundamental frequency. In this study, both the sampling rate of the hydrodynamic terms and the acoustic grid are geared towards the acoustic solution corresponding to the fundamental frequency. As a result, the fact that no wavy oscillations were present in the acoustic far-field signals should be

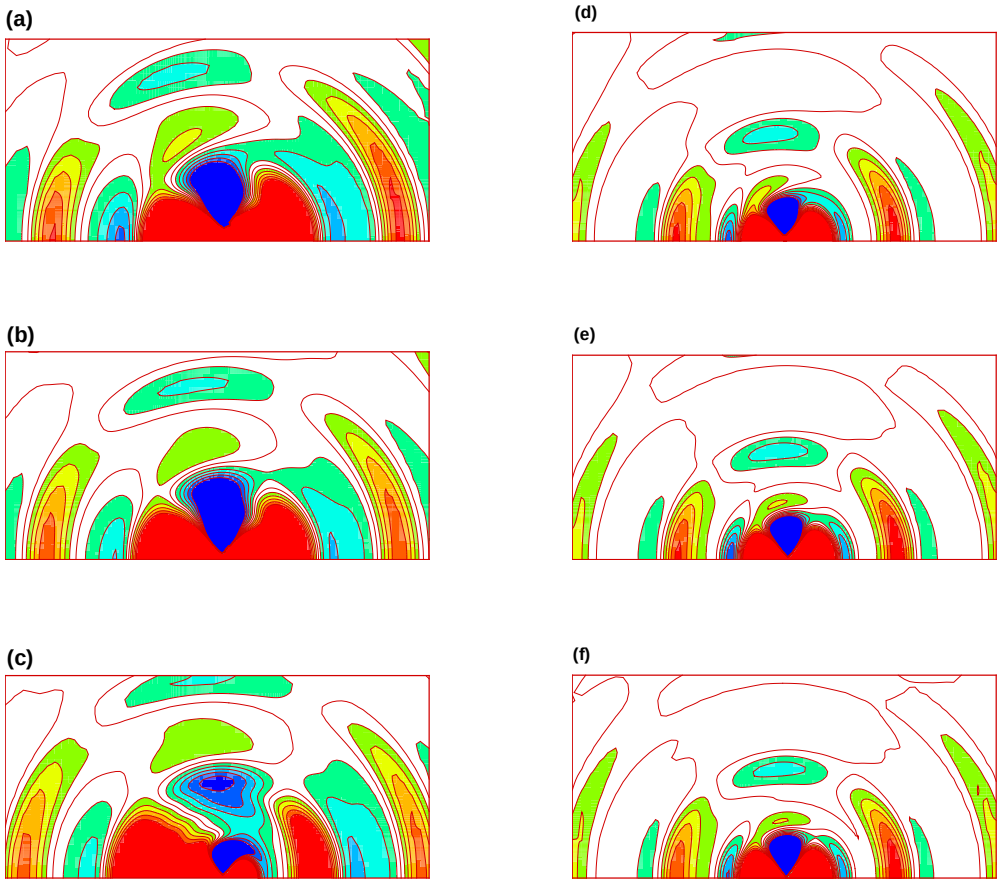

Figure 4.13: Instantaneous contours of the acoustic pressure fluctuations. The left column refers to $(z_o/y_o) = 0.3$ at simulation time $tu_o/y_o = 0.477$, while the right column refers to $z_o/y_o = 0.5$ at simulation time $tu_o/y_o = 1.3$. The three different Mach numbers are Ma = (a)&(d) 0.01, (b)&(e) 0.005, (c)&(f) 0.0025. The range of the contour levels are from (a) $\pm 7 \times 10^{-4}$, (b)$\pm 2.5 \times 10^{-6}$, (c) $\pm 7 \times 10^{-8}$, (d) $\pm 1 \times 10^{-5}$, (e) $\pm 2 \times 10^{-7}$, (f) $\pm 1 \times 10^{-8}$ with 10 increments.

expected. This issue also highlights one of the potential difficulties in solving an acoustic problem with multiple sources with widely different frequencies.

Having ascertained that the vortex cores were thin and thus resulted in the secondary frequency being too high to be captured by the simulations, we now proceed to compare our acoustic results (bearing only the fundamental mutual slip-through frequency) with that of the MAE analytical expression. The time histories of the far-field pressure calculated using the MAE technique are shown in figures 4.12. The observation positions are identical to those used to show the time variations of the signals in the acoustic simulations. It is clear that there is a distinct difference in the time variations of the acoustic signals between the numerical results and the MAE prediction (see figure 4.12). While the time variations of the analytical pressure maintain a perfect symmetry, our results indicate otherwise. In particular, the time variation beginning from the slip-through instant (acoustic peak) and ending at the point where both vortices are aligned horizontally with maximum distance deviated from the classical model. By correlating the temporal variations of the acoustic signals with the vorticity snapshots, it is evident that the differences are linked to the core deformations of the vortex rings sustained during the leapfrogging motions. The fact that the deviation from the classical model is more noticeable at the larger aspect ratio indicates that the core deformation is more intense with smaller rings.

Decay and scaling law of the acoustic pressure

The propagation and decay characteristics of the far-field acoustic signals can be observed through plotting the spatial distribution of the peak pressures. Shown in figure 4.14 are the acoustic peaks measured along the positive axial axis occurring at the second slip-through instant. It is clear that while the acoustic waves are propagating radially outwards, the decay of the peaks in the near-field is not proportional to $(1/r^{0.5})$. This is because in the near-field, the fluctuations are affected by the temporal variations in the sources as well as by the pressure gradients of the vortex core. In the classical model, the decay rate would be uniform everywhere because the acoustic source reduces to a point. This is not the case here, as the vortices are finite. However, it is evident that as the location is further away from the source region, the acoustic peaks tend to decay inversely with $r^{0.5}$ in agreement with Landau & Lifshitz (1987).

4.5.3 Decomposition of the acoustic waves

By decomposing the far-field acoustic signals into a multipole expansion, we can quantify the amplitudes of the various modes present in the predicted acoustic field. Decomposition of the acoustic signal into a multipole expansion is possible because the acoustic waves are linear. The acoustic pressure waves are decomposed into harmonic modes using the following

$$p(z, y) = A_o(z, y) + B_m(z, y)\cos(n\theta). \tag{4.7}$$

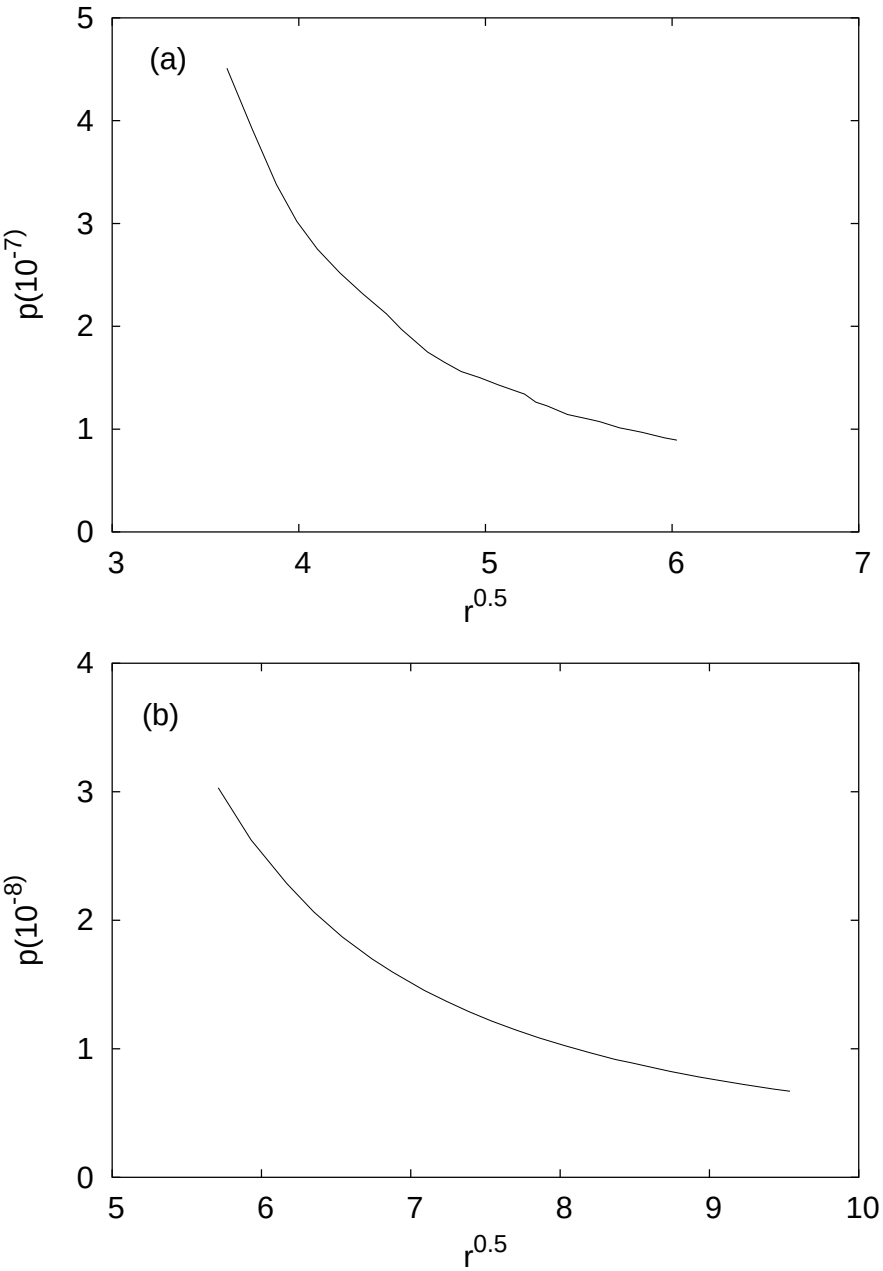

Figure 4.14: Decay of the pressure peaks located along the positive axial axis. Here, z_o/y_o = (a) 0.3, (b) 0.5. The radial distance r has been normalised with respect to y_o.

where the terms, A_o and B_n are defined as follows,

$$A_o = \frac{1}{\pi}\int_0^{\pi} p(z,y)d\theta, \tag{4.8}$$

$$B_m = \frac{2}{\pi}\int_0^{\pi} p(z,y)\cos(m\theta)d\theta. \tag{4.9}$$

Here, m is an integer which ranges from 0 to ∞, and A_o is the zeroth-order mode with uniform directivity while B_m are the m^{th} order cos modes. Owing to the axisymmetric pattern of the vortex pairing sound, the only modes that can be present in the acoustic field apart from the monopole are the cosine harmonics. The amplitudes of the modes are evaluated through integration using Simpson's 1/3 rule. Once we have determined the amplitudes of the modes present, we can then determine the far-field directivity of the sound field. The polar angle of extinction is evaluated at the radial positions by equating the amplitude of the acoustic signal to zero and subsequently using the Newton-Rahpson method to iterate for the extinction angle θ.

On the effect of Mach number on far-field directivity

Using the MAE technique, Kambe & Minota (1981) have argued that in the limit of Mach number Ma ≈ 0, the far-field directivity of the sound radiation from an axisymmetric vortex pairing resembles a lateral axi-quad (axisymmetric quadrupole). Another way of depicting the axi-quad pattern is to decompose the acoustic field into a multipole expansion. Then it can be easily shown that the axi-quad consists of a second-order cos harmonic mode and a zeroth-order mode. With an axi-quad, the values of the polar angles of extinction are located exactly at 54.7° and 125.3°. However, with the MAE technique, the validity of the acoustic solution away from the asymptotic limit is very much open to question as the solution may be affected by both the spatial distribution of the source term and the advection of the source field when the Mach numbers are finite.

Mitchell *et al.* (1999) have argued that when Lighthill's acoustic analogy is applied to predict the sound waves radiated from vortex pairing, the theoretical polar angles of extinction are shifted because the trace of Lighthill's acoustic source term is nonzero. To confirm Mitchell *et al*'s. argument and also investigate the effect of source compactness on the far-field directivity, the decomposition of the acoustic signal is performed at the three different Mach numbers. The pressure fluctuations located along a radial arc of 1.5λ are used in the decomposition routine to determine the corresponding values of the harmonic modes. The time histories of the amplitudes of the harmonic modes at the three different Mach numbers is shown in figure 4.15(a)-(c) for $(z_o/y_o) = 0.3$, and in figure 4.15(d)-(f) for $(z_o/y_o) = 0.5$. Only the first three cos harmonic modes are shown in the figures as the contributions of even higher modes are too small to be of any real significance. In the MAE expression, the predicted sound field consists only of a monopole component and a quadrupole component. However, it is clear from the figures that the acoustic signals present in our simulations contain other modes too. This is because the Mach numbers of our acoustic simulations are finite.

z_o/y_o	Ma(10^{-2})	first angle(°)	second angle(°)
0.3	1.0	72.5	141.32
0.3	0.5	63.925	132.36
0.3	0.25	59.88	128.85
0.5	1.0	64.1	132.17
0.5	0.5	60.26	128.4
0.5	0.25	60.12	123.38

Table 4.3: The first and second polar angles of extinction as a function of Mach number for both aspect ratios. Here the angles are measured at the second slip-through instant.

At both aspect ratios and for all Mach numbers, it is clear that the zeroth-order mode and the second-order cos mode are the dominant terms in the decomposed acoustic signal. However, the amplitudes of other modes being $\cos(\theta)$ and $\cos(3\theta)$ becomes increasingly significant as the Mach number is increased. The polar extinction angle is evaluated from the peaks of the various modes at the second slip-through instant. It is evident from table 4.3 as the polar extinction angles are clearly seen to have shifted towards the upstream direction at higher Mach numbers. The shift is also noticeable from the instantaneous contour plots of the acoustic signals as shown previously in figure 4.13. The shift in the polar angles of extinction is related to the compactness of the source region. We see that at aspect ratio $z_o/y_o = 0.5$, between Mach number of 0.0025 and 0.005, the first polar angle of extinction seems to have converged to approximately 60°. Hence, this implies that the polar extinction angle is never located exactly at the theoretical values, in line with the argument presented by Mitchell *et al.* Hence, the effect of increasing the Mach number is that the far-field directivity becomes less of an axi-quad. As the source region becomes less compact, the contributions of the other order *cos* modes start to become significant and starts to shift the far-field directivity towards the upstream direction.

4.5.4 Analysis of the quadrupole and monopole sources

Kambe & Minota (1981) has shown that the amplitude of the far-field acoustic signal is dependent on rate of change of the mean axial position of the vortex system. To better relate the acoustic signals to the properties and dynamics of the vortex cores, Tang & Ko (1995) further expanded the the quadrupole term, $\partial^3 Q/\partial t^3$ into four source terms as follows

$$\frac{\partial^3 Q}{\partial t^3} \propto \sum (I\frac{\partial^3 z}{\partial t^3}) + 3(\Delta \ddot{z})\dot{I_L} + 3(\Delta \dot{z})\ddot{I_L} + (\Delta z)\frac{\partial^3 I_L}{\partial t^3}. \tag{4.10}$$

Here the symbol Δ in the above equation represents the spatial difference operator. The four source terms describes the quadrupole in terms of the positions, velocities and accelerations of the vortex cores in the axial direction, and the impulses of the initially leading and trailing vortex core centroids.

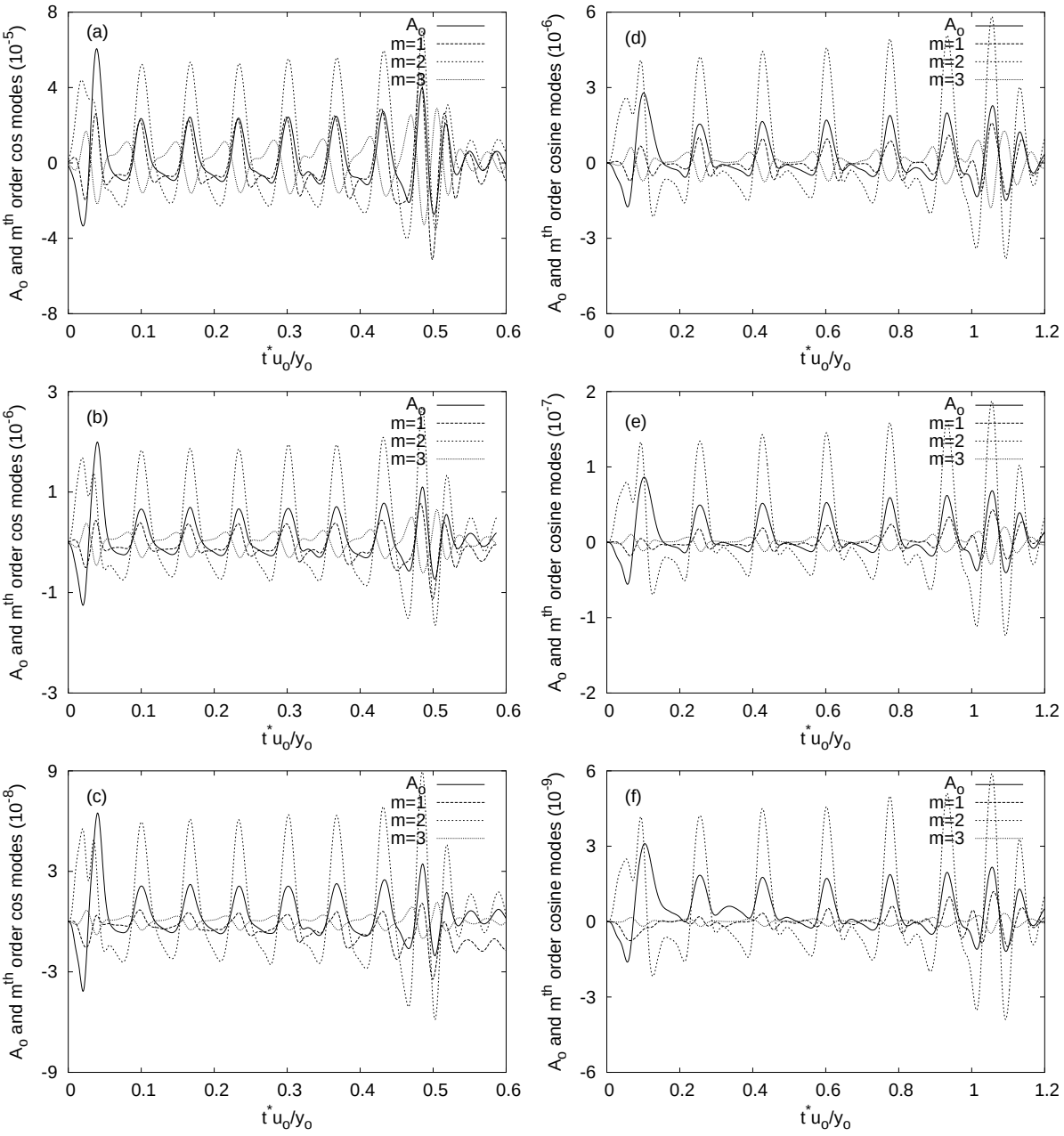

Figure 4.15: Time histories of the amplitudes of A_o and m^{th} order cos modes present in the acoustic signal. The figures on the left column correspond to $(z_o/y_o) = 0.3$ while those on the right column correspond to $(z_o/y_o) = 0.5$. The three different Mach numbers, Ma = (a)&(d) 0.01, (b)&(e) 0.005, (c)&(f) 0.0025. The symbol t^* represent the retarded time.

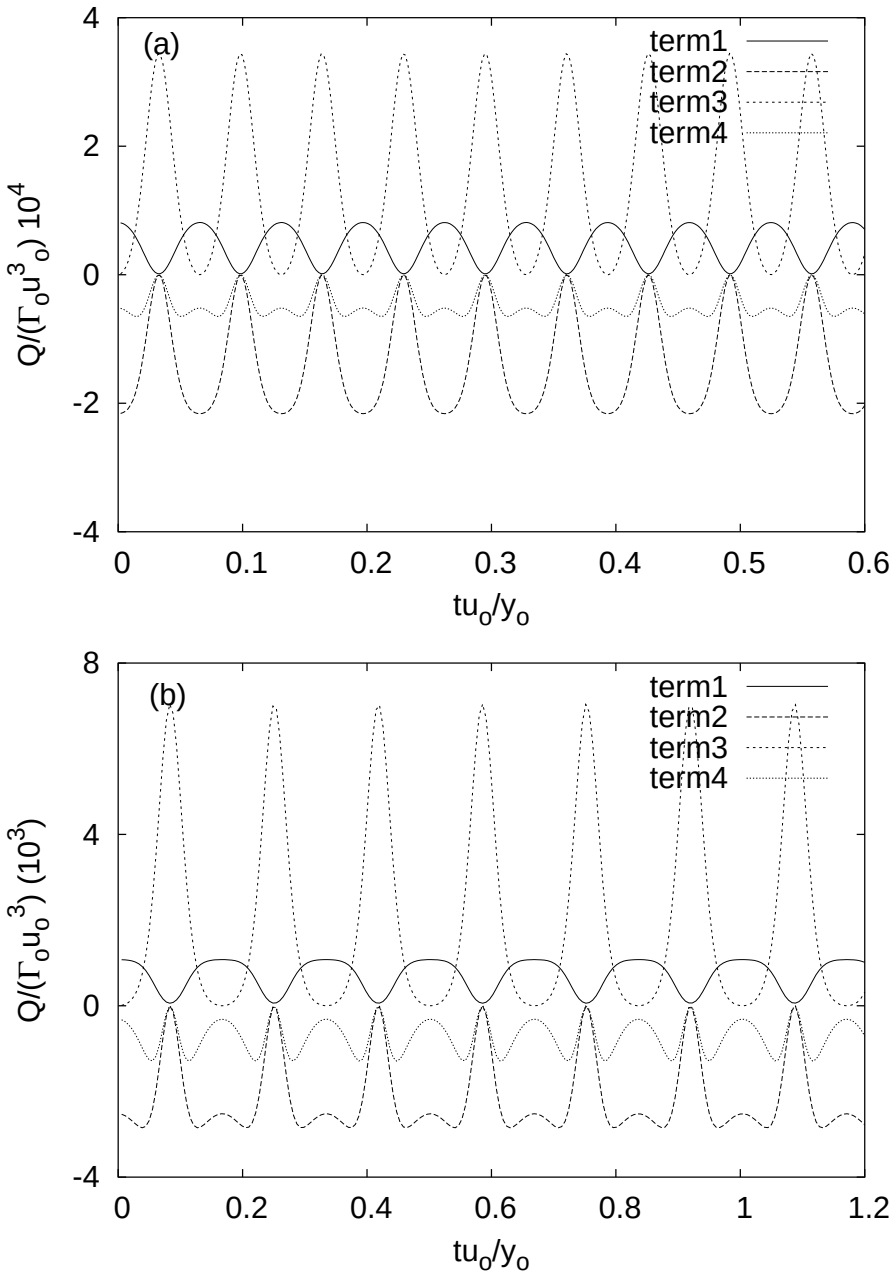

Figure 4.16: Time histories of the amplitudes of the four source terms calculated using trajectories of the classical model. The aspect ratio is $z_o/y_o =$ (a) 0.3, (b) 0.5. In the figures, term 1 is $\sum(I\frac{\partial^3 z}{\partial t^3})$, term 2 is $3(\Delta\ddot{z})\dot{I}_l$, term 3 is $3(\Delta\dot{z})\ddot{I}_l$ and term 4 is $(\Delta z)\frac{\partial^3 I_l}{\partial t^3}$.

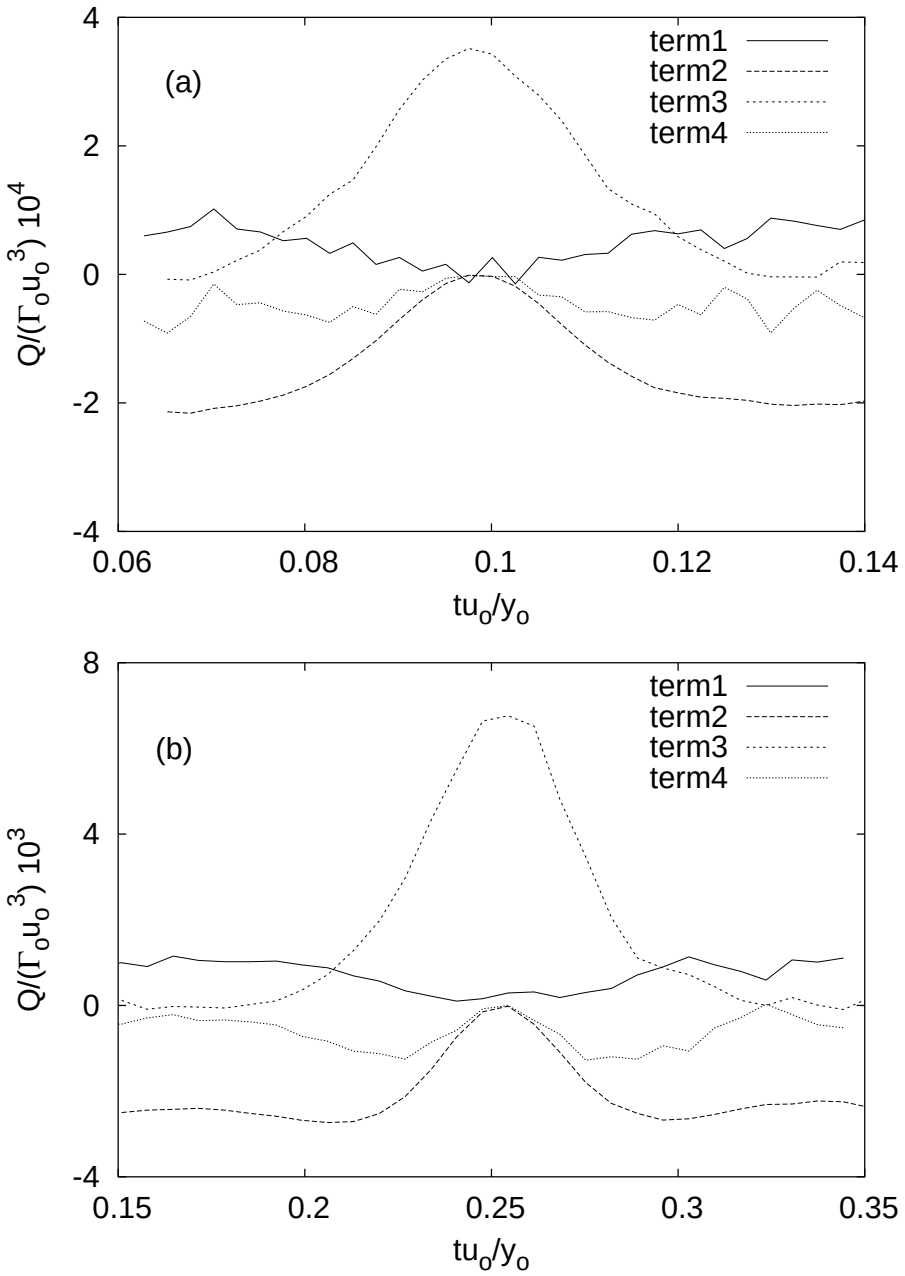

Figure 4.17: A sample time trace of the four source terms of Tang & Ko[11] calculated using the simulation data. Term 1 is $\sum(I\frac{\partial^3 z}{\partial t^3})$, term 2 is $3(\Delta\ddot{z})\dot{I}_l$, term 3 is $3(\Delta\dot{z})\ddot{I}_l$ and term 4 is $(\Delta z)\frac{\partial^3 I_l}{\partial t^3}$. The aspect ratio $z_o/y_o =$ is (a) 0.3,(b) 0.5.

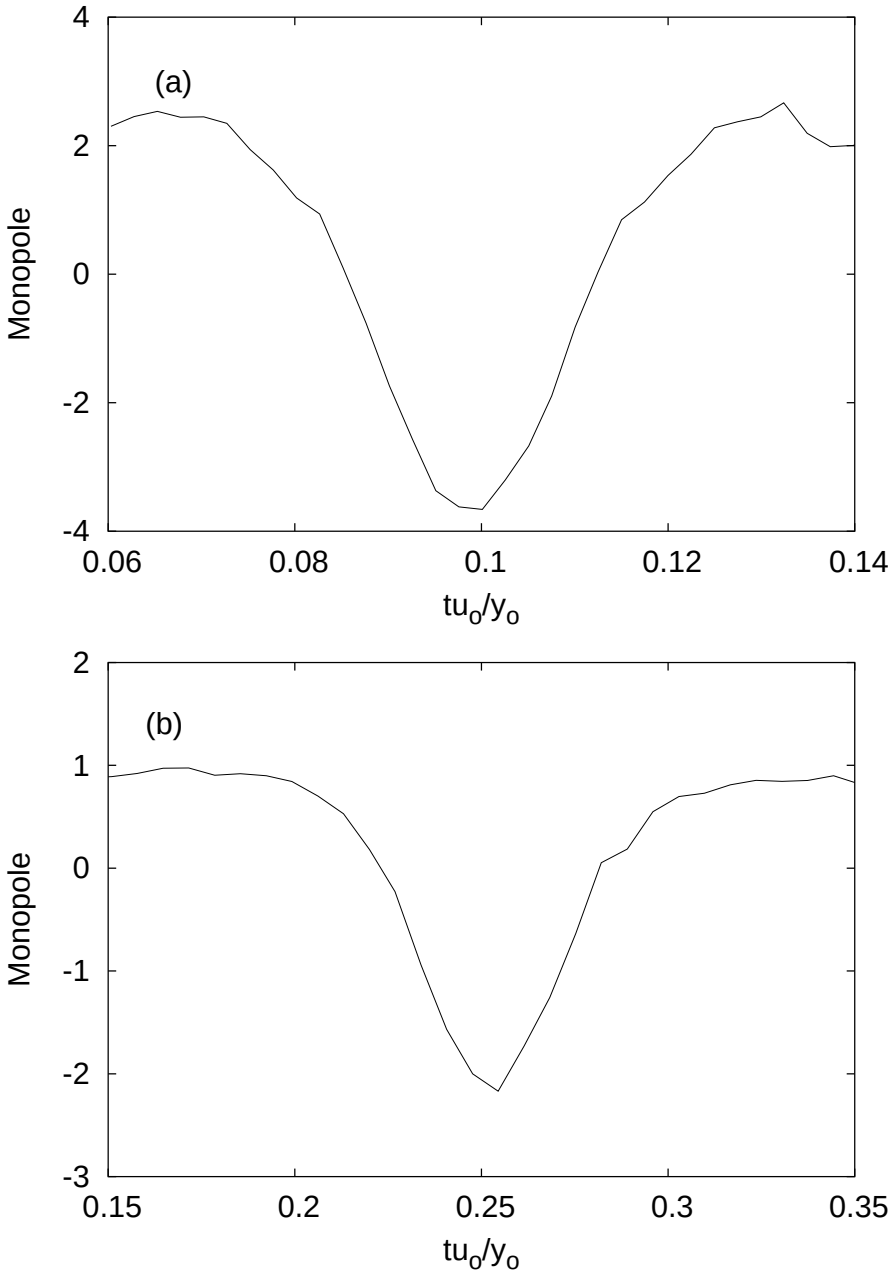

Figure 4.18: A sample time trace of the monopole source term. The aspect ratio $z_o/y_o =$ is (a) 0.3, (b) 0.5. Note that the monopole has been normalised with $\Gamma_o u_o^3$

To compare the behaviour of the source terms between the classical and viscous rings' interactions, firstly, the trajectories from the classical model (Dyson (1893)) are used in the calculation of the four source terms in equation 4.21. The time derivative of each source term are evaluated numerically by using the central-difference method. The analytical source terms are subsequently shown in figure 4.16. From figure 4.16, it is clear that all four source terms have a frequency equal to the fundamental mutual slip-through frequency. In addition, the amplitudes of each term are time-periodic. This is expected because the classical leapfrogging motion repeats itself indefinitely. It is also clear that the dominant source term is $3(\Delta\dot{z})\ddot{I}_l$ as it has the largest amplitude relative to the other three terms. It is also the only significant contribution to the acoustic peak occurring at the slip-through instant. Conversely, the term $3(\Delta\ddot{z})\dot{I}_l$ is the important source term compared to the other three terms when examining the contributions to the acoustic trough. Hence, the acoustic peak is strongly related to the coupling of the relative difference between the axial velocities of the vortex rings and the radial acceleration of the initially leading ring. Similarly, the acoustic trough is greatly influenced by the coupling of the difference between the axial accelerations of the vortex rings and the radial velocity of the initially leading vortex ring.

Next, the time variations of the four source terms are calculated using the data output from the viscous flow simulations. Due to the fact that the vortex core model used in the viscous flow simulations is finite, hence the core centroids used in the calculations of the source terms are based on Lamb's (1932) definitions. The centroids of each core were obtained through numerical integration of the vorticity field associated with each core. A sample time trace of the four terms are shown in figure 4.17. It should be noted that the time trace is representative of the successive leapfrogging cycles because the circulation of the flow is conserved and the trajectories of the core centroids presented earlier in the section on the flow dynamics are largely repeatable with only minor variations. From figure 4.17, it is clear that all four terms have the characteristic frequency of the leap-frogging motion. In addition, the amplitudes of the first term is largest relative to the rest indicating that it is the dominant acoustic source. In contrast to Tang & Ko, there were no wavy oscillations in any of the four source terms. This implies that the rate of change of the axial acceleration of the vortex ring is not an important factor in the sound radiation of co-axial viscous rings.

Apart from the quadrupole, another potential source that needs to be considered in aerodynamic sound generation is the effect of the presence of viscosity. According to Kambe (1984), physical viscosity acts as a monopole sound source. A sample of the time histories of the amplitudes of the monopole term is shown in figure 4.18. It is clear that in both cases, the monopole is negligible because it is several orders of magnitude smaller than the quadrupole term. This result is consistent with the observations of Verzicco *et al.* (1997).

4.6 Concluding remarks

Numerical simulations of the acoustic radiation from a pair of co-axial vortex rings moving along a common axis of symmetry has been investigated in this study. Although the vorticity field of a real jet is much more extensive and complex this simplified flow and acoustic model provides some insight into vortex pairing and leap-frogging which can be present in jet shear layers. Thus, in view of exploring the feasibility of using acoustic analogies in more complex flows, this study can be considered as a building block towards the more complicated case of the sound radiation from flow exiting a round jet.

As the vortex rings are engaging in leap-frogging cycle, the vortex system is actually self-advecting through the fluid. However, the acoustic analysis using the MAE technique assumes that the Mach number is Ma $\rightarrow$ 0, i.e., the advecting vortex system reduces to a stationary point source in the acoustic approximation. The advecting vortex system adds a further complication when using the acoustic analogies. Therefore, in order to be able to compare the results with the MAE solution, the translational velocity of the mean axial position of the vortex system has to be removed from the axial velocity component prior to calculating the acoustic source terms. Hence, the acoustic source terms, either H_l or H_p, are effectively radiating sound from a fixed position in the acoustic domain.

The MAE technique is based on the assumptions of thin rings and an inviscid fluid. As a result, the theoretical far-field acoustic pressure expression is devoid of any effect of core distortion. However, the classical leap-frog motion is a highly idealised model. Shariff *et al.* (1998), and Tang & Ko (1995) have used contour dynamics to show that for vortex rings having finite core thickness, the vortex cores deforms into an elliptical shape during the leapfrogging motion. This results in the presence of wavy oscillations superimposed on the far-field acoustic signals. The aim of this study is to investigate the effect of varying the initial toroidal ring radius on the acoustic radiation using the two-step approach. In sharp contrast to both authors, we found no presence of wavy oscillations in the time-trace of the acoustic signals. Using Verzicco *et al.*'s. (1997) argument, the secondary frequency is approximately one order of magnitude greater than the primary frequency and as such, may be filtered out by the sampling interval.

Numerical simulations are performed at $Re = 7500$ with the ratio of the initial axial distance of the vortex rings to the toroidal ring radius being $z_o/y_o = 0.3$ and 0.5. The deviation of the numerical results with the MAE solution indicates that the acoustic signals are not completely dominated by the largely inviscid leapfrogging motion. In particular, the difference in the acoustic signal's waveform is greater at aspect ratio $z_o/y_o = 0.5$. This is believed to be related to the core distortion which is also more significant at $z_o/y_o = 0.5$. The amplitude of the peaks of the acoustic signal is dominated by the inviscid phenomena while the waveform of the acoustic signal is dependent on both the leap-frogging motion and the vorticity gradients.

On the analysis of the acoustic sources, the magnitude of the quadrupole term increases as the aspect ratio is increased from 0.3 to 0.5. In addition, the magnitude of the monopole term is at least one order of magnitude smaller than the quadrupole term indicating the viscosity itself is a weak sound source. This is consistent with Verzicco *et al*'s. (1997) finding. Comparisons of the quadrupole source term calculated using the data from the simulations with the classical model showed good agreement.

The effect of a finite Mach number is that the far-field directivity is not exactly identical to the stationary lateral quadrupole field. In particular, as the Mach numbers is increased, the contributions of other higher-modes becomes greater and as a result, the polar extinctions angles are shifted towards the upstream direction. In addition, we do not expect to recover the theoretical polar extinction angles. This is because at the lowest Mach number considered where the acoustic wavelength is approximately 63 times that of the initial ring toroidal radius, the polar extinction angles seems to have converged at 60.1° and 123.4°.

Chapter 5

Sound radiated by flow past a rectangular plate

5.1 Summary

This chapter describes a numerical study of the sound radiation associated with the natural shedding from laminar flow past a two-dimensional bluff body. The bluff body is rigid and is immersed in a fluid having a uniform freestream velocity. The body geometry considered consists of a two-dimensional plate (or cylinder) of rectangular cross-section. An interesting aspect of this flow problem is that the shedding of vortices occur at both the leading and trailing edges of the plate. The presence of both leading-edge shedding and trailing-edge shedding leads to more complex flow phenomena when compared to flow past a circular cylinder. The latter related problem has been studied in detail recently by a number of authors using a variety of alternative approaches. Inoue & Hatakeyama (2002) tackled the problem by solving the compressible flow equations directly. Hardin & Lamdin (1984) used a method based on the acoustic analogy. Shen & Sorensen (1999) treated the problem using an approach known as the acoustic/viscous splitting developed by Hardin & Pope (1994). Such numerical studies provide a basis for comparison with the predictions of the present study.

The bluff body under consideration is rectangular and its chord (c) is aligned in parallel to the direction of the freestream velocity. The plate chord-to-thickness ratio is fixed at $c/d = 7$. Here, d is the plate thickness. This particular aspect ratio is chosen because previous flow simulations by Tan (2000) have shown that it leads to a stable and locked periodic shedding from both the leading and trailing edges. In this study, the effect of the Reynolds number is considered by performing the flow simulations at two different Reynolds numbers, $Re = 300$ and 400.

For each Reynolds number, acoustic simulations are then performed at three different Mach numbers, Ma = 0.05, 0.1 and 0.2. The acoustic computations are performed using the acoustic source terms associated with both Lighthill (1952), and with Powell (1964). Both approaches give effectively the same far-field behaviour although the spatial distribution of the near-field source field is surprisingly quite different. This implies that the spatial terms represent potential acoustic sources while the properties of the far-field acoustic signals are ultimately determined by the time variation of the potential acoustic source field. The Lighthill acoustic source, H_l, is not as localised when compared with the Powell acoustic source, H_p, because it retains an extra contribution in the form $\nabla^2(\mathbf{u}^2/2)$, which only decays to zero slowly away from the source. Möhring (1978) has shown that the far-field acoustic pressure is directly proportional to vorticity. This implies that the Powell acoustic source falls to zero outside the boundary layers and vorticity in the wake. In contrast, the slower decay rate of the Lighthill acoustic source away from the bluff body means that, in general, it is more difficult to use in aeroacoustic computations as it involves a larger spatial filter to decay the hydrodynamic terms so that $\nabla^2(\mathbf{u}^2/2)$ converges to zero outside the region of the potential acoustic sources.

In our analysis of the predicted sound field, we expand on the hypothesis first proposed by Yudin (1947), and subsequently adopted by Etkin *et al.* (1954), that the acoustic source can be replaced by a point force acting on the fluid. According to Etkin *et al.*, this point force is equal and opposite to the aerodynamic force experienced by the plate. Assuming that the direction of the point force is varying with time sinusoidally, Etkin *et al.* predicted that the acoustic field is made up of two dipoles of different strengths and orthogonal directivities. The dipole normal to the fluid stream is significantly stronger and is associated with the fluctuating lift force, while the dipole parallel to the fluid stream is related to the fluctuation in the drag force. Curle (1955) has also presented a similar argument from taking a formal mathematical approach by integrating Lighthill's acoustic wave equation over a flow which contained solid boundaries to obtain a volume integral containing a distribution of quadrupoles and a surface integral due to the surface pressure fluctuations over the boundaries. According to Curle, the distribution of the quadrupoles in the wake is insignificant at low Mach numbers because it is a less efficient source than the dipoles.

A primary result of this study is that the far-field sound has a dipolar nature. This dipole field radiates in phase with the fluctuating lift force. It has a directivity normal to the longer sides of the plate. This finding is consistent with to the numerical result from a direct compressible flow simulation of flow past a circular cylinder by Inoue & Hatakeyama (2002). This dipole sound field due to the fluctuating lift force has been well documented by past researchers (Gerrard (1955), Phillips (1956), Etkin *et al.* (1954)) and is commonly known as the Aeolian tone (Strouhal (1878)). Furthermore, as the magnitude of the lift force increases when the Reynolds number is varied from $Re = 300$ to 400, the amplitude of the dipole field also increases. An additional fact, less well-known, is that by increasing the Reynolds number, the weaker dipole sound field, which is associated with the fluctuating drag, becomes more significant. However, at both Reynolds numbers, the drag dipole is still considerably weaker than

the lift dipole.

By using a spatial filtering technique to selectively zero out the acoustic source field over certain regions near the plate and most of the downstream wake, we found two interesting features of the acoustic field. Firstly, the leading- and trailing-edge region can be described as separate sound sources. Furthermore, because of the strong lock-in between the leading- and trailing-edge, both sound sources are in phase and thus, complement each other.

Secondly, the acoustic source is mainly associated with the trailing-edge region. By comparison, it appears that the leading-edge region, which still injects significant time-varying vorticity into the flow, only contributes, at most, approximately 10% of the far-field acoustic amplitude when the Reynolds number is $Re = 400$. This finding is consistent with Howe's (1975) interpretation of the acoustic generation process. The vortices shed from the shear layer associated with the leading edge convect almost parallel to potential acoustic field lines while moving along the sides of the plate. As a result, there is very little injection/removal of energy into/from the acoustic field. In contrast, when the vortices move into the wake (particularly near the trailing edge), they traverse potential acoustic field lines at an angle close to 90°. Hence, at this stage, the vortices can transfer significant energy between the flow and acoustic fields. However, the analysis employed in this study (using spatial filtering) does not associate the sound generation mechanism with either leading-or-trailing edge vortices. This is because to do so would require tracking each individual vortex structure during the time evolution. This is an extremely difficult task due to the merging of the leading-edge vortices with those from the trailing-edge as they interact with each other while moving into the wake downstream of the plate.

After considering the location of the dominant sound source, we turned our attention to the propagation behaviour of the sound waves as they radiate from the near-field to the far-field. Two factors that may affect the characteristics of the propagation of sound waves are source compactness and Doppler shift. The influence of both factors on the propagation characteristics can be studied by performing a multipole expansion on the predicted sound field. The contributions of the various harmonic modes present in the acoustic field are quantified as a function of the Mach number. The generalisation of the pressure into a linear sum of harmonic modes is possible because of the linearity of the acoustic wave equation.

The influence of the non-compactness of the acoustic source is analysed by quantifying the amplitudes of the harmonic modes (which include a zeroth-order uniform directivity term). As the Mach number of the sound field is increased, it is clear that the acoustic source becomes relatively less compact. At both Reynolds numbers, the lift dipole remained the dominant term among the sine modes at all Mach numbers. In contrast, the drag dipole only became the significant term among the cosine modes at $\mathrm{Ma} = 0.05$. The amplitude of the drag dipole was approximately one order of magnitude smaller than that of the lift dipole.

Aeroacoustic computations using Lighthill's acoustic analogy and Powell's vortex sound theory do not explicitly include the influence of non-zero Mach number on the propagation of the sound waves. This is because the acoustic medium is assumed to be stationary, which has the advantage of allowing easier identification of the multipole nature of the sound field. In particular, the lift dipole is very obvious. However, finite Mach numbers are known to lead to significant shifts in the propagation of sound waves to the far-field. This is shown by Inoue & Hatakeyama (2002) where the direction of the acoustic wave propagation is upstream from the circular cylinder. To include the Doppler effect, postprocessing of the predicted sound field is performed using the transformation, $r^{'} = r/(1 - M\cos\theta)$. After applying this post-processing step, the acoustic field distribution is found to be very similar to that found for a circular cylinder using direct simulations of the compressible flow equations by the above-mentioned authors, which include Mach number effects. This postprocessing step has also been adopted by Inoue & Hatakeyama when implementing Curle's (1955) acoustic analogy.

5.2 Introduction

The study of acoustic radiation from flow past bluff bodies is an active area of investigation in the field of aerodynamic sound as it underpins many important engineering issues such as flow-induced acoustic and structural vibrations, mixing of fluids, automobile aerodynamics, fatigue and stress analysis, which in certain cases may trigger structural failure. An important question that is still very much unanswered is the physical mechanism of energy conversion from the fluctuating flow to the acoustic field. While there have been extensive studies on the flow instabilities of bluff body wakes, both two-dimensional and three-dimensional, resulting in a wide range of flow measurements such as lift and drag coefficients, base suction, vortex formation lengths, to name a few, investigations into the acoustics associated with the wake dynamics is however, very much lagging.

Historically, studies of sound generation from flows past rigid bodies have focused on the circular cylinder. One of the earliest experiments on cylinder-induced sound was conducted by Strouhal in 1878. Quantitative measurements were made of the frequency of the sound produced from flow past a wire of circular cross-section. Strouhal observed that this frequency is related to the freestream velocity and cylinder diameter such that $fd/U_\infty = 0.2$ to 0.22 for a range of Reynolds number of $Re = 300$—10^4. This non-dimensional parameter is now commonly known as the Strouhal number (St). Acoustic radiation from flow past a 2D cylinder placed in a fluid stream has been studied experimentally by Etkin *et al.* (1954), Gerrard (1955), and Phillips (1956). One of the earliest theories on the sound radiation from flow past a bluff body came from Yudin (1945) who suggested that the Aeolian tone, which has a cross-stream directivity, may be somehow related to the variable force acting on the circular cylinder.

Flow past elongated bluff bodies has been widely studied both numerically and experimentally by a

number of authors including, amongst others, Parker & Welsh (1981), Stokes & Welsh (1986), Nakamura *et al.* (1991), Ohya *et al.* (1992), Naudascher & Wang (1993), Tan (2000), Hourigan *et al.* (2001), and Mills *et al.* (2002, 2003). The elongated bluff body which forms the basis of this study is a two-dimensional cylinder of rectangular cross-section. This will be referred to as a rectangular plate (or cylinder) in the remainder of this chapter. The plate has square leading and trailing edges, and is immersed in a uniform flow as shown in figure 5.1. This flow is quite complex because vortex shedding occurs from both the leading and trailing edges. There is a strong interaction which is controlled by a feedback loop acting between the boundary layers on the plate surfaces and the wake vortices. This generally results in the locking of both leading- and trailing-edge shedding for Reynolds number below approximately $Re = 1000$. The nature of the flow also depends strongly on the aspect ratio (c/d =chord/thickness) of the plate. The number of boundary layers vortices shed from the leading-edge and distributed along the plate varies in a stepwise manner as the aspect ratio is increased due to the controlling influence of the feedback loop. The mechanism of such flow instabilities appears to be due to a combination of impinging leading-edge vortices (ILEVs) and trailing edge vortices (TEVs) when these vortex structures pass/form at the trailing edge. A detailed explanation of the flow and the underlying mechanisms can be found in articles by Hourigan *et al.* (2001), and Mills *et al.* (2002, 2003). For a more general treatment of flow instabilities, the reader is advised to refer to Naudascher & Rockwell (1994).

For plate aspect ratio in the range $3.2 < c/d < 7.6$, Parker & Welsh (1981), Stokes & Welsh (1986), and Tan (2000) have found a regular wake pattern with a distinct shedding mode of $n = 2$, i.e., there are two vortices originating from the leading edge distributed along both the top and bottom surfaces of the plate at any given time. In this particular flow regime, both the leading- and trailing-edge shedding is 'locked'. Furthermore, the Strouhal number which is based on the plate's thickness is approximately constant across the regime. For the simulations described in this chapter, the aspect ratio is restricted to $c/d = 7$. This is because previous simulations have shown that this aspect-ratio leads to a strong lock-in, i.e., locking occurs rapidly and is relatively stable to perturbations (e.g., Tan (2000), Tan *et al.* (2003)). This is advantageous from an acoustic study point of view because it allows the sound from a strongly periodic source to be studied. Further follow up studies on the influence of different aspect ratio have been planned but these will not be considered in this thesis.

The Reynolds numbers considered in this study are $Re = 300$ and 400. These values are chosen because $Re = 400$ is approximately the Reynolds number at which the flow undergoes transition from two-dimensional flow to three-dimensional flow. Thus, it is reasonable to treat the flow problem as two-dimensional and thus, use a two-dimensional solver. For $Re = 400$, the leading-edge shedding is relatively well-developed. As a result, modelling the low Reynolds number flow allows the main flow features to be captured without the complications of three-dimensionality and turbulence which would otherwise occur at higher Reynolds number. This allows us to focus exclusively on the role of the periodic leading- and trailing-edge vortex structures as the sound generation mechanism in the acoustic study. At the lower Reynolds number, $Re = 300$, the leading-edge shedding is significantly less vigorous. In addition, the

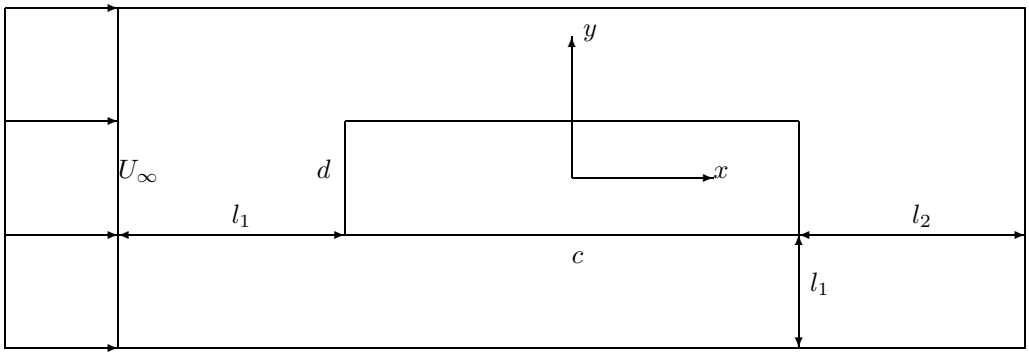

Figure 5.1: Schematic of flow past a long rectangular plate. Note that the sketch is not to scale.

trailing-edge shedding is less compact and not as intense as at the higher Reynolds number $Re = 400$. Hence, the case of $Re = 300$ provides a useful comparison to the choice of $Re = 400$. In addition, the flow dynamics of the vortex shedding from a plate at $Re = 300$ is quite similar to the two-dimensional circular cylinder at $Re = 150$, which has been studied in detail by Inoue & Hatakeyama (2002). As such, the results at $Re = 300$ can also be compared with the results of these authors. The change to the details of the vortex structures has a direct influence on the multipole structure of the acoustic field. This point will be addressed in greater detail in the later part of this chapter.

It comes as a surprise that while the acoustic radiation from flow past a circular cylinder has been studied quite extensively, little attention has been paid to the other body geometries such as two-dimensional plates of rectangular cross-section. Thus, the objective of this investigation is to study the sound generated by laminar flow past a long rectangular plate with square leading and trailing edges. The shedding process is natural, i.e., there is no external forcing imposed on the flow. This study can be considered as a natural extension to the study of the Aeolian tones generated from a circular cylinder. This is a limited parametric study that considers the effect of varying the Reynolds number of the flow on the acoustic radiation. In particular, it was envisaged that the leading- and trailing-edges of the plate act as separate sound sources. In addition, by varying the propagation speed of the sound waves (i.e., Mach number), we aim to clarify the effect of source compactness by decomposing the predicted sound field into harmonic modes. The effect of the Mach number on the directivity and propagation of the acoustic waves is also examined by postprocessing the acoustic solution.

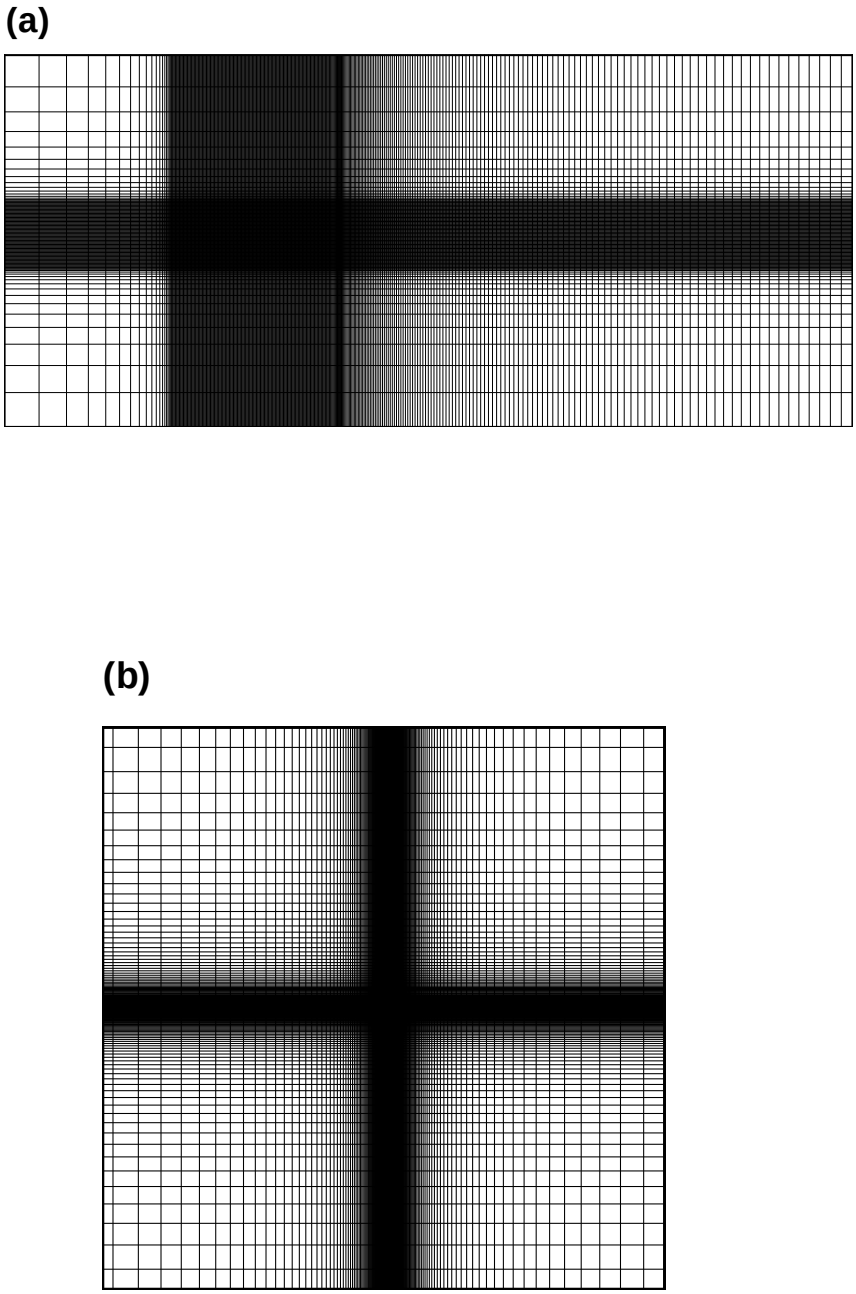

Figure 5.2: Typical mesh used in the respective (a) flow, and (b) acoustic simulations. Note that the size of the CFD and CAA meshes are not to scale.

5.3 Flow modelling issues

The fluid is assumed to be incompressible and Newtonian. As such, it is governed by the incompressible Navier-Stokes equations. A schematic of the flow configuration is shown in figure 5.1. The plate centroid is placed at $(x, y) = (0, 0)$. This is a parametric study that only considers the sound radiation as a function of the Reynolds and Mach numbers. The ratio of plate chord-to-thickness is fixed at $c/d = 7$. As mentioned in the summary of this chapter, the chosen Reynolds numbers are $Re = \rho_o U_\infty h/\mu = 300$ and 400. Here, the Reynolds number is based on the freestream velocity, U_∞ and plate thickness, h. The Strouhal number which is based on the plate chord is defined as $St = fc/U_\infty$. The Mach number of the sound field is based on the freestream velocity and is $\mathrm{Ma} = U_\infty/c_o$ where c_o is the sound speed. Finally, the source compactness is defined as ratio of the acoustic wavelength to plate thickness, λ/d.

5.3.1 Computational domain and boundary condition

The computational domain used in the flow simulation is shown in figure 5.2a. It is clear from this figure that the grid points are concentrated towards the plate. The domain is discretised into a structured mesh consisting of $N_x \times N_y$ grid points. In general, a structured mesh offers better convergence characteristics over an unstructured mesh despite the reduced flexibility. The CFD domain effectively consists of two regions with distinctly different grid distributions. The first region encloses the plate and has a uniform grid spacing. It spans a distance $2d$ from all four plate boundaries (on all sides). This region includes the boundary layers on the plate surface, the sharp velocity gradients as the flow separates from the leading and trailing edges, and finally, the vortex formation region at the rear of the plate. In contrast, the grid in the second region is stretched at the interface of the two regions and continues towards the boundaries of the computational domain. This type of stretching is typical of aerodynamic simulations where the most critical part of the mesh is close to the body.

An important feature of the computational grid is that local rate of stretching applied in the second region across the four lengths (see figure 5.2a) is not identical. In particular, the grid stretching applied towards the pressure outlet, associated with the length l_2, is more gradual relative to the other directions. This is expected since the wake downstream of the trailing face must be resolved adequately.

At the inlet, top and bottom boundaries, a freestream velocity U_∞ in the x direction is applied. At the outlet, a pressure boundary condition is imposed. At the plate surfaces, the no-slip velocity boundary condition is imposed. The flow simulations are started from an irrotational state. Prior to execution of the solver, the interior cells of the entire domain are initialised with the freestream velocity U_∞. This is to accelerate the development of the flow towards the asymptotic state.

5.3.2 Domain size

When simulating viscous flow past a bluff body, the size of the domain can influence the dynamics of flows near the body in three different ways. Firstly, locating the top and bottom boundaries too close to the plate induces an artificial blockage effect. Secondly, incorrect placement of the upstream boundary can prevent the correct development of the vortex shedding process. Finally, if the outflow boundary is placed too close to the plate, it can induce a back-effect on the wake development. Because accurate quantitative simulations of the flow are needed to generate the acoustic source field, it is vital that the three above-mentioned effects are controlled so that the computed solution is acceptable to within a certain tolerance level. In this study, the tolerance level was set at around 5% as a compromise between accuracy, and computer-time and memory requirements.

As seen in figure 5.1, the size of the CFD domain is defined by three parameters. The parameter l_1 is the distance from the inlet to the front face of the plate. It is also the distance from the top/bottom boundary to the plate, while l_2 is the distance from the rear face of the plate to the outlet boundary. These distances are normalised by the plate thickness. Two different trial values were used to determine the appropriate length for l_1. Note that the parameter l_2/d is fixed at 40 for these tests. The mean c_p is shown in Table 5.1. It is clear that the values of c_p for $l_1/d = 15$ and 20 for both Reynolds numbers are within 1%. As such, the smaller length was deemed to be satisfactory.

5.3.3 Spatial and temporal resolution

From experience, it has been found that both the stability and accuracy of the predicted sound field are very sensitive to adequately resolving the flow field (see also Cox *et al.* (1998)). This is because evaluation of the acoustic source term, H_l or H_p, relies on the calculation of high-order spatial derivatives of the hydrodynamic velocity field. In addition, it has been found through experience that the sharp corners of the plate can lead to large local errors. However, the effect of these singularities can be reduced and isolated through increasing the spatial resolution around the edges.

To determine the required spatial resolution, flow simulations were performed with an identical domain but the minimum grid spacing $\Delta x/d$ was varied. In the present spatial resolution study, three grid spacings of $\Delta x/d = 0.0125$, 0.025 and 0.04 corresponding to 81, 51 and 25 grid points across the plate thickness were used. The chosen domain size, which was determined through the study described previously, is used in the spatial resolution study here. Again, the base pressure coefficient was used to judge the difference in the solutions computed with different minimum grid spacings. The results presented in Table 5.2 indicate that a resolution of $\Delta x/d = 0.025$ produced a result with 0.5% of the more highly resolved case.

Re	l_1	l_2	Mean c_p
300	15	40	-0.332
300	20	40	-0.329
400	15	40	-0.483
400	20	40	-0.485

Table 5.1: The mean base pressure coefficient at the simulated Reynolds numbers as a function of domain size.

Re	$\Delta x/d$	Mean c_p
300	0.04	-0.343
300	0.02	-0.332
300	0.0125	-0.331
400	0.04	-0.499
400	0.025	-0.483
400	0.0125	-0.481

Table 5.2: The mean base pressure coefficient at the simulated Reynolds numbers as a function of three different grid resolutions.

In the grid and domain independence studies, the time-step used to advance the flow computations was set at $\Delta t = 0.01$. To verify that this was acceptable, a flow simulation was conducted with a smaller time-step of $\Delta t = 0.005$. The domain and the minimum grid spacing correspond to those used to generate accurate data for the acoustic computation. Again, the values of the mean c_p was used in the comparison study. The change in c_p was less than 0.2% indicating that the time-step of $\Delta t = 0.01$ is indeed sufficient to properly resolve the flow dynamics.

5.4 Acoustic modelling issues

The acoustic wave equation is solved numerically on a square domain. A typical computational mesh used in the acoustic simulation is shown in figure 5.2b. There are several differences to note between the CAA domain and the CFD domain. Firstly, the physical sizes of the CFD domain and CAA domain are widely different. The CAA domain extends two acoustic wavelengths from the plate in both x and y directions. As the Mach number decreases, the disparity of the size of the two domains become even larger. While it would be preferable to capture more acoustic wavelengths, again, the choice is a compromise, this time between computer-time and adequate representation of the properties of the far-field acoustic waves.

5.4.1 Computational domain and boundary condition

Similar to the flow domain, the acoustic domain is discretised into a structured mesh but since it is a square, hence the number of grid points in the x and y directions are equal. It is clear from figure 5.2 that the grid distribution in the CAA domain is different to that of the CFD domain. Here, the grid density near the plate has to resolve the acoustic source field which is calculated through high-order spatial derivatives of the hydrodynamic velocities. In the far-field, the grid spacing is based on the resolution of the acoustic waves with a minimum of 20 points across a wavelength. The disparity between the near-field and far-field grid spacings are handled by a non-uniform mesh. The stretching in the CAA domain from the near-field to the external boundaries has to be gradual to prevent generation of spurious waves at numerical interfaces. Through previous experience with the isolated co-rotating vortex pair structure and the co-axial vortex ring pair, a local rate of stretching of 3% was used in the acoustic simulation for $Re = 400$ and at the lowest Mach number simulated in this study. The results indicated that the acoustic signals were well-resolved. As such, for all further simulations the stretching of the acoustic domain was kept at 3%. A direct result of such a small stretching rate is that the number of grid points in the domain increases quite rapidly as the Mach number is decreased. The time step used to advance the acoustics simulations is the maximum possible under the stability limits of the RK4 method.

At the surfaces of the plate, the reflecting boundary condition of Poinsot & Lele (1992) is applied. With sixth-order spatial schemes, three ghost points were necessary in order to find the normal derivatives of the acoustic variable close to the surface. The values of the acoustic variable at the ghost points are obtained through the reflecting boundary condition. Thus, a central difference stencil can be applied everywhere including the surfaces of the plate. The implementation of the reflecting boundary condition on this particular flow geometry is relatively simple since the wall surfaces are flat. At the four edges of the plate, the local value of the acoustic variable is obtained through averaging over the four neighbouring points. At the external boundaries, the first-order radiation boundary condition of Bayliss & Turkel (1982) is imposed. Here r denotes the radial distance from the source assumed to be at the plate centroid.

5.4.2 Spatial filtering of the hydrodynamic terms

When evaluating the acoustic source term on the CAA mesh, it is essential to ensure that the predicted hydrodynamic fields are fully resolved (Crow (1970)) even away from the potential source terms. Otherwise, local inaccuracies in the velocity field, which are amplified by the numerical differentiations required for the source calculation can lead to the generation of spurious acoustic wave components which can contaminate the acoustic solution.

To assist in reducing the need to fully resolve the flow away from the true acoustic source regions, a spatial filter is used to smoothly reduce the source field to zero. The size of this spatial filter is governed by

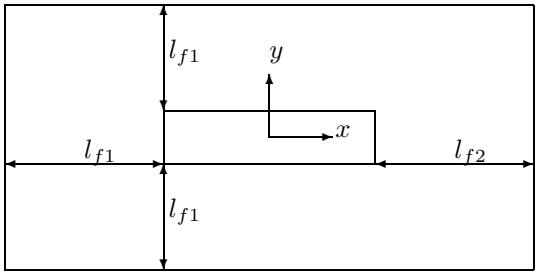

Figure 5.3: Schematic of the spatial filter used in the CAA domain. Note that the sketch is not to scale. The bounds of the spatial filter are defined by the two parameters, l_{f1} and l_{f2}.

two parameters, l_{f1} and l_{f2} (see figure 5.3). The parameter l_{f1} defines the decay length of filter function placed upstream from the leading face, and also normal from the top and bottom side of the plate chord. The other parameter l_{f3} represents the decay length of the filter function placed in downstream direction from the trailing face. The choice of length of parameter l_{f1} is not as important as l_{f2} due to the fact that no eddies actually pass the front or side boundaries. In contrast, sudden or abrupt termination of the wake vortices through the outlet boundary leads to an artificial source of sound. Such an effect can be easily revealed through performing flow simulations at a fixed value of l_{f1} but with different lengths of the parameter l_{f2}. The simulations with different lengths of l_{f2} can give an indication of the strength of the artificially induced fluctuations.

At low Mach numbers, the main sources of sound are associated with the vortices around the plate rather than the wake downstream of the plate (Curle (1955)), and these control the amplitude and phasing of the acoustic signal in the far-field. Therefore the selection of a suitable length for l_{f2} should not affect the acoustic results.

Thus, it is necessary to perform an extensive optimisation study the determine the appropriate decay lengths to minimise the possible introduction of spurious waves. The decay begins at a normal distance of three plate thicknesses away from the plate surface in each direction. To determine the suitable lengths of the spatial filters, the parameter l_{f1}/d is tested with lengths of 3, 4 and 5 while the other filter length l_{f2}/d was fixed at 30. Results show that there was little variation (phase and amplitude) in the acoustic signals using different decay lengths. This was expected because the eddies do not pass through the l_{f1} region. As such, $l_{f1}/d = 3$ was used in the flow simulations. Next, l_{f2} is tested for two more different lengths at $l_{f3}/d = 20$ and 25. In contrast to l_{f1}, with the smaller $l_{f3}/d = 20$, there was some phase variations in the time histories of the acoustic signals when compared with the larger filter lengths. The phase variations decrease as the length of the filter function is increased. Hence, it was decided in this study to use the maximum permissible length, that is $l_{f2}/d = 30$. The typical filter functions used in the truncation of the hydrodynamic terms are shown in figures 5.5 and 5.6. From the figures, it is clear that the filter function f_y is symmetric about x axis and the filter length is largest in the downstream direction. Note that the downstream decay only effectively begins approximately 8d from the trailing

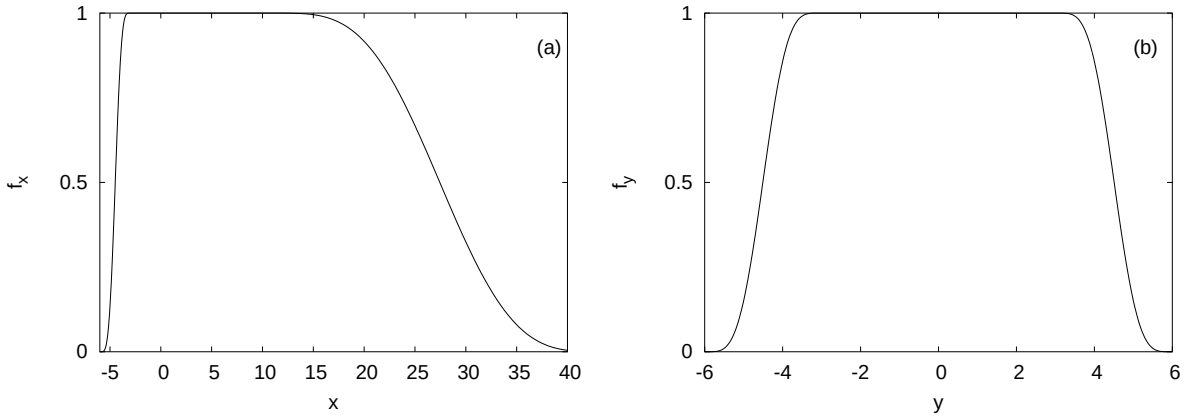

Figure 5.4: Distributions of the typical filter functions.

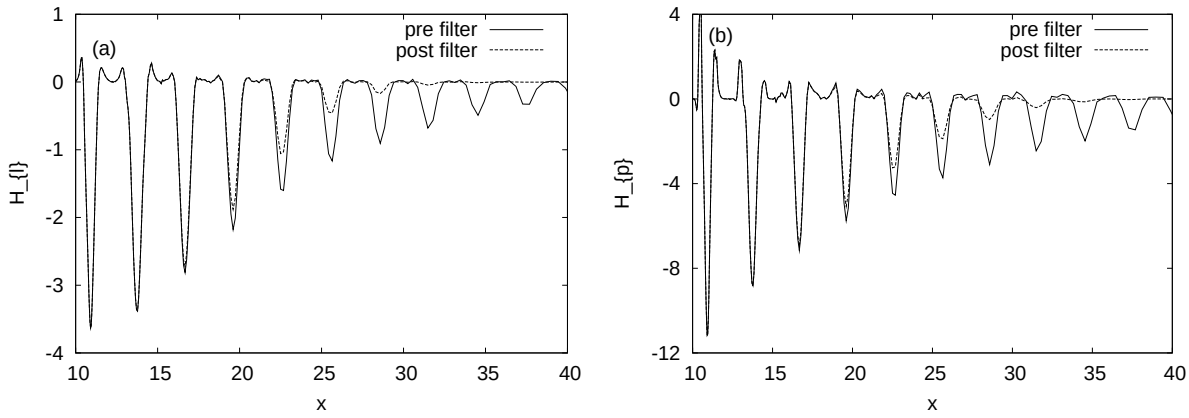

Figure 5.5: A sample of the spatial distribution of the acoustic source term taken along the plate centreline, and starting from three thicknesses away from the trailing face and extending into the downstream. The acoustic source term is $H =$ (a) H_l, (b) H_p.

edge.

Once the hydrodynamic velocity field has been filtered, numerical differencing is then performed on the velocity terms to calculate the respective acoustic source. A sample spatial distribution of the acoustic forcing calculated using Lighthill acoustic source term before- and-after filtering is shown in figure 5.5a. In figure 5.5b, the spatial distribution of the acoustic forcing downstream along the plate centreline calculated using Powell's acoustic source term before- and-after application of the filter function is shown. As both figures show, the source function is finite and extends well downstream from the plate. However, it will be shown that the wake is not an active part of the acoustic generation region at low Mach number flows. In addition, it is evident while the absolute values of the source terms differ, the decay rates of the two source terms away from the plate were approximately equal.

5.4.3 Source decomposition

The acoustic source term derived from the instantaneous hydrodynamic field obtained from the flow simulations cannot be used directly in the acoustic wave equation, or at least, it is preferable not to do this. This is because the acoustic source term effectively contains both the fluctuating pressure (which is unsteady) and the mean pressure (which is a function of space but temporally independent). In turn, the source generates a pressure consisting of both a time-periodic component and a mean component. If the acoustic simulation is undertaken using the acoustic source term as it is, the acoustic solution will be dominated by, or at least contain, a significant contribution from the mean pressure which can mask the fluctuating component. Since the mean component of the acoustic source does not contain any temporal information, it should be removed prior to execution of the acoustic solver. This is analogous to the step taken by Inoue & Hatakeyama (2002) in extracting the acoustic component from the instantaneous pressure field in their direct simulations because the pressure field also contained a time-invariant mean component.

To remove the mean component from the acoustic source term, the instantaneous acoustic source term is decomposed to a time-averaged component, H_o and a fluctuating $H^{'}$ component as follows

$$H^{'}(x, y, t) = H(x, y, t) - H_o(x, y), \tag{5.1}$$

where $H^{'}$ is the instantaneous acoustic source term after subtracting the time-averaged component. Prior to the removing the mean, the time-averaged acoustic source component is calculated through time averaging the acoustic source over a finite number of lift periods.

If the time-averaged component of the acoustic source term is not removed prior to the acoustic computation, the effect can be strong enough to lead the evolving pressure field to diverge. In passing, we note that similar behaviour seems to have been observed by Mitchell *et al.* (1997), in their study of co-rotating vortex pair sound using Lighthill's acoustic analogy. They found that the pressure field diverged during the calculations. The divergent nature of the pressure field in our study is probably due to the introduction of finer scales that are not well resolved on the acoustic grid even though considerable effort was made to maximise grid resolution. In any case, the mean source is irrelevant and even misleading, and thus, decomposition of the source into a mean and fluctuating component is important in numerical implementation of the acoustic analogy. It is worth noting here that the acoustic analogy is incapable of presenting an accurate description of the acoustic pressure in the rotational region of the flow. Direct numerical simulations can produce the fluctuating pressure field over the entire region but some means of decomposing the hydrodynamic and acoustic pressure must be performed if one is interested in the intermediate field acoustic behaviour.

The time development of the acoustic source terms, $H_l^{'}$ and $H_p^{'}$ are shown in a series of snapshots over one shedding cycle in figures 5.6 to 5.9. For both sources, the initial snapshots are taken at the same phase

of the shedding cycle. It is clear that the acoustic source fields of Lighthill and Powell are significantly different spatially. However, temporal-wise, both source formulations oscillate at the shedding frequency. From an implementation viewpoint, the input of the hydrodynamic fields into the acoustic computation is through quintic spline interpolation using 21 stored fields per Strouhal shedding cycle.

5.4.4 Initial condition

The acoustic simulations are started with the source term initially set to zero over the entire domain. Using a start-up function, the acoustic source field is then gradually ramped towards its true time-dependent form. At all three Mach numbers, the ramp interval was set to half the lift period. This amounted to approximately 1400–5600 acoustic time steps (depending on the Mach number) before the acoustic source finally reaches its true value. Such a long ramp interval was required in order to reduce the frequency of the initial wave transient, thereby reducing the generation of spurious waves as the solution propagates across the stretched grid. It is important to note that the selection of this particular ramp interval has been selected in conjunction with the local rate of stretching of 3%. Specifically, if the local rate of stretching was further reduced, the ramp interval could be further decreased. Conversely, the ramp interval might have to be increased if the local rate of stretching was more severe.

5.5 Results and discussion

As a precursor to discussing the results of the acoustic simulations, we first present the results of the flow simulations. The CFD simulations were performed at two different Reynolds numbers, $Re = 300$ and 400. In each case, a plate chord-to-thickness ratio of $c/d = 7$ was adopted. In the flow simulations, the plate is non-moving and is embedded in a fluid stream of unit freestream velocity. On the other hand, both the medium and the plate are assumed to be stationary in the acoustic simulation (due to the low Mach number approximation). This means the Doppler effect is excluded from the acoustic simulations. In the acoustic simulations, the hydrodynamic simulations at the given Reynolds numbers are used to predict the sound field at three different Mach numbers: Ma = 0.05, 0.1 and 0.2.

Flow dynamics

With the imposition of an initial condition of free-stream velocity everywhere in the domain, the flow field took approximately 80 to 100 non-dimensionalised time units to start developing an asymmetric pattern. The simulation then took a further 100 time units for the shedding of the vortices to become periodic. To monitor the flow state, a time trace of the base pressure coefficient, c_p, starting from the non-dimensionalised time of 250 is presented in figure 5.10. The measurement of the base pressure coefficient

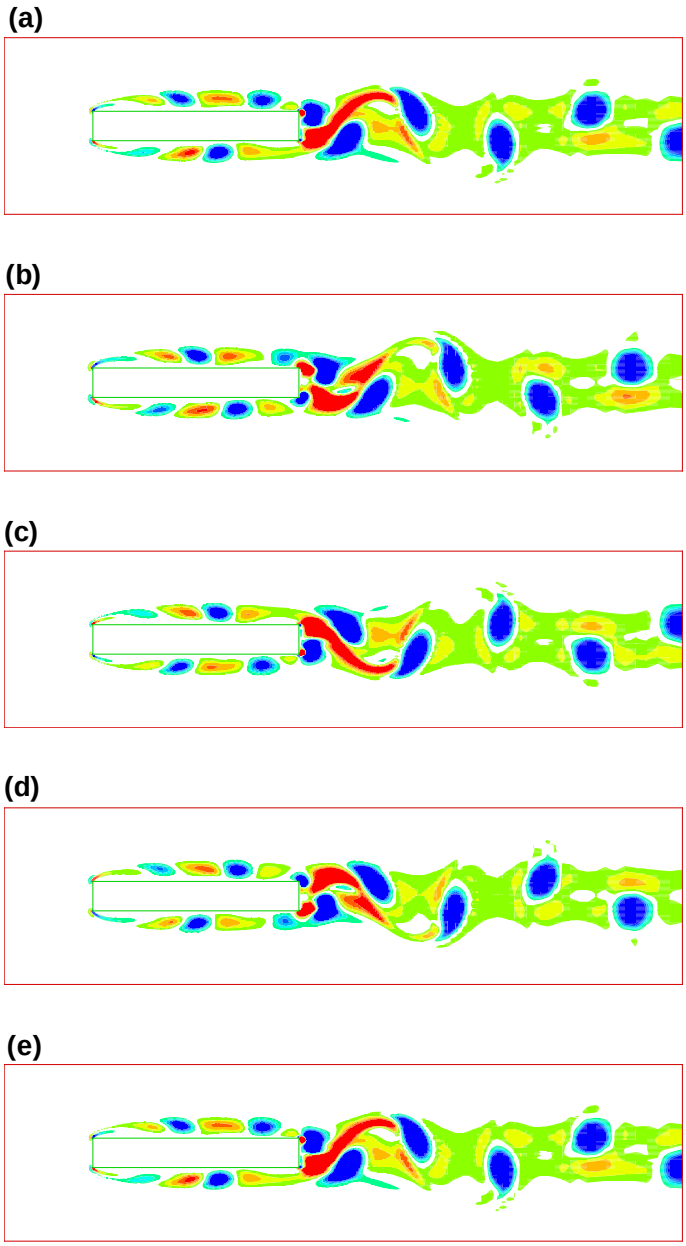

Figure 5.6: Snapshots of instantaneous acoustic source showing the time development of the source region around the plate. The forcing is evaluated using the Lighthill acoustic source term, H_l'. $Re = 300$. The times are: $t =$ (a) 253, (b) 254.5, (c) 256.3, (d) 257.8, (e) 259.6. The contour levels are $H_l = \pm 0.5$ with $\Delta H_l = 0.05$. The source term has been non-dimensionalised with respect to U_∞ and d.

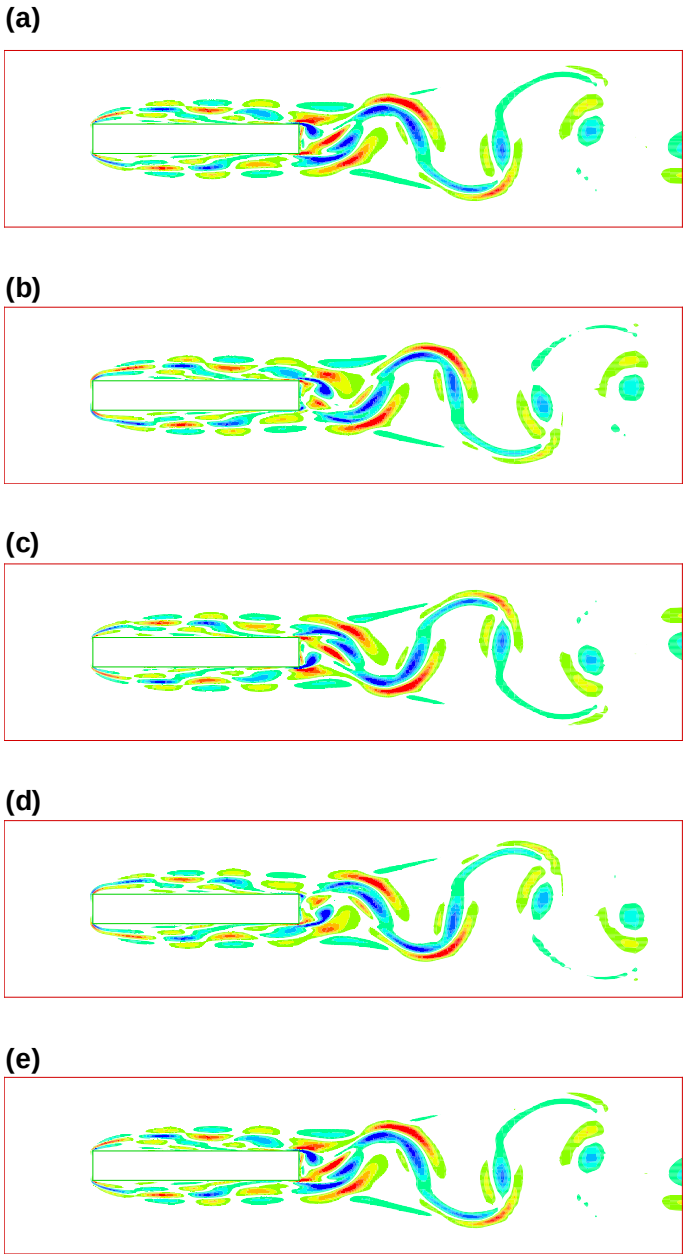

Figure 5.7: Snapshots of instantaneous acoustic source showing the time development of the source region around the plate. The forcing is evaluated using the Powell acoustic source term. $H_p^{'}$. Here, $Re = 300$. The times are: t = (a) 253, (b) 254.5, (c) 256.3, (d) 257.8, (e) 259.6. The contour levels are $H_p = \pm 4$ with $\Delta H_p = 0.4$. The source term has been non-dimensionalised with respect to U_∞ and d.

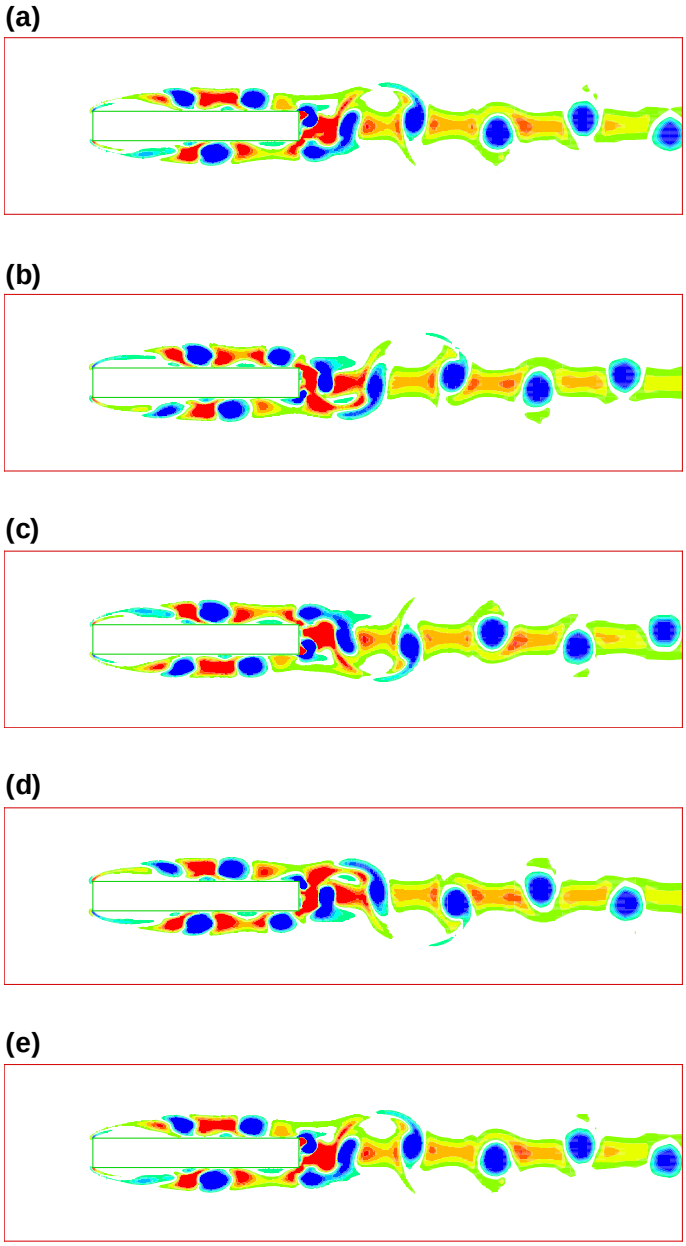

Figure 5.8: Snapshots of instantaneous acoustic source showing the time development of the source region around the plate. The forcing is evaluated using the Lighthill acoustic source term, $H_l^{'}$. Here, $Re = 400$. The times are: t = (a) 250.4, (b) 251.9, (c) 253.4, (d) 255.2, (e) 256.7. The contour levels are $H_l = \pm 1$ with $\Delta H_l = 0.1$. The source term has been non-dimensionalised with respect to U_∞ and d.

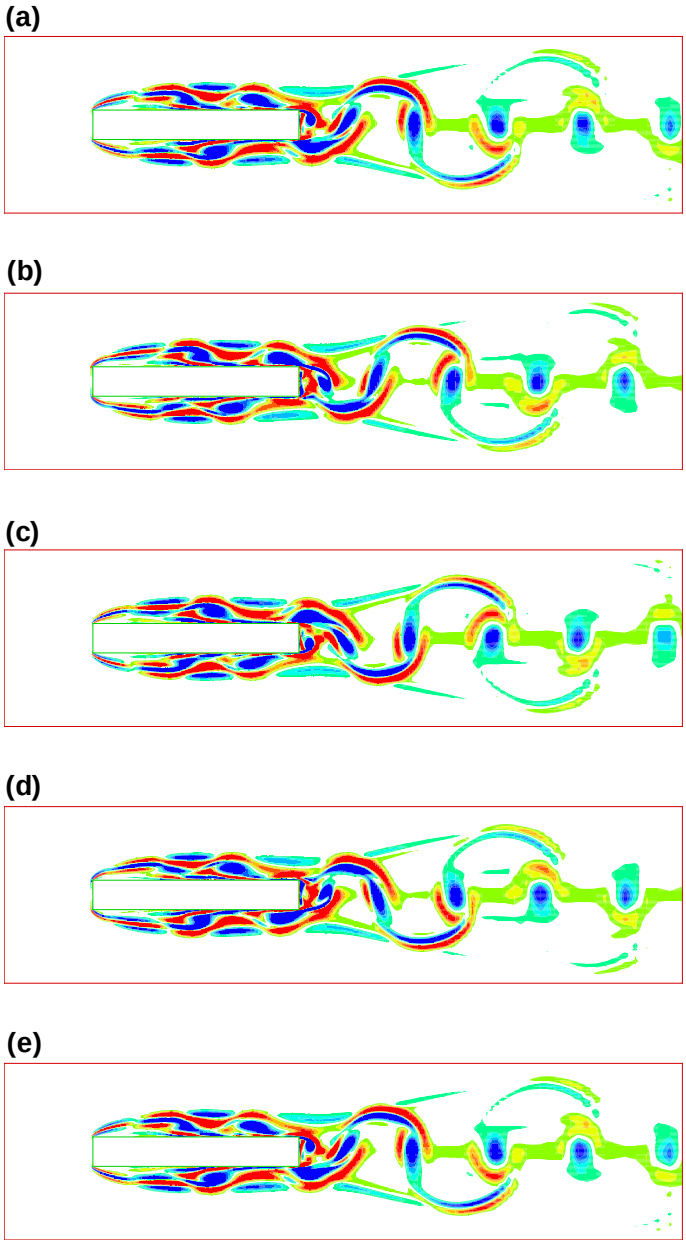

Figure 5.9: Snapshots of instantaneous acoustic source showing the time development of the source region around the plate. The forcing is evaluated using the Powell acoustic source term, $H_p^{'}$. Here, $Re = 400$. The times are: $t =$ (a) 250.4, (b) 251.9, (c) 253.4, (d) 255.2, (e) 256.7. The contour levels are $H_p = \pm 4$ with $\Delta H_p = 0.4$. The source term has been non-dimensionalised with respect to U_∞ and d.

Re	c/d	St	$\bar{c}_p$	$\bar{c}_d$	σ_{c_l}
300	7	0.152	-0.332	0.864	0.0973
400	7	0.156	-0.483	1.005	0.1655

Table 5.3: Shedding frequency, mean base pressure coefficient, mean drag coefficient, and standard deviation of the lift coefficient at the two Reynolds numbers simulated.

was taken at the centre of the trailing edge of the plate. It is clear from the figure that the flow has reached an asymptotic state in the Reynolds number range simulated. The signals at both Reynolds numbers become strictly periodic, indicating that the flow is strongly locked to the particular shedding mode. Furthermore, the mean and amplitude of c_p increase with the Reynolds number. As the base pressure is strongly related to the overall drag, this indicates that the amplitude of the fluctuating drag force also increases with Reynolds number.

The shedding frequency is estimated from the time histories of c_p. The period of c_p is half that of the shedding because the base pressure coefficient is measured at the centre of the trailing face of the plate. There was less than a 3% variation in the Strouhal number between the two Reynolds numbers (see Table 5.3).

The time development of the flow in the near field is depicted through a series of instantaneous plots of vorticity totalling one shedding cycle as shown in figures 5.11 and 5.12 for the two Reynolds number cases. For both Reynolds numbers, the first vorticity plot was taken at approximately the same phase of the shedding cycle. The figures show that the shedding process at both Reynolds numbers correspond to the $n = 2$ shedding mode. The figures also reveal that the vortices shed at the trailing edge occur in between the passing of the leading edge vortices over the trailing edge. Away from the plate, the leading- and trailing-edge vortices form a combined wake vortex which then convects at an approximately constant convective velocity. The phase of the leading- and trailing-edge shedding appears to be the same for both Reynolds numbers. From the figures, it is clear that the vortex shedding is more well-defined for the higher Reynolds number flow. In particular, the vortices along the plate chord are more concentrated and intense. In addition, the vortex formation region at the trailing edge is shorter with the vortices more compact at $Re = 400$. In contrast, at the lower Reynolds number, the vortices along the top and bottom sides of the plate are more diffusive and less compact. This is the likely explanation for the increased drag fluctuations shown later in figure 5.13b. As described previously, this particular aspect ratio leads to a strong lock-in of both leading- and trailing-edge shedding. The phasing just described is associated with this phenomenon. Tan *et al.* (2003) have found that strong lock-in and high base suction are associated with the leading-edge vortex not reaching the trailing-edge until the trailing-edge vortex has time to develop and begins to shed. This phasing varies little between different aspect ratios (due to the existence of a feedback loop), until a switch occurs to a new shedding mode.

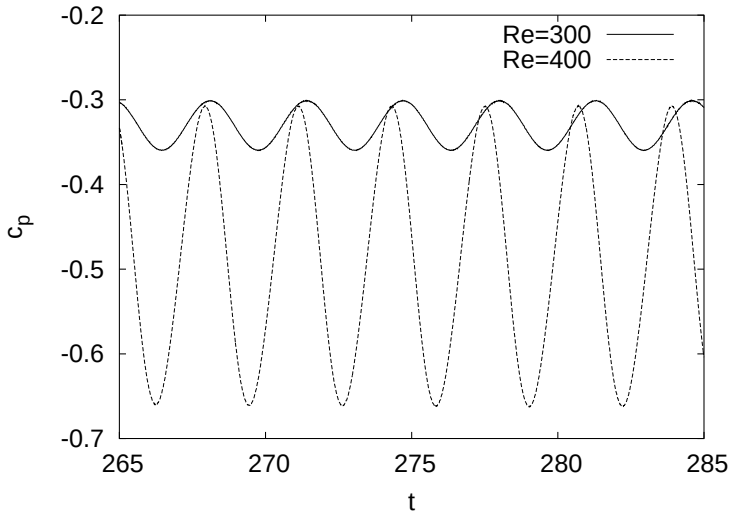

Figure 5.10: A sample trace of 25 time units of the base pressure coefficient taken at the centre of the trailing face.

5.5.1 Lift and drag forces

The aerodynamic forces acting on the plate are global quantities and as such, are obtained through integrating the pressure acting over the entire surface of the plate. In the case of a rectangular plate, the drag force is caused by the difference in pressure across the front and rear faces while the lift force is caused by the pressure difference across the top and bottom surfaces of the plate. Owing to the moderate Reynolds number of the flow, viscous forces are not expected to contribute significantly to the lift and drag forces.

The lift coefficient, c_l, and drag coefficient, c_d, (per unit span) are defined as follows

$$c_l = \frac{L}{0.5\rho_o U_\infty^2 c}, \tag{5.2}$$

$$c_d = \frac{D}{0.5\rho_o U_\infty^2 d}. \tag{5.3}$$

where L and D represent the dimensional lift and drag force components, respectively.

Inoue & Hatakeyama (2002) have shown that there is little variation in the magnitudes of both the lift coefficient and the drag coefficient for flow past a circular cylinder across the Mach number range Ma = 0.1 to 0.3 at a Reynolds number of $Re = 150$. Figure 5.13a and 5.13b show the time histories of the lift coefficient and the drag coefficient at $Re = 300$ and 400. Similar to c_p, the periodic nature of the time traces of both c_l and c_d indicate that the flow is strongly locked to the $n = 2$ shedding mode. As expected, the mean of the lift coefficient is zero because the plate geometry is symmetric about the x axis. Therefore, the standard deviation of the lift coefficient is used in the analysis.

Figure 5.13a clearly show that the variation in c_l increases as the Reynolds number is increased from

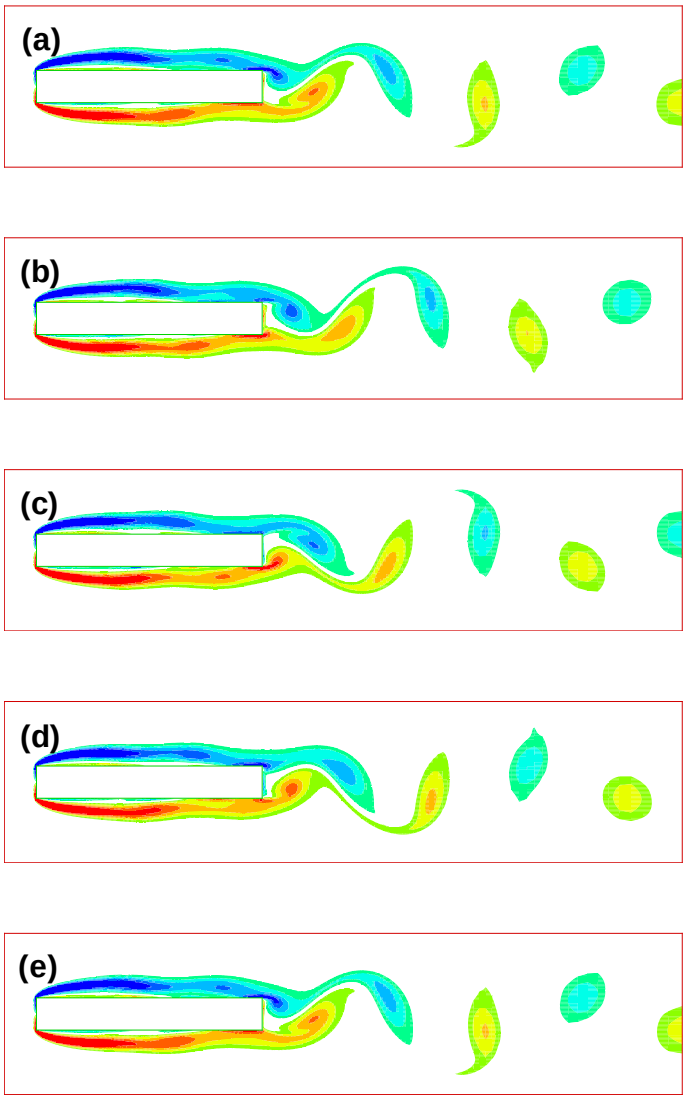

Figure 5.11: Snapshots of instantaneous vorticity to show the time development of the flow structure around the plate at $Re = 300$. The simulation time is $t =$ (a) 253, (b) 254.5, (c) 256.3, (d) 257.8, (e) 259.6.. The range of the contour levels is $\omega = \pm 3$ with $\Delta\omega = 0.3$. The vorticity has been non-dimensionalised with respect to U_∞ and d.

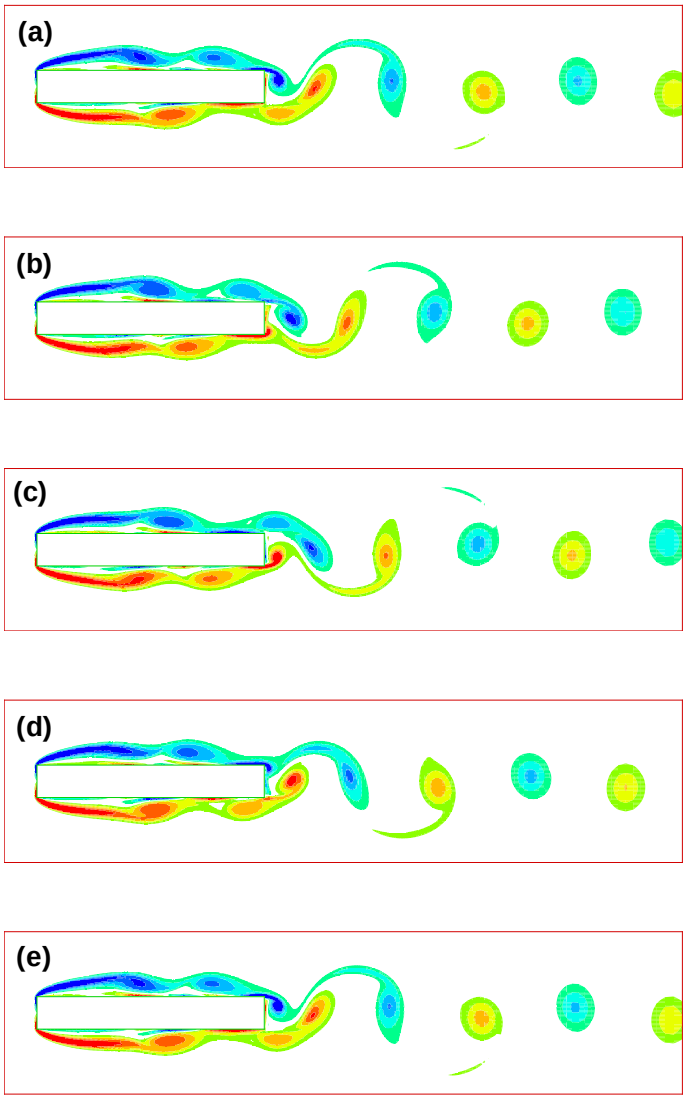

Figure 5.12: Snapshots of instantaneous vorticity showing the time development of the flow structure around the plate at $Re = 400$. The simulation times are: t = (a) 250.4, (b) 251.9, (c) 253.4, (d) 255.2, (e) 256.7. The contour levels are $\omega = \pm 4$ with $\Delta\omega = 0.4$. The vorticity has been non-dimensionalised with respect to U_∞ and d.

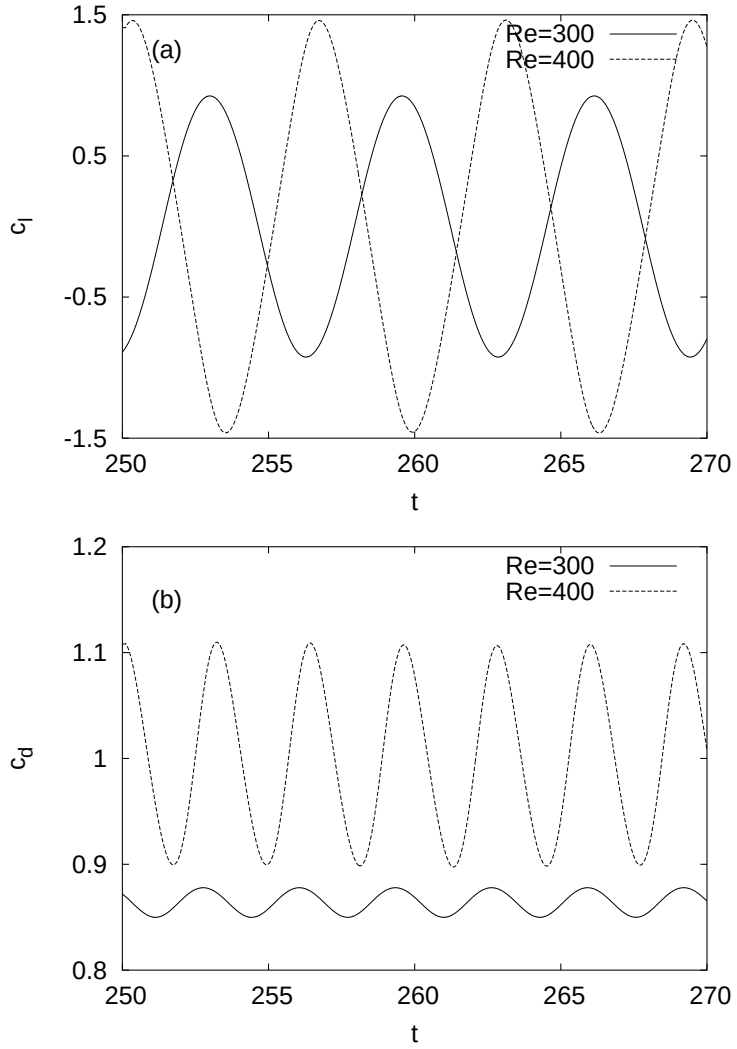

Figure 5.13: A sample trace of 30 time units of the (a) lift coefficient c_l, and (b) drag coefficient c_d, at the two Reynolds numbers.

$Re = 300$ to 400. The peaks in c_l are not in phase between Reynolds number as they are dependent on the initial conditions. This issue is however of little significance in this study. A more important point is that the increase in the magnitude of the lift fluctuations when the Reynolds number is varied from $Re = 300$ to 400 is attributed to the more intense vortex structures at the edge of the plate. The contributions to the lift force from the vortices along the top and bottom sides of the plate chord are negligible as they cancel each other out. Figure 5.13a also shows that the magnitude of the fluctuations in c_l is much greater than that of c_d. Using Etkin's *et al.* (1957) argument that the strength of the acoustic signal is proportional to the amplitude of the fluctuating force, this would suggest that in the present acoustic study, the lift dipole would be be much more significant than the drag dipole. After comparing the relative magnitudes in the lift and drag fluctuations, both lift and drag dipoles are expected to be more intense at $Re = 400$. While Inoue & Hatakeyama (2002) have shown that the acoustic generation mechanism is independent of Mach number in the range $0.1 \leq \text{Ma} \leq 0.3$, our results indicate that the source mechanism is influenced by the Reynolds number. These points will be examined in greater detail subsequently in section 5.5.2.

In the following section, we proceed to present the results of the aeroacoustic simulations. In the analysis of the acoustic-flow interactions, we investigate the effect of Reynolds number on the sound field. The differences in the acoustic solutions obtained from using the acoustic source terms of Lighthill and Powell are also discussed. The finding that the total force coefficient is non-zero, implies the existence of an acoustic monopole in the predicted sound field is plausible. This is analysed through decomposition of the sound field into harmonic modes.

As described, the acoustic simulations are performed at a low Mach number, however, using the spatial transformation $r^{'} = r/(1 - M\cos\theta)$, it is possible to postprocess the field predictions to include the Doppler effect of the moving fluid medium. This is discussed in more detail below.

5.5.2 Propagation and decay of the acoustic waves

As mentioned for the flow simulation, the acoustic simulations were conducted at three different Mach numbers, Ma = 0.05, 0.1 and 0.2. While the flow solver was started from an irrotational, stationary state, data acquisition for the evaluation of the acoustic source term was carried out only after the flow had reached an asymptotic state corresponding to about 30 shedding periods. This is to ensure that the hydrodynamic velocity field used to generate the acoustic source field for the CAA solver corresponded to the fully locked shedding mode. The acoustic simulation was subsequently evolved for approximately four shedding cycles.

Time histories of the acoustic pressure fluctuations located at $(r, \theta) = (0.5\lambda, \pm 90^{\circ})$ for Ma = 0.05, 0.1 and 0.2 are shown in figures 5.14 (calculated using H_l), and figures 5.15 (calculated using H_p). The spatial

term r is the polar radius while the angle θ is measured from the x axis. The designated observation points are representative of the far-field acoustic behaviour because further monitoring positions located between 0.5λ and 2λ showed identical propagation characteristics. The pressure traces are provided for both the predictions based on Lighthill's source and Powell's source. It is clear that both source formulations are producing acoustic signals that are virtually indistinguishable from one another. This is despite the seemingly extreme difference in the spatial distribution of the source fields as seen earlier in figures 5.6—5.9. This emphasizes that it is the temporal variation of the source terms that is ultimately responsible for determining the properties of the acoustic signals.

The first peak in the time histories of the acoustic signals showed a slight difference in both amplitude and frequency when compared with the subsequent peaks. This is because it was partially a result of the start-up function. It is clear that the moderate local rate of stretching coupled with the start-up function has restricted the initial transients so that they do not overly contaminant the true field and can be successfully propagated out of the domain.

At the selected angle of $\theta = \pm 90°$, the amplitude of the fluctuations is at its maximum in accordance with the direction of the lift force. This is expected because the shedding of the leading- and trailing-vortices is symmetric about the x axis. The frequency of the acoustic oscillations matches the shedding frequency indicating the acoustic signals are also locked to the shedding mode $n = 2$. At both Reynolds numbers, each time the Mach number is halved, the amplitude of the sound signal drops by approximately an order of magnitude. At a particular Mach number, the acoustic signal increases with Reynolds number indicating that the strength of the acoustic generation mechanism increases with Reynolds number.

Typical coloured contours of the far-field pressure at the three different Mach numbers are presented in figures 5.16a-c for $Re = 300$, and figures 5.16d-f for $Re = 400$. The far-field pressure contours are taken at the instantaneous time of $t = 274$. At both Reynolds numbers, we can readily see that the acoustic solution is dominated by a dipole that is radiating from the plate in the direction normal to the fluid stream. Because the acoustic analogy does not include the effect of the Doppler shift, the signs of the pressure field at the three different Mach numbers are alternating at $\theta = \pm 90°$. Also, it is clear that the drag dipole is not immediately observable from the instantaneous contour plots. This may be due to the small amplitudes of the pressure fluctuations associated with the drag dipole which are masked by the more dominant lift dipole. This is consistent with previous discussion of the relative magnitudes of the lift and drag fluctuations.

At $Re = 300$, the temporal traces are close to sinusoidal over the entire Mach number range simulated. However, at $Re = 400$, while the traces are periodic over the Mach number range simulated, they become less sinusoidal as the Mach number is decreased. This is particularly apparent at the lower Mach number. This is in contrast to the time variations from those presented by Inoue & Hatakeyama (2002), which showed a sinusoidal time variation from Ma = 0.05 to 0.2. At Ma = 0.2, the time variations are sinusoidal

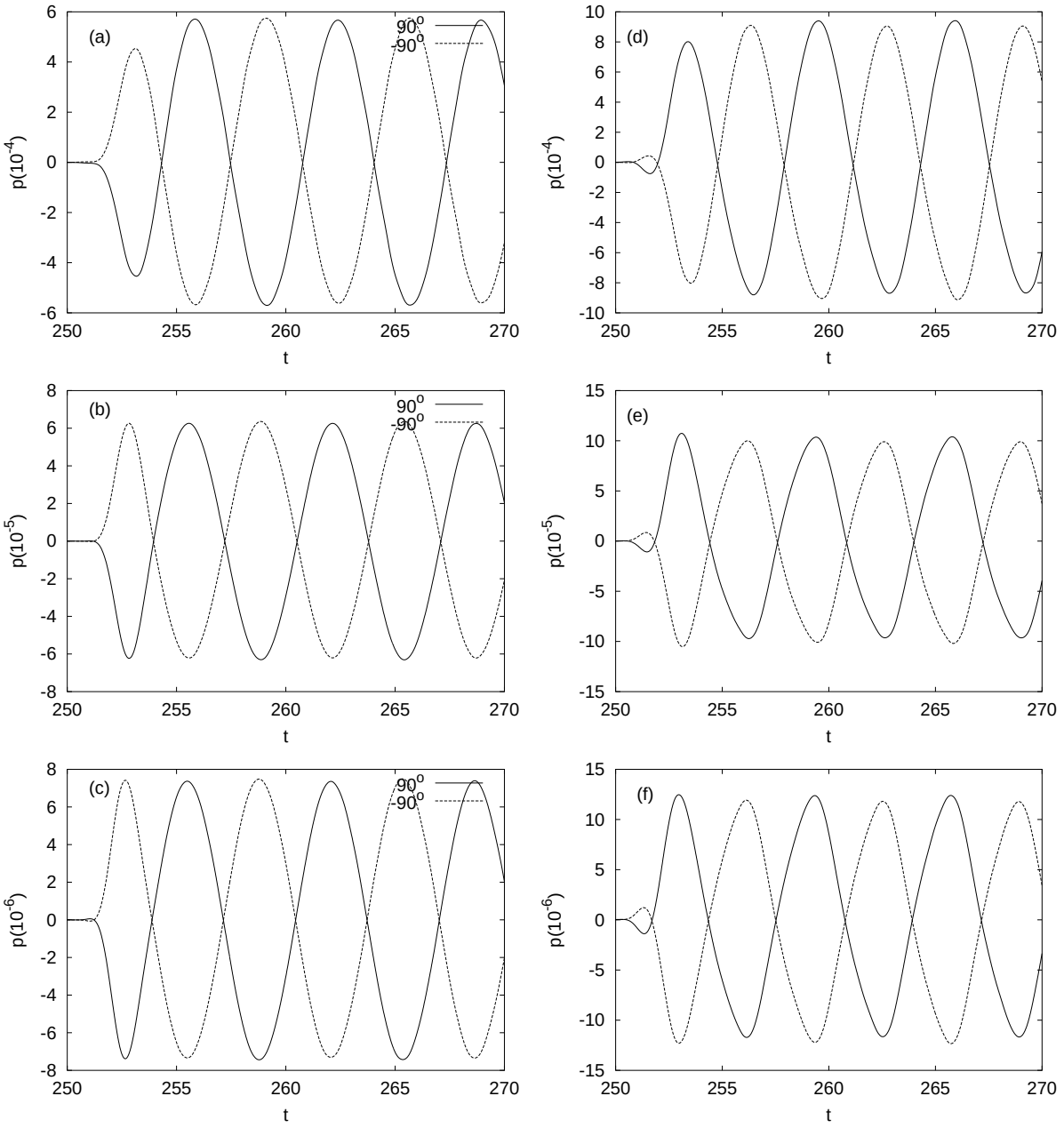

Figure 5.14: Time histories of acoustic pressure fluctuations calculated using H_l and located at $(r, \theta) = (0.5\lambda, \pm 90°)$ at the three different Mach numbers, Ma = (a)&(d) 0.2, (b)&(e) 0.1, (c)&(f) 0.05. Here, the figures on the left column are for $Re = 300$ while the figures located on the right column are for $Re = 400$.

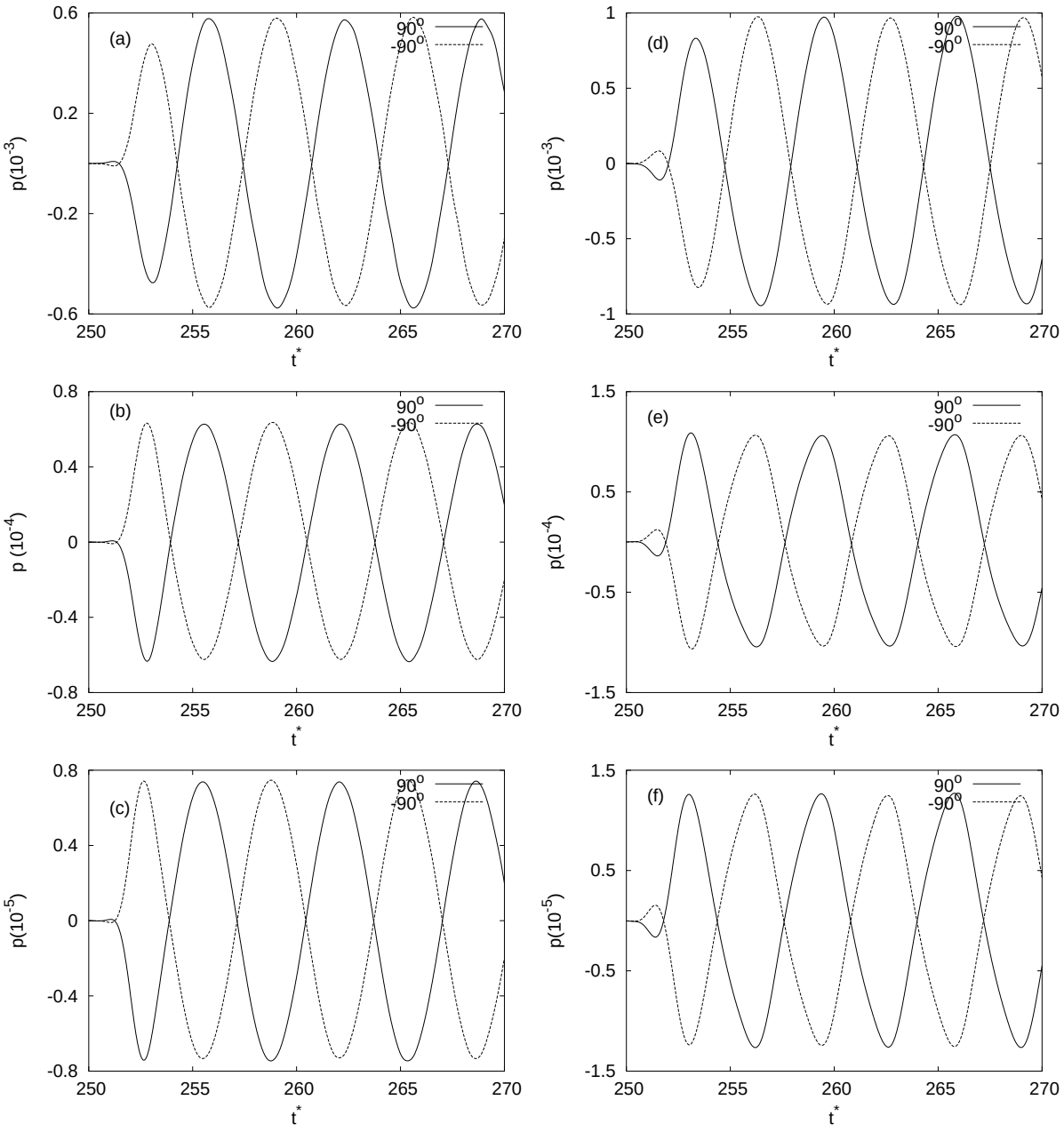

Figure 5.15: Time histories of acoustic pressure fluctuations calculated using H_p and located at $(r, \theta) = (0.5\lambda, \pm 90°)$ at the three different Mach numbers, Ma = (a)&(d) 0.2, (b)&(e) 0.1, (c)&(f) 0.05. Here, the figures on the left column as for $Re = 300$ while the figures located on the right column are for $Re = 400$.

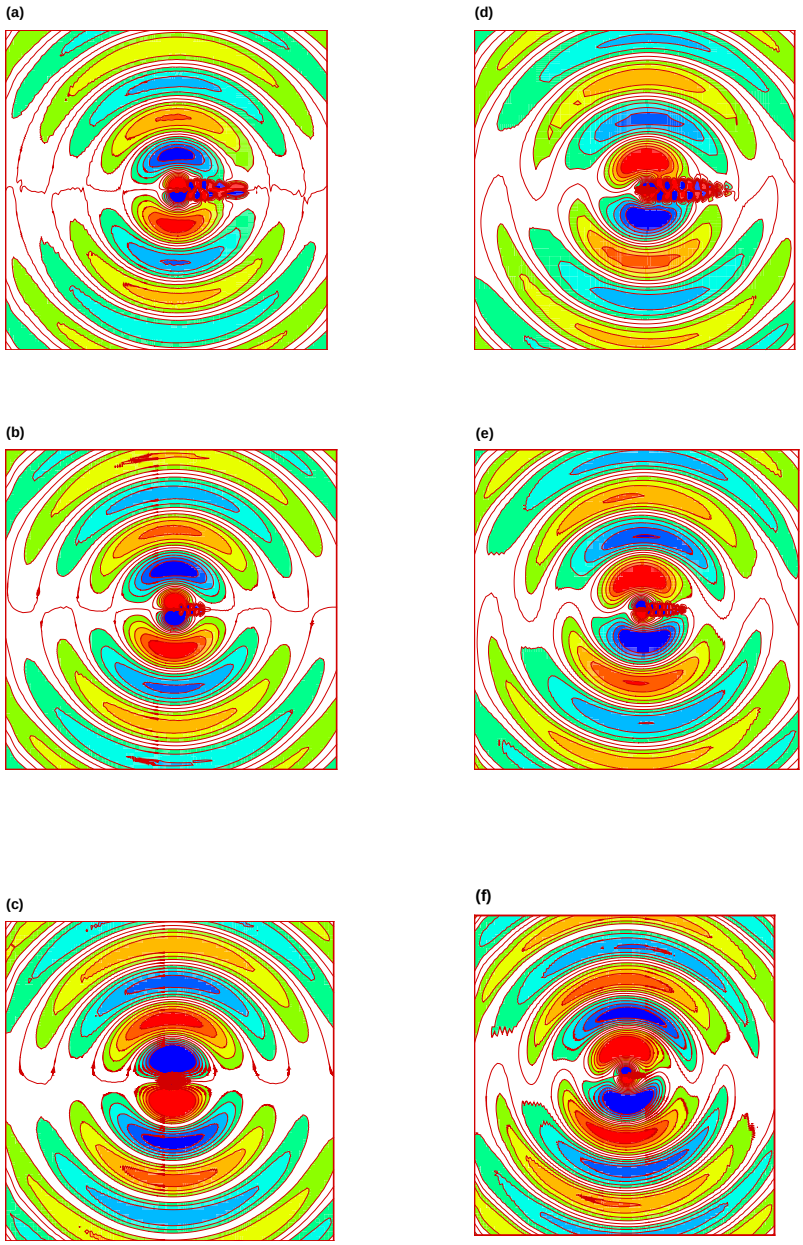

Figure 5.16: Contours of the acoustic pressure at a particular time instant of $t^* = 275$. Left-hand column represents $Re = 300$ and right-hand column represents $Re = 400$. The Mach numbers are: Ma = (a)&(d) 0.2, (b)&(e) 0.1, (c)&(f) 0.05. The minimum and maximum contour levels are: (a) $\pm 5 \times 10^{-4}$, (b) $\pm 5 \times 10^{-5}$, (c) $\pm 5 \times 10^{-6}$, (d) $\pm 7.5 \times 10^{-4}$, (e) $\pm 7.5 \times 10^{-5}$, (f) $\pm 7.5 \times 10^{-6}$. There are 10 increments between the minimum and maximum levels.

because the acoustic signals are more affected by the near-field hydrodynamic pressure fluctuations which are sinusoidal over time (as evident from the c_p plot). The locations of the monitoring positions in terms of the plate thickness decrease as the Mach number is increased. The fact the acoustic signal traces at low Mach number are not sinusoidal at $Re = 400$ is perhaps not surprising as the flow situation here is more complex than that of a circular cylinder. In particular, both the leading- and-trailing edge vortices may be associated with the maintenance of the sound field. In addition, despite the locking of both sheddings, it is not clear that they have the same phase relationship with respect to the acoustic oscillations. The higher Reynolds number also leads to more intense vortex structures that are likely to produce a non-sinusoidal near-field source and its associated acoustic far-field.

To show the decay of the pressure waves, radial distributions of the acoustic pressure fluctuations at $\theta = 90^\circ$ at different times are shown in figure 5.17. Note that the spatial distribution y in both figures do not start from zero. This is because the amplitudes of the pressure fluctuations near the plate are much larger than the amplitudes of the far-field acoustic fluctuations. Since the pressure fluctuations near the plate contain both near-field and far-field effects, the values close to the plate should be ignored when considering the decay of acoustic waves. It is clear that the pressure waves propagating away from the plate decay with radial distance.

The amplitude of the drag dipole is smaller than that of the lift dipole. Comparing the waveforms with those for the circular cylinder, the variation in shape may be explained in terms of pulses generated by vortex shedding. Leading-edge shedding and trailing-edge shedding from each side of the plate generate pulses which are out of phase. If each pulse generates a sinusoidal signal, the superposition from the leading and trailing edges combine to form a non-sinusoidal pressure.

5.5.3 On the relationship between the aerodynamic forces, vortex shedding, and the fluctuating acoustic pressure

In order to see the relationship between the aerodynamic forces and the time-development of the near-field flow structures, the time-history plot of c_l (see figure 5.13a) and the instantaneous plots of vorticity (see figures 5.11a-e and 5.12a-e) were used to correlate the lift force with the vorticity field. We found that whenever the lift coefficient has a positive peak, a vortex is shed off the upper trailing edge of the plate. Conversely, a vortex is shed off the lower trailing edge at times when c_l is a local minimum. This finding is consistent with the observations of Inoue & Hatakeyama (2002) even though the flow situation here is more complex.

Inoue & Hatakeyama have also found that the acoustic peaks on the upper and lower sides of the cylinder were in phase with the alternate shedding of the vortices from both sides of the cylinder. To shed further light into the relationship between the vortex shedding and generation of the acoustic waves in

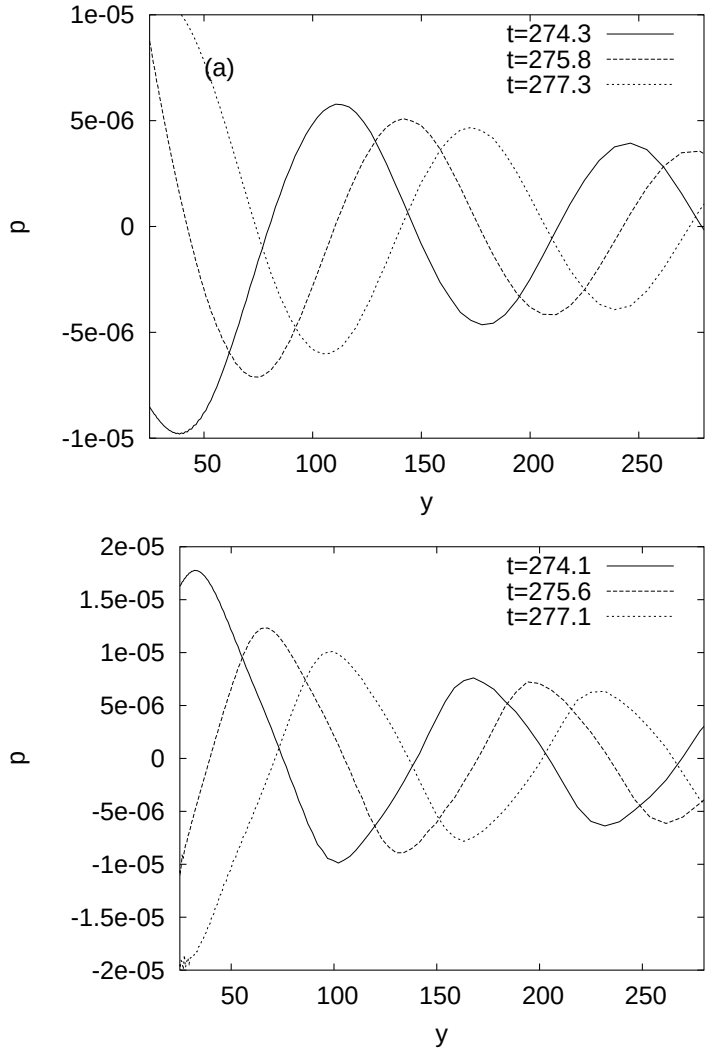

Figure 5.17: Spatial distribution of the acoustic pressure to show the propagation and decay characteristics. Here, Re = (a) 300, (b) 400.

the present study, the phase relationship between the shedding of a vortex structure at the trailing edge and the acoustic peaks is correlated through the instantaneous vorticity plots and the time histories of the far-field pressure fluctuations normal to the top and bottom plate chord. It is clear that the shedding of a vortex at the upper trailing edge corresponds to a negative pressure peak at $\theta = 90^\circ$ and a positive pressure peak at $\theta = -90^\circ$. Conversely, at a typical time instant when a vortex is shed off the lower trailing edge, the pressure peak at $\theta = 90^\circ$ is positive while the pressure peak at $\theta = -90^\circ$ is negative. This finding is similar to Inoue & Hatakeyama. In short, the alternate shedding of the vortices from the upper- and-lower trailing edges of the plate corresponds to the generation of negative and positive pressure peaks from the top and bottom sides of the plate chord.

Furthermore, Inoue & Hatakeyama went on to suggest that the generation of the acoustic waves can be described in terms of pressure pulses. These pulses are generated as a result of the vortex shedding from the sides of the circular cylinder. In contrast to the circular cylinder, vortex shedding occurs at both the leading- and-trailing edges of the plate. Since the leading- and trailing-edge shedding are locked, the pulses generated from the respective leading- and-trailing edge regions will also be locked in frequency. However, it is not clear that there will not be a phase difference between the two regions since vortex growth and subsequent shedding do not necessarily have to follow the same behaviour between the two regions. In addition, as the leading-edge vortices pass the trailing-edge region there may be another burst of sound generation. In fact, the passage past the trailing-edge occurs in between the formation and shedding of vorticity from the trailing edge. Thus, because of these phase differences, even if the individual source components all radiate sinusoidally, the combination is likely to lead to a non-sinusoidal far-field acoustic signal. Note also that the relative strengths of pulses generated from the leading- and-trailing edge are expected to differ.

An attempt is made to try to quantify the effective sound generation from both the leading- and trailing-edge regions in section 5.5.6.

5.5.4 The effect a non-stationary fluid medium: the Doppler shift

Inoue & Hatakeyama (2002) has already shown that the Doppler effect plays a significant role in the propagation of sound waves from the near-field to the far-field. Specifically, they found that at $\mathrm{Ma} = 0.2$, the acoustic waves propagate in the upstream direction at an angle $\theta = \cos^{-1}(\mathrm{Ma}) = 78.5^\circ$. The Doppler shift caused by finite Mach number has so far been ignored in this chapter. This is because the acoustic wave equation does not explicitly include a convective term (and this actually has advantages for interpreting the pressure field in terms of multipoles). However, since the convective term caused by a moving acoustic medium merely transports the pressure signal in the direction of the moving fluid, the effect can be included in the far-field signals through a post-processing step. This involves a spatial shift

in the radial position. The spatial transformation is defined as follows

$$r^{'} = \frac{r}{1 - \mathrm{Ma}\cos\theta} \tag{5.4}$$

where $r^{'}$ is the Doppler-shifted radial coordinate and the angle θ is measured in the clockwise direction from the $-$ve x axis. This relationship is valid if we assume that the Mach number is very small. At the particular angle of $\theta = \pm 90°$, the modified wave propagation speed, $c_o^{'} = c_o$, indicating that the acoustic waves are free from any Doppler's effect. However, $c_o^{'}$ has a local minimum at $\theta = 0°$. This implies that the pressure waves take longer to reach a specified far-field observation position. Conversely, at $\theta = 180°$, $c_o^{'} = (1 + \mathrm{Ma})c_o$ and as such, the pressure waves takes a shorter time to reach an equi-distance far-field observation position.

The instantaneous contour plots with the Doppler shift included in shown in figures 5.18. The deviation of the propagation angle from 90° of the (dipolar) acoustic waves when the Doppler effect is included is clearly seen when the pressure contour plots are compared to those without the Doppler shift. As found by Inoue & Hatakeyama (2002), the Doppler shift causes a twisting of the apparent dipolar field towards the upstream direction. While this effect is clear at Ma = 0.2, as the Mach number is decreased, the upstream twisting decreases and the propagation angle moves towards 90° at Ma = 0.05.

5.5.5 Decomposition of the sound pressure

In the limit Ma $\longrightarrow$ 0, the sound waves effectively propagate from the centroid of the plate. In the study by Etkin *et al.* (1954), the centre of the circular cylinder was assumed to be the location of the sound source. In the present study, the plate centroid is assumed to be the centre of the acoustic far-field.

Decomposition of the pressure waves into multipole components allows us to quantify the amplitudes of the various multipole components contributing to the overall sound field. The phasing of the aerodynamic forces, as presented earlier in section 5.5.3 suggests that the predicted sound field consists not only of dipolar components but a monopole and higher-order multipoles as well. Hence, to determine if this is true, a multipole decomposition needs to be performed. We adopt the same expansion of the pressure field used by Inoue & Hatakeyama (2002), i.e., the fluctuating acoustic pressure p is composed of the sum of harmonic functions as follows

$$p(x, y) = A_o(x, y) + B_m(x, y)\cos(m\theta) + C_m(x, y)\sin(m\theta). \tag{5.5}$$

where A_o is the zeroth-order mode, m is an integer between 1 and ∞, B_m is the m^{th} order cosine mode and C_m is the m^{th} order sine mode. The respective modes are defined from the following relations

$$A_o = \frac{\pi}{2}\int_0^{2\pi} p(x, y, t)d\theta, \tag{5.6}$$

$$B_m = \pi\int_0^{2\pi} p(x, y, t)\cos(m\theta)d\theta, \tag{5.7}$$

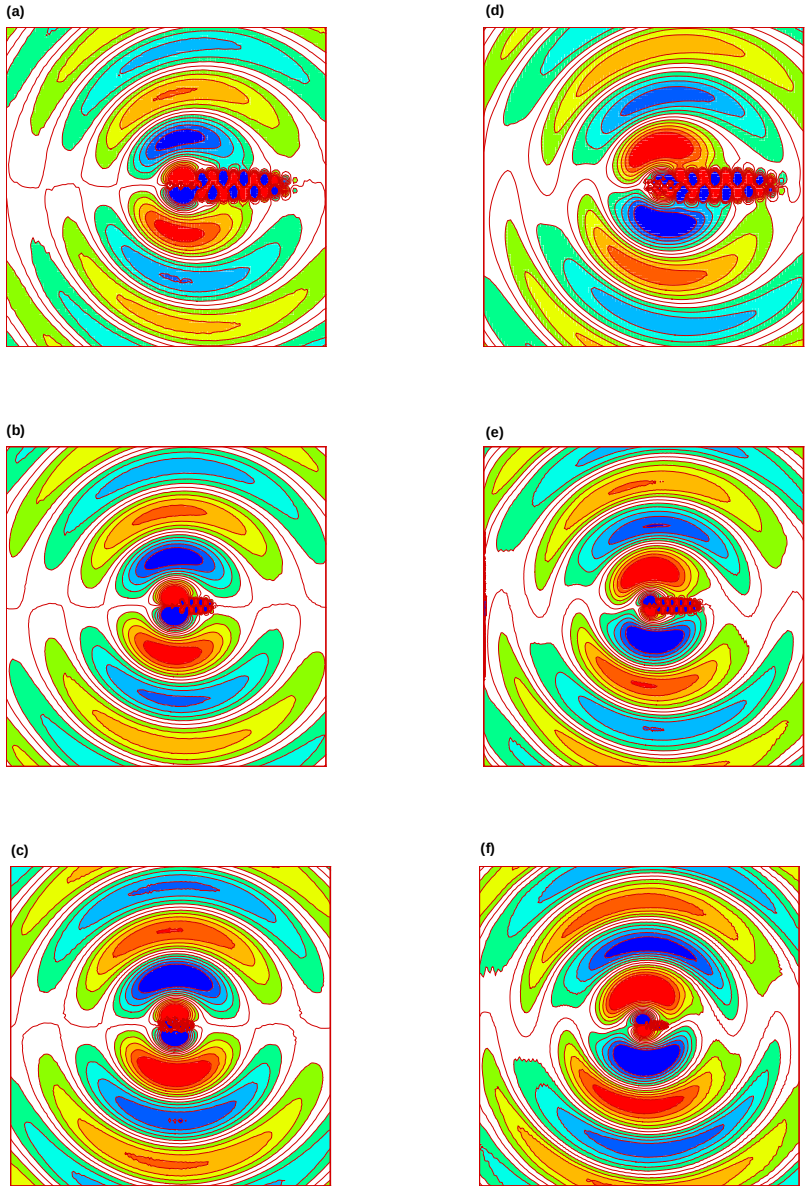

Figure 5.18: Contours of the Doppler-shifted acoustic pressure at a particular time instant of $t^* = 275$. Left-hand column represents $Re = 300$ and right-hand column represents $Re = 400$. The Mach numbers are: Ma = (a)&(d) 0.2, (b)&(e) 0.1, (c)&(f) 0.05. The minimum and maximum contour levels are: (a) $\pm 5 \times 10^{-4}$, (b) $\pm 5 \times 10^{-5}$, (c) $\pm 5 \times 10^{-6}$, (d)$\pm 7.5 \times 10^{-4}$, (e) $\pm 7.5 \times 10^{-5}$, (f) $\pm 7.5 \times 10^{-6}$. There are 10 increments between the min and max contour levels.

$$C_m = \pi \int_0^{2\pi} p(x,y,t)\sin(m\theta)d\theta. \tag{5.8}$$

The first-order sine harmonic component, C_1 is an odd-order function that has a directivity normal to the fluid stream and as such, represents the lift dipole. Conversely, the first-order cosine harmonic, B_1 is aligned parallel to the fluid stream and is known as the drag dipole. The values of the harmonic modes were obtained by numerically integrating the pressure fluctuations along a circle at $r = \lambda$. Only modes up to $m = 3$ are included as the contributions of higher-order modes are too small to be of any real significance. Since the CAA grid is Cartesian, the bilinear method was used to interpolate the nodal values from the grid to the radial integration points. The integration method used was Simpson's 1/3 rule with 50 increments over 2π. It was verified that the results were insensitive to the number of increments.

On the effect of source compactness

Figures 5.19(a)-(c) show the time histories of the amplitudes of the harmonic sine modes, $C_{n=1,2,3}$, at $Re = 300$. It is clear that the dominant mode corresponds to the $n = 1$ sine mode. This indicates that the lift dipole is dominant at all three Mach numbers. The amplitudes of the higher-order sine modes become more prominent as the Mach number is increased owing to the non-compactness of the source region. This is also seen in the time histories of the cosine modes, $B_{n=1,2,3}$, as shown in figures 5.19(d)-(f). The cosine modes oscillate at twice the shedding frequency. In contrast to the sine modes, the drag dipole was found to be only dominant relative to the $m = 2$ and $m = 3$ cosine modes at a Mach number of Ma = 0.05. At Ma = 0.1 and 0.2, the amplitudes of all the three cosine modes were comparable. This indicates that at higher Mach numbers, the drag dipole is not the significant cosine mode because the non-compactness of the acoustic source term results in other modes having similar amplitudes to the drag dipole. This is consistent with the observations of Hardin & Pope (1984) who found that the fourth-order harmonic was larger than the second-order harmonic when measuring the drag coefficient c_d.

The time histories of the amplitudes of the harmonic modes at the higher Reynolds number $Re = 400$ are shown in figures 5.20(a)-(f). Basically, the observations that were reported for the $Re = 300$ case are also found for the $Re = 400$ case. Again, the lift dipole component, C_1 is dominant at all three Mach numbers. In addition, the drag dipole only became significant at the lowest Mach number simulated: Ma = 0.05.

There are, however, two differences that should be noted between the results at the two Reynolds numbers. Firstly, the relative strength between C_l/B_1 was approximately two orders of magnitude when the Reynolds number was $Re = 300$. At $Re = 400$, the difference between C_1/B_1 has dropped to approximately one order of magnitude. This means that the drag dipole becomes more important as the Reynolds number is increased. However, it is also clear that the lift dipole is still considerably larger in the range of Reynolds number simulated in this study. Secondly, the form of the lift dipole signal at

$Re = 400$ is less sinusoidal compared with the lower Reynolds number case.

On the presence of the zeroth-order mode (i.e., monopole)

Apart from the presence of the m^{th}-order harmonic modes, the decomposition also revealed the presence of a zeroth-order mode of uniform directivity oscillating at the drag frequency. As the Reynolds number is increased from $Re = 300$ to 400, the monopole increased by approximately one order of magnitude. Even though the monopole has only negligible influence on the acoustic field, it is however, of interest to understand the cause of its presence. Etkin's *et al.* (1954) mathematical representation of a concentrated point force results only in a pair of orthogonal dipoles and does not have a monopole component as predicted in this study. This is because the variation in phase of the total force vector acting over the cylinder ($\sqrt{c_l^2 + c_d^2}$) was not taken into consideration. While the lift and drag dipoles were proportional to the amplitudes of the fluctuating lift and drag forces, it is argued here that the phase variations of the force distributed over the surfaces of the plate would lead to a pulsating monopole of uniform directivity. Phase plots of c_l vs c_d for both Reynolds number are shown in figures 5.21. If the periodic variations of c_l and c_d were to traverse along the same curve, there would be no phase shift in the total force vector. However, it is clear that from figure this is not the case. Hence, this leads to the presence of a zeroth-order mode.

5.5.6 On the location of the dominant source region

In this section, localised spatial filtering is used to examine the hypothesis that the trailing-edge region is the location of the dominant acoustic source. Here, the acoustic simulation is performed with spatial filtering of the acoustic source field. In particular, the filtering is used to zero the source over certain spatial regions to try to isolate the major spatial contributor leading to energy input into the acoustic field. The resulting amplitude and phase of the far-field fluctuations are then compared with the previous results. This, in effect, then enables us to deduce the percentage contribution of different regions to the overall acoustic field.

In previous simulations, the horizontal spatial filter acts between 3 and 30 plate thicknesses downstream of the trailing edge. Here, to artificially remove the source near the trailing-edge region of the plate, the starting position of the spatial filter is moved inside of the trailing edge towards the plate centroid. The decay length, l_{fx}, is fixed at 3 plate thicknesses. This ensures that only the leading-edge region is captured as an acoustic source region. Simulations were performed with different starting positions to verify that the results were insensitive to this parameter.

Figures 5.22(a)&(b) show the time-histories of the fluctuations at Reynolds numbers $Re = 300$ and 400 at the identical Mach number of 0.05. It is clear that the amplitude of the acoustic signals are now

(f)

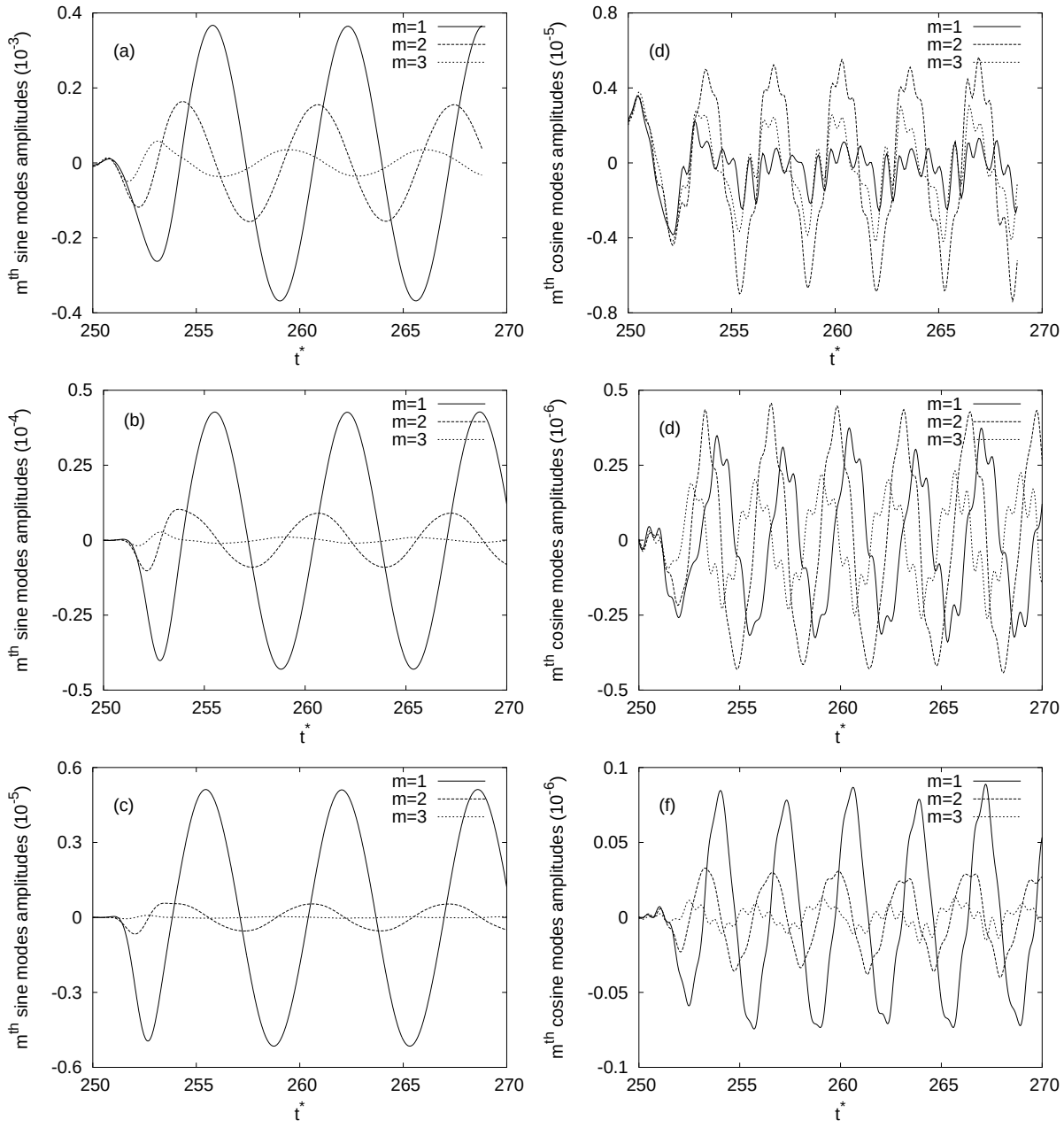

Figure 5.19: Time histories of the amplitudes of the cosine and sine modes at $Re = 300$. The amplitude of the wave modes are calculated by integrating over a circle at $r = \lambda$. The subfigures correspond to Ma = (a)&(d) 0.2, (b)&(e) 0.1, (c)&(f) 0.05.

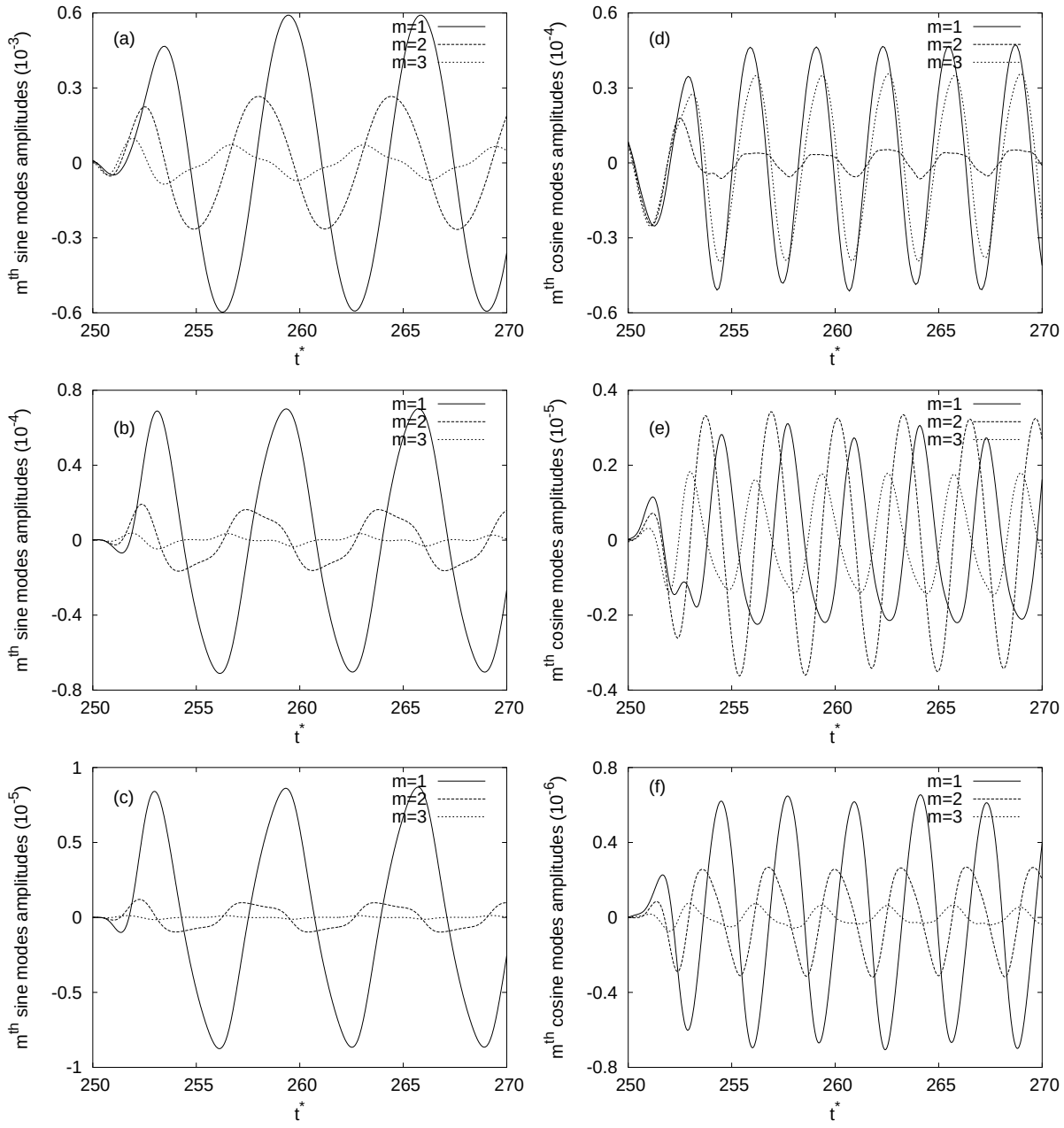

Figure 5.20: Time histories of the amplitudes of the cosine and sine modes at $Re = 400$. The amplitude of the wave modes are calculated over a circle at $r = \lambda$. Different subfigures correspond to Ma = (a)&(d) 0.2, (b)&(e) 0.1, (c)&(f) 0.05.

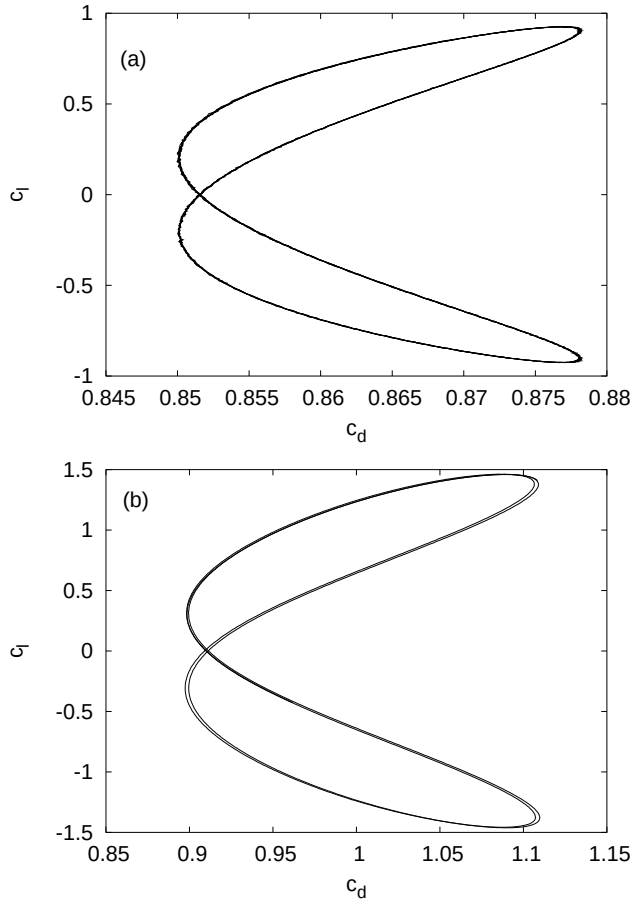

Figure 5.21: Phase plot of c_l vs c_d at $Re =$ (a) 300, (b) 400.

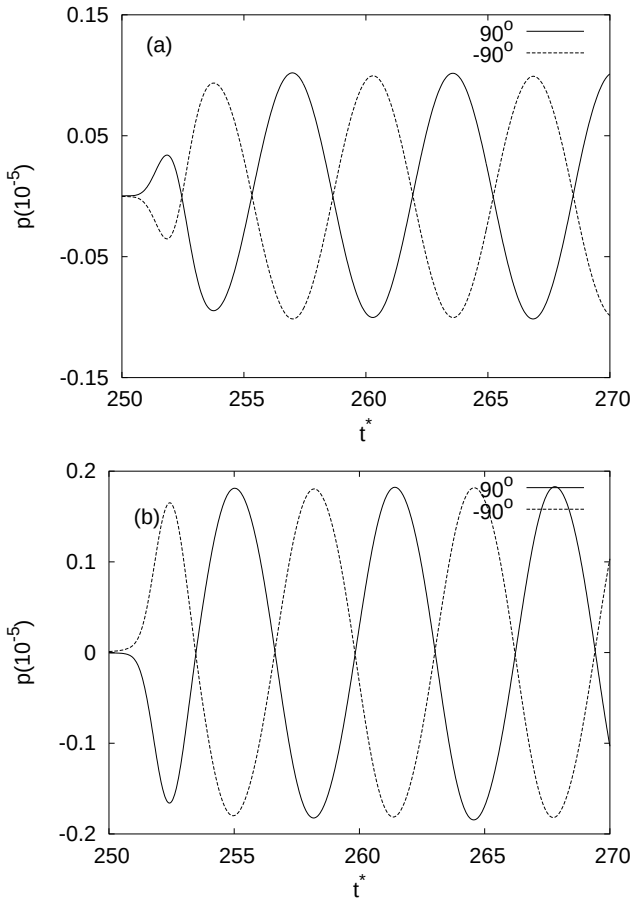

Figure 5.22: Time history of the acoustic signals at radial location $r = 0.5\lambda$. In these simulations, only the leading-edge region of the plate is captured when evaluating the source field. Here, the Reynolds numbers are: Re = (a) 300, (b) 400.

significantly weaker previously when the full acoustic source was included. In particular, at $Re = 400$, the contribution of the leading-edge region to the acoustic field is at most approximately 10% relative to the case with both the leading- and trailing-edge source contributions included. As such, the leading-edge region is a weak source compared to the trailing-edge region. This is consistent with Howe's (1975) interpretation of the acoustic generation mechanism. Another interesting point of note is the fact that time variations of the acoustic signals presented in figures 5.22(a)&(b) are close to sinusoidal at both Reynolds numbers. This suggests that the non-sinusoidal traces present at $Re = 400$ when both leading- and trailing-edge regions were considered are a result of the trailing-edge source region, or at least, the combination of the leading and trailing-edge regions.

5.6 Concluding remarks

Of the three aeroacoustic problems examined in this thesis, the numerical simulation of the aeroacoustics associated with vortex shedding from flow past a long, flat plate proved to be the most challenging. Apart from the increased difficulty in adequately resolving the flow field to provide accurate quantitative data for the acoustic source evaluation, the implementation of the steps in the acoustic modelling for this particular flow geometry was also found to be quite challenging. However, in terms of computational cost, the two-step aeroacoustic method is still considerably less expensive than direct simulations of compressible flows, especially at low Mach number.

Because the spatial decay of the Lighthill acoustic source field is much more gradual than that of the Powell acoustic source field, care must be taken to avoid introduction of spurious noise which may degrade the solution or even lead to divergence. In particular, the Lighthill source is more prone to problems with initial acoustic transients from switching on the acoustic source too suddenly, problems with filtering the source away from the dominant region near the body, and stretching of the acoustic grid. Mitchell *et al.*, (1995) also found similar problems with this formulation from a practical point of view. Since both formulations effectively radiate the identical acoustic signals at low Mach numbers, we strongly recommend Powell's vortex sound theory for further work on the aeroacoustic phenomena from flows past rigid bluff bodies.

In this investigation, the acoustic waves are generated from the strong lock-in between the leading- and-trailing edge shedding corresponding to the $n = 2$ shedding mode. The acoustic computations at $Re = 300$ and 400 produced similar radiating pressure distributions to those observed for a circular cylinder. The lift dipole clearly dominated the drag dipole by at least an order of magnitude in the amplitude of the far-field pressure fluctuations at the higher Reynolds number and more at the lower Reynolds number. However, although the drag dipole was not apparent for sound produced by vortex shedding from a circular cylinder, it was observable in this study. A key difference in the far-field fluctuations between the plate and the circular cylinder is the non-sinusoidal nature of the pressure time histories for the plate. This is especially apparent for the case of $Re = 400$, and for the lower Mach numbers: Ma = 0.05 and 0.1. We have suggested that this may be associated with the phase differences between different contributors to the acoustic source, in particular, the sources associated with vortex shedding from the trailing edge, and those from formation and shedding of leading-edge vortices and from the passage of the leading-edge vortices past the trailing edge. It may also be influenced by the more compact vortex structures for the flow past a plate which are more likely to produce a non-sinusoidal fluctuating force.

Preliminary results from using spatial filtering to isolate parts of the plate indicate that the primary acoustic source region lies near the trailing edge of the plate. The restricted simulations indicated that perhaps 90% of the acoustic energy generation was associated with trailing-edge region. Although we

have mainly concentrated on associating the sound source with the aerodynamic surface force components acting on the body, in future work, it would be useful to consider the alternative approach of Howe (1975, 1998), amongst others. In that interpretation, the acoustic source can associated with localised vortex structures, the flow field and the (potential) acoustic particle velocity. Energy transfer between the flow and acoustic fields can occur when the vortex structures cut across acoustic field lines. In particular, the direction of transfer depends on the phase of the acoustic field. This framework has previously been successful in identifying the main acoustic source with the trailing edge region of rectangular plate for resonant cases when the plate is placed in a duct (e.g., Hourigan (1991), Tan *et al.* (2003)).

Chapter 6

Concluding remarks

6.1 Summary

In this section, some of the important numerical issues encountered in the development of the two-step aeroacoustic prediction method are briefly reviewed. Specifically, the topics relevant to the numerical application of the aeroacoustic theories of Lighthill (1952), and Powell (1964) are covered. These include spatial filtering of the hydrodynamic fields, and the advantage of using a start-up function to slowly introduce the acoustic forcing. Furthermore, conclusions drawn from the interpretation of the results of this research and by past studies are also presented.

The aeroacoustic phenomena of three different flow scenarios have been considered in this study. In the first two cases, the sound field was generated by a spinning vortex pair, and a pair of co-axial vortex rings. In both of these flow situations, the flow field is spatially compact. In contrast, the final case considers the acoustic radiation caused by the natural shedding from laminar flow past a rectangular plate in a two-dimensional space. Owing to the slow recovery of the flow downstream which results in an extended *potential* acoustic source region, a more careful treatment of the downstream region is necessary. Thus, the final case forms a critical examination of the numerical scheme presented in this investigation owing to the increased complexity of the flow dynamics.

6.2 Solution procedure

The two-step prediction method consists of separate computations of the flow and acoustic solutions. In the first step, the viscous flow is predicted by numerically solving the incompressible Navier-Stokes equations. In the second step, the acoustic field is predicted by numerically solving the acoustic wave

equation. The acoustic forcing is specified by using either Lighthill's acoustic analogy or Powell's theory of vortex sound. Because the grids used in the flow and acoustic subproblems are different, the hydrodynamic fields from the flow simulation have to be spatially interpolated from the flow mesh to the acoustic mesh. If was found that it was possible to reconstruct the time-varying velocity field with just 16—24 snapshots per period if quintic splines were used for interpolation.

6.2.1 Numerical technique for CAA

According to Lighthill (1952), and Powell (1964), the governing equation for far-field sound generated aerodynamically is an inhomogeneous wave equation with the acoustic forcing calculated from the incompressible fluctuating flow velocities. Numerical differencing of the spatial derivatives is performed by using a sixth-order central-difference stencil based on a regular grid in computational space. A classical four-stage Runge-Kutta method is used to advance the acoustic solution in time. In general, it is preferable to use high-order methods, both spatially and temporally, when modelling acoustic wave propagation, thus minimising low-order truncation errors which can introduce artificial dissipation and dispersion. The near-field grid spacing is identical to that used to resolve the velocity gradients in the flow simulations. In the far-field, the mesh density was reduced so that there were approximately 20 points across an acoustic wavelength. The matching of the the near- and far-field grid spacings is dealt with using gentle stretching to prevent unphysical reflections as the waves propagate from the source. The time-step used to march the acoustic wave equation is approximately at the stability limits of the RK4 scheme. The radiation boundary condition based on Bayliss and Turkel (1980) is imposed at the computational boundaries.

6.2.2 Benchmark tests

Two benchmark tests are used to validate the numerical scheme, namely, the sound generated by a pair of co-rotating vortices, and the sound radiated from the motion of a pair of co-axial vortex rings moving along a common axis of symmetry in the same direction. These flow configurations were selected because both the flow and acoustic solution can be obtained analytically for the point vortex approximation. Furthermore, governing parameter ranges were selected to be similar to those from past numerical studies in order to facilitate a comparison with previous results.

Isolated co-rotating vortex pair

In the study of the sound generated by the unsteady motion of a pair of co-rotating vortices, the two vortices have identical circulation Γ_o, and are initially separated by a distance $2Z_o$. Owing to mutual

induction, the vortices rotate around one another with an angular rotational velocity of $\Omega = 8\pi^2 Z_o^2/\Gamma_o$. The Reynolds number based on the circulation of the vortex core was chosen as $Re = 7500$ while the Mach number based on the induced co-rotation velocity was Ma = 0.06. A Gaussian distribution was used to define the vorticity distribution of each vortex core. The ratio of the core radius to the separation of the two vortices was $e_o/2Z_o = 0.075$.

To highlight the difficulties associated with the large spatial extent of the Lighthill's acoustic source, the hydrodynamic velocities were abruptly terminated at three radial distances of $3Z_o, 4Z_o$ and $5Z_o$ away from the centre of the vortex system. In all three simulations, a start-up ramp time of $t_r U_o/Z_o = 2.56$ was used. Comparison of these simulations showed that there was considerable contamination of the far-field acoustic field for the two smaller radial distances. At the largest radial length tested, the acoustic field diverged. In practice, the slow decay rate of the source terms in Lighthill's acoustic analogy must be artificially enhanced to prevent divergence. In contrast, Powell's vortex sound theory was found to be less sensitive to the sudden termination of the source terms. This may be because the source term in Powell's vortex sound theory is proportional to vorticity which is localised spatially. In any case, spatial filters were applied to both source formulations.

In addition, the importance of a slow and smooth introduction of the source field to the acoustic computations was also shown through comparison of simulations with an impulsively-started condition and the use of a start-up function. It has been shown not only in these tests but by other researchers that an acoustic forcing that is impulsively introduced results in the generation of a large initial transient wave. Furthermore, the propagation of the initial transient wave through the non-uniform mesh generally results in high-frequency grid-to-grid oscillations. Through the use of the start-up function where the acoustic forcing is gradually ramped up to its true value, the negative impact of the initial transient can be largely avoided.

Co-axial vortex rings

In this study, the acoustic radiation from the leapfrogging motion of a pair of co-axial vortex rings was considered. The Reynolds number based on the circulation of the vortex core was $Re = 7500$. The effect of the toroidal ring radius was considered through a comparison of results for two different aspect ratios of $z_o/y_o = 0.3$ and 0.5. For each aspect ratio, the acoustic simulations were performed at three different Mach numbers of Ma = 0.0025, 0.005 and 0.01. The Gaussian vortex core which was used in the earlier validation study was once again used here.

In this study, the acoustic solutions were compared with the MAE analytical predictions. In the MAE analysis, the vortex system was considered spatially-fixed, radiating sound from a point. In order to compare the predicted acoustic solution with the MAE results, the rate of change of the mean axial

position of the vortex system was removed from the axial velocity component prior to the calculation of the acoustic forcing. This effectively pegs the vortex system so that for the acoustic computation, the source is radiating from a fixed position.

Through this study, we found that the six-point Lagrange interpolating polynomial which was used in the isolated co-rotating vortex pair with success, was not satisfactory in the present study. This was because the reconstruction led to noticeable kinks in the time variation of the acoustic signal. Furthermore, the frequency of these kinks corresponded to the interchanging of the frames used to interpolate the source field temporally. This led us to conclude that the interpolating polynomial is itself a potential source of spurious noise. After extensive testing with different types of interpolating polynomial, a global quintic spline was found to be the most suitable as both the function, derivative and curvature vary smoothly across data points.

6.2.3 Rectangular plate

One of the main objectives of the benchmark tests was to demonstrate that our numerical schemes were capable of accurately predicting sound from flow fields which are localised in space (i.e., compact flows). Comparison of the simulation results for the benchmark cases with both analytical predictions and past studies using more complex approaches have subsequently verified the capability of this numerical approach. As such, further development of the the two-step approach was pursued through applying it towards a more complex flow field. Hence, in a departure of the simple vortical flows, the final case study considers the acoustic radiation from laminar flow past a two-dimensional cylinder of rectangular cross-section. This is a natural extension to the body geometry of a two-dimensional circular cylinder.

In the present study, the effect of the Reynolds number on the sound radiation was considered. The Reynolds numbers chosen were $Re = 300$ and 400. A plate aspect ratio of $c/d = 7$ was used for both Reynolds numbers. This particular aspect ratio was chosen because previous studies (Tan 2000) showed that the lock-in between the leading- and trailing-edge shedding is both strong and periodic. For the acoustic viewpoint, this means that both the forcing and the acoustic field would be periodic.

Several preliminary flow simulations were carried out to determine the appropriate domain size and spatial and temporal resolution of the velocity gradients around the plate. These tests are an important part of the numerical procedure because the flow field was used in the calculation of the acoustic source for the CAA computation. A tolerance level of 5% was chosen as a reasonable compromise between computational cost and numerical accuracy in capturing the physics of the flow. Through a series of tests, a domain size of $15d$ from the leading face to the upstream boundary, and the chord to the top and bottom boundaries, and $45d$ from the trailing face to the outlet boundary was used. A minimum grid spacing of $\Delta x/d = 0.025$ was used to resolve the velocity gradients around the plate. The time-step used

to advance the flow simulations was set at $\Delta t U_\infty / d = 0.01$.

While the application of the spatial filter in the two benchmark cases can be easily justified because the flow fields were compact, this is not so in the case of bluff body flows. This is due to the extensive wake downstream of the plate which implies that the source region extends well away from the plate. However, the contribution to the acoustic source field from the wake was not expected to be relevant at the Mach number range simulated (Curle 1955). As such, the role of the spatial filtering is to remove parts of the wake so that the source field converges to zero. It is also clear that any resulting fluctuations introduced from the application of the spatial filter must be many times smaller than the physical acoustic waves.

In the previous benchmark cases, in general, the magnitude of the fluctuations in the source was greater than its mean and as such, the acoustic pressure field accurately portrayed the effects of the fluctuations in the source terms. However, in the case of the natural shedding from the bluff body, the mean component of the source dominates the fluctuations. As a result, the acoustic pressure field contained a fluctuating component as well as a mean component. Since the mean component of the source field is time-invariant, it is preferable to remove it prior to performing the acoustic simulations. This was done through subtracting the time-averaged component of the source field from the instantaneous source field. The issue of a mean pressure field also occurred in the direct simulations of Inoue & Hatakeyama (2002) who had to perform a similar decomposition of the compressible pressure field into a fluctuating and mean component in order to accurately describe the acoustic pressure fluctuations.

On the decomposition of the sound field into a multipole expansion

In the study of acoustic radiation from simple inviscid flow configurations, Möhring (978), Kambe & Minota (1981), and Kambe (1986) derived an analytical far-field expression which was valid in the asymptotic limit of $\mathrm{Ma} \to 0$. As such, the effect of finite Mach numbers on the far-field directivity of the acoustic signals was ignored. However, this effect can be considered in the present study by performing a multipole expansion of the predicted acoustic field. This analysis was applied by Inoue & Hatakeyama (2002) to quantify the contributions of the various modes present in the acoustic field. The decomposition of the acoustic signals into harmonic modes is possible because the acoustic field is linear. By performing the decomposition over a range of Mach numbers, the contributions of the various harmonic modes can be quantified and their relationship with the Mach number analysed.

6.2.4 Results from simulations

Similarity among the three cases

At low Mach numbers, both Lighthill's acoustic analogy and Powell's vortex sound theory effectively produced identical sound signals. Hence, the assumption that was made by Powell that the term $\nabla^2(\mathbf{u}^2/2)$ can be neglected for low Mach number flows has been validated. This is in spite of the distinct differences in the spatial distributions of the two source formulations. It is clear that the spatial distribution acts like a potential sound source. The properties of the acoustic signals are actually determined from the time variations of the source field. In terms of numerical implementation, as the source field in Powell's vortex sound theory decays more rapidly in space than Lighthill's source, the former is recommended for future studies on aeroacoustic phenomena.

Co-rotating vortex pair

Classical acoustic analysis by Möhring (1978) and Kambe & Minota (1981), has shown that flow unsteadiness in the absence of solid boundaries results in a quadrupole sound field. In the flow configuration of a spinning vortex pair, the quadrupole field assumed a double spiral pattern which rotates in the same direction as that of the induced co- rotation velocity. The number of acoustic peaks corresponded to twice the number of co-rotation cycles owing to the symmetry of the motion. Results from this study showed five and a half co-rotation cycles before the vortices merged into a single entity. The amplitude and time variation of acoustic signals were in good agreement with analytical predictions and previous numerical studies. The direct simulations of Mitchell *et al.* (1995) showed a gradual increase in the amplitude of acoustic peaks leading to a local maximum at the instant of vortex merger. These acoustic features were also captured in our simulations.

Co-axial vortex rings

The acoustic radiation from the interaction of a pair of co-axial vortex rings was considered at two different aspect ratios of $z_o/y_o = 0.3$ and 0.5. In contrast to the near-sinusoidal time traces of the isolated co-rotating vortex pair, the acoustic signals consisted of a series of sharp peaks and rounded troughs. These observations were similar to the classical model. However, in contrast to the findings of Shariff *et al.* (1988), there were no wavy oscillations present. Using the argument given by Verzicco *et al.* (1997), the secondary frequency was related to the nutation of the vortex core and was found to be negligible in the present viscous simulations. The introduction of viscous effects also has an effect on the vortex dynamics during merger and consequently on the sound radiation. While the magnitude of the acoustic peak was largely dictated by the inviscid leapfrogging phenomenon, the variations in the time traces of the acoustic

signals were found to be caused by the quasi-periodic deformation of the vortex cores (particularly by the ring slipping through the other) during the leapfrogging motion. As the initial toroidal ring radius was decreased, the core distortion increases and hence, the variations in the acoustic time traces also became more noticeable. Another point of interest is that with a smaller initial toroidal ring radius, the number of leapfrogging cycles decreased. Through the decomposition of the acoustic signals to the zeroth-order mode and m^{th} order cosine harmonic modes, the first and second polar extinction angles were located at 59° to 61° and 123° to 129°. These values differ from the theoretical ones as predicted using the MAE technique because the trace of the source terms is not zero (Mitchell *et al.* (1999)).

Rectangular plate

The results from this study showed that the shedding at the leading- and-trailing edges of the plate led to a dipolar sound field. The dominant dipole, associated with the lift fluctuations radiates normal to the fluid stream, while the much smaller dipole (typically one order of magnitude less) is linked to the fluctuations in the drag force and radiates preferentially along the free-stream direction. While the lift dipole was easily obtained from the simulations at all three different Mach numbers simulated in this study, a decomposition of the sound signals had to be performed in order for the magnitude of the drag dipole to be quantified. It was also apparent that at Mach numbers of Ma = 0.1 and 0.2, that the drag dipole was not the dominant cosine harmonic mode indicating that if the source was not compact, the amplitudes of the higher-order cosine modes become comparable to those of the drag dipole. Whilst the effect of the free-stream velocity on the wave propagation is not explicitly included in the acoustic analogies, a post-processing step was carried out whereby the spatial positions of the predicted acoustic field were varied to take into account wave advection by the flow velocity. This spatial transformation has earlier been applied by Inoue & Hatakeyama in the acoustic solution calculated using Curle's (1955) acoustic analogy. Results showed that at Ma = 0.2, the directivity of the propagation pattern of the acoustic field shifted towards the upstream direction. This is in agreement with the direct simulations of Inoue & Hatakeyama (2002) for the circular cylinder.

One major difference between the rectangular plate and the circular cylinder is that with the former geometry, shedding occurs at both leading and trailing edges. Using the argument that the sound generation is a direct result of the vortex shedding, then, it is clear that the leading- and trailing-edge regions may act as separate and distinct sound sources. Furthermore, the vortices convecting along the longer sides of the plate are not expected to radiate much sound as they are expected to cancel each other out (this is also the reason why they are not expected to contribute towards the fluctuations in the lift force). The acoustic signals at the lower Reynolds number of $Re = 300$ were nearly sinusoidal. This is in agreement with the direct simulation results of Inoue & Hatakeyama (2002). However, at the higher Reynolds number of $Re = 400$, the traces became less sinusoidal at the lower Mach numbers. In order to isolate the dominant source region and also explain the non-sinusoidal nature of the time variations, the

role of the spatial filter was expanded so that only the leading-edge region of the plate contributed to the source field. It was found that the contribution from the leading-edge region was at most approximately 10% of the total sound pressure level, suggesting that the trailing-edge region is the dominant sound source. Furthermore, the non-sinusoidal nature of the temporal variations of the acoustic signals are caused by the phase difference between the passing of the leading-edge vortices in between the shedding of the vortices at the trailing edge.

Chapter 7

References

Batchelor, G.K., 1967, An introduction to fluid dynamics, Cambridge University Press.

Bayliss, T., and Turkel, E., 1980, Radiation boundary conditions for wave-like equations, *Comm. Pure Appl. Maths.*, Vol. **XXXIII**, 707–725.

Brentner, K.S., Cox, J.S., Rumsey, C.L. and Younis, B.A., 1996, Computation of sound generated by flow over a circular cylinder: an acoustic analogy approach, presented at the Second Computational Aeroacoustics Workshop on Benchmark Problems, Tallahassee, FL.

Bridges, J.E., and Hussain, A.K.M.F., 1987, Roles of initial condition and vortex pairing in jet noise, *J. Sound and Vibration*, Vol. **117**, 289–311.

Bridges, J. and Hussain, F., 1992, Direct evaluation of aeroacoustic theory in a jet, *J. Fluid Mech.*, Vol. **240**, 469–501.

Colonius, T., Lele, S.K., and Moin, P., 1997, Sound generation in a mixing layer, *J. Fluid Mech.*, **330**, 375–409.

Cox, J.S., Brentner, K.S., and Rumsey, C.L., 1988, Computation of vortex shedding and radiated sound for a circular cylinder: subcritical to transonic Reynolds number, *Theoret. Comp. Fluid Dyn.*, **12**, 233–253.

Crow, S.C., 1970, Aerodynamic sound emission as a singular perturbation problem, *Studies in Appl. Maths.*, Vol. **XLIX**, No. 1, 21–44.

Crighton, D.G., 1993, Computational aeroacoustics for low Mach number flows, *Computational aeroacoustics*, ICASE/NASA LaRC Seris, edited by J.C. Hardin and M.Y. Hussaini, Springer-Verlag, New York, 50–68.

Curle, N., 1955, The influence of solid boundaries upon aerodynamic sound, *Proc. Roy. Soc. A*, **231**, 505–514.

Dowling, A.P. and Ffowcs Williams, J.E., 1983, Sound and sources of sound, Ellis Horwood Limited.

Dyson, F.W., 1893, The potential of an anchor ring, Part II, *Philosophical Trans. of the Royal Soc. of London*, **A104**, 1041–1106.

Ekaterinaris, J.A., 1999, New formulation of Hardin-Pope equations for aeroacoustics, *AIAA J.*, **37**, No. 9, 1033–1039.

Etkin, B., Korbacher, G.K., and Keefe, R.T., 1957, Acoustic radiation from a stationary cylinder in a fluid stream, *J. Soc. Acoust. Am*, Vol. **29**, No. 1, 30–36.

Gerrard, J.H., 1955, Measurements of the sound from circular cylinders in an air stream, *Proc. Phys. Soc. B Lond.*, Vol. B**68**, 453–461..

Ffowcs Williams, J.E., and Hawkings, D.L., 1968, Shallow water wave generation by unsteady flow, *J. Fluid Mech.*, Vol. **31**, 779–788.

Fedorchenko, A.T., 2000, On some fundamental flaws in present aeroacoustic theory, *J. Sound and Vibration*, **232**(4), 719–782.

Fletcher, C.A.J., 1991, Computational techniques for fluid dynamics, Vol. 1 & 2, Springer-Verlag.

Hardin, J.C., and Lamdin, S.L., 1984, Aeroacoustic computation of cylinder wake flow, *AIAA J.*, **22**, 51–57.

Hardin, J.C., and Pope, D.S., 1994, An acoustic/viscous splitting technique for computational aeroacoustics, *Theoretical and Computational Fluid Dynamics*, Vol. 6, 323–340.

Hardin, J.C., and Pope, D.S., 1995, Sound generation by flow over a two-dimensional cavity, *AIAA J.*, Vol. 33, No. 3, 407–412.

Hourigan, K., Mills, R., Thompson, M.C., Sheridan, J., Dilin, P., and Welsh, M.C., 1993, Base pressure coefficients for flows around rectangular plates, *J. Wind Engng Ind. Aerodyn.* **49**, 311-138.

Howe, M.S., 1975, Contributions to the theory of aerodynamic sound, with application to the excess jet noise and the theory of the flute, *J. Fluid Mech.*, **71**, Pt. 4, 625–673.

Inoue, O., and Hatakeyama, N., 2002, Sound generation by a two-dimensional circular cylinder in a uniform flow, *J. Fluid Mech.*, **471**, 285–314.

Kambe, T. and Minota, T., 1981, Sound radiation from vortex systems, *J. Sound and Vibration*, **74**(1), 61–72.

Kambe, T., 1984, Influence of viscosity on aerodynamic sound emission in free space, *J. Sound and Vibration*, **95**(3) 351–360.

Kambe, T., 1986, Acoustic emissions by vortex motions, *J. Fluid Mech.*, **173**, 643–666.

Kato, C., Iida, A., and Ikegawa, M., 1995, Numerical simulation of aerodynamic sound radiated from low Mach number turbulent wakes, *ASME Computational Aeroacoustics*, FED-Vol. **219**, 53–58.

Lamb, H., 1932, Hydrodynamics, Cambridge University Press.

Landau, L.D. and Lifshitz, E.M., 1987, *Fluid Mechanics*, 2nd edn. Course of Theoretical Physics, Vol. 6, Pergamon.

Lee, D.J., and Koo, S.O., 1995, Numerical study of sound generation due to a spinning vortex pair, *AIAA J.*, **33**, No. 1, 20–26.

Lighthill, M.J., 1952, On sound generated aerodynamically I. General theory, *Proc. R. Soc. Lond.*, **A211**, 564–587.

Leonard, B.P., 1979, A stable and accurate convective modelling procedure based in quadratic upstream interpolation, *Comput. Methods Appl. Mech. Eng.*, Vol.**19**, 59–98.

Mankbadi, R.R. 1990, The self-noise from ordered structures in a low Mach number jet, *AIAA J.*, **32**, 897–906.

Mills, R.H., 1998, Vortex interactions in flows over bluff bodies, Ph.D. Thesis, Dept. of Mechanical Engineering, Monash University, Melbourne, Australia.

Mills, R.H., Sheridan, J., Hourigan, K. and Welsh, M.C., 1995, The mechanism controlling vortex shedding form rectangular bluff bodies, *12th Australasian Fluid Mechanics Conference* 10-15 Dec., Sydney, Australia, edited by R. W. Bilger, 227-230.

Mitchell, B.E., Lele, S.K. and Moin, P., 1995, Direct computation of the sound from a compressible co-rotating vortex pair, *J. Fluid Mech.*, **285**, 181–202.

Mitchell, B.E., Lele, S.K. and Moin, P., 1999, Direct computation of the sound generated by vortex pairing in an axisymmetric jet, *J. Fluid Mech.*, **383**, 113–142.

Möhring, W., 1978, On sound at low Mach number, *J. Fluid Mech.*, **85**, 685–691.

Müller, E.A. and Obermeier. M., 1967, The spinning vortices as a source of sound, *AGARD-CP22*, 22.1–22.8.

Naudascher, E., and Rockwell, D., 1994, Flow-induced vibrations: An engineering guide, Rotterdam, Brookfield, : A.A. Balkema.

Naudascher, E., and Wang, Y., 1993, Flow-induced vibrations of prismatic bodies and grids of prisms, *J. Fluids and Structures*, **7**, 341–373.

Nakamura, Y., Ohya Y. and Tsuruta, H., 1991, Experiments on vortex shedding from flat plates with square leading and trailing edges, *J. Fluid Mech.*, **222**, 437–447.

Nakayama, R., Nakamura, Y., Ohya, Y., and Ozono, S., 1993, A numerical study of the flow around flat plates at low Reynolds number, *J. Wind Ind. Aerodyn.*, **46 & 47**, 255–264. Norbury, J., 1973, A family of steady vortex rings, *J. Fluid Mech.*, **57**, 417–431.

Ohya, Y., Nakamura, Y., Ozono, S., Tsuruta, H., and Nakayama, R., 1992, A numerical study of vortex shedding from flat plates with square leading and trailing edges, *J. Fluid Mech.*, **236**, 445–460.

Oshima, Y., Kambe, T., and Asaka, S., 1975, Interactions of two vortex rings moving along a common axis of symmetry, *J. Phys. Soc. Jpn.*, Vol. **38**, No. 4, 1159–1166.

Parker, R., and Welsh, M.C., 1983, Effects of sound on flow separation from blunt flat plates, *Intl.*

J. Heat and Fluid Flow **4**, 113–127.

Patankar, S.V. and Spalding, D.B., 1972, , A calculation procedure for heat, mass and momentum transfer in three-dimensional parabolic flows, *Int. J. Heat Mass Transfer*, Vol. **15**, 1972, 1787.

Phillips, O.M., 1956, The intensity of Aeolian tones, *J. Fluid Mech.*, **1**, 607–624.

Powell, A., 1960, Aerodynamic noise and the plane boundary, *J. Acoust. Soc. Am.*, **32**, No. 8, 982–990.

Powell, A., 1964, Theory of vortex sound, *J. Fluid Mech.*, **36**, 177–195.

Powell, A., 1990, Some aspects of aeroacoustics: from Rayleigh until today, *J. of Vibration and Acoustics*, **112**, 145–159.

Rayleigh, Lord, 1896, The theory of sound, Vol. I & II, Macmillan.

Ribner, H.S., 1962, Aerodynamic sound from fluid dilatations, Univ. Toronto Inst. Aerophysics Report No. 86.

Roshko, A., 1954, On the development of turbulent wakes from vortex sheets, *NACA Rep.* 1191.

Shariff, K., Leonard, A., and Ferziger, J.H., 1988, Acoustics and dynamics of co-axial interacting vortex rings, *Fluids Dynamics Research*, **3**, 337–343.

Shariff, K., Leonard, A., and Ferziger, J.H., 1989, Dynamics of a class of vortex rings, *NASA Technical Memorandum*, No. 102257.

Shen, W.Z., and Sorenson, J.N., 1999, Comment on the aeroacoustic formulation of Hardin and Pope, *AIAA J.*, **37**, 141–143.

Slimon, S.A., Soteriou, M.C., and Davis, D.W., 1999, Computational aeroacoustics simulations using the expansion about the incompressible flow approach, *AIAA J.*, **37**, No. 4, 409–416.

Stokes, A.N., and Welsh, M.C., 1986, Flow-resonant sound interaction in a duct containing a plate II: square leading edge, *J. Sound Vib*, **104**, 55–73.

Strouhal, V., 1878, Ueber eine besondere art der tonerregung, *Annu. Phys. Chem. (Weid. Annu. Phys.)* **5**, 216–251.

Tam, C.K.W., and Webb, J.C., 1993, Dispersion-relation-preserving finite difference scheme for computational acoustics, *J. Comp. Physics*, Vol. **107**, 262–281.

Tam, C.K.W., Webb, J.C., and Dong, Z., 1993, A study of the short wave components in computational acoustics, *J. Comp. Acoust.*, Vol. **1**, No. 1, 1–30.

Tam, C.K.W., 1995, Computational aeroacoustics: issues and methods, *AIAA J.*, Vol. **33**, No. 10, 1788-1796.

Tan, B.T., 2000, Vortex shedding and interactions in flows around bluff plates, Ph.D. Thesis, Dept. of Mechanical Engineering, Monash University, Melbourne, Australia.

Tang, S.K., and Ko, N.W.M., 1993, A study on the noise generation mechanism in a circular jet, *Transactions of the ASME, Journal of Fluids Engineering*, **115**, 425–435.

Tang, S.K., and Ko, N.W.M., 1995, On sound generated from the interaction of two inviscid coaxial vortex rings moving in the same direction, *J. Sound and Vibration*, **187**(2), 287–310.

Tang, S.K., and Ko, N.W.M., 1997, Sound generation by interaction of two inviscid two-dimensional vortices, *J. Acoust. Soc. Am*, **102**, (3), 1463–1473.

Versteeg, H.K., and Malalasekera, W., 1995, An introduction to computational fluid dynamics: the finite volume method, Longman Scientific & Technical.

Verzicco, R., Iafrati, A., Riccardi, G., and Fatica, A., 1997, Analysis of the sound generated by the pairing of two axisymmetric co-rotating vortex rings, *J. Sound and Vibration*, Vol. **200**(3), 347–358.

Wang, M., Lele, S.K., and Moin, P., 1996, Computation of quadrupole noise using acoustic analogy, *AIAA J.*, **34**, 2247–2254.

Wells, V.L., and Renaut, R.A., 1997, Computing aerodynamically generated noise, *Annu. Rev. Fluid. Mech.*, **29**, 161–199.

Williamson, C.H.K., 1996, Vortex dynamics in the cylinder wake, *Annals Rev. Fluid. Mech.*, **28**, 477-539.

Yamada, H., and Matsui, T., 1979, Mutual slip-through of vortex rings, *Physics of fluids*, Vol. **22**, No. 7, 1245–1249.

Yates, J.E., 1978, Application of the Bernoulli enthalpy to the study of vortex noise and jet impingement noise, *NASA Contractor Report*, **2987**.

Yudin, Y.E., 1947, On the vortex sound of rotating rods, Nat'l Advisory Comm. Aeron. Tech. Mem. No. 1136.

Yule, A.J., 1978, Large scale structures in the mixing layer of a round jet, *J. Fluid Mech.*, **89**, 413–432.